Earth, Environmental and Life Sciences
Princetonlaan 6
3584 CB Utrecht
P.O. Box 80015
3508 TA Utrecht
The Netherlands

www.tno.nl

T +31 88 866 42 56
F +31 88 866 44 75
infodesk@tno.nl

TNO report

TNO 2013 R10060

Anatomy of the Cenozoic Eridanos Delta Hydrocarbon System

Date 8 April 2013

Author(s) J. ten Veen, H. Verweij, T. Donders, K. Geel, G.de Bruin, D. Munsterman, R. Verreussel, V. Daza Cajigal, R. Harding, H. Cremer

Number of pages 217 (incl. appendices)
Appendices A-J (10)

Sponsors
- Energie Beheer Nederland B.V.
- Dana Petroleum Netherlands B.V.
- Total E&P Nederland B.V.
- Oranje Nassau Energie B.V.
- Chevron Exploration and Production Netherlands B.V.

Project name Shallow Gas 2
Project number 056.01718

Contents

Summary

In the Southern North Sea, shallow gas is defined as gas that occurs in unconsolidated sediments of Cenozoic age. It mainly resides in shallow marine to continental (deltaic) deposits of the Plio-Pleistocene Southern North Sea (SNS) delta. In seismic data, shallow gas appears as seismic reflections with anomalously high amplitudes, so-called bright spots. Despite the fact that shallow gas forms a challenge for production — it resides in unconsolidated sediment at shallow depth (<1 km) and reservoir pressures are low — several producing fields are located in the Netherlands. This report describes the results of the Joint Industry Project “Shallow Gas 2”, which aims to develop a reliable and effective workflow to de-risk these bright spots (DHI for shallow gas), which are observed in the Upper Cenozoic SNS delta in the Northern offshore. Next to bright spot volumetrics, gas saturation is a key, but hard to asses, parameter since no evident relationship exists between gas saturation and acoustic properties of bright spots in post-stack seismic data. Therefore, a multidisciplinary workflow was applied that attempts to quantify essential bright-spot properties and which allow the user to better predict the location, quantities, and quality of shallow gas prospects in the SNS Delta, as well as to quantify the conditions at which the gas is present. The main objective of the project is to generate a high resolution reservoir property model of all bright-spot occurrences, i.e. the potential shallow gas fields, and their hosting sediments. The main focus is on the A/B/F-blocks of the Dutch offshore, defined as a high potential shallow gas area. In order to assess the reliability and effectiveness of the developed workflow, as well as to place the model in larger context of the full Delta, critical data and information from the entire northern offshore is also incorporated. The model geometry is based on 2D- and 3D seismic interpretation of key horizons that are constrained by geobiological data that provided both an age model and a depositional model for the SNS delta succession. The precise coupling to absolute ages is derived from geomagnetic polarity data of well A15-3. Based on seismic analysis, core description and petrophysical well-log evaluation the model also predicts the distribution of lithofacies and depositional facies. In order to obtain an increased understanding of how the distribution of these facies are related to external (climate, tectonics, sea-level) and internal (delta lobe switching, avulsion) processes, a sequence-stratigraphic framework of the ABFDEG blocks was developed through integration of results from a pilot study performed on the A15 block (ten Veen et al., 2011), which in turn was used to guide seismic interpretation. This framework describes the strong coupling between climate and sediment properties related to glacial-interglacial cycles that show a marked contrast in grain size, sea surface temperature and climate. This framework provides critical knowledge of the architecture and distribution of these, yet not-well understood reservoirs and the continuity of sealing clays. Next to facies, the reservoir property model is also populated with petrophysical properties (V_{shale}, Phi, S_w) that might be relevant for assessing the reservoir quality. Another important aspect, next to reservoir quality, is to obtain information on seal integrity, to quantify the distribution of gas column heights that can be retained by sealing clays. The seal integrity is based on a grain size-based method to calculate capillary seal capacities of mud stones (sand <20%) and provides reasonable good estimates of maximum gas column heights for mudstone layers in the SNS Delta deposits. Deviations between grain size based calculated capillary seal capacities and actual gas column heights may be due to a wide variety of causes, such as insufficient gas charging and lateral changes in capillary seal properties (due to facies changes).

All individual, and occasionally, stacked bright spots are semi-automatically mapped from 2D/3D seismic data based on their anomalous amplitude values. These seismic interpretations are used to construct Bright Spot (BS) surfaces to which properties from the ABF property model are assigned. A BS data base was constructed that stores all relevant properties and other characteristics such as depth, size and stratigraphic interval. The BS can be classified as either “stacked 4 way dip closure”, “small stacked” (<2 km^2), “flat medium sized”, “elongated” or “foreset type”. Given the regional character of the study and large amount of BS data, a complete description of every BS is not

possible (the data can be consulted in a data base and Petrel© project provided). For this reason, the report summarizes BS property distribution both graphically and spatially in qualitative way in order to distillate certain rules for potential shallow gas fields.

The most important rules are:

- Elongated BS dominate in prodelta setting (at the paleo basin floor), non-stacked foreset type dominate in the inclined foreset beds, and stacked 4WD BS dominate in the topset all stratigraphic levels, Foreset type BS, only occur in unit. The presence of BS seem unrelated to depositional setting, the type, however, is strongly controlled by the structural setting, which appears to have dominant control on the formation of potential shallow gas traps. The only exception to this rule is the Foreset type BS in S5.
- Many of the small- and large stacked BS in the ABF blocks are associated with salt structures and/or faults. These BS types often appear “filled-to-spill as the BS reaches the structural spill point. However, gas column heights, either calculated using the grain size method or measured from cross-over plots or RFT data, show that many traps are not filled to structural spill point. Thus, the filled-to-spill criterion for BS appears unreliable measure for reserve estimations since large parts of the BS may not represent high-saturation gas.
- The occurrence of BS in a certain lithofacies is strongly coupled to stratigraphy and, due to the prograding and coarsening upward delta system, also to depth.
- Gas saturations known from well-penetrated BS, in general, are low but reach values up to 40% especially in Stacked 4WD BS and in the one foreset type BS observed. All other BS plausibly represent gas-filled sediment with Sg < 20%. It should be noted however that both petrophysical- and property modelling techniques applied tend to underestimate Sg.

Subsequently, these generalities were used to elaborate on four possible shallow gas system scenarios. These include, in a rough descending order of prospectivity:

- 4WD stacked gas reservoirs associated with foresets. The 4WD stacked gas reservoirs formed through syn-depostional salt doming,were charged with gas, and are located underneath previously charged foreset type depositional traps. The salt-dome related stacked reservoirs have higher gas saturations whereas residual gas remains in the foresets.

- Elongated sandwave reservoirs, which formed through syn-depositional salt doming and and were charged with gas in and through (up to 20 m high) contourite sand bodies. The salt-dome related stacked reservoirs have higher gas saturations, whereas the vast sand body-related BS have very low gas saturations.

- 4WDstacked gas reservoirs which formed through syn-depositional salt doming and were charged with gas in 4WD closures exclusively.

- Pockmark and local vent related gas accumulations, which form generally small and isolated gas pockets with low saturations.

1 Introduction

1.1 Southern North Sea (SNS) Shallow Gas systems in the Netherlands

In the Southern North Sea, shallow gas is defined as gas that occurs in unconsolidated sediments of Cenozoic age. It mainly resides in shallow marine to continental (deltaic) deposits of the Plio-Pleistocene Southern North Sea (SNS) delta (also referred to as Eridanos delta; Overeem et al., 2001), in Pleistocene tunnel-valley fill deposits and in volcanoclastics at the base of the Palaeocene (e.g. Basal Dongen Tuffite). Shallow gas is either structurally trapped in anticlines above salt domes or occurs in stratigraphic or depositional traps. Traditionally, shallow gas occurrences were regarded as hazardous or non-economically because of low gas saturations ("fizz gas"). However, interest in the Late Cenozoic Southern North Sea (SNS) delta deposits, especially in the northern Dutch offshore, has increased in the last few years due to the presence of commercial "shallow" gas. The location and size of the shallow gas fields are generally determined from seismic surveys, where sediments with a gas content of 5 % or more appear as areas of high reflectivity ("bright spots").
Based on a preliminary inventory of such bright spots (Muntendam-Bos et al.,, 2009) it follows that Netherlands has highest potential for offshore shallow gas fields in the northern offshore sector (A/B/F blocks). Kuhlmann and Wong (2008), linked the occurrence of potential gas (or rather bright spots in seismic data), to specific delta sub environments and stratigraphic intervals related to the inception of Late Cenozoic glaciations. This study was instrumental in illustrating the importance for exploration and production to understand the regional extent and characteristics of the delta. De Haan (2010) also suggests a systematic, though insufficiently understood relation between the occurrence of shallow gas (bright spots) and depositional environment. Stuart and Huuse (2012) focus on the interpretation of several bright spots in terms of fluid and lithological content through well log and seismic facies analysis in order to discuss the origin of these features.
None of these previous studies successfully determined the relation between bright spot properties and the volume of shallow gas contained in a trap. This especially applies to the estimation of gas saturations. In addition, shallow gas plays may be stacked in several layers. Therefore, based on the current state of knowledge, it is difficult to quantitatively estimate the volumes contained in shallow gas prospects. Despite these exploration challenges, to date, Chevron produces from two shallow gas fields in block A12 (since 2007) and B13 (since 2011), respectively, and Dana produces from a shallow gas field above the Hanze oil field in block F02 since 2009 (Fig. 1-2). Next to this, some proven reserves are still undeveloped although production licenses either have been granted (A15-A, Centrica; A18-FA, Chevron) or are requested (B17-FA, Centrica; B10-FA, B16-FA; Chevron, source www.nlog.nl).

1.2 Aim

The original aim of this study was to develop a reliable and effective workflow to de-risk observed bright spots, i.e. to distinguish between economic and fizz gas. Given the fact that gas saturations appear almost impossible to estimate based on the available data (except if actual well measurements exist) this aim has been slightly altered. Ideally, the results of the applied workflow should allow the user to derisk the shallow gas play of the SNS Delta based on predictions of the location and quality of the reservoirs and seals, as well as the conditions under which the gas is present. Given the research character of the project and the data at hand, at the start of the project, it was hard to estimate if all parameters necessary could be obtained by the proposed workflow. This requires information on both static and dynamic conditions of the rock layers in which the bright spots appear. Both type of conditions directly or indirectly relate to the original position (in time and space) within the delta environment and any change that can be achieved by later processes up until present-day. Basically what needs to be known is what the reservoir anatomy looks like (internal

organization and function) and how it works in terms of gas generation, -migration, -accumulation and/or -leakage.

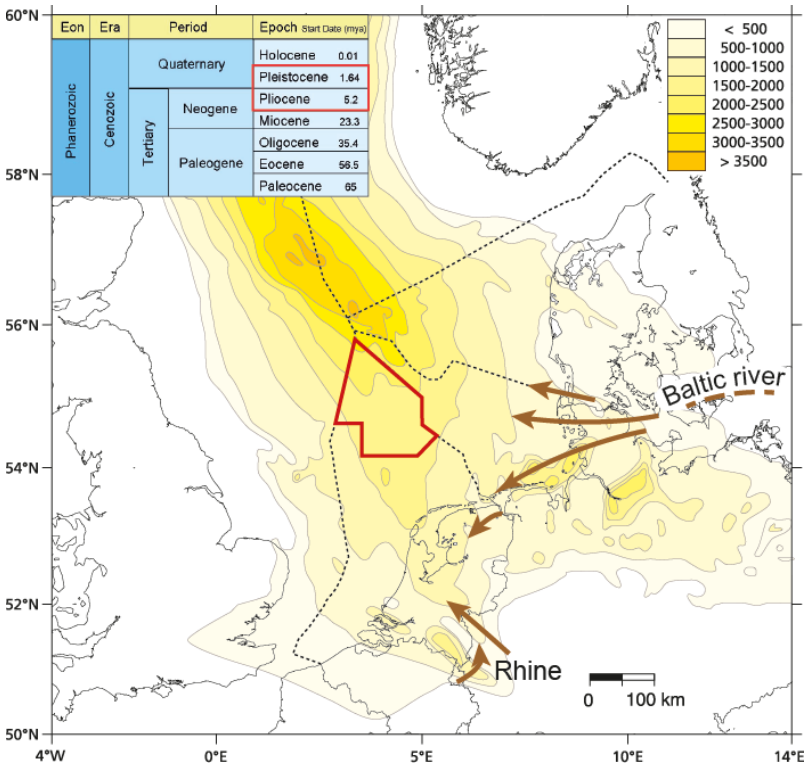

Fig. 1-1. Map showing outline of Southern North Sea (SNS) Basin with thickness (metres) of Cenozoic sediments (excluding Danian) ;after Ziegler (1990) and Huuse (2002), modified from Wong et al, 2007. Arrows show course of main river systems that fed the SNS Basin. Inset show stratigraphic interval of interest.

1.3 Scope and objectives

The scope of the project is to generate a high resolution reservoir model of all bright-spot occurrences and their hosting sediments, i.e. the potential shallow gas fields. The main focus areas are the A/B/F-blocks of the Dutch offshore, defined as the high potential area (Fig. 1). In order to assess the reliability and effectiveness of the developed workflow, as well as to place the model in larger context of the full Delta, critical data and information from the D/E/G/H-blocks is also incorporated.

The objectives of the study are:

1) In order to obtain an increased understanding of how the distribution of depositional environments is related to external (climate, tectonics, sea-level) and internal (delta lobe switching, avulsion) processes, a sequence-stratigraphic framework of the ABFDEG blocks for the evolution of the SNS delta needs to be developed, This framework provides critical knowledge of the architecture and distribution of these, yet not-well understood reservoirs and the continuity of sealing clays.
2) Based on 2D- and 3D seismic interpretation of key horizons guided by the sequence stratigraphic framework a 3D basin scale model of the shallow gas occurrences in the SNS delta will be constructed in which key external controls can be linked directly to

depositional elements (fans, valley fills, clinoforms, topsets, etc) calibrated by extensive existing- and new well data.

3) A reservoir property model for the ABF blocks will be constructed in which petrophysical properties (V_{shale}, Phi, Lithofacies and, if data is available, S_w) and core analysis data are distributed using property modelling.
4) The reservoir model will be combined with information on seal integrity, to assess the distribution of gas column heights that can be retained by sealing clays.
5) Based on all data available, to make qualitative descriptions of shallow gas occurrences, i.e. describe what are the conditions that make an economically potential shallow gas field, rather than providing volumetrics.

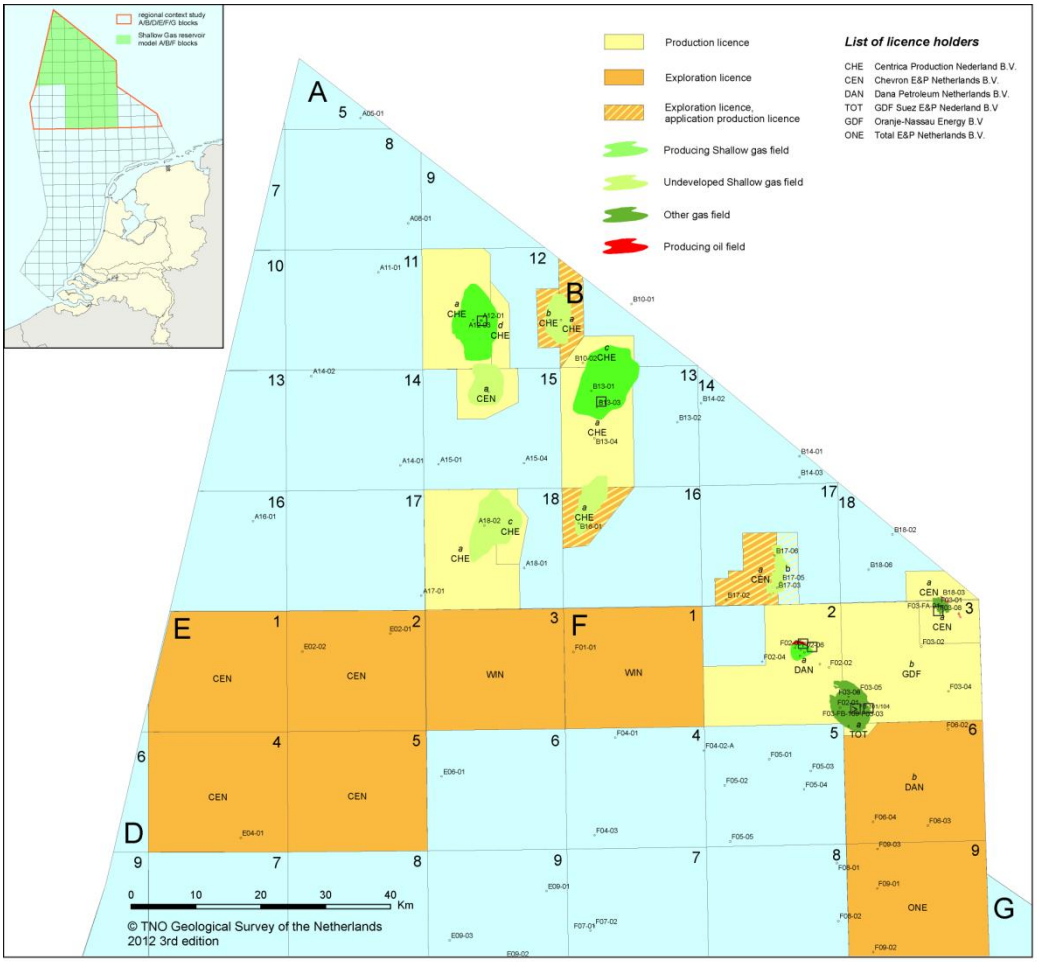

Fig. 1-2. Gas fields in the northern Dutch offshore with indication of license holders and production status. Both undeveloped and producing shallow gas field are indicated as well as other gas fields. The inset map shows the extent of the study area (red box) and the geomodel (in green).

1.4 Not included in the project.

The following activities are not included in the project, because they are beyond scope and / or discarded by the steering committee during the course of the project. This can be due to scientific-, data availability- or budgetary reasons:

- It should be noted that TNO is not allowed to do prospect evaluation. However, based on all data available in the model, example maps (ArcGIS) can be generated that describe shallow gas plays in a qualitative way without quantitatively providing GIIP values.

- The data analysis and modelling within this project focuses explicitly on the Dutch offshore A/B/D/E/F/G-blocks. It does not include any modelling or data analysis on acreage across the Dutch borders.

- Due to resolution problems at hand and the regional character of the study, extensive seismic inversion and Neural-Network property modelling is not be included in the current regional study.

- Full incorporation of available high resolution (multi-channel) seismic data in the project workflow is beyond the scope of the project. However, the mapping results derived from the pilot study on the E-blocks, done within the KIP-program, will be included

- Based on a pilot study comparing SGS with NN-modelling, it was concluded that trained neural network modelling of Sg, Vclay, Phi, K trained by seismic properties and steered by geometry can be successfully generated. However, as was concluded by the A15 pilot study (ten Veen et al., 2011), that seismic amplitude anomalies such as bright spots are reproduced in the properties. Given the unclear relationship between BS parameters and properties of gas sands, this footprint of the BS is undesired. It was therefore decided to distribute properties based on high resolution geometry alone, using standard functionality of Petrel (such as SGS).

- Following the recommendations of an AVO feasibility study a full incorporation of AVO analysis on the post-stack data used is not incorporated in the workflow because it is not able to give clues on gas saturation (as would be better possible with pre-stack data).

- Originally it was planned to study, for specific areas, generation, migration and charging scenarios for shallow gas reservoirs based on present-day fluid dynamic data and basin modelling. For budgetary reasons it was decided to focus on seal integrity instead.

1.5 Project workflow

1.5.1 *General*

The project workflow described here (Fig. 1-3) represents the final version as it resulted from small adjustments and alterations applied in the course of the project. It therefore differs from the workflow presented in the original project plan, but fully reflects the input and decisions of the projects steering committee (see 1.4).

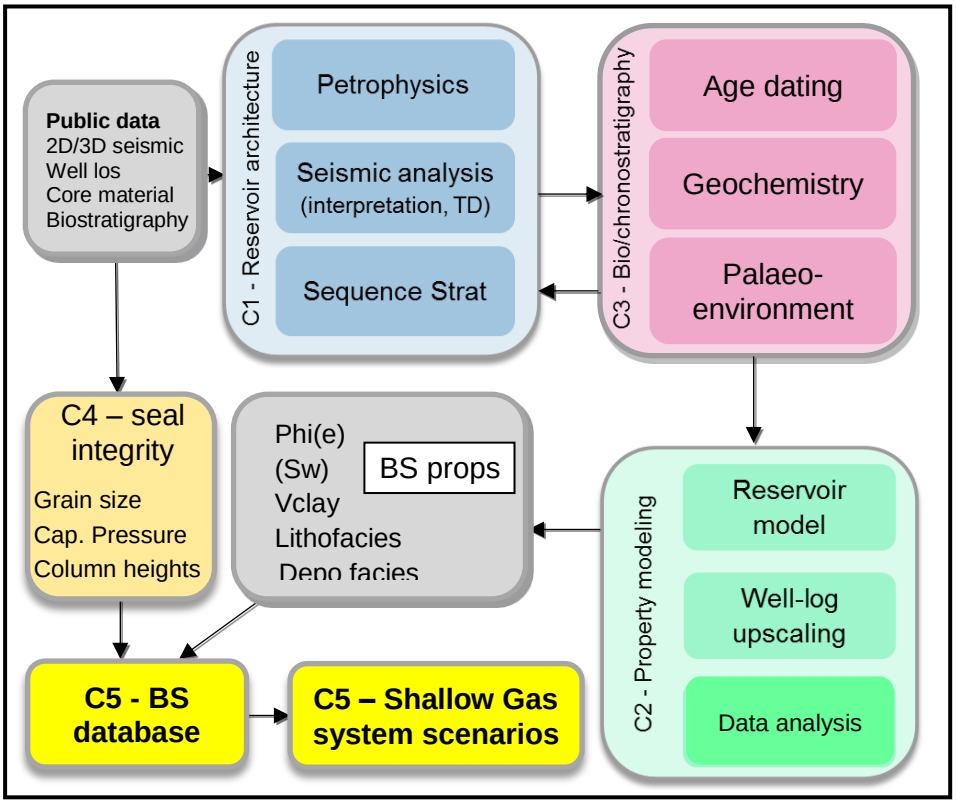

Fig. 1-3. Project workflow, with workflow components as described in text. BS stands for bright spot.

1.5.2 *Workflow components*

C1: Reservoir architecture, bright spots distribution and analysis

a. Petrophysical evaluation of well logs
   Evaluation of well logs for Sg, Phi, Vclay, K (input for C2), including production data where available.
b. Bright spot seismic analysis
c. Horizon interpretation of bounding surfaces of depo units, Seismic well tie (T/D conversion, synthetic seismic, etc.)
d. Sequence stratigraphy
   Together with palaeo-environmental info, ages, sediment- and geochemical properties (based on C3) reservoir architecture will be put into a sequence-stratigraphic framework (TVD). Main input for C2a – Reservoir model
e. AVO feasibility study
   Investigation into the feasibility of discerning fizz water from commercial gas using seismic data in shallow thin-layer accumulations with AVO (outcome provided in separate document).

C2: Reservoir model, seismic- and rock properties prediction

a. Reservoir model
   Geometrical model of delta architecture at the appropriate resolution. Intermediate step requires multi horizon definition and subsequent “layering” of the models.
b. Well-log upscaling
   Up-scaled logs to desired resolution
c. Property-modelling using standard Petrel functionality requires a proper analysis of the input data in order to estimate modelling parameters to the best extend (e.g. search radius of data, data interdepency, etc.).

C3: Bio/chronostratigraphy, geochemistry & sedimentary data

a. Age dating
   - Table of analysed wells, sample overview, and derived indices for facies typing
   - Table per well of age and facies interpretation of all analysed wells (input/compare to C1), new and existing data
   - Independent 3D interpreted layer model based on interpreted surfaces study area
   These activities will be continually improved throughout the project depending on problematic areas.
b. Geochemistry
   - Compilation of geochemical data (TOC, C/N, palaeotemperature) of key wells for parameterization petroleum systems modelling (C4), new and existing data
   - Gas isotopic data compilation and scenario verification (tests of C4 model results)
c. Palaeoenvironment
   Compilation of geochemical data (TOC, C/N, palaeotemperature) of key wells for parameterization petroleum systems modelling (C4), new and existing data

C4: Seal Integrity

a. Core and cutting sample collection from seal above known gas fields
b. Grain size analysis
c. Calculation of capillary seal capacity and gas column height based on pore throat size.
d. Evaluation of results against known gas-column heights

C5: Integration and reporting

a. Integration of the results of the components C1-C4. This leads to a regional overview on how the basin was filled, how the seals were formed, where the sediments originate.
b. Description concepts/scenarios concerning generation, migration, charging, leakage of shallow gas leading.
c. Reporting
d. Recommendations (specifically on the usefulness of high-resolution (multi-channel) data. A separate report will be provided for the AVO feasibility study.)

2 Geological setting of the SNS delta system

2.1 Introduction

The Southern North Sea is characterised by the interaction of structural elements associated with the E-W trending Southern Permian Basin and the NW-SE/NNE-SSW structural elements of the Mesozoic sub basins (Remmelts, 1996). The main structural element in the Southern North Sea is the Central Graben, a Mesozoic structural element to which an intercratonic sag basin developed in the Cenozoic (Huuse and Clausen, 2001), referred to as the Central Trough. This represents the area of greatest accommodation during the deposition of the Late Cenozoic Southern North Sea delta in the study area (Ziegler, 1990). Rapid subsidence in the centre of the basin and uplift at margins are attributed to intra-plate stresses (Overeem et al., 2001).

As well as the Mesozoic structural elements, salt structures are a key feature of the Southern North Sea (Fig. 2-1). Halokinesis of the Permian Zechstein salt layer occurred during both the Mesozoic and Cenozoic (Remmelts, 1996), and continued until the Quaternary.

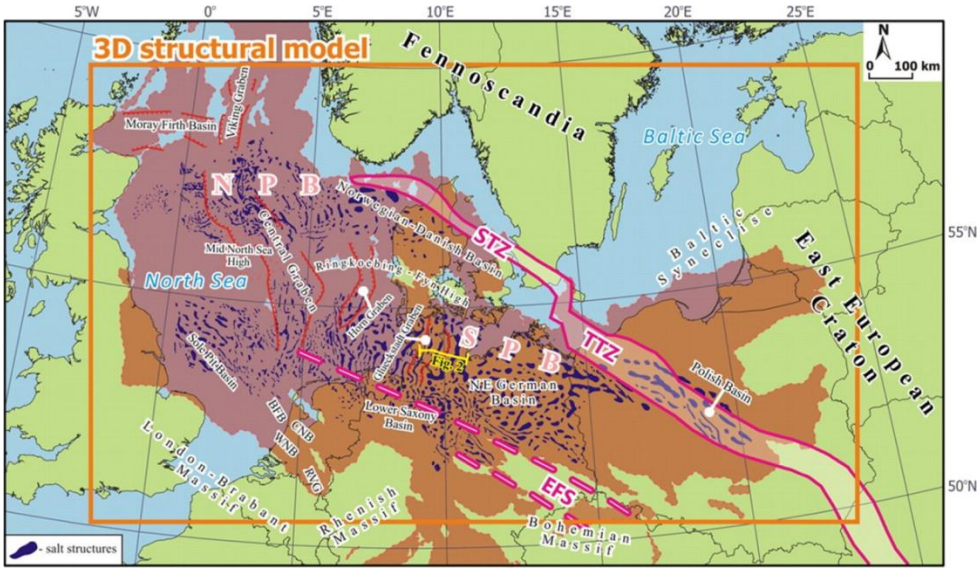

Fig. 2-1. Major tectonic setting of the Central European Basin System: from Maystrenko et al., 2012; BFB Board Fourteens Basin; EFS Elbe Fault System; NPB Northern Permian Basin; RVG Roer Valley Graben; SPB Southern Permian Basin; STZ Sorgenfrei- Tornquist Zone; TTZ Teisseyre Tornquist Zone; WNB West Netherlands.

In the early Miocene the North Sea basin covered most of present day Denmark, northern Poland, Germany and the Netherlands (Møller et al., 2009). During the Cenozoic, the North Sea basin became bordered by the structural highs of Fennoscandia to the north east, western and central Europe in the south and the British Isles in the west (Wong et al., 2007). From Fennoscandia, a giant Late Cenozoic delta system advanced though northern Poland, northern Germany and into the Southern North Sea draining 1.1 x 106 km^2 of Fennoscandia and Northern Europe. The delta is comparable in size to the modern Amazon Delta (Bijlsma, 1981; Overeem et al., 2001). The entire fluviodeltaic system is known as the Baltic River System (Gibbard et al., 1991), the Eridanos delta (Overeem et al., 2001) or the Southern North Sea delta (SNS delta). In the Netherlands subsurface

offshore, it is mainly the shelf-edge delta that is preserved and that is characterised in seismic data as clinoforms down-lapping onto the Mid Miocene Unconformity (MMU). The system is capped by the Late Pleistocene glaciogenic unconformity. Progradation of deltaic sediments into the Dutch realm occurred broadly from the north east to southwest during the Late Miocene to Pleistocene. From the Middle Miocene Unconformity upward this progradation is also reflected by overall upwards coarsening. These trends are associated with eustatic sea level lowering by 100-150m (Miller et al., 2005) and a general climatic cooling from subtropical to icehouse conditions (Anell et al., 2012).

2.2 Literature review of SNS Delta evolution

The seismic expression of the Late Cenozoic of the Southern North Sea has been studied previously using 3D and 2D seismic surveys by Cameron et al. (1987, 1993), Sørensen et al. (1997), Clausen et al. (1999), Huuse and Clausen (2001), Steeghs et al. (2000), Overeem et al. (2001), Kuhlmann and Wong (2008), Møller et al. (2009) and Knox et al. (2010). These studies form the basis for a review of the regional setting and evolution of the SNS delta.

2.2.1 *General trends*

From Oligocene to Middle Pleistocene the North Sea basin was filled with prodeltaic and deltaic sediments successively from the North, Northeast, East and latterly the Southeast (Huuse and Clausen, 2001; Fig. 2-2). During the Middle Miocene, the coastline lay along the line Jutland - eastern Germany with sediment input directions mainly from the east. In the Zanclean (Early Pliocene) the coastline lays in western Germany/east Netherlands, near the present day Danish coast line, with progradation directions having a more southern component.

By the end of the Late Cenozoic, in the Middle Quaternary, the coastline was in the centre of the North Sea, north of the present day northern European coastline. At that time, sedimentation was dominated by Northern European rivers, such as the Rhine rather than Fennoscandian and Baltic river systems (BRS) which had dominated sediment supply during previous periods (Bijlsma, 1981). The delta growth became to an end due to widespread North Sea Glaciation. The first ice sheets reached the basin at 1.1ma (Anell et al., 2012). The Menapian ice sheet destroyed the course of the upper BRS (Overeem et al., 2001). The evolution of the sedimentary system through time is discussed in more detail below.

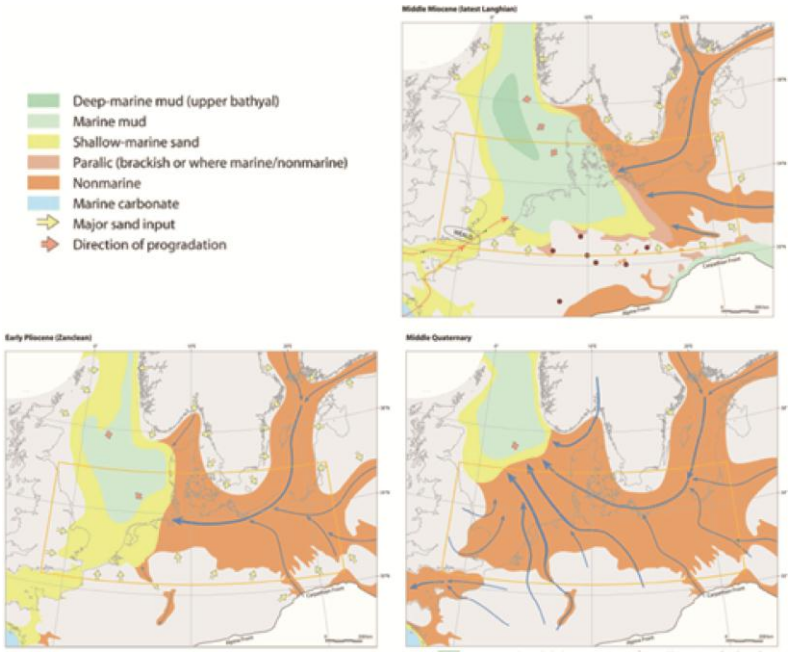

Fig. 2-2. Middle Miocene, Early Pliocene and Mid Quaternary palaeogeography. Modified after Knox et al., 2010 (Southern Permian Basin Atlas). Blue arrows represent postulated river courses and show change in sedimentation routes throughout the study period.

2.2.2 *Oligocene to Mid Miocene*

During the Oligocene large amount of fine grained siliciclastic sediments from the Fennoscandian entered the North Sea basin for the first time in the Tertiary, (Møller et al., 2009), with Scandinavia becoming an increasingly important sediment source through time (Anell et al., 2012). Progradation directions were from north (Norway) to south into the basin, with little or no eastern input (Knox et al., 2010). In Denmark, an Upper Oligocene-Lower Miocene delta system filled available accommodation space in the eastern Danish North Sea, (Huuse and Clausen, 2001), this delta system is capped by the MMU and is thus older than the interval considered where the Dutch shallows gas fields reside.

The Lower Miocene delta system is exposed on Jutland, Denmark (Fig. 2-3). Late Early Miocene palaeogeographical reconstructions by Rasmussen (2005) show several adjacent deltas delivering sediment to the basin along the prograding shoreline. In this period in the Netherlands, several transgressions led to flooding of the Roer Valley Graben in which a delta system developed that built out into the marine area and is known as the Breda Formation (Fig. 2-2).

Fig. 2-3. Sand rich fluvial sediments, Lower Miocene, Voervadsbro gravel pit, Denmark. Picture taken April 2012 on GEUS field trip.

2.2.3 *Mid Miocene Unconformity (MMU)*

In the area of study, the Late Cenozoic deltaic sediments downlap successively onto the MMU, prograding broadly from northeast to southwest (Sørensen et al., 1997; Overeem et al., 2001; Kuhlmann, 2004). The origin of this MMU as a single unconformity is controversial. In the Danish sector it is interpreted as a major transgressive surface with a 14.8 Ma age, marking the end of the Mid-Miocene Climatic Optimum as it correlates with low $\delta^{18}O$ values representing high eustatic sea level and warm climate. This transgressive surface relates to prolonged sediment starvation in the basin (Huuse and Clausen, 2001). In the Danish North Sea, the MMU has a steep dip due to differential basin subsidence as do the deltaic sediments above and below, but represents a correlative conformity (Rasmussen, 2005). Here, the MMU represents the top (maximum regressive surface) rather than the base of a large delta system and becomes a correlative conformity in the central part of the Danish North Sea 100 m below a downlap surface, (Huuse and Clausen, 2001). In the southern North Sea Basin, the MMU represents a significant hiatus that spans 5-12 Myr (Anell et al., 2012) which becomes younger towards the west of the North Sea basin (Huuse and Clausen, 2001) depending on the age of the downlapping sediments. In the Dutch area studied the MMU is given a Middle Serravallian – Late Tortonian age (Kuhlmann, 2004). The Langhian (14.8 Ma) transgressive surface is not recognized as such, but the Middle Miocene section is very condensed in general. These observations corroborate that the MMU seismic reflector is a combined Middle Miocene transgressive and Mid-late Miocene erosive surface. The erosion is related to a general eastward tectonic tilt of the MMU, before westward progading deltas advanced. This tilt and associated erosion is absent in Denmark (Fig. 2-4).

Wong et al., 2007 suggest that the huge sediment input is related to uplift in the Fennoscandian shield and accelerated subsidence in the North Sea Basin. This rapid subsidence is attributed to sediment loading into an over-deepened basin, rather than tectonic subsidence (Anell et al., 2012). Palaeogene uplift in the south Norway could have created this increased sediment supply (rather than renewed Neogene tectonics), by acknowledging that a lag of tens of millions of years in denudation and sediment supply to the basin exists (Huuse et al., 2001; Huuse, 2002). This notion is supported by

Anell et al. (2012) who suggest that increased sedimentation into the basin did not occur until the Plio-Pleistocene boundary (~2.5 Ma), i.e. coeval with first glaciations in Fennoscandia.

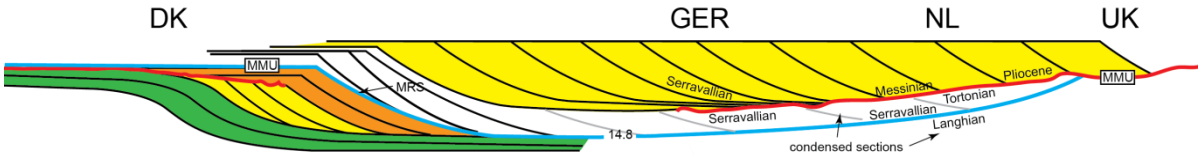

Fig. 2-4. Cartoon representing the stratigraphic relationship around the MMU surface, showing the different interpretations and geological meaning of the MMU going from Denmark (NE) to UK (SE). Not to scale. Yellow = forced-regressive wedge, Orange = low-stand wedge, green = Highstand wedge.

2.2.4 *Late Miocene to Middle Pleistocene (focus of this study)*

The key studies for the Late Cenozoic in the Dutch realm include Kuhlmann (2004), Kuhlmann et al. (2004), Kuhlmann et al. (2006), Kuhlmann and Wong (2008), Overeem et al. (2001) and Sørensen et al. (1997). Sørensen et al. (1997) and Overeem et al. (2001) derived absolute ages from biostratigraphy, though their studies represent regional studies. Also, their chronostratigraphy gives ages that are older than are now thought. A positive result of the earlier regional studies is that they are tied to seismic interpretations of units whilst Kuhlmann's sequence boundaries were defined based on well logs and age significant boundaries rather than seismic. Kuhlmann however, correlated the units defined to Sørensen and Overeem units. Overeem et al. (2001) recognised 27 units; and Sørensen et al. 1997, 45 sequences. Kuhlmann's, chronostratigraphy is based on a comprehensive suite of magnetostratigraphy, pollen, foraminifera, dinoflagellate cysts and strontium isotope analysis. The study only concerns a small area in the A-B blocks of the Netherlands North Sea, where it interpreted 18 log units and 13 seismic units. In this study the chronostratigraphy of Kuhlmann's is adopted because, to date, it is the most accurate one since it is linked to the Global Magnetic Polarity Scale. Fig. 2-5 represents the regional correlation of these units with Danish and German interpretation.

Stuart and Huuse (2012) expand on Kuhlmann's work in Block A and B to parts of block D, E and F. The paper identifies several additional key surfaces and focuses on origins and timing of contourites and the association with shallow gas. Their view will be commented upon in this report. Benvenuti et al. (2012) deal mainly with sediment instability and delta front failure in Block G and M in the southeastern part of the Netherlands North Sea, and how this relates to high sediment supply and constant or even decreasing accommodation space (linked to glacio-eustatic sea level fall).

2.2.5 *Sediment Provenance*

Several heavy mineral analysis studies have been carried out on Late Cenozoic deposits in the Netherlands, which can be used to derive the source area for the basin fill. Huisman and Klaver (2007) found that the Baltic River System (BRS) dominated onshore Netherlands deposition during the Early Pleistocene. Later in the Early Pleistocene, the Rhine, Meuse and Schelde were also contributing. From the Middle Pleistocene onward, the BRS became the Proto Weser, a continuation of the BRS with a smaller drainage area.

The source region of the BRS varied in relation to climate variations in the Late Cenozoic (Kuhlmann et al., 2004). The Gelasian sediments of the Early Pleistocene are characterised by glacial-interglacial cycles controlled by 41,000 year obliquity cycles (Kuhlmann, 2004). Cold periods coincide with Archean provenance from the Scandinavian shield with a high percentage of illite and chlorite

due to physical weathering of metamorphic rocks by glaciers. During the warmer climate conditions younger provenance delivered to the basin by precursors of the rivers Elbe, Weser and Rhine (Kuhlmann et al., 2004). This denotes that more proximal mainland European sources became prominent, with a high smectite content related to chemical weathering of volcanic material point. The BRS system deposited sediments until the Middle Cromerian, and can be found as predominantly white quartz sands of the Peize and Appelscha formations (de Gans, 2007), i.e. the fluvial equivalents of the SNS delta deposits that are represented by the Oosterhout and Maassluis FMs. Prograding seismic reflectors incline towards the NE or SE in seismic formations adjacent to East Anglia during the Early Pleistocene. Therefore, it is suggested that there was riverine input by UK sources into the basin as well (Cameron et al., 1987).

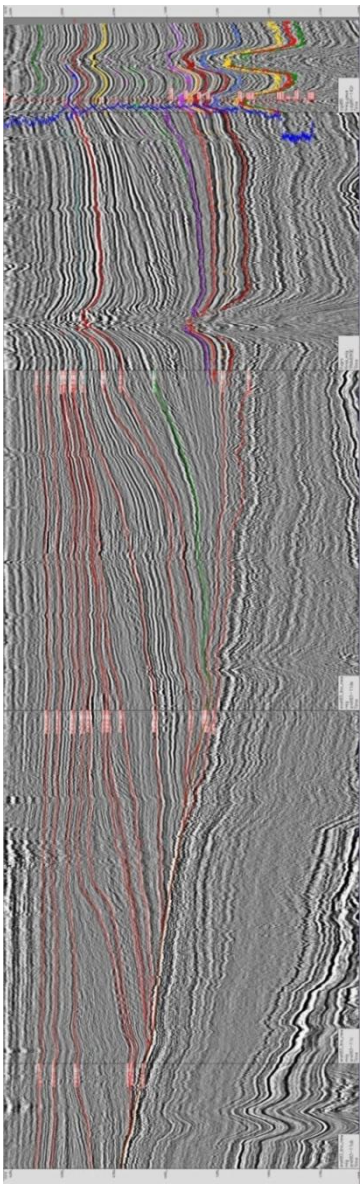

Fig. 2-5. NE-SW 2D Seismic section from DK (right) to NL (left) with interpreted horizons. No exact locality given for confidentiality reasons.

3 Bio / chronostratigraphy, geochemistry & sedimentary data

3.1 Introduction

The geobiological data provide an age model and a depositional model for the Eridanos succession in the A/B/F/G blocks, supplemented by earlier reported data from literature sources that also include the E/D blocks. Data are calibrated and compared to the regional standard from (mostly) cored A15-3 and A15-4 wells.
The age model is important to constrain the sequence stratigraphic interpretation, derived from the seismic interpretation, in terms of absolute time. Also, the age model is to correlate wells and calibrate the seismic interpretations, especially in regions with limited 3D seismic data coverage.
The depositional model is important because it contributes in the understanding of the petroleum system in the area of interest. The shallow gas occurrences in the northern Dutch offshore are constrained to specific stratigraphic intervals with recurring combinations of physical properties. The physical properties of the sediments are determined to a high degree by palaeoenvironmental parameters such as climate, productivity and sea level. The depositional model provides the link between the physical properties and the palaeonvironmental parameters. The depositional model is made explicit through a series of ratios based on the proxy data for each well. These ratios are used as parameters together with the geophysical well log data to upscale and populate properties between the seismic horizons (see Chapter 4).

3.2 Database

At TNO there is a large amount of biostratigraphic data available with respect to the Cenozoic North Sea Group in the northern offshore, especially the A and B blocks (Table 3-1, Appendix A). New data is generated for the F-blocks in 4 wells to assess the North to South variability and stratigraphic control. Based on the initial seismic review and available data at the start of the project, it was expected that most variability occurs in the A, B, F blocks since the SNS delta front prograded westward during deposition. Within the, Upper Miocene, Pliocene and early Pleistocene interval of interest (~11-1.8 Ma), the B and F blocks contain the most complex prograding units with internal truncations and laterally diverging palaeoenvironments due to frequent lobe switching. Well stratigraphy from D and E blocks are evaluated based on public well reports.

3.2.1 *Data treatment*

Data produced by TNO in this or previous projects of which the original data are available are used as the main dataset on which the seismic QC and property distribution are based (Fig. 3-1). Information from literature is secondary to that since in most cases the primary data is not available and/or mostly proxies (foraminifera and nannofossils) that are less suitable for the high-resolution interpretations that are used. All previous interpretations from the available wells were reviewed, corrected when necessary based on the A15-3 standard, and summarized by picking the most important age horizons. With the age information, log zonations were applied following the Kuhlmann (2004) standards to provide a more detailed zonation were possible. The biostratigraphical dataset, hence, can be compared and interpolated according to a single, consistent interpretation.

Table 3-1. Data sources, type of proxies analysed, relative sample density and intervals.

well	logzones	biozones	AP/NAP	SD	SSTdino	Sample type	pollen interval		pollen res	dinocyst interval		dinocyst resolution	forams interval		foram res	other	Remark
						SW= side wall											
A12-3	x	x	x	x	part	core	467-921	high	488.5-915.35	low							TNO data
A15-3	x	x	x	x	x	core, SW, cut	400-1280	high	400-1280	high		400-1280	high		magneto		TNO data
A15-4	x	x	x	x	x	core	918-1089	high	918-1089	high							TNO data
A17-1	x	x		x	x	cuttings	no		440-1140	high							TNO data
A18-2	x	x	x	x	part	core, SWS	350-1143	high	350-1143	low							TNO data
B10-3	x	x	x	x	part	core, SWS	374-1230	high	374-1230	low		250-1350	high				TNO data
B13-3	x	x	x	x	part	core, SWS	325-1143	high	325-1143	low		300-1350	high				TNO data
B13-4	x	x			x	SWS	no		406-923	med							TNO data
B14-1	x	x			x	cuttings	no		500-1400	low					nannos		TNO data
B16-1	x	x	x	x	x	SWS	282-1093	med	282-1093	med					magneto		TNO data
B17-5	x	x	x	x		core, SWS	386-1079	high	no			320-1100	high				TNO data
B17-6	x	x			x	Cuttings, core	no		240-850	high							TNO data
F06-02	x	x	x	x	x	Cuttings	300-1130	med	300-1130	med							TNO data
F12-03	x	x	x	x	x	Cuttings	620-1130	med	620-1130	med							TNO data
F01-01	x	x	x	x	x	Cuttings	600-1140	med	600-1140	med					bad quality		TNO data
F2-06	x	x				Cuttings	450-1150	med	450-1150	med							TNO data
G10-01	x	x		x	x	Cuttings			480-1000	med							TNO data, slump study
G10-02	x	x		x	x	Cuttings			480-920	low							TNO data, slump study
G16-06		x				Cuttings			600-1010	med							TNO data
A12-01		x				Cuttings			232-1340	med		232-1340	med				literature, reinterpreted
A15-02		x				Cuttings			400-1320	med		400-1320	med				literature, reinterpreted
A18-01		x				Cuttings			360-1300	med		360-1300	med				literature, reinterpreted
B10-02		x				Cuttings						150-1270	med				literature, reinterpreted
B13-01		x				Cuttings			378-1260	med		378-1260	med				literature, reinterpreted
B17-01		x				Cuttings						285-1080	low				literature, reinterpreted
B17-04		x				Cuttings						137-1061	med				literature, reinterpreted
D12-01		x				Cuttings						300-560	low				literature, reinterpreted
E02-01		x				Cuttings						70-990	med				literature, reinterpreted
E02-02		x				Cuttings						470-1070	med				literature, reinterpreted
E12-01		x				Cuttings						520-948	med				literature, reinterpreted
E16-01		x				Cuttings						229-625	low				literature, reinterpreted
E17-01		x				Cuttings						70-650	med				literature, reinterpreted
F02-03		x				cuttings & core			1203-1205	low		550-1203	med				literature, reinterpreted
F04-01		x				Cuttings						76-1060	med				literature, reinterpreted
F04-03		x				Cuttings						475-1131	med				literature, reinterpreted
F06-03		x				Cuttings						510-1135	med				literature, reinterpreted
F07-01		x				Cuttings						89-989	low				literature, reinterpreted
F13-01		x				Cuttings						150-1000	med				literature, reinterpreted
F14-04		x				Cuttings						360-1120	med				literature, reinterpreted
F16-02		x				Cuttings						140-1010	med				literature, reinterpreted
F18-02		x				Cuttings						88-1034	med				literature, reinterpreted
F18-04		x				Cuttings						110-1050	med				literature, reinterpreted
G17-01		x				Cuttings						98-646	med				literature, reinterpreted

3.3 Methods

3.3.1 *Sampling and splicing of wells*

The borehole samples from A15-03 were used by Kuhlmann et al. (2006) to construct a solid integrated chronostratigraphy for the Upper Neogene deposits. This chronostratigraphy is based on palaeomagnetic data and dinoflagellate- and foraminiferal proxies. Hence, A15-03 is used as the reference well for this shallow gas study and is updated to the latest stratigraphical insights (De Schepper et al., 2009a, 2009b). Gaps in the studied interval were closed to provide a continuous record. This detailed well provides both a regional depositional model and a reference for interpretation of the remaining wells that are sampled at a lower resolution.

New samples for the F-block wells (F01-01, F02-06, F06-02 and F12-03) were collected at the TNO core repository to extend the framework to the south. The specific results of these wells are reported here. Other, interpretations of the A, B and F blocks have been thoroughly QCed, evaluated and synchronized to the latest stratigraphical insights. These results are presented in Ten Veen et al. (2011) and available on request.

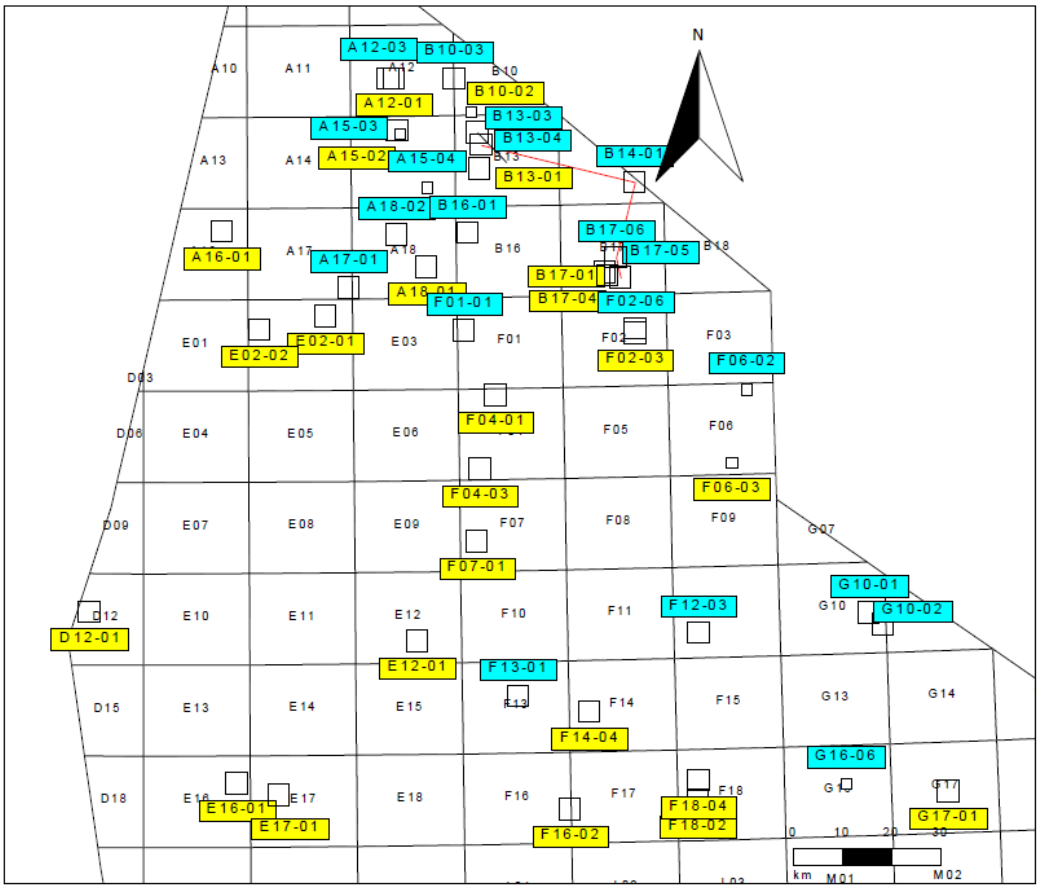

Fig. 3-1. Distribution of wells with biostratigraphical data, both from literature (yellow labels) and in-house TNO data (blue labels).

3.3.2 *Palynology processing and analyses*

The samples were processed using standard marine palynological procedures (e.g. Wood et al., 1996) involving HCl-HF-HCl digestion, heavy liquid separation, and sieving over 18 µm mesh. For pollen, it is at present generally accepted that morphological characteristics of late Pliocene to early Pleistocene pollen types can directly be related to extant genera and families (Donders et al., 2009). This correlation potential is a sound basis for floristic analysis of the assemblages and the recognition of similarities with modern vegetation types. For the Plio-Pleistocene associations the microscopy slides were initially counted up to 200 sporomorphs and dinoflagellate cysts. The remainder of the slide is thereafter scanned for “new” often (very) rare dinocysts. Semi-quantitative analysis is applied for the Miocene. It includes an estimation of the main palynomorph categories, the determinable sporomorphs, dinocysts and miscellaneous fossils. Dinocyst taxonomy follows that cited in Fensome and Williams (2004).

Table 3-2. Abbreviations used in this report.

CO	Core sample
SC	Sidewall core sample
CU	Cuttings sample
m	Meter
Ft	Feet
LOD	Last Occurrence Datum
FOD	First Occurrence Datum
LCOD	Last Common Occurrence Datum
FCOD	First Common Occurrence Datum

The age interpretation is based on the LODs and numbers (acmes) of dinoflagellate cysts. Palynological interpretation is based on key-references concerning the palynostratigraphy of the Tertiary to Early Pleistocene from the North Sea region such as: Bujak and Mudge (1994), Costa and Davey (1992), De Schepper (2009a), Heilmann-Clausen (1985), Köthe (2003), Kuhlmann et al. (2006), Lourens et al. (2004), Luterbacher et al. (2004), Munsterman and Brinkhuis (2004; see Fig. 1) and Powell (1992). Absolute ages are based on Gradstein et al. (2004).

3.3.3 *Organic geochemistry*

For the organic geochemical analyses, 78 samples were studied. Most of these samples (41) originate from core A15-4. The studied samples range between 907.8 and 1057.62 metres spliced depth (925.45 and 1089.9 mbsl). About half of these samples (below 972 metres spliced depth) were obtained from sidewall cores. All 37 samples from A15-3 were obtained from cores. The studied samples range between 890.8 and 964.02 metres of depth below sealevel.

3.3.4 *Total organic carbon*

Total Organic Carbon (TOC) content provides information on the amount of organic carbon present in sediments relative to the mineral fraction. For the determination of the TOC content, about 0.3 g of freeze dried and powdered sediment of each sample was weighed and stored in Greiner centrifuge tubes of 15 ml. To remove carbonates, 7.5 ml 1 M HCL was added. After bubbling of gas ceases, the tubes were closed and placed on a shaker for 4 hours. After that, the acid was removed upon centrifugation. This step was repeated one more time for 12 hours on the shaker. Finally, the samples were washed twice with demineralised water and stored in an oven at 40-50°C for 96 hours. To determine the weight loss by the removal of carbonates the dried samples were weighed again. The

samples were grinded and ~15 to 20 mg per sample was weighed in tin foil cups. Measurements were performed using a Fisons NA1500 NCS elemental analyser with a normal Dumas combustion setup. Three external standards, BCR, atropine and acetanilide, were analysed before and after the series, and after each ten measurements. Measurements were normalized to these standards.

%TOC per gram of sediment was calculated using the following formula:

%TOC = C% * W2/W1
C% = result of NCS analyser
W1 = weight of sample before decalcification
W2 = weight of sample after decalcification

3.3.5 *Biomarkers*

Many microorganisms leave traces behind in sedimentary records in the form of fossilized chemical components. If these components are specific to a certain organism or a group of organisms, these molecules are referred to as biomarkers. In addition to being specific for an organism, these molecular fossils might also provide information on the palaeoenvironment and palaeoclimate in which organisms lived. Saturated hydrocarbons, termed n-alkanes, are important constituents in different groups of organisms. Marine organisms typically contain short chain (C16-C24) n-alkanes, whereas the leaf waxes of land plants dominantly contain long chain (C25-C35) n-alkanes. Here, specific biomarkers for *Sphagnum* (peat moss) are shown to corroborate the pollen data. Detailed results and methods are given in Van Helmond (2010).

3.4 Results & discussion

3.4.1 *Age Model A15-3*

In well A15-3 a geomagnetic tool has been run along the hole. The resulting magnetic polarity intervals were tied to the global standard and calibrated to Chrons by using a couple of well calibrated biostratigraphical events (Fig. 3-2). Thus, it was possible to pinpoint 1) the Gauss-Matuyama boundary, which is calibrated to the absolute age of 2.56 Ma and to Marine Isotope Stage 103, 2) the X-event, calibrated to 2.44 Ma, 3) the base of the Olduvai, calibrated to 1.94 Ma. Absolute ages for well A15-3 are listed in Table 3-3.

Based on this initial information from A15-3 and coupling to the absolute timescale, relevant regional seismic horizons were selected for interpretations in the ABDEF blocks.

Table 3-3. Absolute ages versus depthsand seismic reflectors in well A15-3.

	TNO 2011	MD	Z	Kuhlmann and Wong, 2008	Log unit Kuhlmann 2006	Unit Age	Unit TOP Age (Ma)	Unit Base Age (Ma)	Palaeo Water depth
A15-03	X_S13	431.42	-390.84	S13	18		1.8		
A15-03	W_S12	470.91	-429.46	S12	17			1.9	0-50
A15-03	V	482.00	-440.31						
A15-03	U_S11	532.60	-489.86	S11	16				
A15-03	T	539.00	-496.13						
A15-03	S_S10	583.26	-539.50	S10	15				
A15-03	R	597.00	-552.96						
A15-03	Q_S9	633.88	-589.10	S9	14				
A15-03	P	643.00	-598.03						
A15-03	O	660.00	-614.69						
A15-03	N_S8	689.84	-643.90	S8	13	Gelasian			50-100
A15-03	M_S7	712.00	-665.59	S7	12				
A15-03	L	769.00	-721.35		11				
A15-03	K_S6	802.00	-753.63	S6					
A15-03	J	845.00	-795.69		10		2.16	2.44	150
A15-03	I_S5	918.00	-867.04	S5	9		2.44		
A15-03	H	967.00	-914.90		8				
A15-03	G	1003.00	-950.08		7				
A15-03	F	1028.00	-974.51		6 + 5				
A15-03	E	1070.00	-1015.55					2.58	200
A15-03	D_S4	1100.00	-1044.89	S4	4	Piacenzian	2.58		
A15-03	C_S3	1142.00	-1085.97	S3	3			3.6	200
A15-03	B_S2	1182.00	-1125.11	S2	2	Zanclean			
A15-03	A_S1	1205.00	-1147.64	S1	1			5.2	200
A15-03	MMU	1247.00	-1188.72						

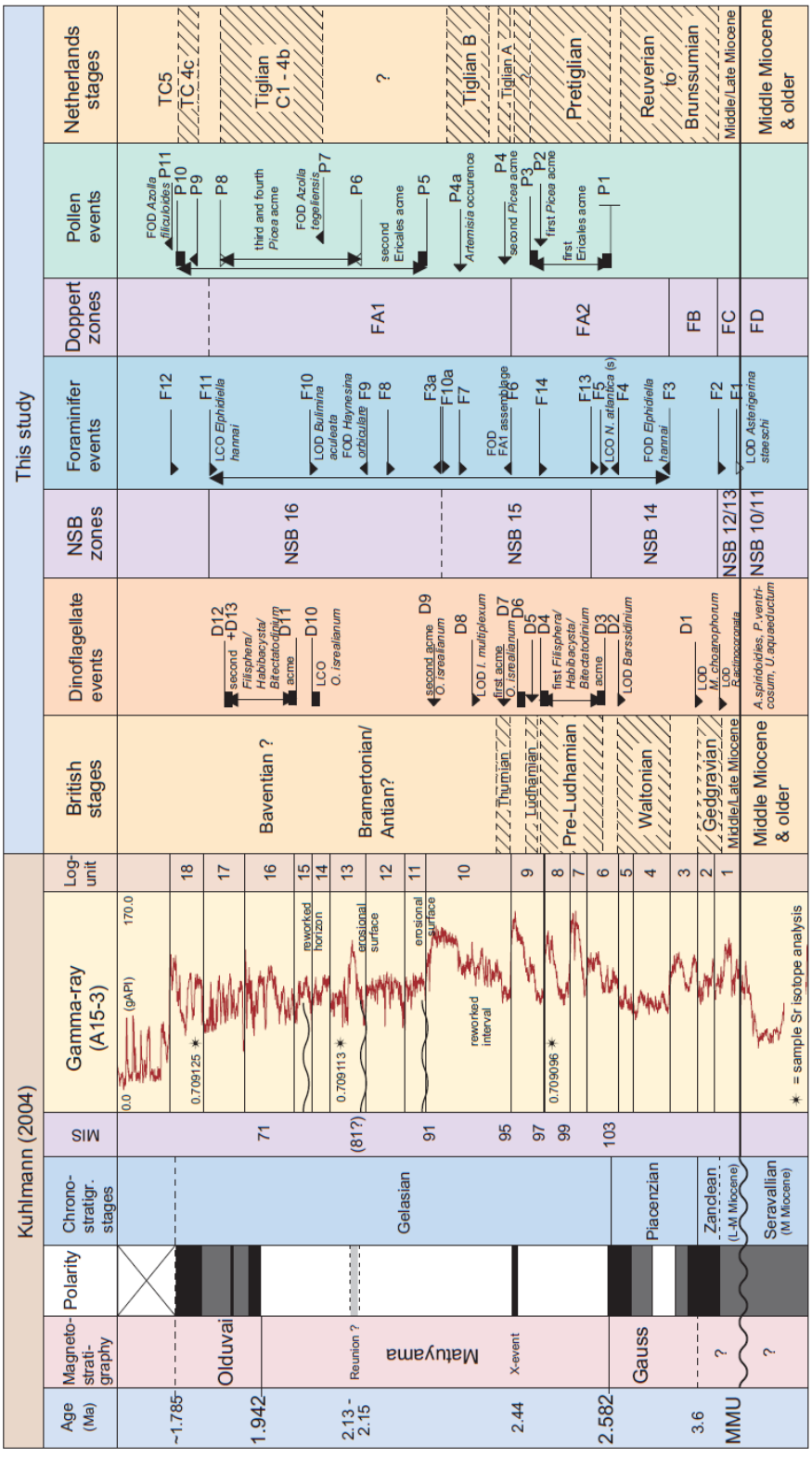

Fig. 3-2. Stratigraphical framework and biostratigraphical events for the MMU - Gelasian in well A15-3. NSB = North Sea Basin benthic foraminifera zonation; Doppert zones = Neogene planctic foraminifera zonation.

3.5 Stratigraphic interpretation wells (F02-06, F06-02, F01-01 and F12-03

The F-block wells do not have cored intervals, so exclusively cutting material was used for the palynological analyses. Samples per well are listed in Appendix B.

3.5.1 *Interpretation F02-06*

The palynomorph associations of well F02-06, interval 450-1150 m, are all relatively rich. The sporomorphs dominate (84-93 % of the total sum dinocysts and sporomorphs) the assemblages from 450-930 m. In the two deepest samples (i.e. at depth 1020 and 1150 m) the marine signal predominates. Reworking from older strata is present in low numbers. Although caving from younger successions is not always apparent, it may be common in ditch cuttings. It impedes in particular facial interpretation.

Sample/Interval	Age/Zone
450-670 mCU	Early Pleistocene, Gelasian

The age interpretation is based on:

- LOD *Habibacysta tectata* (consistent: 2.1 Ma) at 450 m
- Acme *Impagidinium multiplexum* at 595 m
- FCOD of (sub)arctic genera: *Brigantedinium*, *Habibacysta* and *Filisphaera* at 670 m

Remarks: the acme of Impagidinium multiplexum is associated with MIS 96/97. *Reticulosphaera actinocoronata* (450 m), *Systematophora placacantha* (450 m), *Cordosphaeridium cantharellum* (670 m) and *Palaeocystodinium* spp. (670 m) are considered as reworking.
The freshwater (*Pediastrum*) and brackish water (*Botryococcus*) algae are well- represented.

Sample/Interval	Age/Zone
750-930 mCU	Late Pliocene, Piacenzian

The age interpretation is based on:

- LOD *Barssidinium wrenni* at 750 m
- LOD *Barssidinium graminosum* at 930 m
- LOD *Achomosphaera andalousiensis suttonensis* at 930 m

Remarks: Glaphyrocysta spp. (750 m), *Cordosphaeridium cantharellum* (930 m) and *Palaeocystodinium golzowense* (930 m) are attributed to reworking.
The numbers of fresh- and brackish water algae are reduced compared to those from the Early Pleistocene interval.

Sample/Interval	Age/Zone
1020 m	CUEarly Pliocene, Zanclean

The age interpretation is based on:

- LOD *Reticulosphaera actinocoronata*

Remarks: freshwater algae are absent. Brackish water algae are recorded in rare frequency (?caved).

Sample/Interval	Age/Zone
1150 mCU	Middle Miocene, mid Serravallian, Zone M7

The age interpretation is based on:

- LOD *Palaeocystodinium ventricosum*
- LOD *Palaeocystodinium striatogranulosum*
- LOD *Apteodinium spiridoides*
- LOD *Unipontidinium aquaeductum*

Table 3-4. Summary of the palynological results of well F02-06.

Depth (m)	Age
450-670	Early Pleistocene, Gelasian
595	MIS 96/97
750-930	Late Pliocene, Piacenzian
1020	Early Pliocene, Zanclean
1150	Middle Miocene, mid Serravallian, Zone M7

3.5.2 *Interpretation F06-02*

The palynomorph recovery and preservation are very good. The sporomorphs dominate the assemblages in the interval 300-915 m (83-98 % of the total sum dinocysts and sporomorphs). Deeper, the relative marine signal increases from 26 % (950 m) to 34 % (1040 m). In the deepest sample at 1130 m the dinocysts dominate the associations. Reworking is present in low values.

Sample/Interval	Age/Zone
400-540 mCU	Early Pleistocene, Gelasian

The age interpretation is based on:

- LOD *Habibacysta tectata* (consistent: 2.1 Ma) at 400 m
- acme *Impagidinium multiplexum* at 500 m
- FCOD of (sub)arctic *Filisphaera* at 540 m

Remarks: the acme of *Impagidinium multiplexum* is associated with MIS 96/97. Here in well F06-02 the acme coincides with high numbers of *Lingulodinium machaerophorum* indicating a relatively warm phase which preferably refers to MIS 97.
The high numbers of *Operculodinium israelianum* at 460 m may be associated with MIS 95 (see e.g. wells A/15-03 and A/15-04). *Eatonicysta ursulae* (460 m), *Ischyosporites* (500 m), *Densosporites* (500 m), *Classopollis* (500 m), *Cauca parva* (500 m), *Sirmiodinium grossii* (500 m), *Systematophora* (500 m), *Chatangiella* (540 m) and *Glaphyrocysta* (540 m) etc. are considered reworked. Freshwater *Pediastrum* is recorded in relatively abundant values and brackish *Botryococcus* is commonly present.

Sample/Interval	Age/Zone
580-950 mCU	Late Pliocene, Piacenzian

The age interpretation is based on:

- LOD *Barssidinium wrenni* at 580 m
- LOD *Barssidinium graminosum* at 620 m
- LOD *Achomosphaera andalousiensis suttonensis* at 620 m

Remarks: reworking is present from older Tertiary, Mesozoic and Palaeozoic strata.
Pediastrum disappears from the spectra and *Botryococcus* decreases in values (except at depth 760 m).

Sample/Interval	Age/Zone
1040 mCU	Late Miocene, Tortonian, Zone M14, or older

The age interpretation is based on:

- LOD *Labyrinthodinium truncatum*

Remarks: *Cordosphaeridium cantharellum* is considered as reworking from the Early Miocene.

Sample/Interval	Age/Zone
1130 mCU	Middle Miocene, mid Serravallian, Zone M7

The age interpretation is based on:

- LOD *Cerebrocysta poulsenii*
- LOD *Palaeocystodinium ventricosum*
- LOD *Palaeocystodinium striatogranulosum*
- LOD *Apteodinium spiridoides*
- LOD *Unipontidinium aquaeductum*

Remarks: *Cordosphaeridium cantharellum* is, albeit with doubt, considered as reworking. However, if this taxon is insitu, the age inferred is Early Miocene, Burdigalian, Zone M3. After all, the current sample interval is 90 m, which leaves room for multiple interpretations. The last occurrences of the present taxa indicating a Middle Miocene (mid Serravallian, or older) age, could be caved from a higher succession, e.g. from interval ca. 1082-1119 m (see gamma-ray “breaks”).

Table 3-5. Summary of the palynological results of well F06-02.

Depth (m)	Age
400-540	Early Pleistocene, Gelasian
460	MIS 95
500	MIS 97
580-950	Late Pliocene, Piacenzian
1040	Late Miocene, Tortonian, Zone M14
1130	?Middle Miocene, mid Serravallian, Zone M7

3.5.3 *Interpretation F12-03*

The assemblages of well F12-03, interval 620-1130 m, are well-preserved and very rich in palynomorphs. Sporomorphs dominate the palynomorph spectrum in the interval 620-980 m (81-99 % of the total sum dinocysts and sporomorphs). The dinoflagellate cysts prevail from 1070 m (62 %) to 1130 m (96 %). Reworking is represented in all samples and may become very common (e.g. in the cuttings sample at depth 890 m).

Sample/Interval	Age/Zone
620-980 mCU	Early Pleistocene, Gelasian

The age interpretation is based on:
LOD *Impagidinium multiplexum* at 700 m
LOD *Habibacysta tect*ata (consistent) at 740 m
"Acme" *Impagidinium multiplexum* at 740 m
FCOD of (sub)arctic genera: *Filisphaera* and *Bitectatodinium/Filisphaera/Habibacysta* complex at 980 m

Remarks: based on the LOD of *Amiculosphaera*, the cuttings sample at depth 620 m is definitely not younger in age than mid- Calabrian (ca. 1.5 Ma). The acme of *Impagidinium multiplexum* is associated with MIS 96/97. Reworking recorded in this interval is e.g. *Achilleodinium biformoides*, *Chatangiella, Areosphaeridium, Charlesdowniae coleothrypta, Classopollis, Eatonicysta ursulae*, *Fibrocysta, Systematophora placacantha, Thalassiphora* and *Wetzeliella*.
Brackish water algae fluctuate between common and abundant values. Freshwater algae (*Pediastrum* and Zygnemataceae) are also recorded in common to abundant numbers.

Sample/Interval	Age/Zone
1070 mCU	Late Pliocene, Piacenzian

The age interpretation is based on:
LOD *Barssidinium wrenni*
LOD *Barssidinium graminosum*
LOD *Achomosphaera andalousiensis suttonensis*

Remarks: reworking from older Tertiary and Mesozoic strata is rarely represented. Freshwater algae are also in reduced to rare frequencies. *Botryococcus* is still present, but in relatively moderate numbers.

Sample/Interval	Age/Zone
1130 mCU	Middle Miocene, early Langhian, Zone M6

The age interpretation is based on:
LOD *Cerebrocysta poulsenii*
LOD *Palaeocystodinium ventricosum*
LOD *Palaeocystodinium striatogranulosum*
LOD *Apteodinium spiridoides*
LOD *Cousteaudinium aubryae*

Remarks: the presence of *Thalassiphora pelagica* is considered as reworking from the Early Miocene, Burdigalian.
Freshwater and brackish water algae disappeared from the spectra.

Table 3-6. Summary of the palynological results of well F12-03.

Depth (m)	Age
620-980	Early Pleistocene, Gelasian
740	MIS 96/97
1070	Late Pliocene, Piacenzian
1130	Middle Miocene, early Langhian, Zone M6

3.5.4 *Interpretation F01-01*
The palynofacies from interval 600-1140 m is very strongly dominated by bisaccates, *Pediastrum* and organic matter. The preservation is moderately good, but the microfossils are often fragmented, rounded or subject to deterioration, resulting in doubtful determinations. Furthermore, the relatively very weak marine signal is diluted by caving and reworking. (Early-Late) Miocene reworking reaches up to at least 870 m. Noteworthy is the near absence of marine (sub)arctic taxa. The palynofacies points to fluvial transport. New seismic interpretation shows the setting to be a fluvial valley. Hence, reliable age interpretation of the current cuttings samples from well F01-01 in the desired resolution is statistically impossible. Meanwhile the gamma-ray log has proved to be a useful expression for correlation. The age interpretation of well F01-01, interval 600-1140 m, is undifferentiated Neogene-Pleistocene. The gamma-ray log of well F01-01 however, offers good perspectives for correlation to local wells (the Mid Miocene Unconformity (MMU) may be associated with the gamma-ray “break” at ca. 1118 m, the MIS 100 with high gamma-ray values at 960 m, the MIS 98 at 920 m, the MIS 96 at 870 m and the MIS 95 at 860 m).

3.5.5 *MMU interpretation*
Based on the palynological analyses and the gamma-ray logs the MMU in well F02-06 is unequivocally put at depth ca. 1127 m, and in well F12-03 at ca. 1111 m. MMU candidate in well F06-02 is at (ca. 1083 m or) ca. 1118 m.

3.6 Regional interpolation and seismic QC

The results of the individual wells analysed were compared to the A15-3 standard and correlated to levels that can be well identified. The majority of the dated levels in Table 3 could be identified in the other wells. Reports for individual wells are available at TNO on request, the wells analysed specifically for this study are reported here. The age breakdowns for all available wells have subsequently been imported in the Petrel project database to serve as a guide and a QC tool for the regional seismic analyses.

In the QC process, all biostratigraphic data in wells analysed by TNO could be matched well with the seismic interpretations; mis ties are generally the result of the seismic velocity effects (“pull down) due to gas, which caused the available checkshots to not align well with the regional model. Also interpolation problems of the regional surfaces due to small local structures (salt domes) caused some of the mismatches with biostratigraphic horizons. Since most wells in the study area are positioned on an anticlinal structure and often pass through a gas saturated zone that blanks out the seismic signal the biostratigraphic control has been important in flexing the horizons correctly at such locations. Given the position of most wells on local anticlines, interpolation of the biostratigraphic

horizons would, on average, provide a too shallow position of the marker horizons. This demonstrates the value of the integrated seismic and biostratigraphic interpretation of the geological model.

In one level (S4) the biostratigraphic horizon was consistently higher than the seismically picked horizon. At the reference well A15-3, this difference is small but it becomes more significant in blocks B and F since the units thicken eastward. Since the biostratigraphic marker of horizon is S4 very clear and is calibrated by magnetostratigraphy the difference is likely caused by an offset in the picked seismic horizon. In practice, it means that the top of log unit 4, not 5 of Kuhlmann et al. (2006) (see Table 3-3) is picked as the S4 seismic horizon. This offset is consistent and therefore does not interfere with the quality of the model. It differs however, from the A15 study (Ten Veen et al., 2011).

3.7 Relation with established regional Upper Cenozoic stratigraphy

The stratigraphic subdivision in block E8 was obtained from Rijsdijk et al. (2005; Fig. 3-3) and formed the basis for horizon interpretation for the North Sea Palaeolandscapes Project in the E blocks using multichannel shallow seismic data. Shallow seismic data and -interpretation was compared with the ages of lithostratigraphic units and correlate to the S6-S12 horizons interpreted in this study (Fig. 3-3).

3.8 Depositional model

The quantitative palynological data is used to calculate ratios between groups with clear environmental affinities to help constrain the sub-environments in the delta, these are the AP/NAP, SD and SSTdino ratios

3.8.1 *Pollen data and AP/NAP ratio*

Note that pollen preservation is reasonably good, but shows the effects of relatively long-distance transport since the assemblages are dominated by comparatively and few exclusively wind-pollinated taxa that disperse well. Hence, the results are not directly representative for the vegetation cover on-land, but changes should be interpreted as the relative dominance of certain environments and vegetation types.

The occurrence of thermophilous trees and *Picea, Tsuga* and *Osmunda* mark relatively warmer (wetter) climatic conditions on land. In contrast, occurrences of Ericales, *Sphagnum* and herbs in general, mark relatively cooler and dryer conditions on land. *Pinus* abundance is also strongly related to the relative distance to the coast, and hence can be caused by sea-level changes.

The AP/NAP ratio (tree pollen over non-tree pollen), shown in Fig. 3-4, represents these changes and is indicative of temperature. AP is defined as all tree pollen except bisaccate forms since they are transported across large distances. NAP are all upland herbs including grasses (excluding ferns, aquatics, sedges and heath as they might be controlled by water availability rather than temperature).

3.8.2 *SD ratio*

The sporomorph/dinocyst ratio is a ratio based on all terrestrial-derived palynomorphs, expressed as a fraction of the total palynomorphs. It effectively can be interpreted as a terrestrial tot marine ratio. This is indicative for the relative distance to the coast (see e.g. Donders et al., 2009), which varies with sea level and progradational changes in the basin. As the organic material is largely terrestrial-derived this is an important variable for characterising the different subunits (topsets, foresets, and toesets) of the delta system (see Chapter 5).

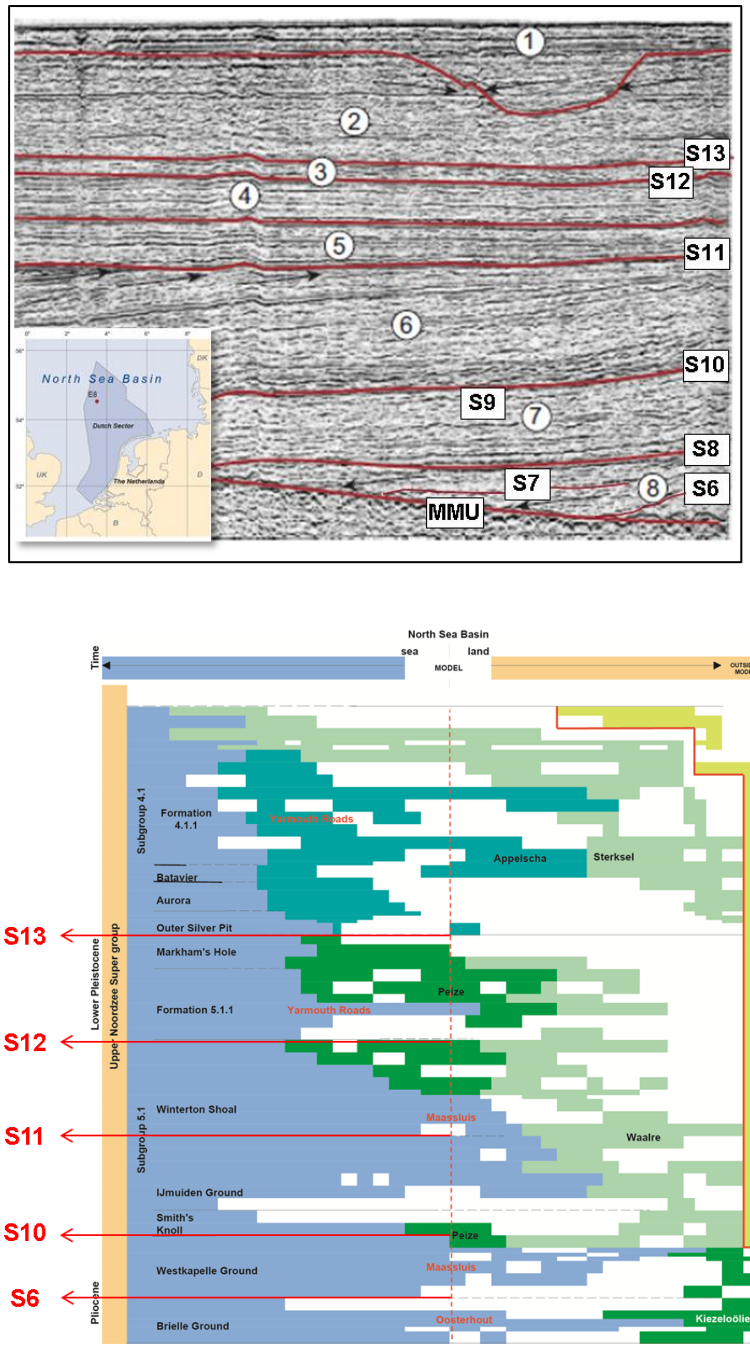

Fig. 3-3. Correlation with regional Upper Cenozoic stratigraphy a) seismic section in block E8 with stratigraphic units of Rijsdijk et al. (2005, numeric label) and interpreted horizons used in this study (alphanumeric labels) based on the age model for A15-3; b) correlation with lithostratigraphic units.

3.8.3 *Dinoflagellate cyst data and SST dino*

The SSTdino ratio (sea surface temperature ratio based on dinoflagellates cysts) is a relative index based on the preference of dinoflagellates to occur in cold or warm surface watermasses. The ratio is calculated as warm taxa sum/[warm+cold], and is based on the taxa listed in Table 3-7 (sensu Donders et al., 2009):

Table 3-7. Taxa in the SSTdino ratio.

Cool SST dinocyst taxa:	Warm SST dinocyst taxa
Bitectatodinium tepikiense	*Nematosphaeropsis* spp.
Filisphaera filifera	*Operculodinium israelianum*
Habibacysta spp.	*Tuberculodinium vancampoae*
Headinium miocenicum sensu Zevenboom	*Tectatodinium pellitum*
Also intermediate forms of the above taxa are included	

The SSTdino -based regional palaeotemperature trends, indirectly, provide input for the glacial/interglacial sequence stratigraphic interpretation of the sedimentary units, and should change at the same time on a basin-wide scale. Hence, they provide a check on whether the interpreted sedimentary units are time equivalent. Geochemical data for A15-3 and 4 (TOC and biomarkers for cold-adapted vegetation), SD, AP/NAP and SSTdino ratios and additional major pollen groups that are not included in the ratios are shown in Fig. 3-4.

3.8.3.1 Sea level, Sea Surface Temperature and depositional system

The most important aspect of the Neogene SNS delta succession in the A15 Block, is the strong coupling of sediment deposition and climate (see Ten Veen et al., 2011). The SNS delta progrades across the A15 Block at the time that the first ice caps appeared on the Scandinavian shield. This so-called onset of northern Hemisphere glaciations resulted in a series of glacial-interglacial cycles that had a profound impact on the delta behaviour and on the resulting basin-fill. These first glacial-interglacial cycles, unlike the present ones, were paced by the 40.000 obliquity cycles. Fig. 3-4 clearly shows the strong coupling or even forcing of lithology (based on gamma-ray log) and climate. The SSTdino and AP/NAP trend clearly show the cooling trend during the Mio- and Pliocene, while the early Gelasian (MIS 102-94) show sharp alternations of cool and warm phases coupled to clay and silty sedimentation, respectively.

Surprisingly, the warmest intervals or interglacials are coupled to the most coarse-grained sediments, and the coldest intervals or glacials are linked to the most fine-grained sediments. The sea level trend is in line with the expected trend associated with ice sheet build-up: high sea levels during the interglacials and low sea levels during the glacials.

The relevance of these climatic cycles lies in the fact they occur basin-wide and control the deposition of clay - silt couplets with good sealing capacity (clays) and reservoir bodies with a likely biogenic source (enhanced TOC in the silts). The data in Fig. 3-4 shows high TOC contents in the silts (low gamma ray), coupled to high SST (based on dinoflagellate cysts), and relatively warm climate (increased forest cover based on high AP/NAP). Shaded bars in Fig. 3-4 show colder intervals where open landscapes increases regionally, SST decreases and the relative distance to the coast decreases (high sporomorph/dinocyst; SD ratio). These climatically controlled clayey intervals represent cold conditions and occur basin-wide and act as regional seals.

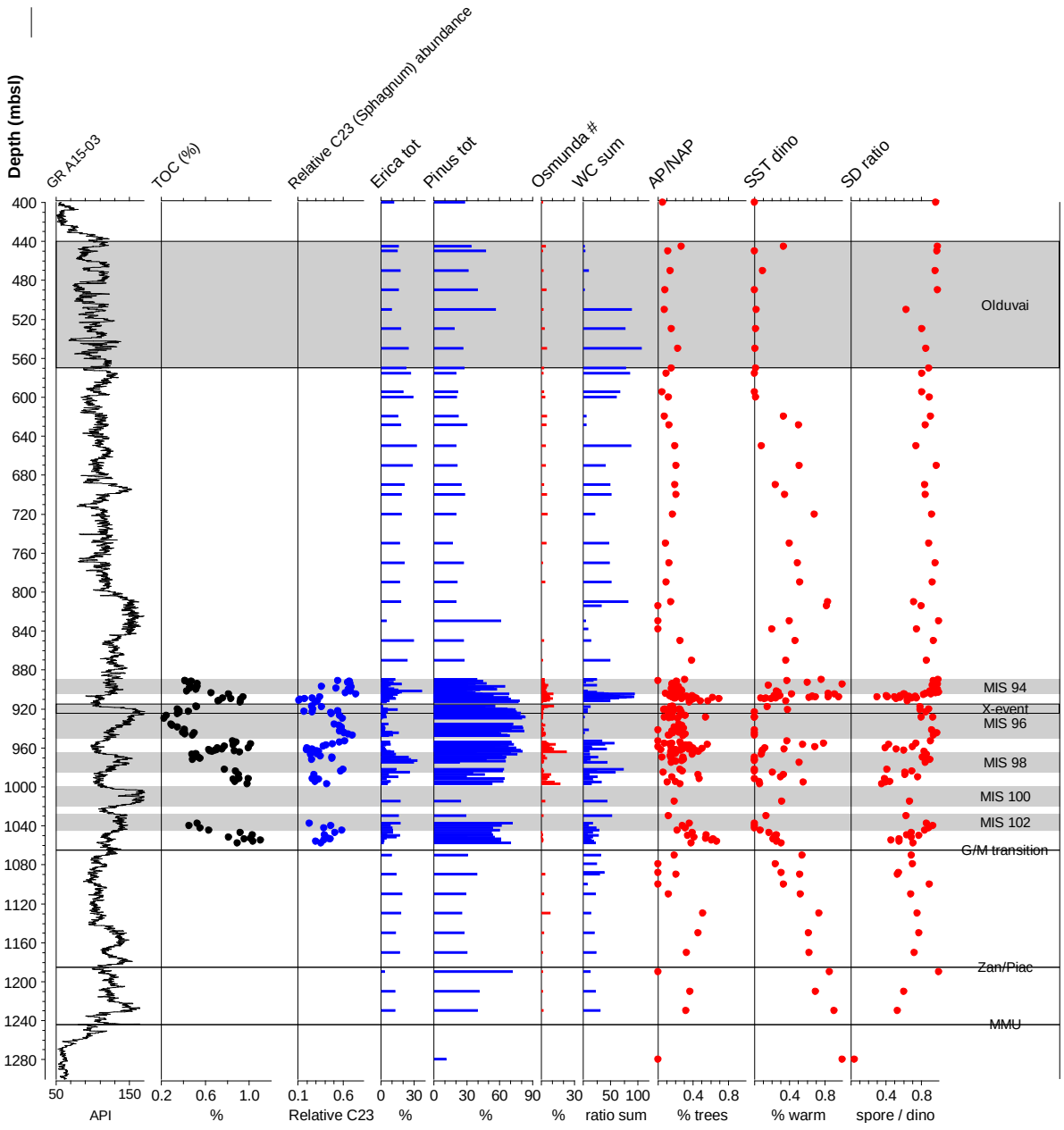

Fig. 3-4. High resolution proxydata of 15-3 and 15-4 (spliced to a common depth scale of the A15-3 standard). These data are from core and side wall plugs and provide a reliable overview for regional trends in palaeoenvironment during the late Miocene, Pliocene and Gelasian. Beside the AP/NAP, SD and SSTdino indices, *Pinus* pollen here indicate relative distance to the coast, while *Erica* shows cold or coastal nutrient poor conditions on land. WCsum shows the sum of specimens included in the SSTdino ratio, which in some intervals is too low for reliable determination.

3.8.4 *Long-term sea level trend*

Sea level is strongly controlled by climate: the glacials force low sea levels, the interglacials force sea level to return to “normal” levels. The long-term sea level trend is shallowing (Fig. 3-5 and Appendix F of ten Veen et al., 2011) from the MMU upward. The progressive shallowing trend is controlled by infill of accomodation space through the advancing delta. In the lower part (S1-S4), the Eridanos succession in well A15-3 contains open marine dinoflagellate cyst and benthic foraminifera assemblages. These are roughly correlating with the toe sets of the delta. The part with the characteristic bell-shaped GR-cycles, is transitional, with strongly fluctuating sea levels. In the middle part (S5-S10), the Eridanos succession is changing via a transitional assemblages (S5-S6) to restricted marine (S7-S10), with high-dominance and low-diversity dinoflagellate cyst assemblages. A short-lived return to an open marine setting is achieved in the upper part (S11), with abundant dinoflagellate cysts. The uppermost part of the Eridanos succession (S12-S13) is basically non-marine. The general sea level trend inferred from geobiological data is summarized in Table 3-8.

One intriguing interval remains unexplained: the upper part of the Gelasian in well A15-3, unit S11-S12. The palynological assemblages indicate open marine conditions in combination with cold Sea Surface Temperatures (Fig. 3-4). A possible explanation may be a significant “melting event” that has been recorded in the literature. This melting event appeared to be related to a temporary change in oceanic circulation: for a short duration of time warm Atlantic waters flowed west of Iceland into the arctic (Baumann and Huber, 1999). This warm water current caused melting of the existing sea ice cap and possibly pushed the cold arctic surface waters into the proto-North Sea.

Table 3-8. Palaeoenvironment with respect to sea level. Interpretation is exclusively based on geobiological data.

Log unit TNO 2011	Top A15-3	Base A15-3	Palaeoenvironment
S12-S13	400	500	Non-marine, deltaic or paralic
S11-S12 (level V)	500	600	Open marine
S7-S10	600	800	Restricted marine
S5-S6	800	1230	Transitional: open – restricted marine
S1-S4	1230	1050	Open marine

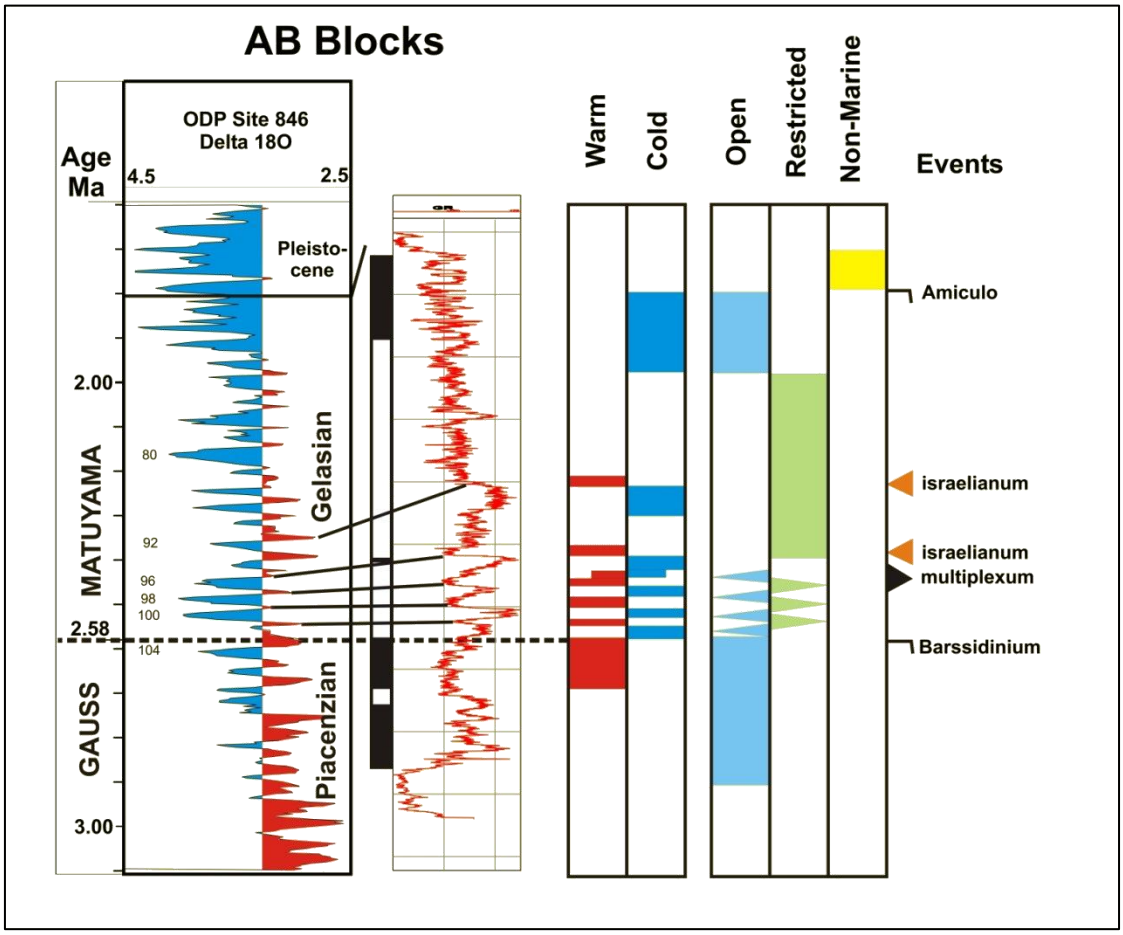

Fig. 3-5. Summary of palaeoenvironmental trends in well A15-3 showing the relationship between sea level, climate and sea surface temperature.

3.9 Conclusions

Based on the Geobiological input in Phase I of the project (Ten Veen et al., 2011), the following conclusions can be made:

- In the A15 Block an excellent chronostratigraphic framework is available for the Eridanos succession. The precise coupling to absolute ages is derived from geomagnetic polarity data of well A15-3. The polarity intervals are coupled to the global standard by a number of well calibrated biostratigraphic events.
- A strong coupling exists between climate and sediment properties.
- Specific intervals are of interest i.e., the intervals that are interpreted as glacial-interglacial cycles.
- The glacial-interglacial cycles show a marked contrast in grain size, sea surface temperature and climate and are the key control on the presence and distribution of potential sealing clays and coarser-grained reservoir units.
- Interglacials are characterised by:
    - Relatively warm climate and relatively high Sea Surface Temperatures
    - High freshwater input at the base of the interglacials
    - Relatively open marine conditions
    - Relatively coarse grain size (moderate to good reservoir properties)
    - Relatively high sea level
    - Relatively high TOC content (possible source for biogenic gas)

- Glacials are characterised by:
    - Relatively cold climate and relatively low Sea Surface Temperatures
    - Almost no freshwater input
    - Relatively restricted marine conditions (water stratification)
    - Very fine grain sizes (excellent seal properties)
    - Relatively low sea levels
    - Relatively low TOC content

Based on the additional analysis done for the current project, the following conclusions are reached:

- The regional biostratigraphic model is mostly based on cutting material, but the results are considered reliable for the TNO in-house data. The new well F01-01 is not reliable due to reworking and bad quality samples
- Literature data from other sources have a secondary quality since the primary data is not available and the interpretation is based on foraminifera that are less suited for high-resolution work. These data are supportive of the regional model but not of high enough quality to do accurate QC of the seismic data.

4 Geological model

4.1 Introduction

This chapter describes the analysis of petrophysical well logs and their transformation into reservoir properties relevant to formation evaluation. These properties are subsequently used in upscaling and property modelling in order to distribute them throughout the geological model that is based on seismic interpretation and constrained by biostratigraphic data and seismic to well tie of key horizons.

4.2 Petrophysical evaluation - methodology

A petrophysical evaluation of the upper Cenozoic sediments in blocks A, B, D, E, F, and G was performed on all released wells insofar as logs were available for that shallow interval. Drilling and logging in the Cenozoic section has long been considered a necessary evil by most operators, which resulted in a paucity of well logs that have been collected on this interval. Recent wells, especially those that were drilled on the shallow gas fields, have a wider log suite available for formation evaluation purposes. However, the majority of the wells only contain a very basic set consisting of gamma-ray-, sonic- and induction logs. Furthermore, in a substantial number of wells only a gamma-ray log was recorded. It will be clear that in those cases a full formation evaluation is not possible. At best a Vsh can be calculated.

4.2.1 *Data used*

Annex 1 contains a list of wells that have been considered for this project. For each well the availability of logs is indicated (from www.nlog.nl), whether there are spliced composite logs available, and which petrophysical evaluations were eventually done.
A project that was carried out as a pilot for the current one focused on block A15 (ten Veen et al., 2011). Within this project a comprehensive study on the petrophysical evaluation of the shallow gas sands was undertaken. For detailed discussions on- and motivation for selected methods, the reader is referred to that report. The experiences gained during that project served as a basis for the petrophysical evaluations of the current study. Where necessary these experiences are recapped here.

4.2.2 *Methodology*

One of the conclusions of the A15 pilot project was that evaluation of porosity, shale content, water saturation, and permeability in the Neogene strata is not straightforward, as there are several factors that complicate the process of log interpretation:

- Well to well differences. Different logging suites and log sampling rates have been used. This implies that each well needs an individual approach.
- Hole conditions. Because the studied rock sequence consists of unconsolidated sands and clays, most wells have many washout sections. This affects all contact-type logging tools and causes many aberrant readings, especially in the porosity logs.
- KCL / Polymer mud. In order to fight the instability of the unconsolidated sediments that consist for a large part of swelling clays, many operators use KCL/Polymer additives to the drilling mud. This creates a substantial bias in the gamma-ray and spectral gamma-ray logs.
- Complex lithology. The Neogene sediments of the Eridanos delta contain many minerals that are either heavy, or radioactive, or both. A standard suite of logs (including spectral gamma ray and pef) cannot resolve all these minerals. In addition, a substantial amount of charcoal particles complicates the interpretation even further.

- Clay-Bound Water. The sediments are in general fine-grained and muddy, and they are unconsolidated. This means that they contain a considerable amount of clay-bound water. This in turn creates challenges for porosity and water saturation evaluation. Core porosities cannot be directly compared to effective porosities, and water saturation calculation based on total porosity concepts need either robust lab measurements for Cation Exchange Capacity (CEC), or a volumetric log analysis of the constituting clay minerals, or both.

Given all these difficulties, the main recommendation of the A15 pilot, as adopted herein, was to use a simple shaly-sand model, preferably using the gamma-ray, neutron, and density logs to compute effective porosity (PHIE) and shale content (VSH). The Indonesian equation should then be used to calculate water saturation (Sw). An estimate of permeability can be made using the poro-perm relation derived from NMR and core measurements from A15. All computations were done with Interactive Petrophysics version 4.2. Annex 1 lists the results, plus the petrophysical parameters that were used (Gr minimum/maximum, Rmf, etc.).

4.2.3 *Petrophysical results*

Out of 285 wells that were selected in the ABDEFG Blocks, 40 wells were not yet released at the time of evaluation and were therefore not evaluated. Another 124 wells either had no logs recorded at the interval of interest, or these logs were not available at the www.nlog.nl repository. This resulted in a total of 121 wells that were evaluated for shale content (Vsh) and 70 wells had enough log data to calculate effective porosity and water saturation. The evaluated logs were exported as LAS files and imported into Petrel to be used for further modelling, as is described in Chapter 5.

As discussed in ten Veen et al (2011), the accuracy and reliability of the results depend mainly on the quality of the input logs and the borehole conditions. When these are favourable, the shaly sand model yields quite accurate values for effective porosity (PHIE), in the order of 2 percent point, and shale volume (VSH), estimated to be accurate plus or minus 5 percent point. Water saturation has much larger error bars because of the uncertainty in clay mineralogy and CEC. It is estimated to be plus or minus 15 percent point. Although this may seem to be quite a large uncertainty, it is believed that for the current regional project the values are of sufficient accuracy to distinguish between commercially exploitable gas and residual, “fizz” gas (at the well location).

The vertical resolution of the evaluated intervals should be considered with caution. As made quite clear in the A15 study (ten Veen et al, 2011), the gas-bearing zones are actually composed of a series of quite thin beds (0.6 to 1.0 m) with widely varying gas saturations. These can only be sufficiently distinguished through the use of high-resolution logging tools (with e.g. 2” sample increment). Normal logging tools tend to average out the values, so especially high-porosity, high gas saturation streaks tend to be smoothed out. This effect becomes even stronger when the log values are subsequently upscaled in the Petrel 3D model, where the average gridblock height is some 8 m. It will be clear that these upscaled values, especially the gas saturations, will be on the low side.

4.3 Seismic interpretation of key horizons ABF blocks

4.3.1 *Seismic data*

In order to make a detailed interpretation of the Late Cenozoic southern North Sea delta, a large dataset has been used. The seismic data consists of a series of 2D (Figure 4-1a) and 3D seismic surveys (Figure 4-1b), which are all publically available through www.nlog.nl. See Appendix C for full list of seismic surveys available for the project. The main 2D surveys used are the SNST83 and SNSST87 surveys.

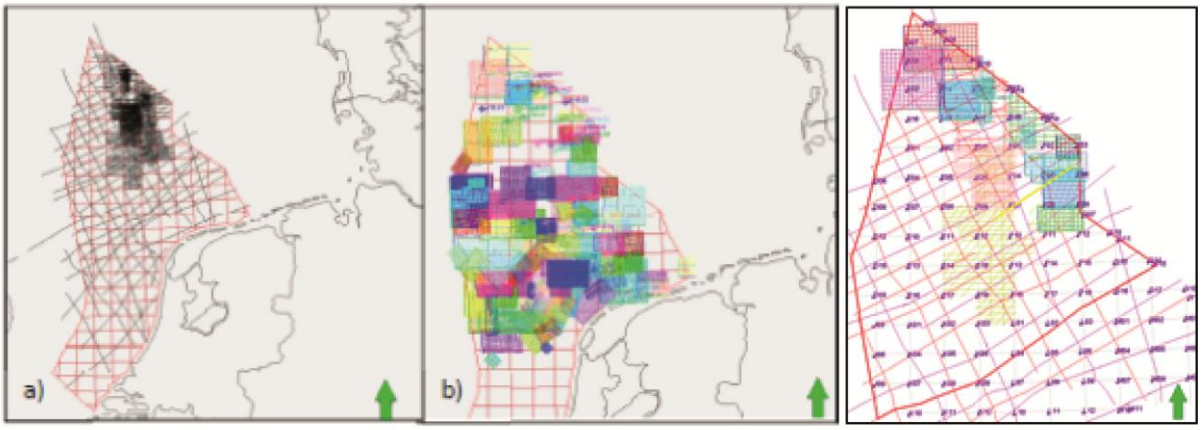

Fig. 4-1. Used 2D (a) and 3D (b) seismic data for the regional ABCDEFG model and seismic data coverage for the ABF reservoir model (c). See Appendix C for full list of seismic data used.

4.3.2 *Methodology*

Seismic interpretation was carried out using Petrel 2010. Key stratigraphic horizons were identified in the A15 pilot project (ten Veen et al., 2011, their Appendix F) and based on bio-stratigraphic levels and/or log units as defined in Kuhlmann and Wong (2008) and represent climatically-controlled sedimentary cycles. All horizons are defined as the top of the unit below it, with the exception of the MMU which is the base below all units. Therefore the name of the surface is identical to the name of the unit below it. Based on the climatic control on glacioeustasy and sediment supply, all horizons can be given a sequence stratigraphic meaning by relating them to specific accommodation/sediment supply conditions (see ten Veen et al., 2011 for explanation). This conceptual approach helps to trace and extended the horizons throughout the area of interest.

The A15 survey (Z3WIN2000A) used in the precursor study (ten Veen et al., 2011) has been used a reference for the seismic interpretation (Figure 4-2) of the entire ABF area. Subsequently, a set of regional 2D seismic lines (the SNS83 and SNS87 surveys) have been levelled to the A15 survey by applying time shifts.

Individual 3D surveys are then levelled to the calibrated 2D regional lines. Another issue with using individual 2D and 3D seismic surveys is that there are large mis-ties between surveys with different polarities, thus potentially leading to mis-ties within the TWT structure maps. The polarity issues are identified and solved for. Despite all these corrections, in some areas the confidence in the structure maps created are low to medium due to 1) unsolvable mis-ties between seismic survey and 2) the difficulty tracing the basic horizons of Kuhlmann and Wong 2008, which are not everywhere present in the current study area.

Outside the A, B, F blocks, interpretations from the D, E, G blocks have been added through the work of Rachel Harding (PhD. Manchester). Note that these interpretations are used to increase the regional extent of the study, but that the subsequent reservoir characterization step (Chapter 5 and further) only apply to the A, B, F blocks.

TWT structure maps with 250 m grid size are created from the interpreted horizons MMU, S1-S13 and additional parasequence boundaries that represent the present day geometry of the surface. Well data and stratigraphic markers (well tops) are converted to the time domain, using seismic-to-well tie, sonic- and checkshot data (see section 4.2.4. for a full description of the TD conversion workflow).

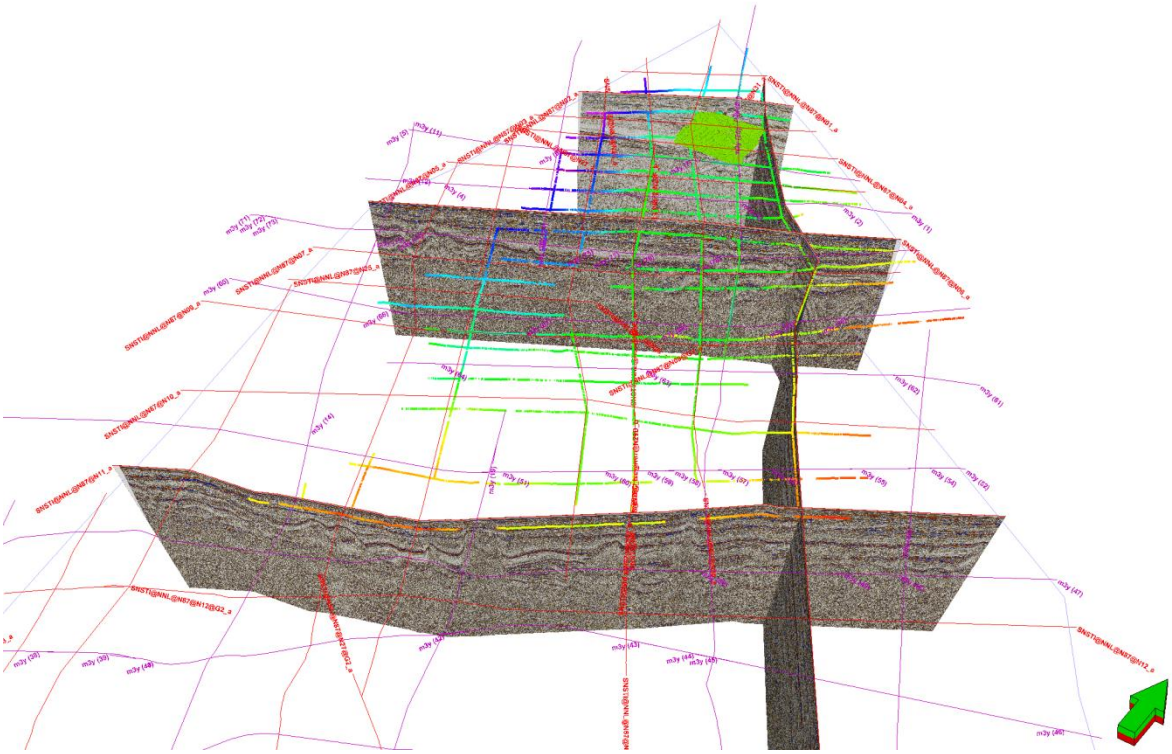

Fig. 4-2. Seismic mapping methodology: Key stratigraphic horizons were identified in the A15 (green square) and interpreted over the entire area of interest on a set of regional 2D seismic lines (the SNS83 and SNS87 surveys). Here, S10 horizon is shown as an example.

4.3.2.1 Seismic interpretation issues and resolution

Seismic interpretation and horizon making has been done with the utmost care, however, resolution issues are present. In Table 4-1 we give the types of errors and where they occur. Any of these errors can occur at a given place and some are cumulative but most have no relationship, which makes it very difficult to estimate the effective error for the surfaces.

Table 4-1. Palaeoenvironment with respect to sea level. Interpretation is exclusively based on geobiological data.

Type	Error	Comments
2D Seismic mis-ties	Up to 6 m	In steep dipping geology
Survey to survey shift	Up to 15 m	Surveys are shifted relative to A15 and 2D Lines
Survey to survey seismic resolution differences	Up to 6 m	In condensed sections and thin bedded layers (tuning thickness)
Interpretation errors	Up-to 18m	Local cycle skips. QCed by interpreting circularly
Interpolation	Locally up to 50 m	Faults, Salt domes and velocity anomalies in-between 2D lines
Make surfaces	Up to 6 m	The interpretation is smoothed to make surfaces with a resolution of 250x250m

4.3.2.2 Well-to-Seismic tie (Depth Time Conversion)

Since the seismic is characterised by numerous velocity anomalies caused by shallow gas tying the seismic to the wells is extremely difficult. Converting the seismic surfaces to depth with Vellmod II was not considered since this model has a single velocity for the entire Upper North Sea group and is therefore too simplistic. Therefore, it was decided to tie the wells to the seismic data and the wells are converted to time (TWT) See figure 4-5. Unfortunately, synthetic to seismic matching yield very poor results (cross-correlation coefficients for the A15 wells are 0.05, 0.27, 0.38) due to the quality of the sonic and density logs (probably caused by mud invasion, wash-outs, etc.). Checkshots provide the most reliable data-source, but not all wells have checkshots. Based on all available checkshots a general Depth-to-Time model is extracted for the wells without checkshots (Fig. 4-3).

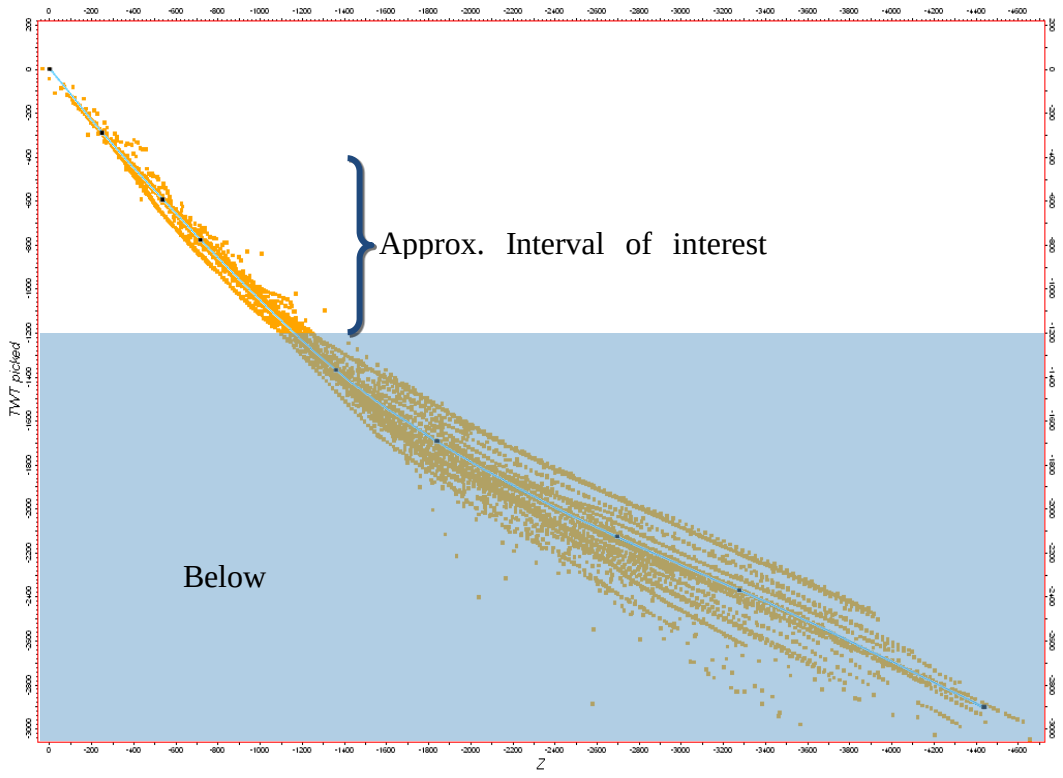

Fig. 4-3. General Depth-Time Curve (light blue) represented as best-fir curve based on best fit from available check-shot data.

The data spread around the general DT trend is relatively small for the interval of interest, suggesting the trend is generally representative. In order to check this general time curve, a residual map (difference in milliseconds between the picked marker and the seismic surface) is made at the MMU and S5 (Fig. 4-4). The MMU was selected since it is the base of the target interval and the cumulative error of the depth- time conversion is expected to be largest at the MMU. Furthermore, the MMU is present throughout the entire area and it is a prominent seismic reflector and it has a distinguishable log response. All wells that have a residual higher than (+/-) 12 ms are corrected manually. In doing so, it should be kept in mind that one or more of the following can be wrong: the seismic interpretation, the position of the marker and the DT-curve. Therefore, first the position of the marker and the seismic interpretation are checked and corrected where needed. If both are correct than the DT curve is wrong and is therefore corrected. First, the checkshots of a neighbouring well are tested

to see if this improves the residual. If not, the general DT is corrected by a multiplier. In rare cases the checkshots were discarded and replaced by the general time curve of Fig. 4-.

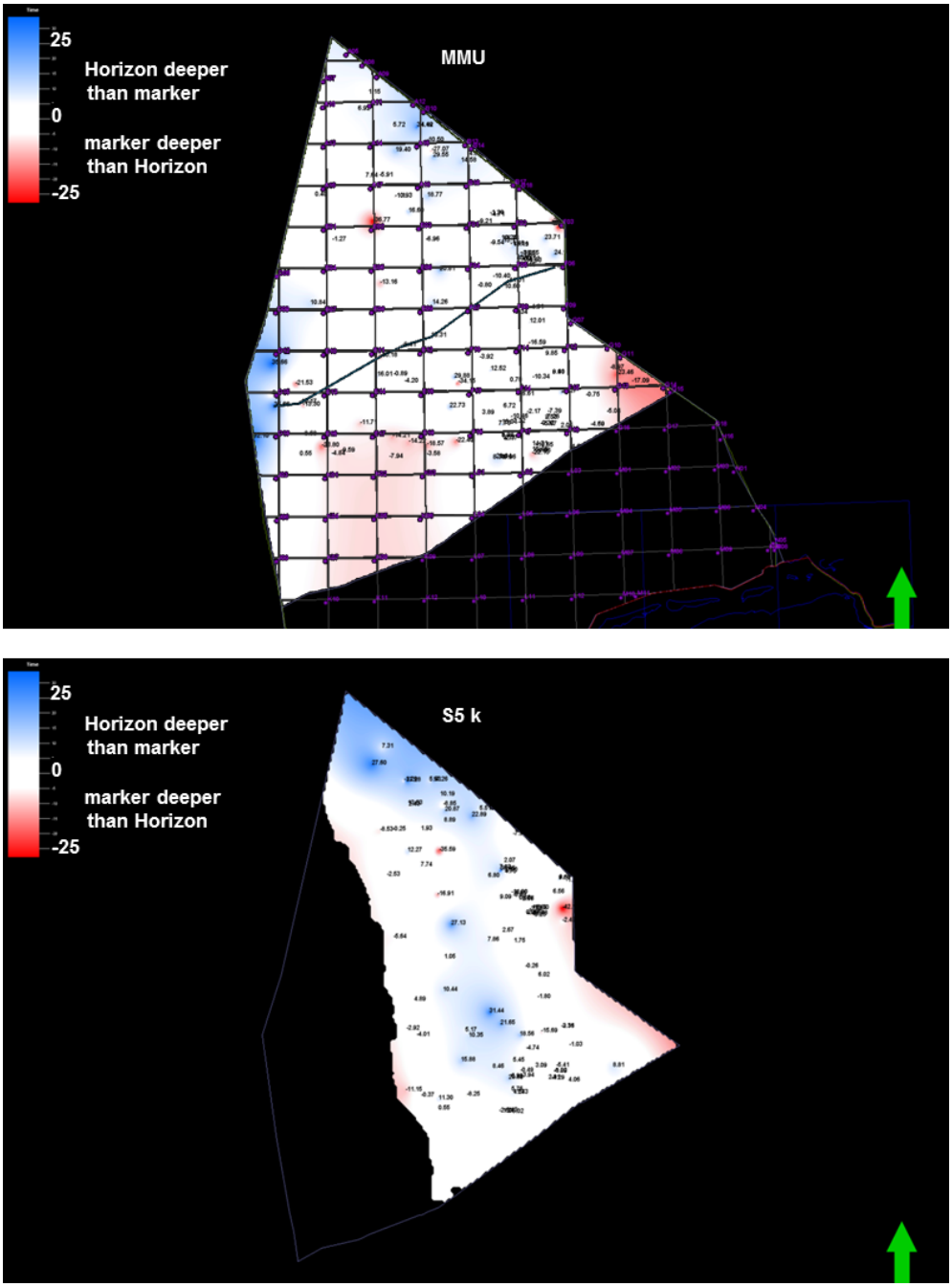

Fig. 4-4. Residual maps (difference in milliseconds between the picked marker and the seismic surface) for the MMU and S5k units.

Fig. 4-5. (next page) Well-correlation panel that roughly follows seismic line SNST87-10a which is depicted below it. Both the picked well markers and the seismic surfaces of the MMU and the top of S5 (S5k) are shown, which gives an indication of the uncertainties of the well tie.

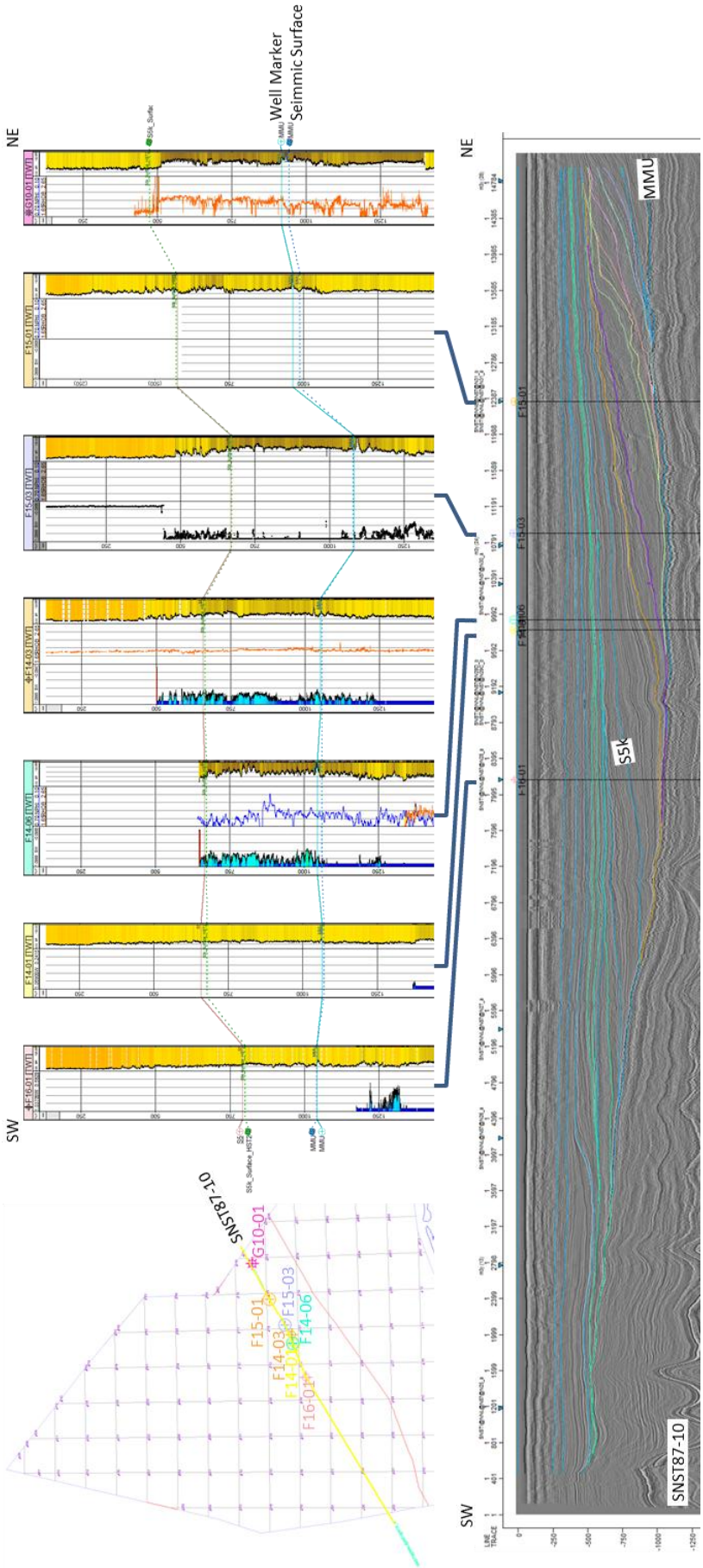
Well Marker
Seimmic Surface
NE
SW
MMU
SNST87-10
G10-01
F15-01
F15-03
F14-06
F14-03
F14-01
F16-01

4.4 Results (restructure and present as results paragraph)

The overall depositional trend of the Upper North Sea Group is an East-West prograding system, which downlaps onto the Mid Miocene Unconformity (MMU). The Upper North Sea Group can be divided into three main depositional units (see Chapter 3 also), which are strongly affected by palaeoclimate that controlled sea level, sediment supply and energy regime (currents):

- Temperate Climate Shallowing Sequence (MMU-S4)
- Alternation of Warm and Cold Periods (S5-S7)
- Artic Infill (S8-S13)

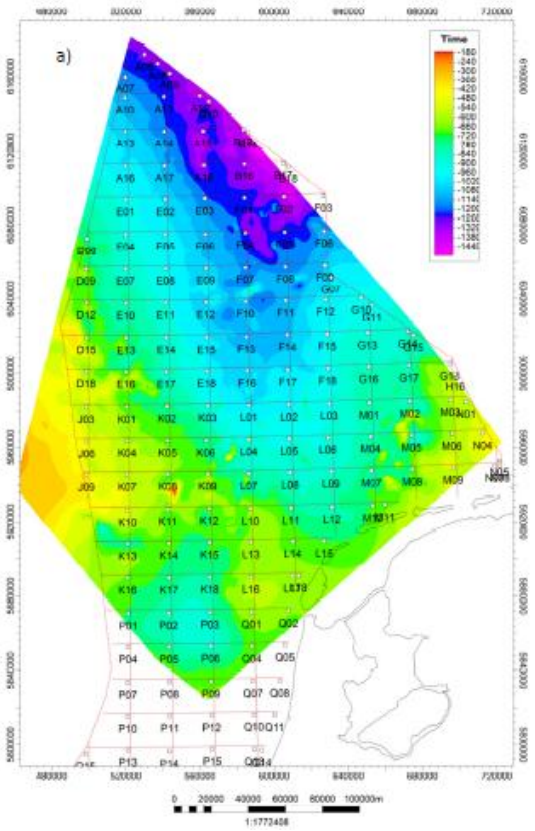

Fig. 4-6. TWT structure map of the MMU in the area studied.

4.4.1 *MMU*

The interpretation has been obtained and modified from TNO regional mapping, where it is regarded as the base of the Upper North Sea Group (Fig. 4-6). The MMU consists of two unconformities close together in this area (see Chapter 2). We mapped the youngest unconformity which is deepest in the B blocks. It becomes shallower toward the west. In the west, more erosion of the underlying sediments occurred, and since the overlying sediments fill in from the east, the hiatus is greatest in the west. There, the mapped event is most likely an amalgamation of several condensed sections and the reflector becomes very prominent. In the east, a package is preserved which is characterised by polygonal faults (heavily faulted reflector). These polygonal faults are most probable related to dewatering of water-wet sediments or caused by gas escape. The presence of bright spots seems to dominate in the area where polygonal faults are present. Taking the water depth of the overlying

sediments and their inclination into account, the western part of the MMU, i.e. towards the U.K., may represent a sub-aerial exposure surface. Palaeovalleys in seismic data that can be observed in at the UK-NL boundary may support this interpretation.

Definition: Unconformity
Reflector: Very strong in the west, faulted in the east
Event: SEG: Negative | North Sea: Positive (??)
West: End of Survey
East: End of Survey

4.4.2 *Temperate Climate Shallowing Sequence (S1-S4, Fig. 4-7)*

4.4.2.1 Summary

This unit directly overlies the Mid Miocene Unconformity (MMU) and is deposited during a temperate climate and represents an overall shallowing sequence. The basal sediments are deposited in relatively deep water and fill the relief of the MMU as it is created by regional tectonics and salt tectonics on a more local scale. There are strong contour currents mainly in the east (F-block), which create elongated pockmarks and sandwaves. The top of this unit is deposited in a shallow marine environment. Due to the temperate climate the influx of sediments is high and therefore this is considered to be a supply driven system, which is characterised by steep dipping clinoforms with a high relief. Sea- level fluctuations create higher order cycles (systems tracts). There are indications for fluvial erosion in the eastern part of the F blocks. These may connect to fluvial channel system observed in the German offshore at the same horizon. The top unit marks the transition to a colder climate. The clinoform becomes flatter and has less relief.

4.4.2.2 S1: Syn-Salt-Tonic Infill

The S1 unit infills relief of the MMU caused by salt tectonics. Since the internal structure is convergent towards the salt diapirs it is interpreted as a syn-tectonic depositional unit. S1 is deposited in a relatively deep epicontinental basin associated with relatively high gamma ray values (silt/shale) in wells. It is expected that S1 has a large regional extent and expands in the German/Danish sector.

The age of this unit is Late Miocene. The S1 surface was assigned to the Top Miocene (Kuhlmann and Wong, 2008), more specifically 5.3 Ma (Stuart and Huuse, 2012). The top of the unit onlaps from all directions onto the MMU at salt dome localities, while it downlaps towards the west at its western limit.

In the B and F blocks, pockmarks elongated by strong bottom currents are present.

S1 Surface: Unconformity
Reflector: Strong when present. Look for U shaped pockmarks
Event: SEG: Negative | North Sea: Positive
West: Onlap on MMU
East: End of survey

4.4.3 *S2: Wedge shaped aggradational clinoforms*

S2 is a wedge shaped, low angled aggradational clinoforms (1-2°), and a low seismic energy unit (little lithological variation) deposited in a well-mixed and ventilated water column. Near the top brighter silt-prone sediment waves indicate the presence of strong bottom currents. The top is defined as a downlapping surface of the overlying progradations on which submarine channels are found in the F blocks. It is placed at the Zanclean-Piacenzian boundary which is dated at 3.6 Ma.

The gamma ray characteristics show a great difference from block A to F. In block A the unit is thinner and is characterised by high gamma values (>100 API) whilst in Block F where the unit is thickest (>300m), it is characterised by coursing upwards-fining upwards-coarsening upwards sequence, all together lower gamma values 40-80 API and therefore much sandier than block A, and more proximal to the sediment source.

S2 Surface: Downlapping Surface (progradation above)
Reflector: Strong reflector in F, weaker toward west (condensed)
Event: SEG: Negative | North Sea: Positive
West: Downlap on S1 or MMU
East: End of survey

4.4.3.1 S3: High Angled Clinoforms

The S3 unit is characterised by a series of high angle (6°), high relief progradations deposited during warm conditions with forested areas. The system is driven by a large sediment influx and has a secondary imprint of sealevel fluctuations. The following system tracts can be recognized:

TST?: Only a small part of first systems tracts is present within the F blocks. Therefore it is hard to determine the nature of this systems tract.
HST: Normal Regression, high relief clinoformal progradation (bright reflectors), with a some preserved topsets. Prominent angular unconformity, SU (?) on top. Shelf edge valley cuts and sediment waves with on the slope with small amplitude anomalies.
FSST: High angled, downstepping, bright reflectors, with gravity failures

S3 intra Surface: Sequence Boundary, angular unconformity
Reflector: Strong reflector in F, weaker toward west (condensed)
Event: SEG: Positive | North Sea: Negative
West: Downlap on S2
East: End of survey

HST: 2 parasequences normal regression, Incised valley on top F03 east
FSST: small downstepping, weak reflectors bounded by a sequence Boundary, incised valley [Not interpreted]
LST: Small, poorly visible
TST: Large healing phase wedge, and locally coeval transgressive prism (Floodplains)
S3: Top of the healing phase wedge (MFS) merges with sequence boundary

S3 Surface: MFS, Top of healing phase wedge at end of steep clinoforms
Reflector: Strong in F, weaker to the west, merges with SB to the east
Event: SEG: Negative | North Sea: Positive
West: Downlap on MMU
East: End of survey

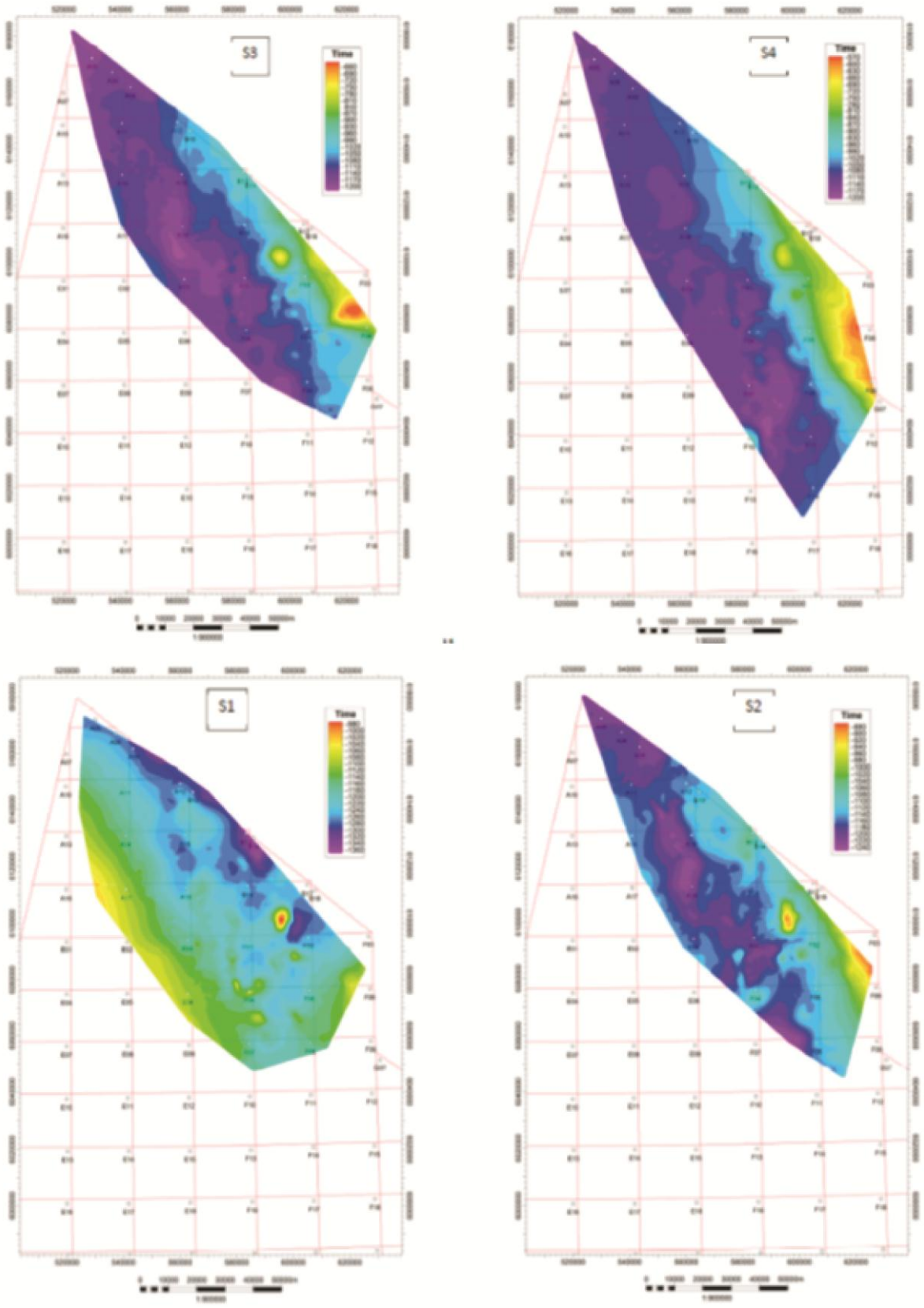

Fig. 4-7. TWT structure maps of the S1-S4 top surfaces (Temperate Climate Shallowing Sequence).

4.4.3.2 S4: Transition from a temperate to a cold climate

Highstand deposition occurs during the transition from a temperate to a cold climate. It has no distinct clinoform geometry, but is characterised by a lower relief progradation with a slope angle decrease with respect to the older units.

The top S4 is shallowest in the easternmost part of blocks B and F with the extent of the delta being rather arcuate to straight, with many lateral variations in the south, where high and lows geometry inter-finger. S4 has a maximum thickness of 450 m in block F06-09. This infers that the depocentre at the time had shifted south with respect to previous units. The majority of the unit is between 50-100 m thick, with local thickness variations associated with salt diapirs.

The S4 surface is important as it corresponds to the Gauss-Matuyama magnetic reversal at 2.58ma, which coincides with the Pliocene-Pleistocene transition.

S4 Surface: Top of HST. It does not appear to represent a regionally significant seismic sequence boundary, though it does appear to be a top lap surface and possibly be erosional in blocks A18-B17.
Reflector: Weak reflector in the west and east, strong in middle
Event: SEG: Negative | North Sea: Positive
West: Downlap on MMU
East: End of survey

4.4.4 *Alternation of Warm and Cold Periods (S5-S7, Fig. 4-8)*

Units S5 to S7 are deposited during an alternation of glacial- and interglacial periods. These contrasting climate conditions control the sediment supply both in quantity and type. During the glacial periods the basin is starved and the limited terrestrial supply resulted in a condensed shale layer (Kuhlmann, 2004). During the interglacial periods there is a higher sediment influx and sands are deposited that were prone to being captured by contourite currents and which accumulated in sandwaves. Glacial plough marks are a common feature since sea ice was present in the North Sea.

4.4.4.1 S5

Unit S5 is an alteration of glacial and interglacial sediments which is thickest (300-450 m) over a large area of the south east of the Netherlands North Sea. It is characterised by pronounced progradations related to high sediment influx. This notion is supported by the short timespan in which this unit was deposited (142,000 years). Secondary, sea-level fluctuations resulted in the deposition of various parasequences that are due to normal- and forced regressions and lobe switching. To the north, the unit is more condensed and has a stronger aggradational character. The alternation of strong and weak reflectors represents frequent changes in lithology. Westwards (Block E02), the unit thins rapidly and consists mainly of weak reflectors, representing a more distal location from the sediment source at that time. Local thickness variations as seen in the south of the area are related to salt structures, which importantly affected the seabed morphology during S5 deposition. Most likely salt movement occurred syn-depositionally (see Chapter 9).

The gamma ray characteristics of the S5 unit in Block A show three clear fining upwards sequences with a sharp boundary above the coarsest sediments at the top. In block F these fining-upward trends are not seen. It is suggested that the position of block F is more landward and therefore does not show large changes in lithology during events that (at the same time) creating clear trends in a more basinward position such as in block A. Many (10) intra S5 key surfaces have been recognised during the interpretation that were deemed necessary in order to obtain sufficient guiding for creating a realistic geomodel (see Chapter 5). Several stacked and adjacent depositional lobes are identified; the contacts between the lobes are erosional in nature and younger lobes onlap the older ones.

These erosional surfaces could be created by breaks in sediment accumulation related to either autocyclicity, glacio-eustatic sea level changes associated with the 41,000 year obliquity cycles (Kuhlmann et al., 2004), or changes in the sediment supply. As mentioned in Chapter 2, in glacial periods the sediment source was predominantly from the Scandinavian shield, and during warmer interglacials the sediment was of mainland European origin. The switching in sediment provenance may have been accompanied by varying progradational directions which would create lobe switching geometries.

S5 surfaces (from old to young):
S5a Surface: HST 1, Parasequence 1
S5b Surface: HST 1, Parasequence 2
S5c Surface: FSST Parasequence 1
S5d Surface: FSST Parasequence 2
S5e Surface: FSST Parasequence 3
S5f Surface: FSST Parasequence 4 (Lobe switch, not traceable everywhere)
S5g Surface: FSST Parasequence 5 (large bright spot!)
S5h Surface: LST (thick clayey sequence)
S5i Surface: HST 2, Parasequence 1
S5j Surface: HST 2, Parasequence 2
S5k Surface: HST 2, Parasequence 3 **Top S5 unit**, Maximum glaciation, condensed shale layer
Reflector: Regional Strong marker below (latest) contourites, fades to the east
Event: SEG: Negative | North Sea: Positive
West: Downlap on MMU
East: End of Survey (reflector stops, push interpretation through)

The top of S5 is picked at a regional reflector that corresponds to a max glaciation event corresponding to a shale layer (GR Peak). This reflector fades out to the east. Below and above the marker, sand bodies shaped by bottom currents (sediment waves) are found. The top S5 surface is linked to the global polarity time scale by Kuhlmann (2004) and assigned an age of 2.44 Ma corresponding to the X-event within the Matuyama chron.

4.4.4.2 S6: low-angle progradation

Unit S6 consists of two parasequences. The J surface marks the boundary between these parasequences. The unit consists of low-angled progradation (>2°) with a strong aggradational character and occasionally contains small and chaotic bright-spots. Glacial plough marks are observed in the eastern part. The progradation of unit S6 is further southwest than S5 and reaches into block K and L, with the surface dipping towards the NW.

There is a large difference in the thickness maps of S5 and S6. The greatest thickness of S6 is deposited along an almost N-S orientated elongate trough to the west of the main depocentre of S5 sediments. There appears to be a large area of sediment bypass with respect to S5, illustrating the strong progradational character of the system. Note that the thickest vertical sediment accumulation often corresponds to the steepest inclined (slope) part of a clinoform.

S6 appears to be a regional, highly correlatable surface that forms a distinct downlap surface to smaller scale progradational packages of S7 in the majority of the area. The reflector is most distinct basinwards.

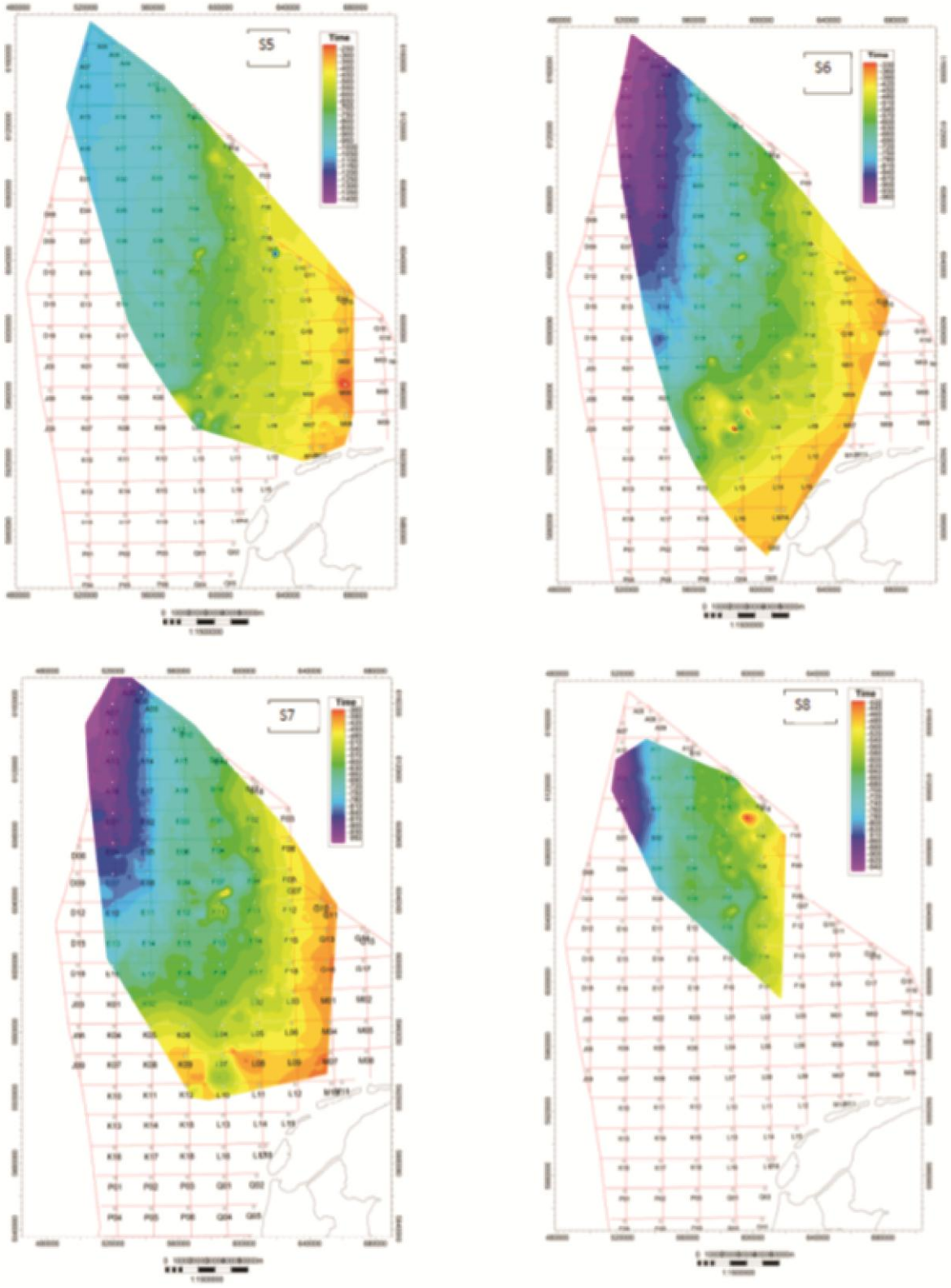

Fig. 4-8. TWT structure maps of the S5-S7 top surfaces (Alternation of Warm and Cold Periods) and S8 at the base of the Arctic Infill depositional unit.

Definition: Top of low angled progradation, downlapping surface
Reflector: Moderately strong, regionally
Event: SEG: Negative | North Sea: Positive
West: Downlap on MMU
East: End of Survey or onlap onto S5

4.4.4.3 S7: small scale progradation

Unit S7 is characterised by a small scale progradation that downlaps onto S6. There are no clear reflectors; however the small scale progradations are a prominent feature. The seismic characteristic of the surface is discontinuous to chaotic in places, weak amplitude, becoming stronger towards the top of the unit. The surface almost merges with S6 in the south of the area. Petrophysical analysis suggests a fine-medium grained lithology. The unit is thickest along an elongate depocentre, just as in S6 however the depocentre is ~20km west, with the thickest sediments in blocks E17-18 and K02, again attesting the the overall progradational character of the system.

S7 Surface: Top of small scale progradation
Reflector: Weak
Event: SEG: Positive and negative | North Sea: Negative and Positive
West: Downlap on MMU or S6
East: Onlap onto S6 or end of survey

4.4.5 *Artic Infill (S8-S13; Fig. 4-8, Fig. 4-9)*

The youngest depositional unit is deposited in a shallow sea under Arctic conditions with sea ice cover. Glacial plow marks are a frequent sight. Some of the units represent warmer periods with an open vegetation and more open marine conditions. The main depositional architecture is characterised by low-relief-, low-angle progradations.

4.4.5.1 S8

S8 is a small unit, which is hard to map regionally and its significance is questionable. It downlaps onto an unmapped shelf edge wedge that sits in front of the shelf break of S7 and is mainly aggradational in character. The reflection characteristics of the unit are chaotic and discontinuous in places but with stronger amplitudes than S7. The gamma ray characteristics are consistent with S7.

S8 Surface: Base of S9
Reflector: Strong to very weak
Event: SEG: Negative | North Sea: Positive
West: Downlaps on S7 (see above) or MMU
East: Onlaps on S7

4.4.5.2 S9: Chaotic progradation

Unit S9 is a chaotic progradation with some bright patchy clinoforms. The surface is defined as the top of these clinoforms. Towards the west these clinoforms disappear, so the S9 event is defined there as the base of the overlying low energetic unit (S10). The depocentre appears to be in a trough NNW-SSE in the area of block A-E. Where the unit is thickest, the unit shows a chaotic progradation with reflectors stronger in amplitude than to the south of the main depocentre. In the south the unit is thinner, more aggradational and weaker in seismic amplitude.

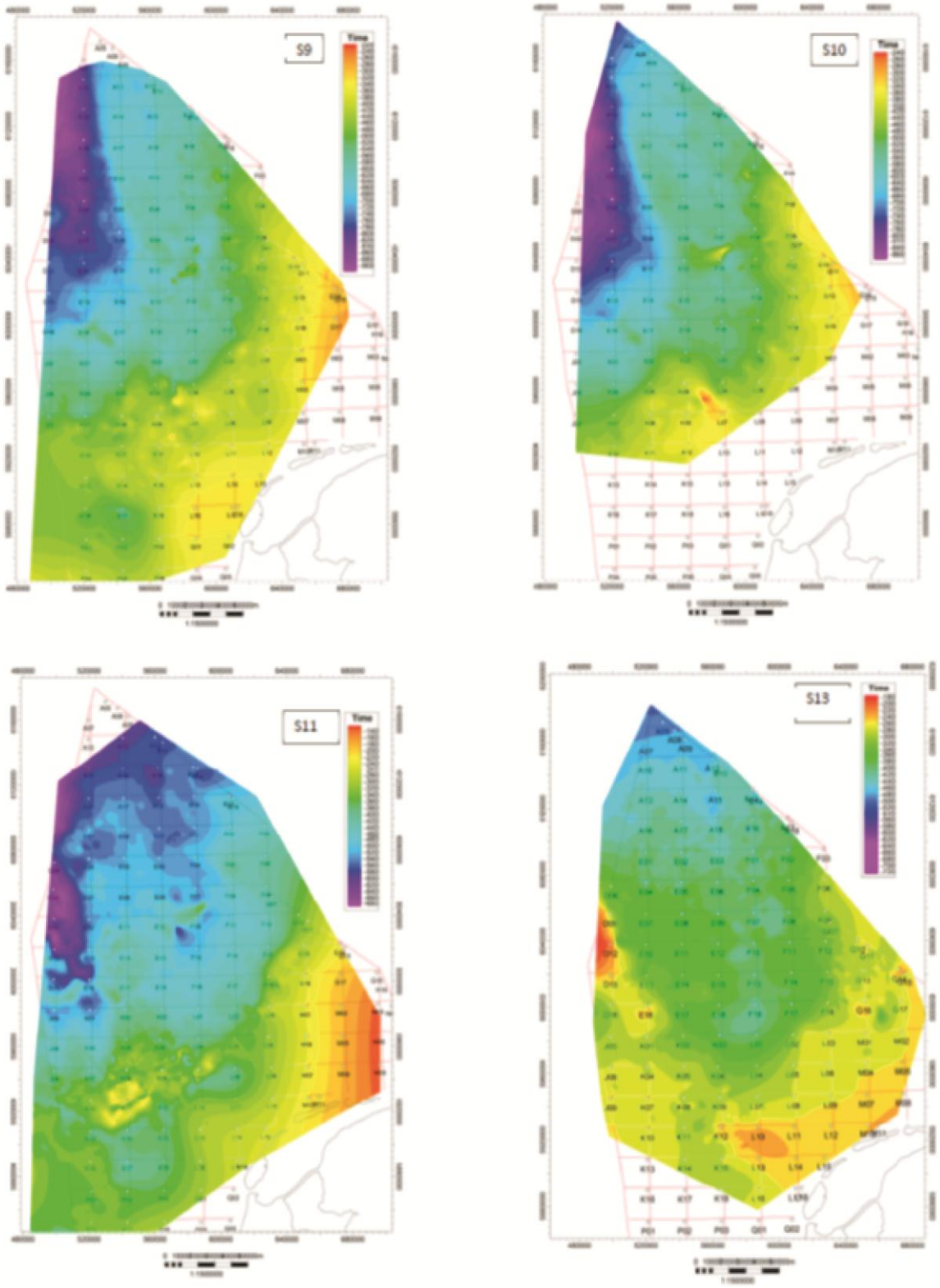

Fig. 4-9. TWT structure maps of the S9-S13 top surfaces (Arctic infill), S12 is not shown since there are no marked differences in its geometry compared to S13.

S9 Surface: Top chaotic progradation, base of low energetic unit S10
Reflector: -
Event: No reflector
West: Downlaps on MMU
East: Onlap on S8 or end of survey

4.4.5.3 S10: Aggradational progradation

The seismic response of Unit S10 is of a low energy. Although some bright wavy reflectors are found in the north-western part S10 is a largely aggradation unit. In the south it is a clear downlapping surface, because a small progradation overlies it, but this is not so easily recognised elsewhere in the basin. In the north this progradation is not well developed. Sandwaves along the shelf strike are identified at the top of S10 unit.

S10 Surface: Top of progradation, downlapping surface
Reflector:
Event: SEG: Negative | North Sea: Positive
West: Downlaps on MMU
East: Onlaps on S9

4.4.5.4 S11

Unit S11 has some small scale progradational units in the south, but a more chaotic nature in the north where the unit is thicker. The top has an erosional character in the west. The S10 and S11 thickness map shows that the greatest thickness of these units follows a narrow NW-SE trending slope, with thicknesses up to 300 m. The depocentre is ~ 40km west of the S8 and S9 depocentre.

Wells in block F have low gamma readings (30 API), with higher readings in block A. In the thickest part of the succession, in block E, the gamma log has more variation and zonations. This supports earlier observations that lithological variations in clinoforms slopes are highest.

The top S11 surface is dated by magnetostratigraphy in block A and corresponds to the Olduvai subchron at 1.9ma.

S11 Surface: Erosional event in the western part
Reflector: Strong
Event: SEG: Negative | North Sea: Positive
West: Downlaps onto the MMU or end of survey
East: End of survey

4.4.5.5 S12 and S13

The units S12 and S13 are grouped because there characteristics are rather similar. These units are the first that span the entire study area. The unit characteristics are mainly aggradation with horizontal-subhorizontal reflectors across the majority of the basin. They are deposited under open marine to near shore conditions. The deepest part of the basin is to the north, becoming shallower to the south. The slope is no longer expressed as an elongate feature. The depth variation across the basin (200-500m) at this time was much less than in the Early Gelasian, suggesting the basin has been filled in with sediment. Well correlations between block A and F show a coarsening trend (increasingly lower gamma ray) to the south west. The average gamma ray API of ~30 suggests a coarser grained lithology.

The S13 surface) is Top Gelasian in age (1.8 Ma). In a large part of the area, the S13 surface demarcates the transition between predominantly horizontal, continuous reflectors to chaotic reflectors above.

S12 Surface: Regional marker
Reflector: Moderately strong reflector on top of lower energy unit
Event: SEG: Negative | North Sea: Positive
West: End of survey
East: End of survey

S13 Surface: Regional marker often cut by tunnel valleys.
Reflector: Weak
Event: SEG: Negative | North Sea: Positive
West: End of survey
East: End of survey

4.5 Summary of results

This chapter describes the interpretation of all input data that enable to construct the geological model which forms the basis for the reservoir/property model. These data include a geological framework based on a sequence stratigraphic/seismic interpretation of key horizons (constrained by biostratigraphic data) and petrophysical data, used to populate zones in between the horizons. The studied sequence can be divided into three main depositional units, which are strongly affected by palaeoclimate that controlled sea level, sediment supply and energy regime (currents) and that include:

- Temperate Climate Shallowing Sequence (MMU-S4)
- Alternation of Warm and Cold Periods (S5-S7)
- Artic Infill (S8-S13)

5 Reservoir model and rock-property prediction

5.1 Introduction

The interpreted horizons form the basis for a regional geological model (“reservoir model”) that represents the internal architecture (“anatomy”) of the SNS delta to the best extent. This reservoir model is used to distribute lithological and petrophysical properties, such that a property model is obtained. The main objective, based on the property model, is to predict these properties for all bright spots identified. The method described here focuses on honouring the reservoir properties at the well location, since many bright spots are penetrated by wells or in close vicinity. The modelling of properties is also aimed at getting insights in the regional distribution of relevant properties and forms the basis for the discussion on shallow gas scenarios (see Chapter 8). However, some relevant properties, such as gas saturation, are not easily extrapolated from gas-free to gas-containing strata and require different prediction methods than for reservoir properties that are considered unrelated to gas content.

5.2 Methods

5.2.1 *Reservoir model construction*

From the 13 interpreted horizons and the guiding horizons within unit S3 and S5 (total of 25 horizons) a regional geological model was built for the stratigraphic interval MMU – S13 (1.8 Ma). All results are contained in the accompanying Petrel project (Annex 3). The applied workflow is common practice in oil and gas exploration and is based on the interpretation of horizons from 3D and 2D seismic data in the time domain (two-way travel time). Since the model is also presented in the time domain, a depth-time conversion was applied on the well markers and well logs based on sonic logs and checkshot data. The interpreted well markers help identify the horizons in the seismic data and provide anchor points for the well tie. A full description of the time-depth conversion method is presented in Chapter 4.

Given the small number of faults with significant offset in the stratigraphic interval considered and considering the relative large size of the model area, it was chosen not to build a model following “standard” fault modelling in order to keep computation time within reasonable limits. Instead, the model was build using “simple” modelling techniques using horizons only. The horizons include the observed fault steps, but are not cut by faults in the model. However, faults are presented in the accompanying Petrel project and are taken into account for Bright Spot classification.

The horizontal model resolution is set at 1000 m, since higher resolution dramatically increases computation time. Considering relative small amount of wells (227) in the 17632 km^2 area, the 1 km grid size is small enough to honour single well data and avoids introducing a pseudo-accuracy. Moreover, the chosen grid resolution complies with the intention to provide insight in the regional distribution of properties. The zones in the resulting model were layered proportionally, such that each zone consists of 10 layers with a minimum layer thickness set to 1 m. The layering provides a realistic internal clinoform geometry as observed in seismic data (Fig. 5-1).

5.2.2 *Property selection and upscaling*

Based on petrophysical evaluation several well logs and core-measured data are used that exist for most wells. The GR, DT, neutron and RHOB logs are not directly used to populate the model, but are used as input for calculating petrophysical properties such as PHIE, Vcl (also named Vsh or VSH) and SW. Next to the petrophysical logs, palaeoclimatological and –environmental data interpretations

are made based on cores and cutting, these include: AP/NAP, SD ratio, SST dino (see Chapter 3 for explanation). Geochemical data include TOC% and CaCO3%measurements. Based on these logs and data (within Petrel) a number of additional discrete properties are defined, including delta element, litho-, and delta-element facies.
It should be noted that Petrel regards such discrete properties as “facies” since all data fall within a certain class. Accordingly, the process used to populate the model with these discrete values is called facies modelling. Originally, sedimentology uses “depositional facies” to denote distinctive rock units that form under certain conditions of sedimentation, reflecting a particular process or environment in a certain position within a basin (this position is referred to as delta-element facies). Lithofacies represent grain size classes, these can be either based on grain size analyses on sampled core material (as done for the seal capacity study; Chapter 6) or derived from petrophysical analysis (as is used here for the property modelling).

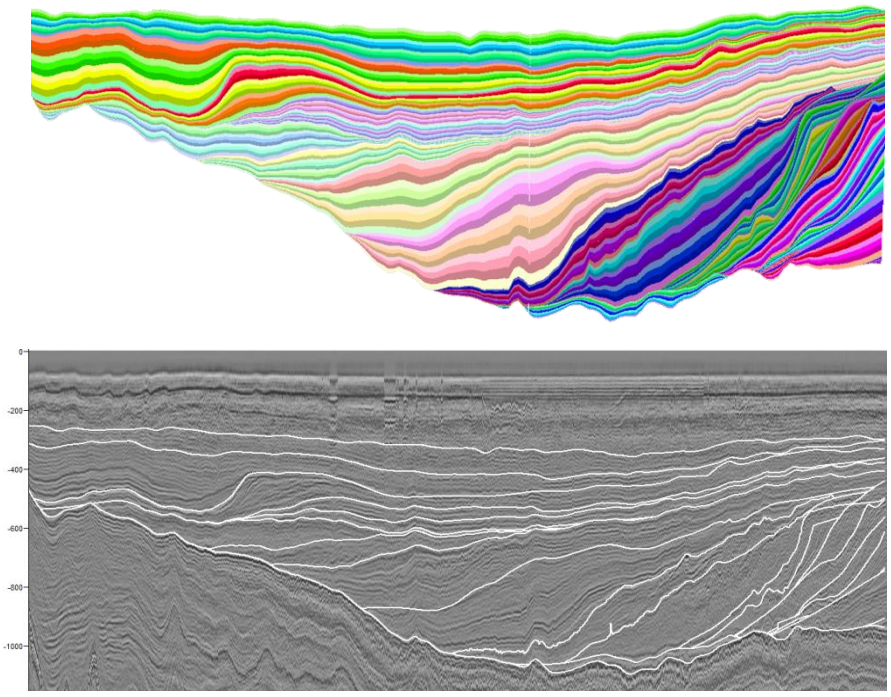

Fig. 5-1. Internal layering applied on stacked interpreted horizons (top figure) and seismic line SNS87@N10a with interpreted horizons (bottom figure).

5.2.2.1 Delta-element facies definition, upscaling and modelling

All interpreted surfaces delineate the top surface of distinct clinoforms and have a significant sequence stratigraphic meaning (see section Chapter 4.). For all these surfaces the distribution of delta elements has been determined, resulting in zonal maps indicating the distribution of topset-, foreset- and toeset-to-prodelta settings. Determination of delta element type is based on 1) the geometry of the surface constraint by 2) the relation with internal geometry of the zone beneath and above (downlap, toplap, etc.), which in turn forms the basis for 3) the sequence stratigraphic interpretation of the clinoform. In theory, prograding clinoforms can occur during sea-level highstand (Highstand Normal Regression; HNR) or during sea-level lowstand (Lowstand Normal Regression; LNR). In combination with the top-, fore-, and bottomsets, this potentially results in six delta element types. However, lithologically, the difference between HNR or LNR delta elements is not expected to be significantly different. For both HNR and LNR types, topsets represent marginal shallow marine

depositional setting, foresets occur seaward of the shelf-edge break and the prodelta occurs seaward of the shelf-toe break. Therefore, initially the model is populated with the three basic delta element types.
The vertical interpolation of two of the zonal maps, forms the basis for distributing the delta-element property throughout all layers of the model and illustrates depositional trends such as progradation or retrogradation. Several zones only consist of one delta element, such as the S1 unit (deep marine facies) and the S12 and S13 units, which consist entirely of delta topset facies.

Outline of method applied:

- Generation of surface attribute maps that give the distribution of 3 delta-element facies
- Conversion to points with attributes
- Upscaling of properties at horizon level
- Conversion of properties to well log at well locations to assure that vertical trends are honored
- Distribution of property using Facies modeling in Petrel with the following settings:
    - Anisotropy based on average dimension of the smallest delta lobes (see Appendix D)
    - Angle varying dependent on main shelf edge orientation (N330E – N350E)
    - Truncated Gaussian simulation to honor the sequential order in which the facies occur.
    - Smoothing to remove unwanted noise (i.e. topset facies cells in the middle of prodelta) that might be an artifact of the TGS algorithm.

Where appropriate, the delta element facies is used to guide other properties to avoid random property assignment in areas where well-data coverage is low. As such, property distribution is conditioned in a deterministic- rather than stochastic way. Considering the size of the area studied and the low number of available wells for some properties (see section 4.1) it is safe to state that this holds for the entire model generated.

5.2.2.2 SD ratio facies definition, upscaling and modelling

The SD ratio describes the ratio between terrestrial/marine flora, i.e. between sporomorphs and dinocyst and can be used to define the proximity of a deposit in terms of marine influence. By establishing a relationship between the count rates and facies (litho- and depositional element facies) the SD can be classified and subsequently transformed into a discrete log. Fig. 5- show a cross plot of the SD values against Vclay and classified according the lithofacies. This plot shows that the both high and low SD values (% terrestrial) occur in all lithologies. This can be interpreted such that all the delta sediments studied have a high terrestrial input. The second plot shows the same SD vs. Vlay data but then color-coded against the depositional element facies. This shows that there is a slight tendency of the higher (>0.92) SD values to coincide with the delta topsets, the values between 0.74-0.92 to coincide with slope facies, and lower values are concentrated in the delta-toe/prodelta facies. These values have been used to define class boundaries and to transform the SD values into discrete values as well as follows:

SD_discrete = if(SD_ratio<0.74, 0, if(SD_ratio>0.92,2, 1))
(with delta element 0 = deep marine , 1 = shallow marine , 2= terrestrial/marginal marine)

The resulting SD values have been classified based on the estimated correlation with delta-element facies. To ensure that after upscaled intermediate SD values fit within one delta-element class, the calculated discrete SD logs are biased by the delta-element facies type as well. Note that selection of cut off values is indirectly based on calibration with seismic interpretation of delta elements.

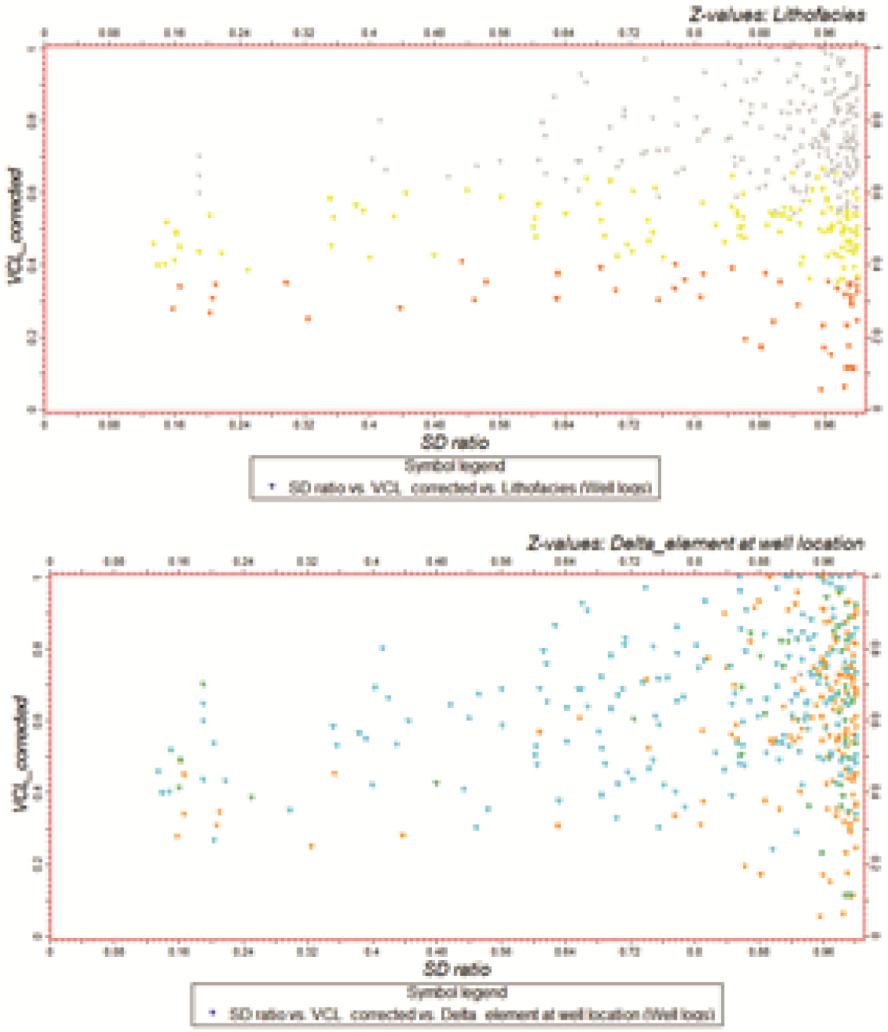

Fig. 5-2. SD vs Vclay, color-coding = lithofacies (top figure). SD vs Vclay, color-coding = delta-element facies (bottom figure).

In the studied part of the SNS delta, many topsets contain ice-berg scratch marks, which are indicative for shallow water depths. This means that the topsets of most clinoforms under scrutiny represent the shelf and are thus marine. Therefore, it is expected that the terrestrial input (sporomorphs) never reaches 100% since it is mixed with marine flora (dinoflagellates). This results in SD ratios (terrestrial/marine ratio) that are always less than 1, where delta topsets are prone to store most of the terrestrial material and prodelta and basinal facies store most dinoflagellates cysts.

The obtained SD class values at well location are first upscaled to the layer thickness at well location and subsequently distributed throughout the model based vertical and horizontal variograms as described in Appendix D.

5.2.2.3 Lithofacies facies definition, upscaling and modelling

*LithoFacies = if(VCL<Vsand,3,if(VCL>(2*Vsand),1,2)) (with 1= shale, 2 = silt , 3 = (very fine) sand)*

Where (following the simple shaly-sand model): Vsand = 1-(VCL-PHIE) and Vcl represents the wet clay volume, which can be subsequently used to calculate Sw (see section 4.1). Thus,

LithoFacies = if(VCL<(1-(VCL-PHIE)),3,if(VCL>(2(1-(VCL-PHIE))),1,2))*

In order to bring the lithofacies logs at the layered model resolution they can be up-scaled using either "**most of**" or "**mid-point**" averaging methods. The mid-point method may over represent occurrences of clayey thin beds. The most-of method is a proper representation of surrounding cells, but might underrepresent low values (Fig. 5-3). For instance, a sand value might be given to cells where both sand and shales occur. In order not to "loose" potential reservoirs layers, the most-of option is chosen as favourable.

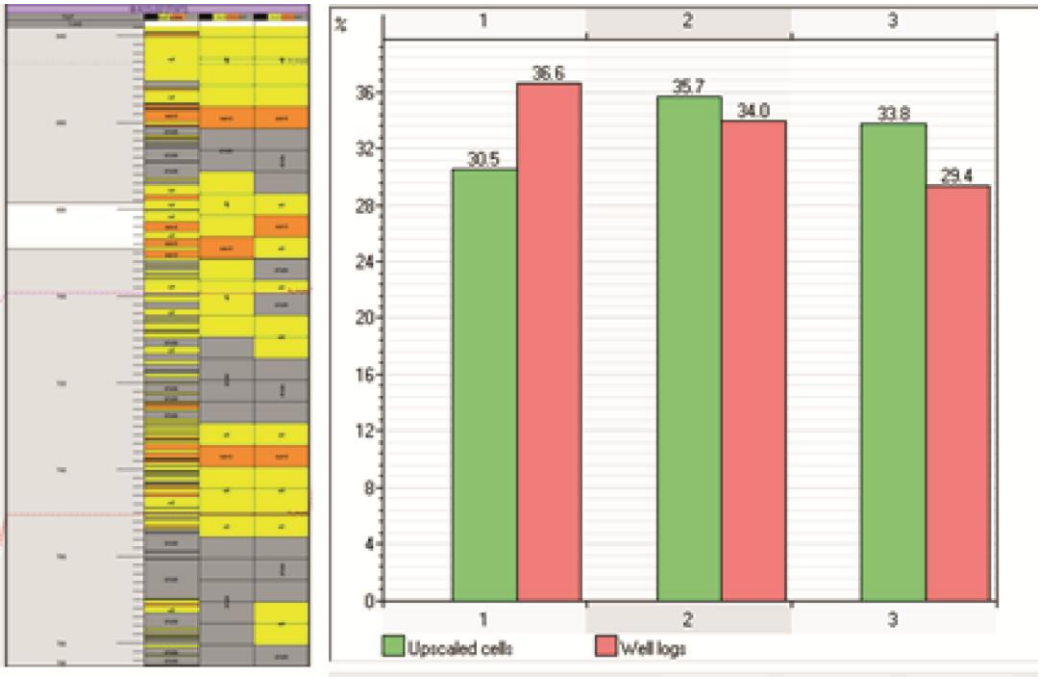

Fig. 5-3. Example of original (left) lithofacies derived from well log with petrophysical evaluation and upscaled logs: mid-point (middle) and most-of (right) averaging method. Notice swap in facies. Histogram of " most-of" upscaled vs. well log values of lithofacies (1 = clay, 2 – silt, 3 = vfine sand), showing the effect of over-representing thin beds with coarser sediment (lithofacies code 3) and underrepresenting thin beds with clayey sediment (lithofacies code 1).

The relationship between Vcl and PHIE is shown in the scatter plot of Fig. 5-. The PHIE =-Vcl linear trend drawn describes a monomict lithological composition (the more clay, the less porosity). Overall this is true, but the high amount of data left of this trend shows that even low PHIE values may exist in sandy lithofacies with low Vcl. A possible explanation is that the sediments are polymict in composition, with two or more grain size classes present.

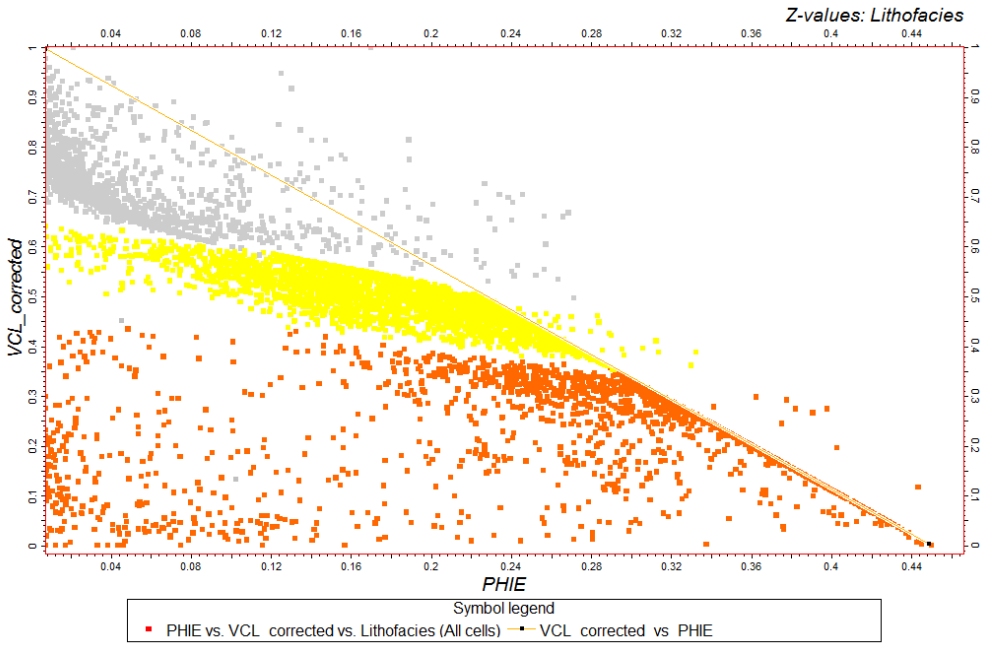

Fig. 5-4. Scatter plot of upscaled PHIE at well location agains upscaled t Vcl, classified according lithofacies type.

In modelling the lithofacies property a bias towards delta element facies has been introduced. However, this has been done in such a way that a non-exclusive tie between lithofacies and delta element is produced. This means that lithofacies can in theory occur anywhere, but might show a tendency towards a certain delta element. Therefore, the depositional element property is translated into a probability of a certain lithofacies to occur.

This probability is derived from the least square regression of upscaled lithofacies vs. delta_element properties at the well location. It indeed seems that all three lithofacies occur in all delta elements, but that there is slight tendency of shaly facies to dominate the prodelta/basinal setting. Following the regression:

Y = 0.260003 * X + 1.69358

It follows that the change for a lithofacies to occur in a certain depositional setting can be reviewed against the expected optimum (Y = X+1) and its reverse (Y = -X+3). It than appears that for the three delta elements:

Prodelta: shale = 0.70; silt = 0.15, sand is 0.15
Foresets: shale = 0.25; silt = 0.50, sand is 0.25
Top sets: shale = 0.22; silt = 0.22, sand is 0.55

These probabilities are implemented in the facies modelling of the “most-of” up-scaled lithofacies in order to distribute lithofacies throughout the model. For facies modelling the lithofacies property truncated Gaussian random function simulation is used, which honours well data, input distributions, variograms (see Appendix D) and trends. This algorithm is based on kriging and randomly places highs and lows between data in a manner that honours the horizontal and vertical variogram. Superimposed on these highs and lows are smaller noise features. The TGS algorithm is a parallelized kriging algorithm, which makes this a workable modelling mode for a regional model. For

the facies models, the same anisotropy range and orientation settings are used as for petrophysical modelling.

5.2.2.4 Depositional facies definition, upscaling and modelling

Based on lithofacies and delta element, a depositional facies is calculated, which can be used alongside the seismic interpretation of sedimentary facies and depositional geometries (Fig. 5-5). The rationale is that the different lithofacies are not restricted to a particular position on the delta and that the proximity to riverine input is reflected by the SD ratio (to some extent and only locally) and the delta element (regionally). Note that the resolution of lithofacies is much higher than SD-discrete since it is derived from petrophysical well log data (basically, VCL and PHIE, see above). The SD ratio is a palynological analysis performed on cuttings and scarce cored wells. Therefore, the depositional facies modelling can only be conditioned locally by the SD-discrete property. The conditions used to create the property:

depofacies_deep= if(D-element =2, if(LithoFacies=1,6,if(LithoFacies=3, 8,7)),U)
depofacies_shallow= if((D-element =1), if(LithoFacies=1, 3,if(LithoFacies=3, 5,4)),U)
depofacies_terrestrial= if(D-element =0, if(LithoFacies=1,0,if(LithoFacies=3, 2,1)),U)

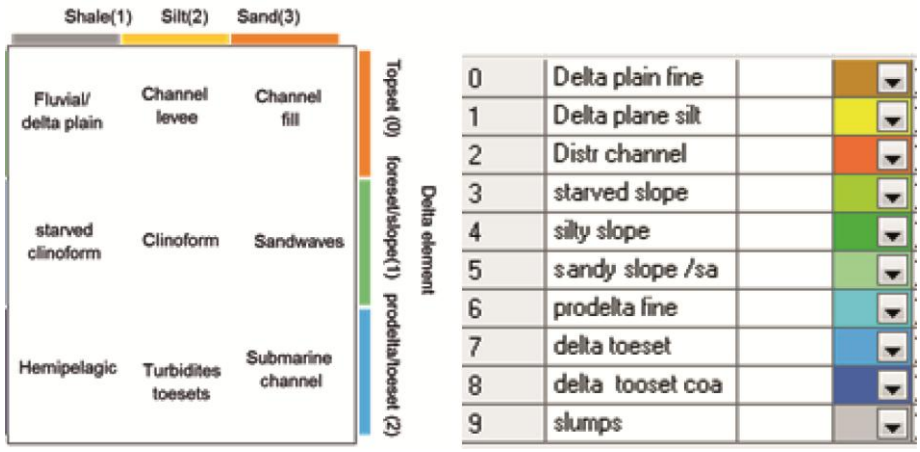

Fig. 5-5. Logic behind the depositional facies classes (left) and used colour-coding (right).

Subsequently, the three are combined to produce the 9 different facies types listed in Fig. 5-5.

Depofacies = if(depofacies_terres<>U,depofacies_terres,
if(depofacies_shallow<>U, depofacies_shallow, depofacies_deep))

The 10th facies type represents the slumps and is added to the geological model at a later stage by replacing the other facies types at those grid cells where a slump is present. The resulting property is already up-scaled and distributed throughout the model since it is calculated from the modelled properties “delta_element” and “lithofacies”. The property is distributed throughout the model using facies modelling functionality in Petrel and steered by vertical and horizontal variograms as described in Appendix D.

5.2.3 *PHIE facies definition, upscaling and modelling*

Effective porosity (PHIE) is obtained from petrophysical modelling and is directly used in the upscaling and modelling process. Normally it is advocated to upscale continuous well logs using a bias to facies to ensure that all PHIE values at any place in the model fit within one of the facies classes, without producing exclusive bonds. Here lithofacies is used for biasing. The histogram of well vs. up-scaled PHIE values (Fig. 5-6) allows a first semi quantitative analysis that shows that the raw data is honoured after upscaling, but that in general up-scaled values show somewhat higher porosities. This is the effect of biasing by up-scaling, which slightly over represents coarser beds that have higher porosities.

Population of the model by continuous PHIE and Vcl values has been performed by a combined stochastic-deterministic approach, applying a Sequential Gaussian Simulation (SGS) algorithm steered by horizontal- and vertical variogram models (Appendix D) and by co-kriging with the depositional element type. The SGS algorithm populates the grid based on input data statistics, whereas the co-kriging introduces the geological knowledge. Given the low amount of well data and the regional character of the study, the addition of this deterministic component is considered the best for modelling continuous logs since it minimizes the introduction of new values based on the data statistics only (the stochastic component). For instance applying SGS algorithms introduce a lot of noise in areas where data coverage is low. The SGS algorithm is intended for interpolating continuous variables which are assumed to have values with a more or less normal (Gaussian) distribution. The SGS algorithm in the Petrel software therefore applies a normal score transformation on the absolute property values before interpolation (i.e. transforms the data set such that the variable has a normal Gaussian distribution with a mean of zero and a standard deviation of one). The interpolated values are finally back-transformed to absolute values.

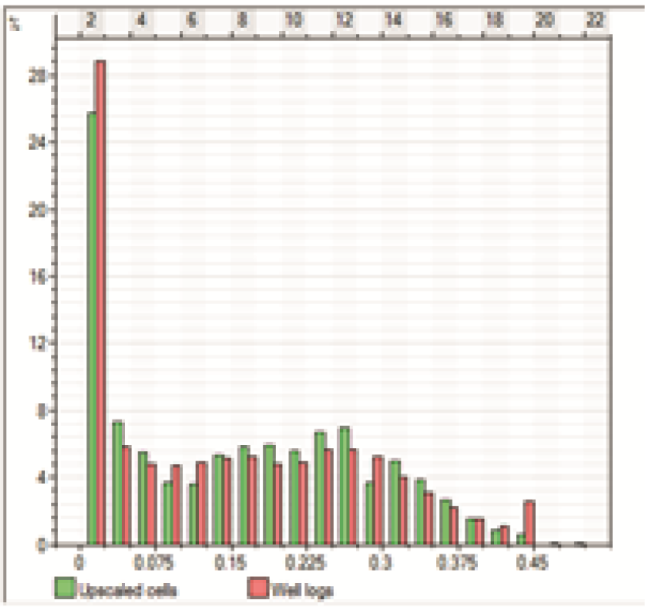

Fig. 5-6. a) Cross-plot of upscaled PHIE vs. Lithofacies, showing positive correlation of porosities and grain size. b) Histogram of raw vs. upscaled PHIE.

5.2.4 *Vclay facies definition, upscaling and modelling*

The Vclay are up-scaled and conditioned in exactly the same way as done for PHIE. The first reason is that logs may be derived from or related to (amongst others) PHIE, secondly this assures that in up-scaling the same weight on log values is applied.

5.2.5 *Gas saturation (Sw) definition, upscaling and modelling*

Water saturation (Sw) or gas saturation (Sg; and Sw = 1 - Sg) was determined using petrophysical evaluation. For a discussion on the value of these obtained values the reader is referred to Chapter 4. Although there is a strong correlation between Sw and lithofacies and/or depositional element, the occurrence of gas is determined by many other conditions as well. Populating the model on basis of up-scaled Sw values using SGS or kriging will most likely overestimate the continuity of gas sands, i.e. low Sw values will be extrapolated beyond the limits of bright spots since lithofacies boundaries are not linked to the BS extent. To overcome this problem, property distribution can be conditioned by properties (well log or seismic) that are representative for gas content. Inversion of seismic amplitude intensity, however, is not the right approach, because the relationship with gas saturation is unclear. Assuming that such a relationship exists would only reproduce the bright spots (ten Veen et al., 2011). For this reason, and in order to honour the input log data as much as possible, no conditioning was applied and Sw values where distributed using a Nearest Neighbour method. As such, bright spots that are penetrated by wells will get values that are representative for that well location and which may only be extrapolated with the same closure. This assumes that for closures 1) spill points can be determined and that 2) within the trap the Sg is laterally continuous and that vertical trends in Sg indicate either charging or leakage. The Nearest Neighbour method will populate Sg throughout the entire model, but is should be kept in mind that values outside the well-penetrated bright spots (or compartments within BS) should be regarded unreliable, i.e. the model cannot be used to study regional trends in Sw/Sg. For this reason regional results are not shown here.

5.2.6 *Uncertainties of the property modelling*

Uncertainty analyses for continuous property modelling is based on the stochastic method applied to populate the grid cells of the model. This also provides statistics that can be presented as P10, 50, 90 values. The P50 represents the mean property value of all realisations and is identical to a normal Kriging interpolation result. The P10-P90 value represent the range that includes 80 % of the modelled property values; the larger this range the larger the uncertainty. At well locations (where data is honoured) this value is close to 0 and precision is high. The P90-P10 range thus represents an uncertainty that can also be interpreted as precision (Fig. 5-7) or reproducibility of the data based on the expected variability as represented by the input variogram (Appendix D).

The question of how accurate or reliable the modelling approach is, can be answered by assessing the proximity of modelled values (P50 values) to the true value in the wells. This is valuable to know because it also predicts how well the modelling approach is able to predict values in between well locations. However, since the (upscaled) well values are honoured in property modelling, this accuracy measure is not a default product given by Petrel. Statistical packages such as Isatis are able to perform so-called blind well test where the modelling is performed by sequentially taking out each input well and comparing the resulting model property with this input well. Exporting the complete model geometry and upscaled wells from Petrel to (e.g.) Isatis is pain-stacking and time-consuming manual labour and for this reason it was not performed. Some random test showed that accuracy was rather low, i.e. the model cannot predict properties at the well location. With a relatively low data density and a combined stochastic-deterministic modelling approach as applied here, it is expected that accuracy is low, but that regional trends can be determined adequately.

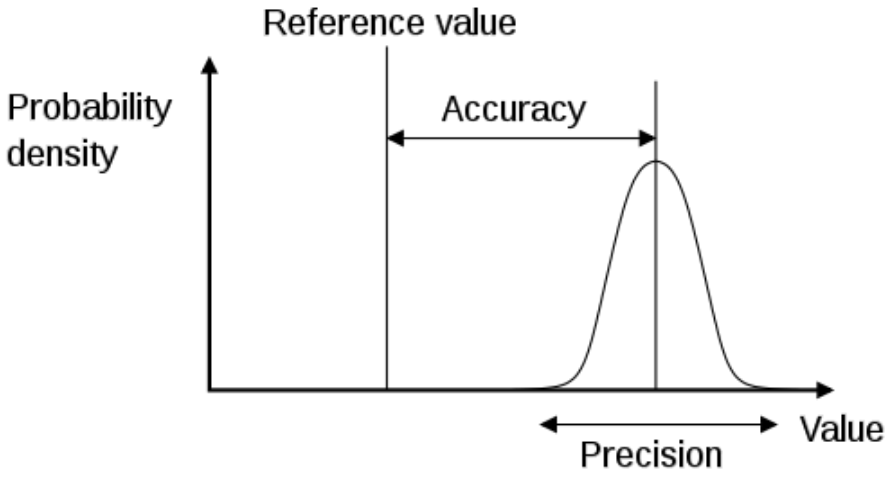

Fig. 5-7. Accuracy indicates proximity of measurement results to the true value, precision to the repeatability, or reproducibility of the measurement.(Source: http://en.wikipedia.org).

5.2.7 *Representation of model result.*

Representation of 3D properties by means of 2D maps has several drawbacks which should be taken notice of. Properties are only represented for key horizons. These horizons may represent erosional surfaces or flooding surfaces (or lobe switching events) and for this reason it remains questionable to what extent these are representative for the whole unit below the horizon. To avoid effects at discontinuity surfaces to be over represented, it was decided to show average property values of the whole sequence on the layer just below the key horizon. Note that these maps are able to highlight the evolution of regional trends, rather than internal details of the unit studied.

5.3 Property modelling results

5.3.1 *PHIE*

Results of the PHIE property model is shown as average PHIE_P50 maps for all main units. The values are attributed to the preventative surface (Fig. 5-9). A general deduction from these maps is that the porosity values increase upward in the S1-S13 interval, which corroborates the overall prograding trend of the delta. At a higher level of detail it is also noticeable that lateral trends in PHIE do not coincide entirely with the palaeogeographic trends, i.e., with the delta element facies (the boundaries of which are also indicated in Fig. 5-9). This observation has implications for tying reservoir characteristics to depositional setting and will be illuminated in Chapter 9.

The SGS algorithm builds multiple (20) random realisations that both honour the up-scaled values and represent the expected target distribution and heterogeneity. All realisations were used to calculate mean effective porosity models. The presented P10 and P90 values are based on the assumption that the modelled values have a normal (Gaussian) distribution. Under the same assumption P50 is represented by the mean PHIE. With this information a P10-P90 property (-maps) can be generated that represent the range that includes 80 % of the modelled PHIE values. Smaller values indicate a narrower range and thus a lower uncertainty (Fig. 5-8). Uncertainty tends to increase up to 0.45 to the west where data coverage is low, is relatively low (~0.15) in areas of high data coverage and 0 at well locations.

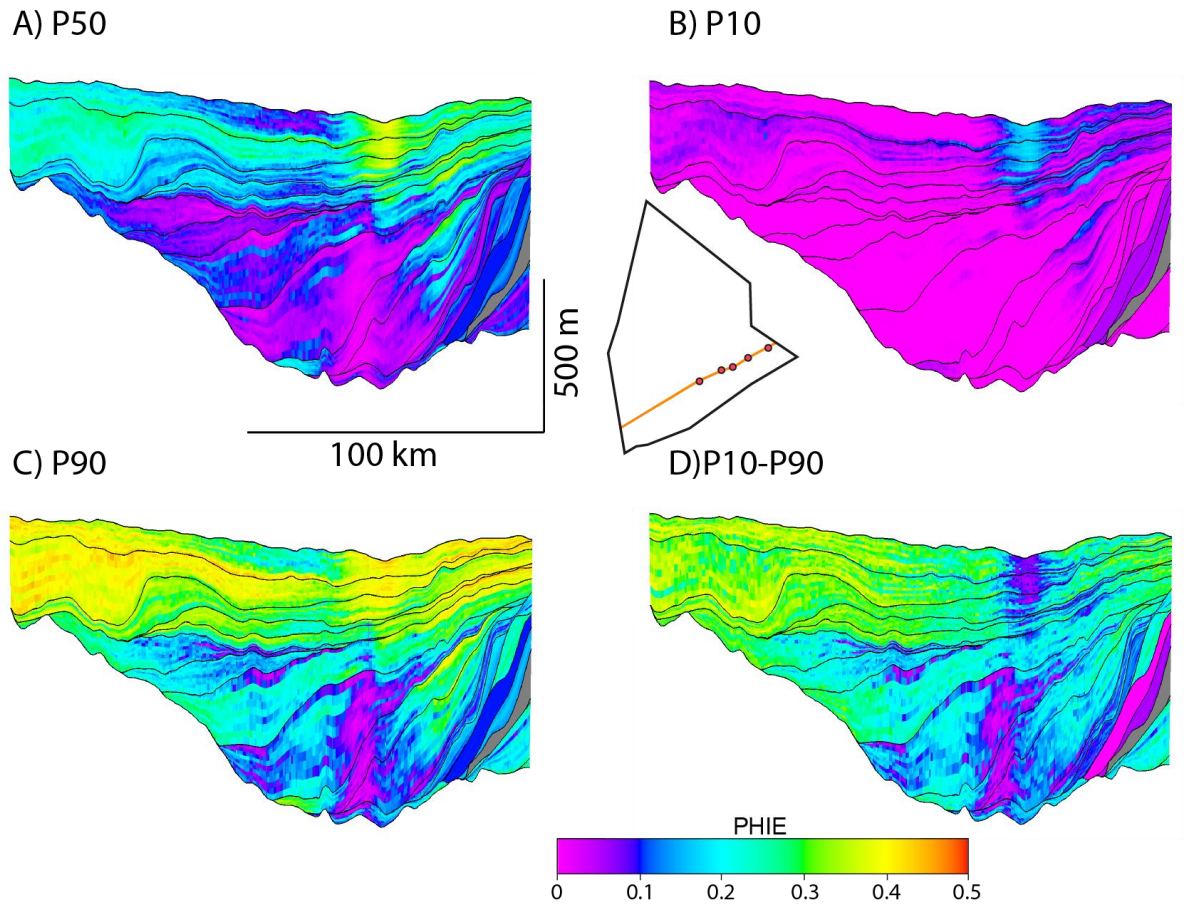

Fig. 5-8. Example of PHIE property distribution in a SW-NE cross-section through the ABF model at location of 2D seismic line SNS87-10A (inset). a) mean PHIE (P50), b) P10, 10 % probability that value is higher; c) P90, 90 % probability that value is higher; d) P10-P90, indicating range in probable PHIE values, lower values denote lower uncertainty. Areas with 0 range in the P10-P90 plot correspond to well locations. Grey zones represent those zones of the model without data coverage (properties are not distributed across zone boundaries).

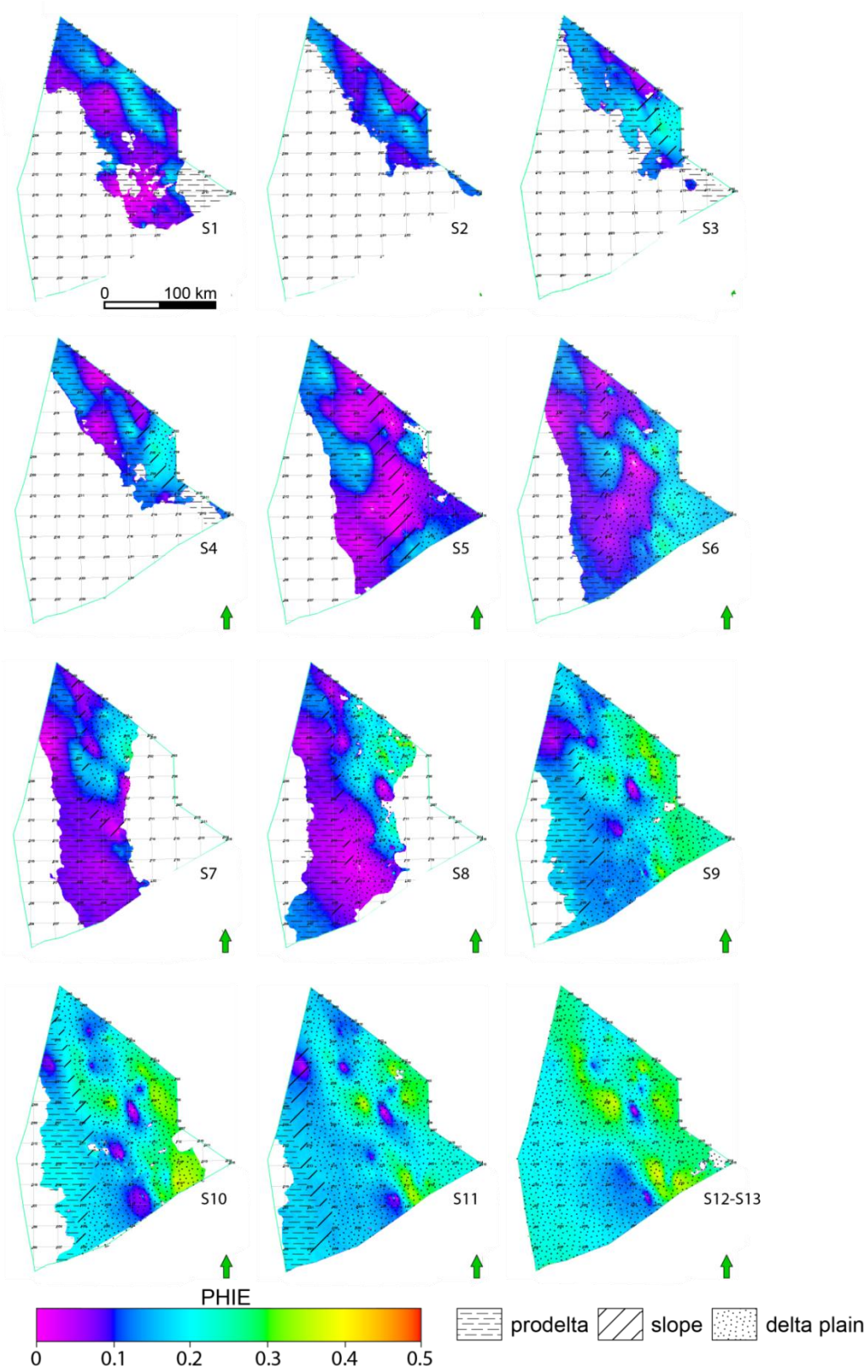

Fig 5-9. Average PHIE (P50) maps for all (S1-S13) horizons,showing the regional distribution of PHIE through time. Delta element as BW pattern.

5.3.2 *Vcl*

Result of the Vclay property modelling is shown as average Vclay_P50 maps for all main units. The values are attributed to the representative surface (Fig. 5-11). A general deduction from these maps is that the clay percentages decrease upward in the S1-S13 interval, which corroborates the overall prograding trend of the delta. At a higher level of detail it is also noticeable that lateral trends in Vcl do not coincide entirely with the palaeogeographic trends, i.e., with the delta element facies (the boundaries of which are also indicated in Fig. 5-11). This observation has implications for tying reservoir characteristics to depositional setting and will be illuminated in Chapter 9. The uncertainty assessment is shown in Fig. 5-10.

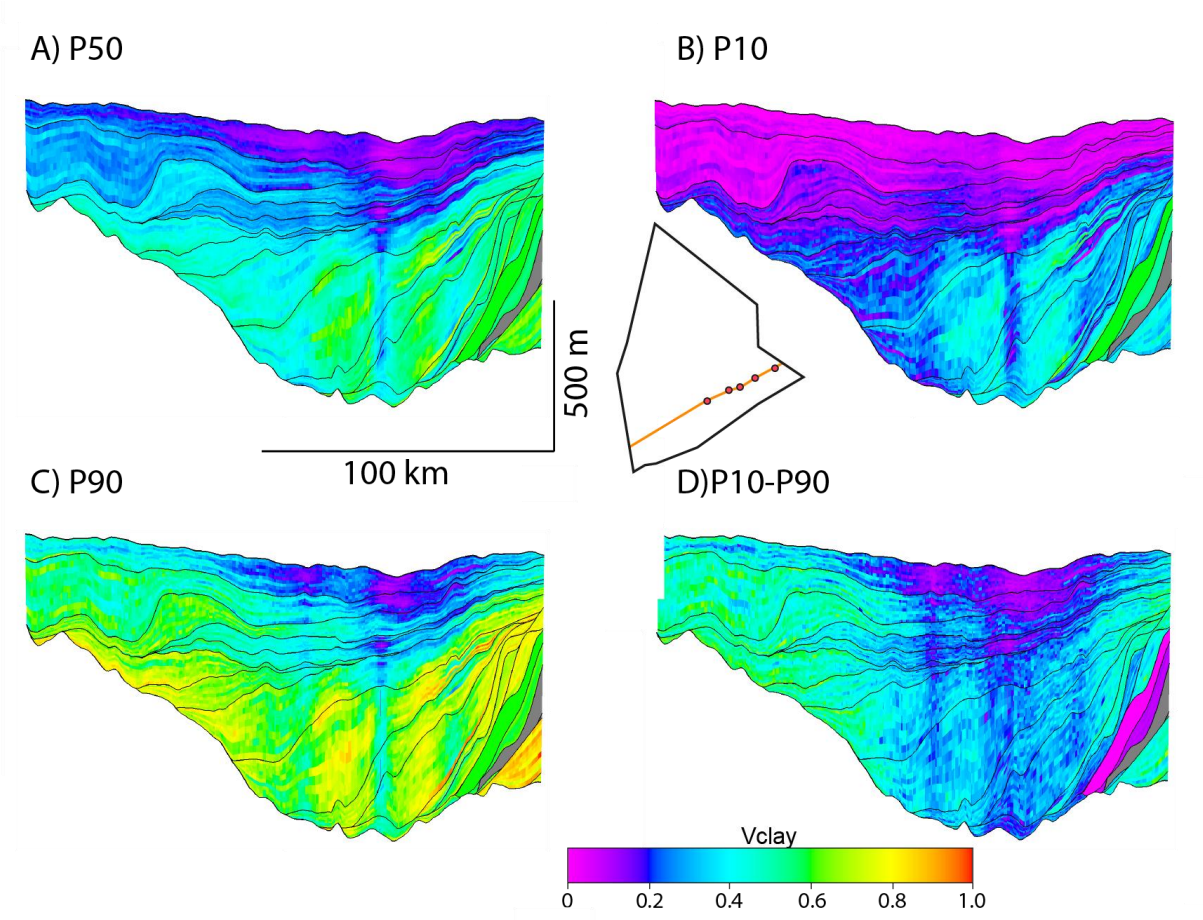

Fig. 5-10. Example of Vclay property distribution in a SW-NE cross-section through the ABF model at location of 2D seismic line SNS87-10A (inset). a) mean Vclay (P50), b) P10, 10 % probability that value is higher; c) P90, 90 % probability that value is higher; d) P10-P90, indicating range in probabilities Vclay values, lower values denote lower uncertainty. Uncertainty tends to increase to the west where data coverage is low and away from well locations. Grey zones represent those zones of the model without data coverage (properties are not distributed across zone boundaries).

The P10-P90 values represent a range of probably Vclay values and are a measure for uncertainty. This uncertainty tends to increase up to 0.6 to the west where data coverage is low, is relatively low (~0.25) in areas of high data coverage and 0 at well locations.

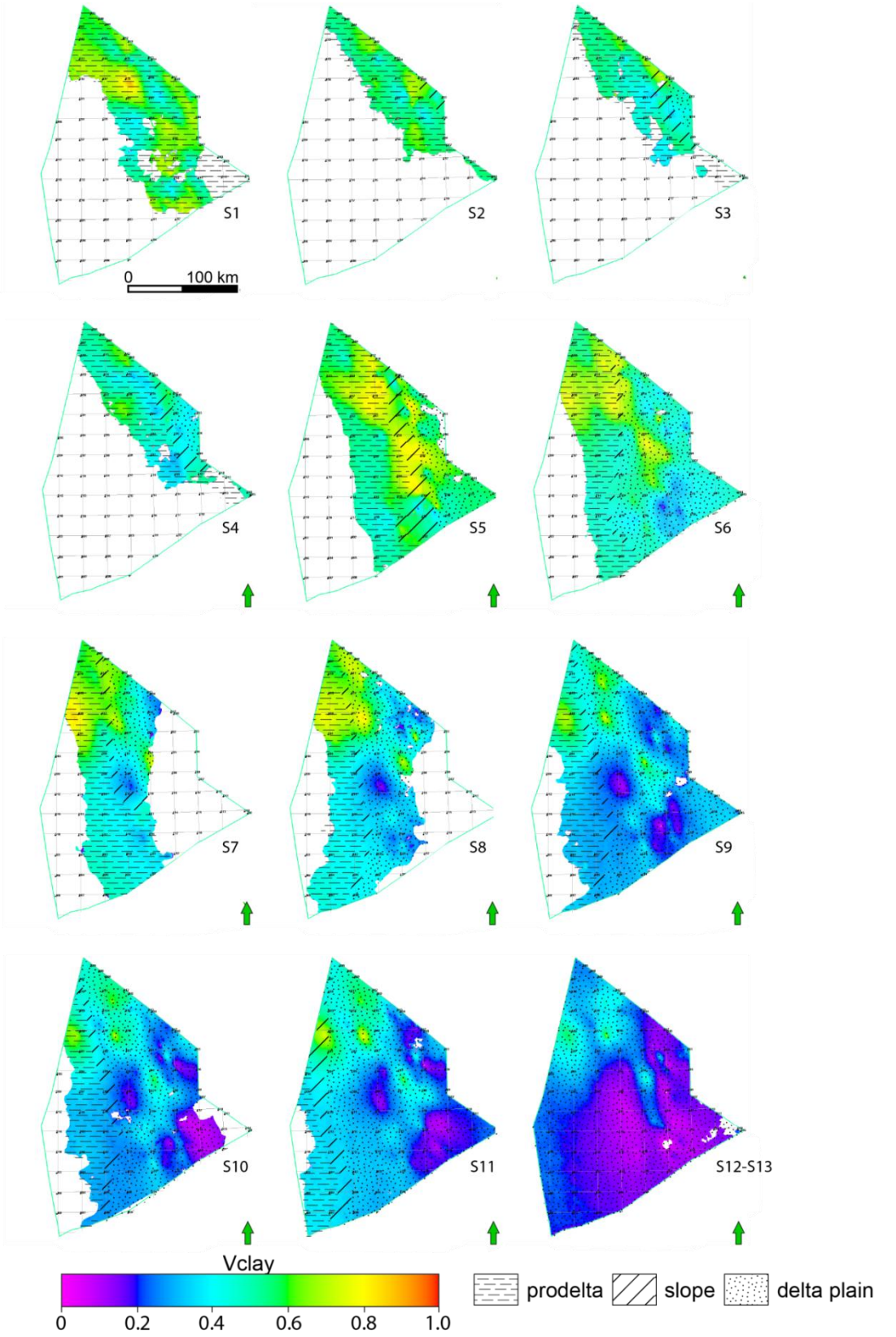

Fig. 5-11. Average Vclay (P50) maps for all (S1-S13) horizons showing the regional distribution of Vclay through time. Delta element as BW pattern.

5.3.3 *Delta element, litho- and depositional facies modelling*

Results of the facies property models are represented as they are since no statistical information is available, since modelling was not done by a Sequential Gaussian simulation method. Lithofacies results are shown in Fig. 5-13, Delta element in Fig. 5-14 (and also shown in BW patterns on the other property maps), and depositional facies in Fig. 5-12 and Fig. 5-15.

Lithofacies evolution shows the overall coarsening of the delta sequence and nicely reflects the non-exclusive tie with delta element facies. An Interesting feature that emerges is the apparent northward deflection of coarser grained sediment “plumes” at the toe of slope, which is best visible in especially in units S7-S11. Counter-clockwise sea-bottom currents were held responsible for the generation of giant sandwave (“contourite”) fields (see Ten Veen et al., 2011). Although the sandwaves are not reproduced by the property models, the along-slope sediment transport can be inferred from the observed distribution patterns.

The delta element facies directly relates to the input as described in section 1.2.2.1.The distribution of the depositional facies, show close resemblance to the delta element and is explained by the method it is calculated. The higher detail is obtained through incorporating lithofacies information and potentially allows differentiating depositional facies. The facies patterns, strongly suggest the presence of coarser grained distributary channel fills to be linked to delta lobes and occasionally to sub-marine lobes. However, the patterns provide not enough detail to reconstruct the channels in great detail.

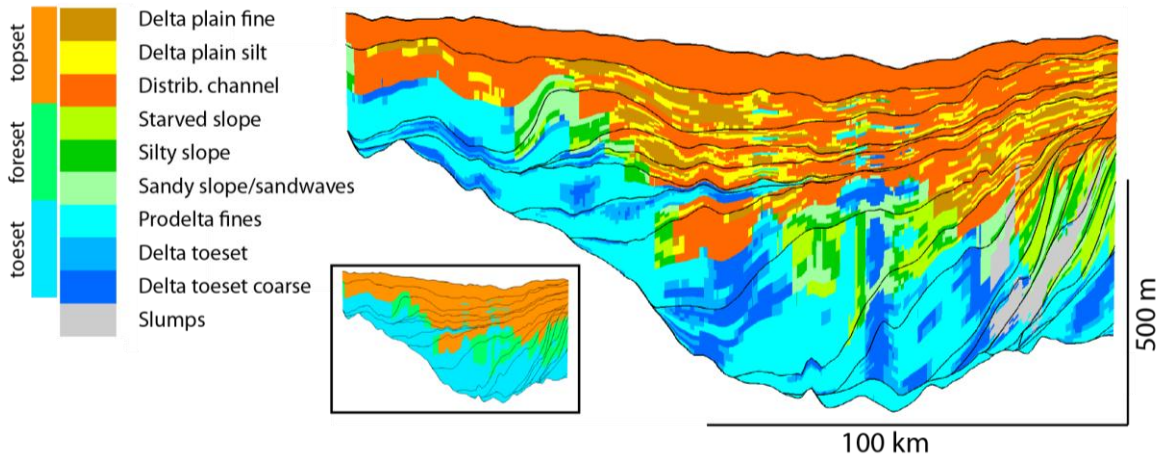

Fig. 5-12. Example of depositional element property distribution in a SW-NE cross section through the ABF model at location of 2D seismic line SNS87-10A.. Delta element (as partial input to the depositional facies) in shown in inset.

5.4 Conclusions

Property modelling has been performed on a number of petrophysical well logs and derived properties. The PHIE and Vclay lithological properties obtained by petrophysical evaluation are used unchanged and have been used to define the lithofacies property. Sw/Sg values as calculated by petrophysical evaluation can less straightforwardly by applied to populate the geological model, since saturations outside gas-bearing strata can never be applied to predict the saturation inside a prospect. For this reason regional saturation maps are not shown. Next to lithological properties, a delta element type is defined on the basis of horizon geometry, sequence stratigraphic interpretation and seismic attribute information of palaeomorphological features. The delta element interpretation is used to populate the entire geological model with topset, foreset and toeset elements and adequately mimics the internal organisation of the units defined. Both the delta element and the lithofacies

models are used to set up a matrix of possible depositional facies by combing information on the settings and grain size. As such 9 depositional facies are defined, which are complemented by information on the presence of slump features. The prograding and coarsening upward nature of the delta interval studied is reflected by the vertical development of all properties. The distribution of PHIE and Vclay for individual units is not that clearly related to distribution of delta elements and depositional facies. This latter observation suggests that those lithofacies classes forming potential shallow gas reservoirs and those clay-rich layers forming potential seals are not exclusively related to a certain position on the delta. This has direct implications for understanding the distribution of bright spots.

Uncertainties in the property modelling are assessed by applying Sequential Gaussian Simulation procedures, which provides statistics for the modelled property. The calculated uncertainties (represented as P10-P90 range) relate to the reproducibility of the property with the algorithm and input variograms applied. The uncertainty is importantly related to data density and tends to be high in the west of the model area (D and E blocks) where well data density is lower than in the A, B and F blocks. The uncertainty assessment does not include statements on the accuracy of the modelling procedure, since this would require very long computation time.

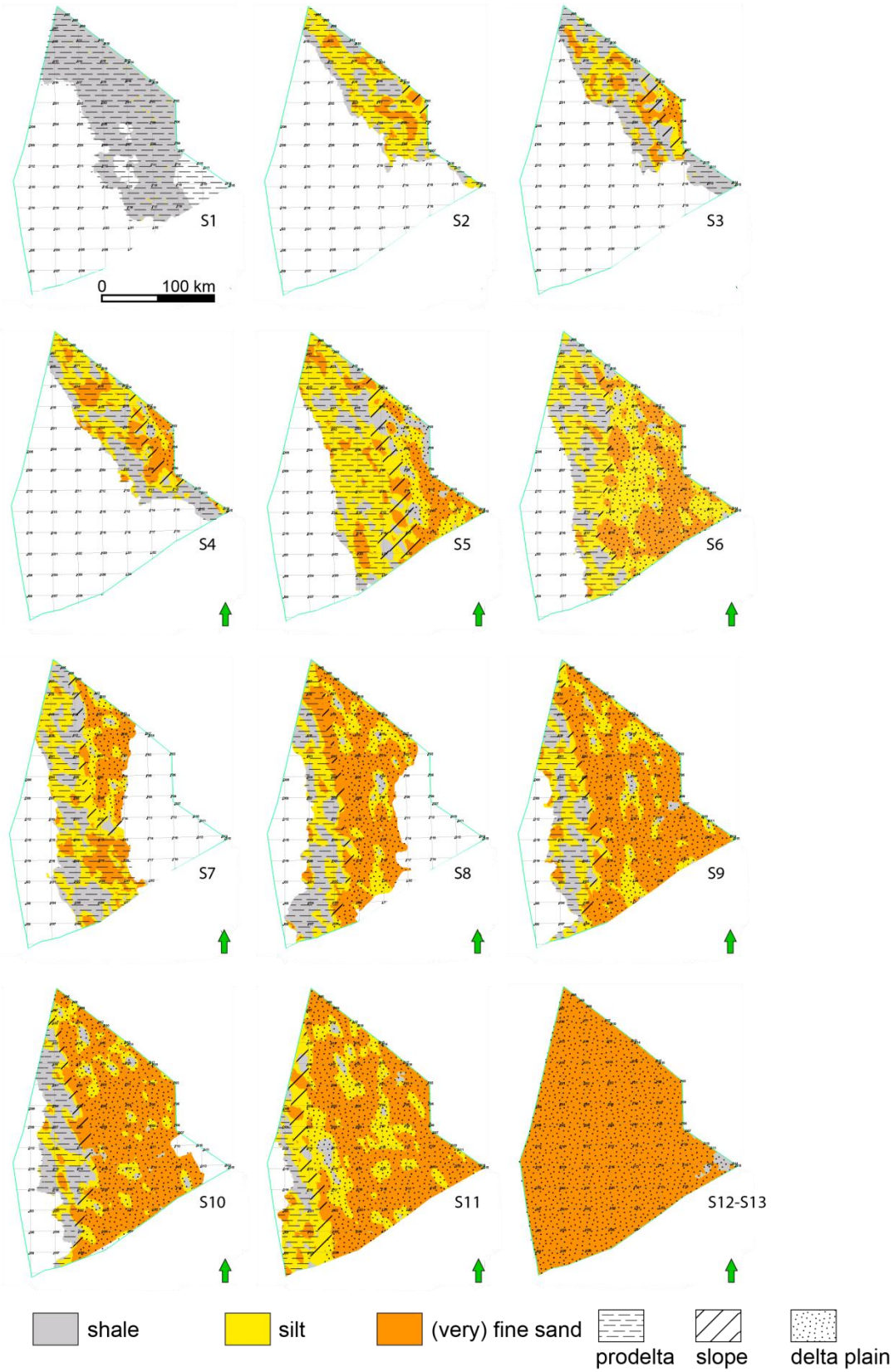

Fig. 5-13. Average lithofacies property maps for all (S1-S13) horizons, showing the regional distribution of Lithofacies through time. Delta element as BW pattern.

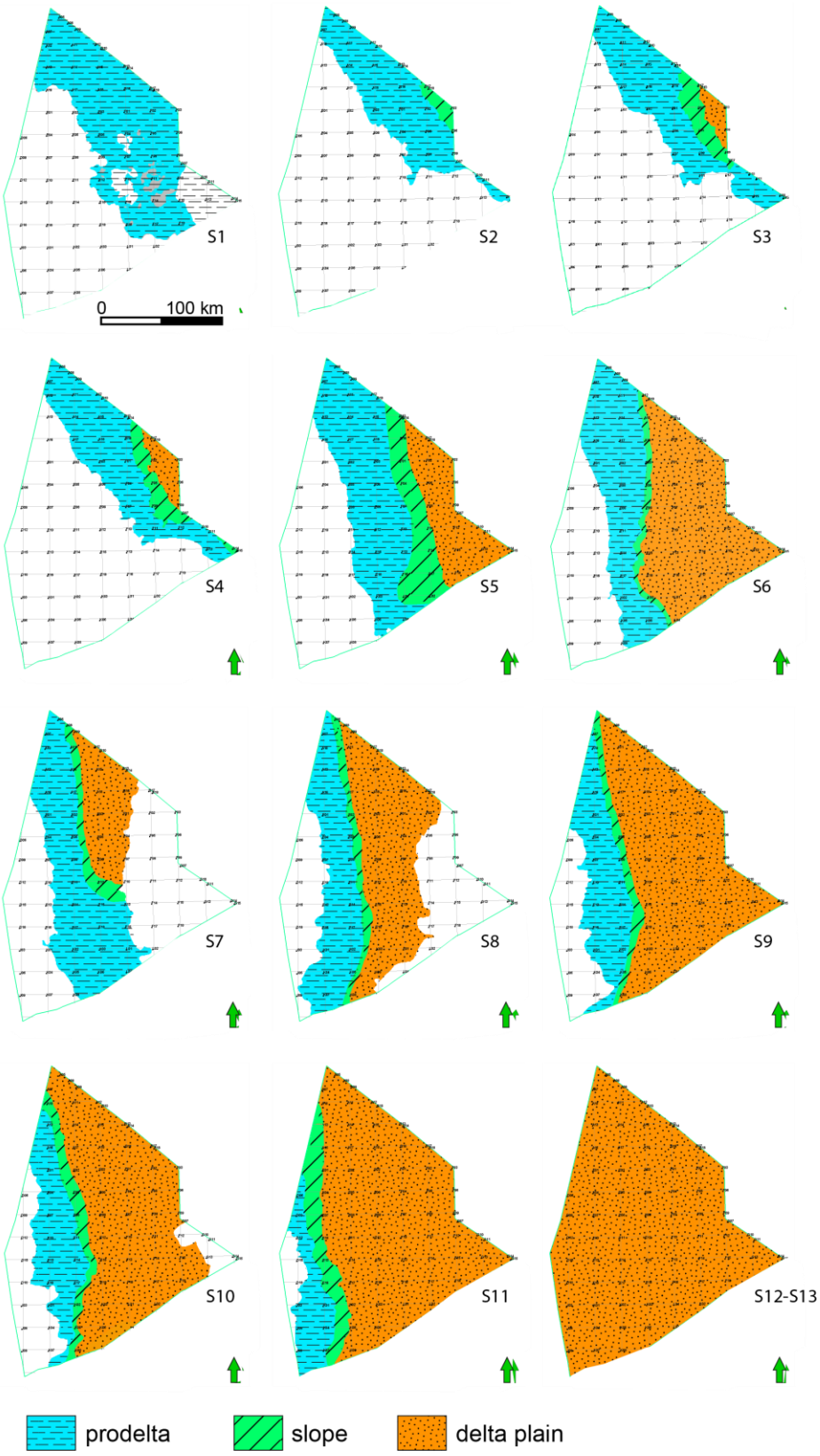

Fig. 5-14. Delta element property maps for all (S1-S13) horizons showing the regional distribution of delta elements (delta evolution) through time.

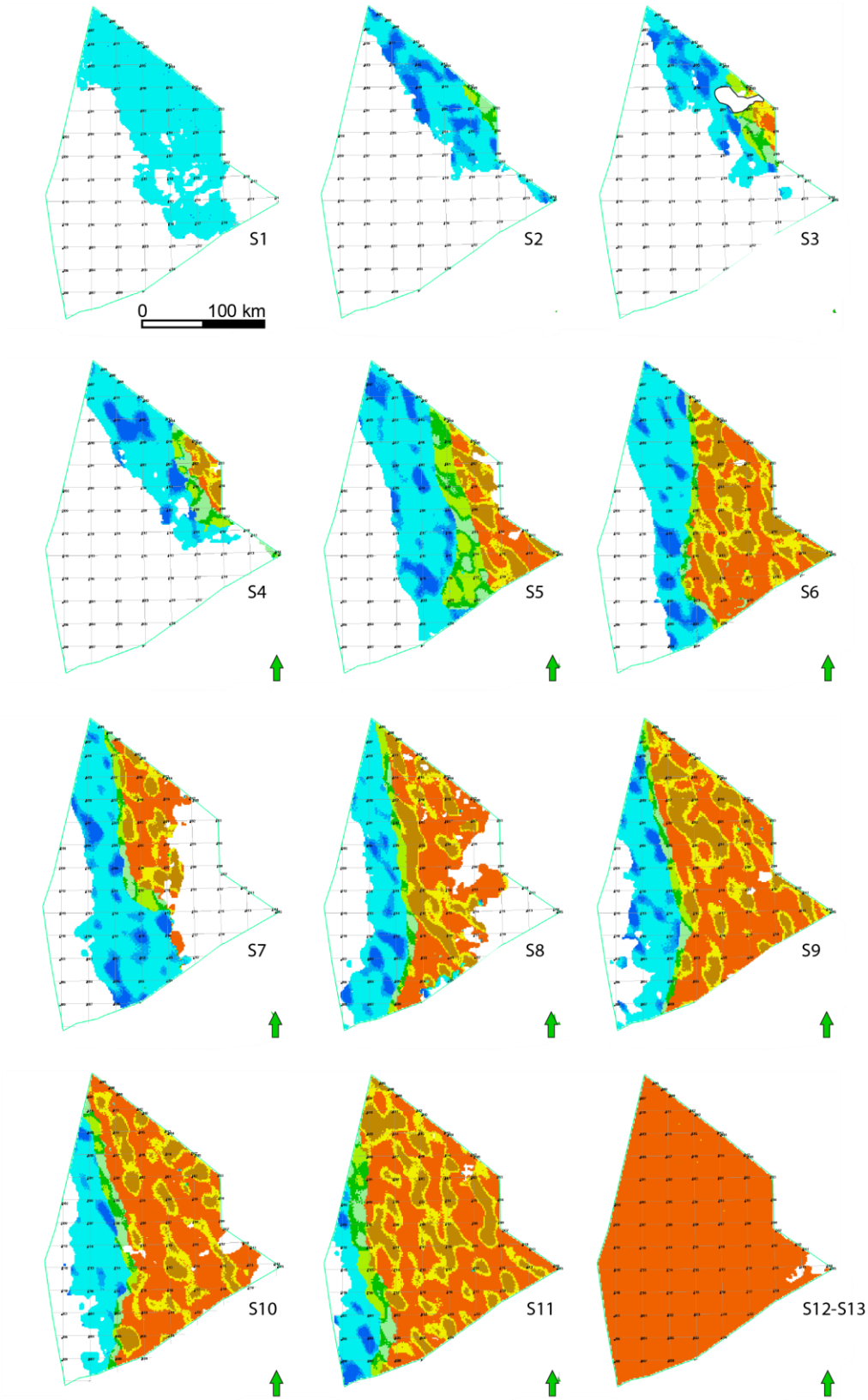

Fig. 5-15. Average depositional facies property maps for all (S1-S13) horizons showing the regional distribution through time. Legend as in Fig. 5-5.

6 Capillary seal capacity of mudstones in the Plio-Pleistocene SNS Delta deposits, Dutch northern offshore

6.1 Introduction

The seal integrity study focuses on the evaluation of the capillary seal capacity and permeability of mudstones in the Plio-Pleistocene Delta deposits in the Dutch northern offshore. The evaluation is restricted to wells that cut through bright spots. The two main objectives of this part of the project are to create a database of relevant properties of identified sealing layers and to interpret the database in relation to the stratigraphic position and depths of the sealing layers in the SNS Delta deposits.

The inventory of bright spots (DHI for shallow gas) in sedimentary units above the Mid Miocene unconformity has shown that many of the potential shallow gas accumulations occur in the SNS Delta sedimentary units in stratigraphic traps or in multiple stacked structural traps above salt structures (Schroot et al., 2005, Van den Boogaard and Hoetz, 2011, Ten Veen et al., 2011; Chapter 7 of this study). Seismic attribute analysis suggests that the salt structures are important, or were important in the past, in conducting fluids/gas from deeper levels (Ten Veen et al., 2011; this study). At present migration and charging of gas within the SNS delta takes place under normal to close-to-normal pore pressure conditions (Verweij et al., 2012a,b). Most geochemical analyses from shallow gas accumulations in the northern offshore Netherlands show typical characteristics of biogenic gas (Verweij, 2011; Appendix E of this study).

The seals of the shallow gas occurrences are formed by siliciclastic intra-delta mudstones with higher capillary entry pressure and lower permeability than those of the underlying reservoir.

6.1.1 *Mudstones*

Mudstones are sediments of fraction < 63 µm, i.e. consisting of a clay fraction (< 2 µm) and a silt fraction (2µm – <63µm). There are no publicly available measured values of capillary entry pressures of sealing mudstones for shallow gas accumulations in the Netherlands offshore.

6.1.1.1 Porosity and permeability of mudstones

In general, depositional porosities of muds are high, the more so for the clay-rich muds, reaching magnitudes of 80-90 % (e.g. Aplin and Macquaker, 2011). Porosity decreases with increasing burial depth. At shallow depths porosity reduction is mainly due to mechanical compaction driven by the increase of effective stress. Compressibility of mud, and therefore its rate of compaction, is strongly influenced by grain size: finer-grained muds have higher depositional porosities, but their rate of compaction is higher (Yang and Aplin, 2004; Aplin and Macquaker, 2011). At a given porosity, finer-grained clay-rich mudstones have smaller poresizes than silt-rich mudstones. Permeability closely relates to poresize and poresize distribution. Recently, Schneider et al. (2011) found that mudstone permeability increases with a decrease in clay fraction due to the development of a dual-porosity system, where large pore throats between silt grains that act as high permeability pathways are preserved in addition to small pores within the clay matrix. Just like porosity, permeability of mudstones is also strongly controlled by their grain size, and grain size distribution. At the same porosity, clay-rich mudstones have lower permeabilities than clay-poor ones.

Depositional porosities of muds (reaching 80-90%) are much higher than those of sand (40-60%). Hence, at shallow burial depth the porosity of mudstones will be higher than that of sands. Muds are more compressible than sands, especially at shallow depths, and as a consequence mud porosity

decreases faster with depth than sand porosity: at greater burial depths, the porosity of the compacted mud will become smaller than the porosity of the sand.

6.1.1.2 Seal capacity of mudstones

The seal capacity of a mudstone is given by the height of the hydrocarbon column that the seal holds prior to leaking. The seal capacity for hydrocarbons of a water-wet mudstone is strongly controlled by the capillary entry pressure of the seal which in turn is a function of the pore throat size distribution along the largest interconnected pore throat path through the seal (see Appendix F for more detailed information on capillary seal capacity). Hence, the capillary seal capacity of mudstones is strongly controlled by grain size. The capillary seal capacity of a mudstone is not influenced by the thickness of the seal, because capillary forces at the interface between the reservoir and the seal are not related to the thickness of the seal. A water-wet mudstone will act as a capillary seal for hydrocarbons until the buoyancy pressure of the hydrocarbon column exceeds the capillary entry pressure of the seal (e.g. Ingram et al., 1997; Sylta, 2005). If the buoyancy pressure exceeds the capillary entry pressure the hydrocarbons will leak through the seal by two-phase Darcy flow. Hydrocarbon saturations required to breach mudstone seals are highly variable, ranging from < 1 % to > 20 % (Kurtev et al., 2012). Following Darcy's law, the leakage rate is directly related to the buoyancy pressure of the hydrocarbon column, the relative permeability of the seal and inversely related to the thickness of the seal. The leakage rate through a thin seal will be much faster than that through a thick seal for the same (relative) permeability. Below thick seals and continued charging of the trap, the hydrocarbon column height continues to increase after capillary seal breaching, because the leakage flux is smaller than the flux into the trap. Under such dynamic conditions the hydrocarbon column height that can be maintained by the topseal will be greater than the maximum height of the hydrocarbon column related to the capillary seal capacity. After charging of the trap has stopped, leakage through the top seal will continue by two phase Darcy flow, and the hydrocarbon column height may decrease again, i.e. the trap may be emptied by leakage through the caprock to a greater or lesser extent in time.

Hence, capillary entry pressures are not the only control on maximum column heights of mudrock top seals. Charging and top seal leakage history also control maximum and present-day column heights.
In addition to the capillary and permeability seal properties, trap geometry and the presence of faults and their properties and hydraulic failure of a top seal when fluid pressures exceed seal rock strengths may also influence the present-day gas column heights or may have played a role in the past. Here, focus is on the capillary seal capacity and permeability of mudstones.

6.1.2 *Approach*

We developed, tested and applied a systematic approach to evaluate porosity and permeability and capillary seal capacity of mudstones at shallow depth based on new grain size analysis data and publicly available pressure data. After testing different approaches we finally selected equations including clay content as important parameter. These equations were developed by Yang and Aplin (2004) and Yang and Aplin (2010) for calculating mudstone porosity and permeability, respectively. The pore throats are calculated from approaches that use the calculated porosities and median grain size, based on equations published by Nakayama and Sato (2002). Knowing the pore throats, the sealing capacity could be determined by estimating the water densities from RFT pressure measurements, and gas densities and gas-water interfacial tensions from established relations using known temperature and pressure changes with depth (NIST Chemistry WebBook: http://webbook.nist.gov/chemistry/fluid/; Nordgård Bolås et al., 2005, respectively). Appendix F provides a detailed outline of the approach.

After identifying sealing layers at wells, using different types of logs and hydrocarbon indicators from seismic, sealing layers were selected for sampling. In total 77 samples (73 cutting and 4 core samples) from 45 sealing layers in 10 wells were analysed for grain size distribution by Laser Particle Sizer Helos KR Sympatec/Windox5.6 at the sedimentology laboratory of the Vrije Universiteit Amsterdam.

From the grain size distribution of the sealing layers, a database was constructed with relevant properties such as clay content, median grain size, porosity, permeability and critical pore throat radius. This initial database was used to calculate the capillary seal capacity of each layer (i.e. the height of the gas column that the seal may retain prior to leaking), which was compared with the gas column calculated using the RFT pressure measurements available for the reservoir underlying the seal and with other indicators of gas column heights, such as the heights of gas occurrences detected from crossovers of neutron (NPHI) and density (RHOB) logs and information on GWC from end-of-well reports.

6.2 Grain size analysis and lithological characterization

6.2.1 *Sampling and grain size analysis*

The selection of appropriate sealing layers for sampling was based on the evaluation of a combination of logs and hydrocarbon indicators from seismic (bright spots) to identify gas occurrences at initially 14 wells. The logs included mud logs (providing information on gas peaks), and neutron (NPHI) and density logs (RHOB). The crossover of NPHI and RHOB log curves are indicative of the presence of gas. Based on the identified gas occurrences and the gamma-ray logs, we identified 45 apparent sealing layers overlying the gas occurrences (Daza Cajigal, 2012). These 45 sealing layers were selected for sampling and analysis at the TNO geological sample repository in Zeist.

In total 77 samples (73 cutting and 4 core samples) from 45 sealing layers in 10 wells (A12-03, A15-04, A18-02, B10-03, B13-03, B13-04, B17-05, B17-06, F01-01, F02-06) were analysed for grain size distribution by Laser Particle Sizer Helos KR Sympatec/Windox5.6 at the sedimentology laboratory of the Vrije Universiteit Amsterdam.

6.2.2 *Grain size distribution*

Appendix G presents the results of the grain size analysis of the 77 samples from 45 sealing layers in the 10 selected wells. The < 8 µm grain size fraction defined by Laser Particle Sizer corresponds to a grain size of < 2 µm defined by classical pipette analysis (Konert and Vandenberghe, 1997). The selected sealing layers belong to seismostratigraphic units from s2 to s13 of the SNS Delta sequence. The relative percentages of clay, silt and sand are plotted in Shepard's (1954) ternary diagram (Fig. 6-1). The sampled layers classify predominantly as mudstones composed of silty clay and clayey silt. Six samples have a sand content of >20% and classify as sand-silt-clay.

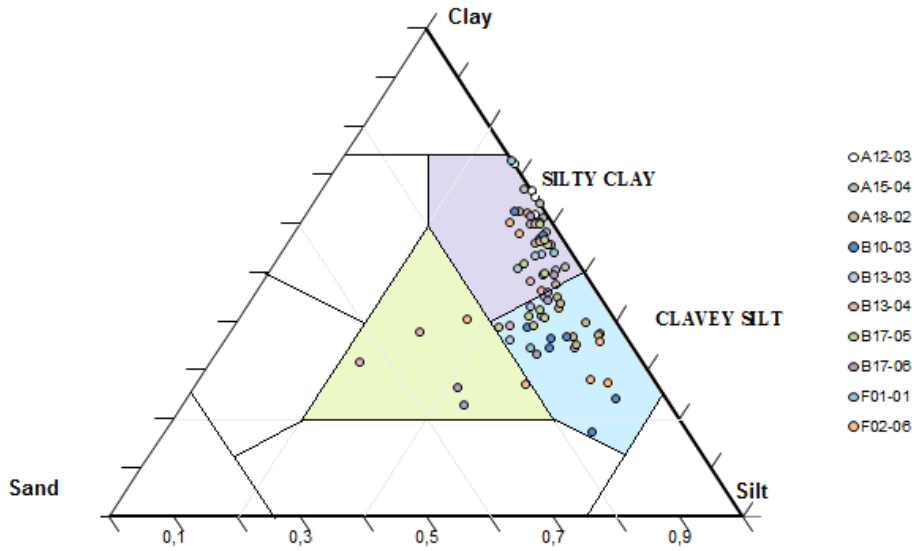

Fig. 6-1. Shepard's (1954) classification ternary diagram based on relative percentages of clay, silt and sand for samples from the wells A12-03, A15-04, A18-02, B10-03, B13-03, B13-04, B17-05, B17-06, F01-01 and F02-06 (percentages of grain sizes are given in Appendix G).

The clay content of the mudstones in seismostratigraphic unit s6 shows an increase with depth (Fig. 6-2). The increase in clay content in unit s6 also seems to increase from east (clay content of c. 40-50% at depths of around 500 m in well B17-05) to west (clay content of c. 60-64% at > 850 m in wells A15-04 and A18-02). A possible explanation of the east to west increase in clay content is the increasing distance from the sediment source during deposition. The clay contents of the other seismostratigraphic units do not show such a relation with depth and/or well location (Fig. 6-3).

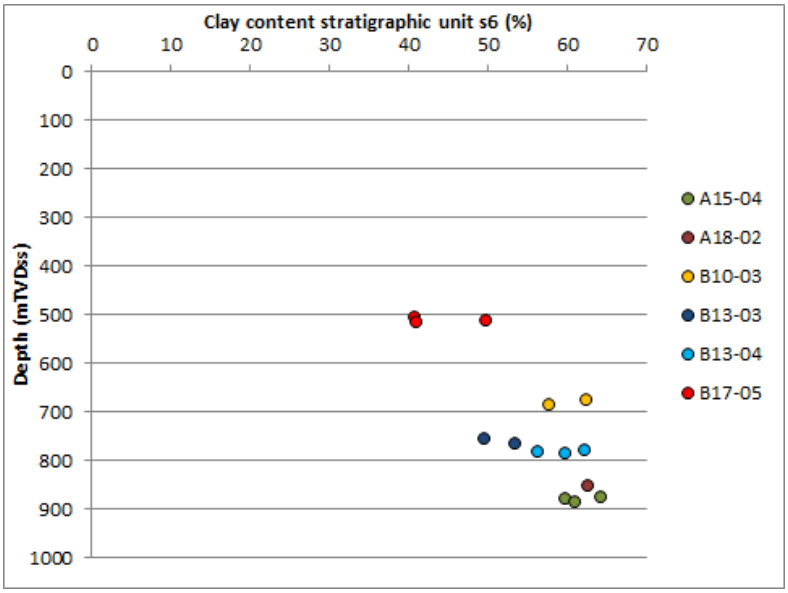

Fig. 6-2. Cross plot of clay content in the sampled mudstones of seismostratigraphic unit s6 versus depth for different well locations.

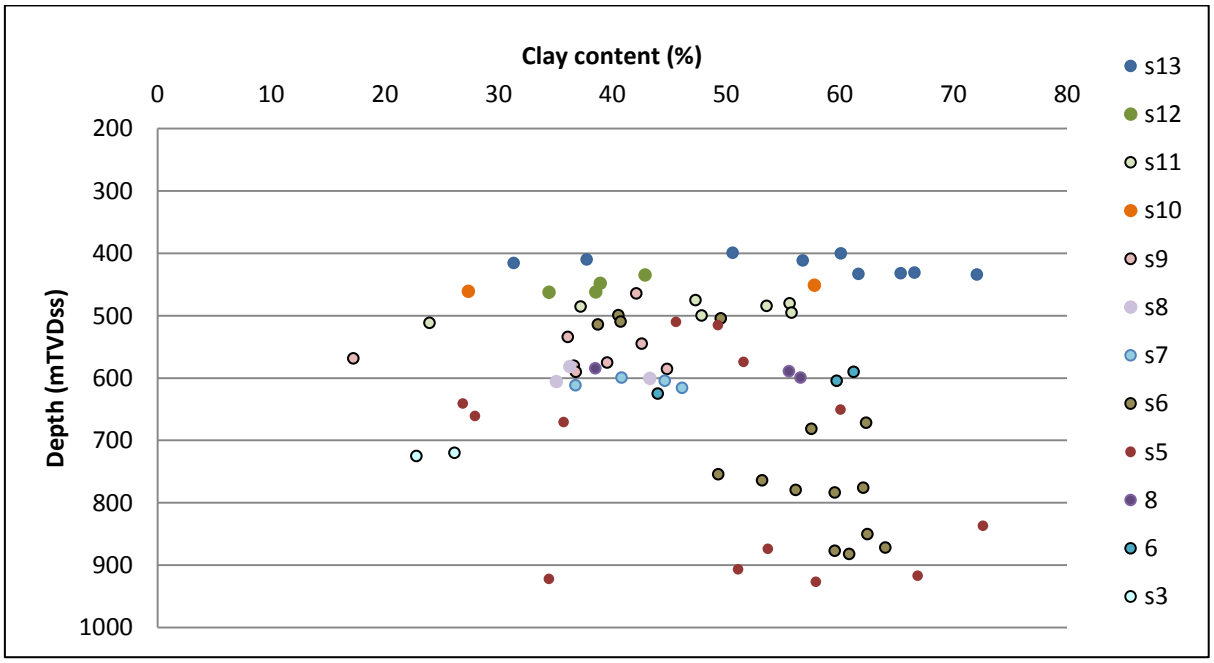

Fig. 6-3. Cross plot of clay content in sampled mudstones with depth for different seismostratigraphic units.

The clay percentages and median grain sizes (Appendix G) are the basic data used to calculate porosity, permeability and pore throats of the mudstones.

6.3 Porosity and Permeability

6.3.1 *Porosity*

The porosities for the mudstone samples are calculated following workflow step 2 (Appendix F). The thus determined porosities (Appendix G) are influenced by both clay content and effective stress (depth). Fig. 6-4 illustrates that for the same depth of measurement the calculated mudstone porosities vary widely: more than 20% difference in porosity between mudstones with clay content < 30 % and those with clay content > 60 %. The porosities decrease with depth for mudstones with similar clay contents.

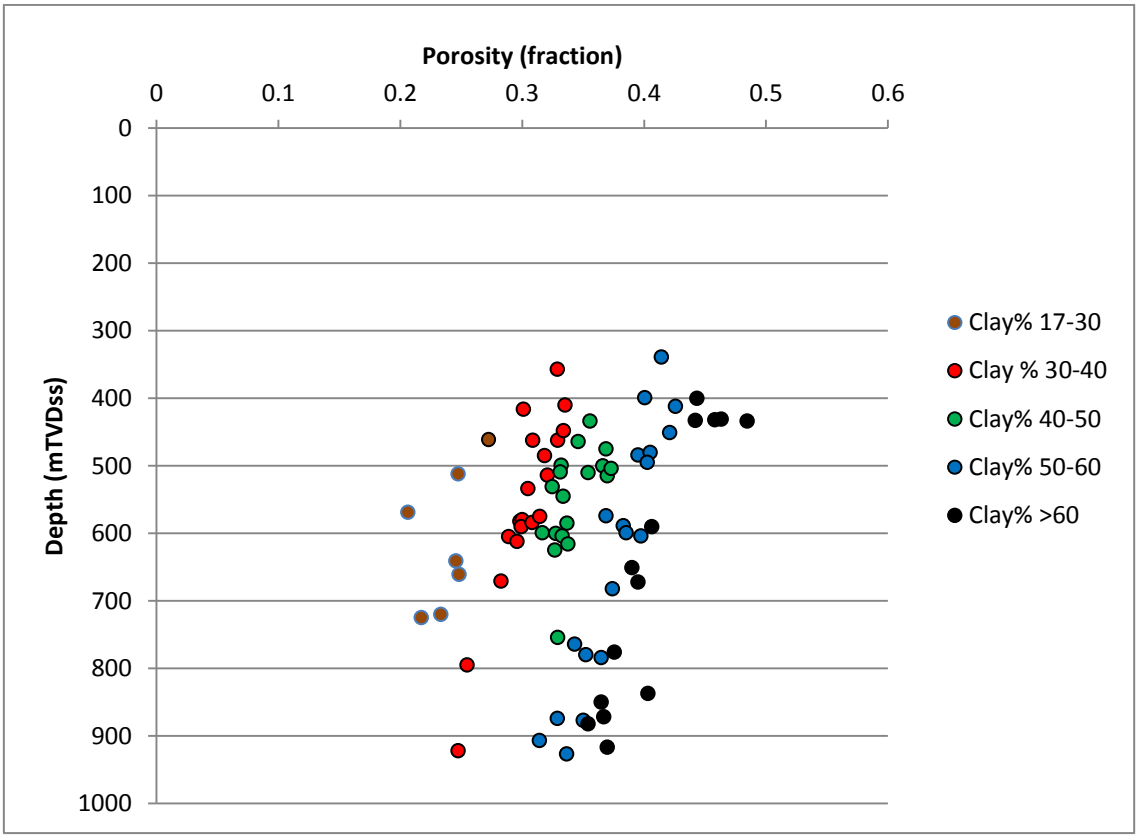

Fig. 6-4. Cross plot of calculated porosities of the sampled mudstones versus depth for different clay contents.

6.3.2 *Permeability*

The calculation of the vertical permeabilities according to step 3 of the workflow (Appendix F) is based on both clay content and void ratio. The calculated vertical permeabilities for the mudstone samples are quite low and vary between 2.8E-20 and 1.1E-18 m2 (Appendix G). The cross plot of calculated permeability of the sampled mudstones versus depth for different clay contents (Fig. 6-5) shows the expected general decrease of permeability with depth. In addition, for the same depth of measurement the permeability is lower for mudstones with high clay content.

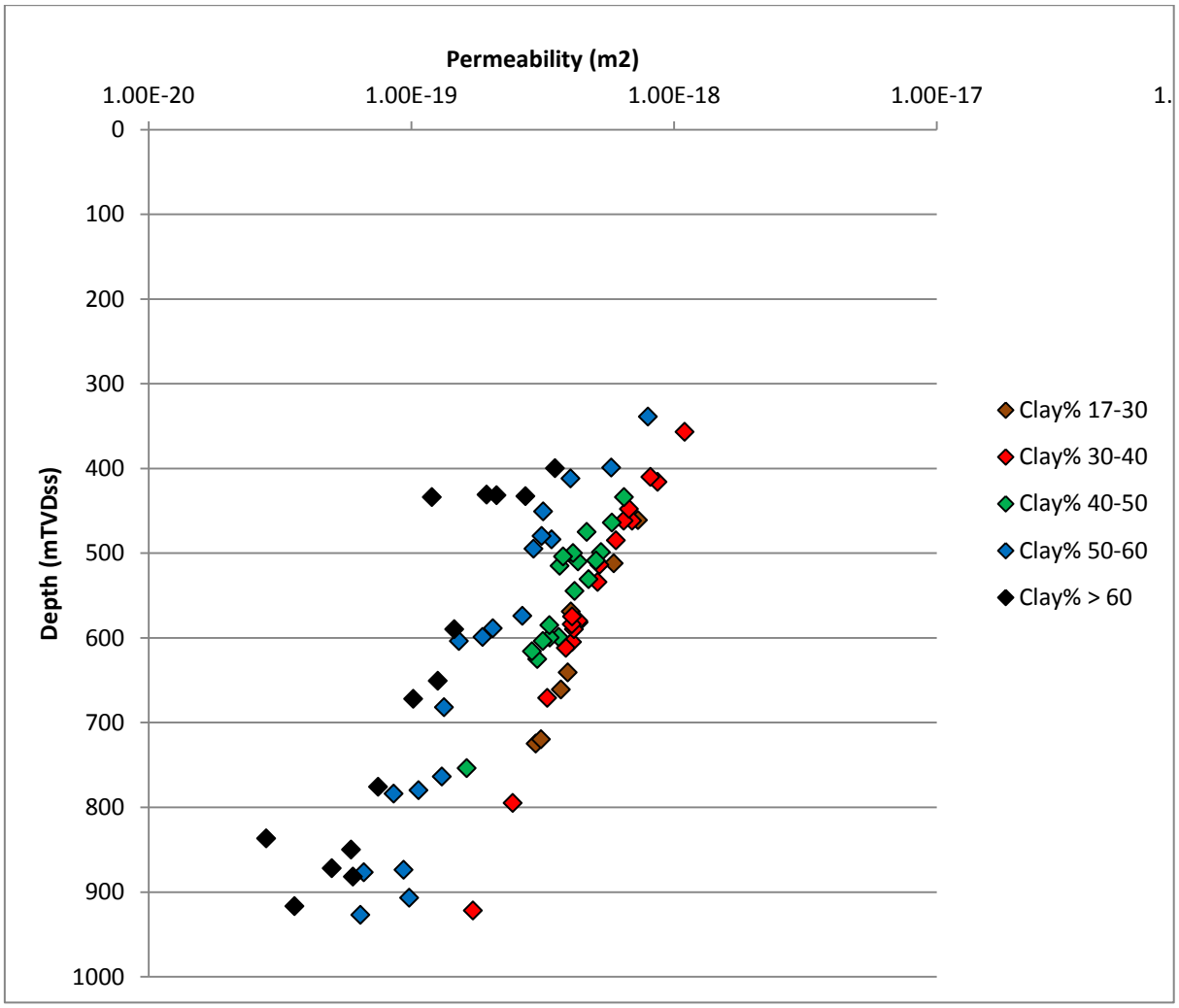

Fig. 6-5. Cross plot of calculated permeability of the sampled mudstones versus depth for different clay contents.

6.4 Pore throat size

Appendix G and Fig. 6-6 present the pore throat radii, resulting from the calculation procedure outlined in step 4 (Appendix F). Most of the pore throat radii vary between 0.5 and 1.5 µm. The calculated pore throat radius of 2.37 µm is a clear outlier and is associated with a sample of unit s13 taken at 456 m depth at well B13-04 containing a high sand percentage (45 %).

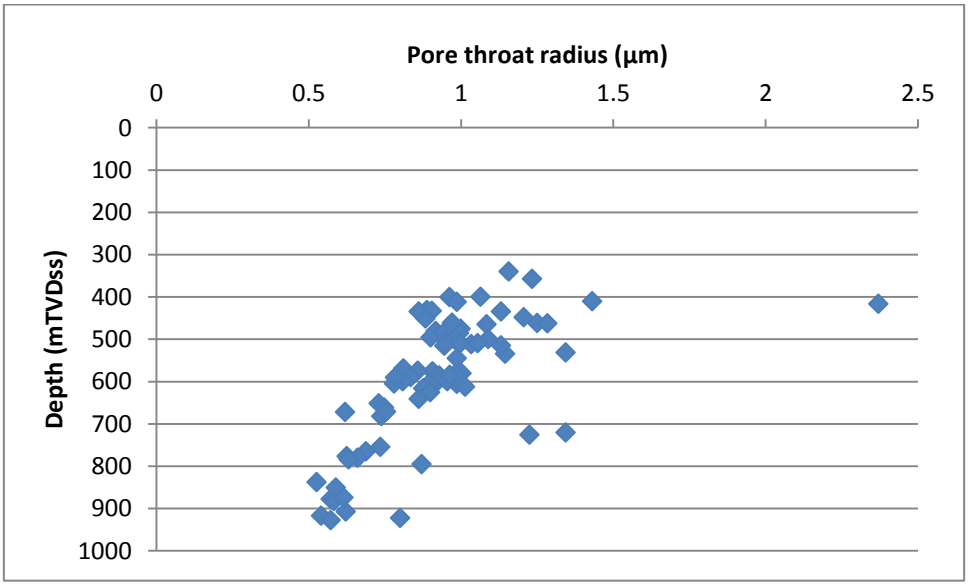

Fig. 6-6. Cross plot of calculated pore throat radius of the sampled mudstones versus depth.

6.5 Capillary seal capacity

6.5.1 *Capillary seal capacity calculated by grain size method*

The gas column heights were calculated for all 10 wells and all samples using step 5 of the grain size method as outlined in Appendix F. In addition gas column heights were calculated using measured pressure data (procedure outlined in Appendix F) that were available for 5 wells (A12-03, A18-02, B10-03, B13-03, B13-04, B17-06).

The calculated capillary seal capacities of the mudstones vary between approximately 10 and 24 m (Appendix G and Fig. 6-7). The calculated capillary seal capacities (and pore throat sizes) for samples with a sand content of > 20% and relatively large median grain size appear as clear outliers with relatively low magnitudes of capillary seal capacity in Fig. 6-7 and Fig. 6-8. For example: the seal capacity of less than 10 m at 410-416 m depth corresponds to two samples taken from a thin **s13** sealing layer encountered in well B13-04; the seal capacity of 10-11.7 m at 720-725 m depth corresponds to samples of a s3 layer at well B17-06.

The capillary seal capacity of the mudstones increases with depth (Fig. 6-7 and Fig. 6-8). Fig. 6-7 illustrates that the decrease in pore throat size and the increase in gas density exert an important influence on the increase in seal capacity of the mudstones with depth. The variation in seal capacity at the same depth is directly related to the variation in pore throat size at that depth.

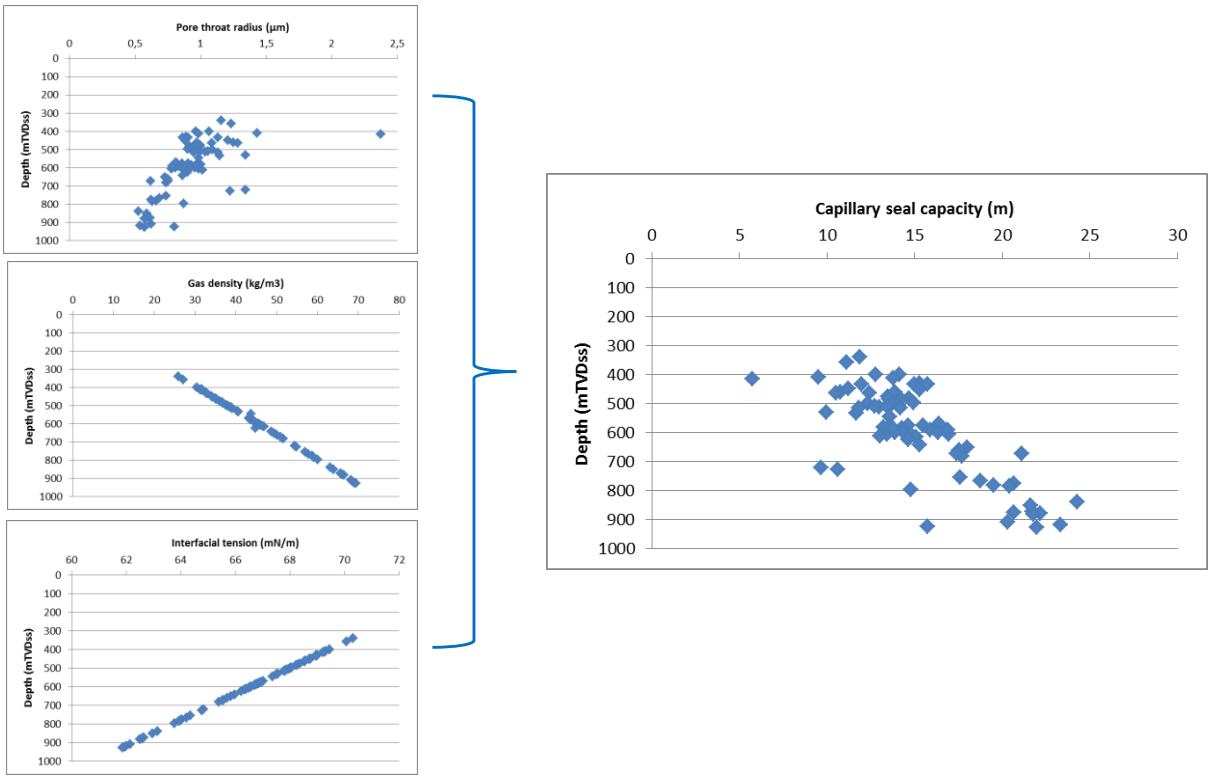

Fig. 6-7. Cross plots of pore throat radius versus depth, gas density versus depth and interfacial tension between gas and water versus depth and in relation to the change in capillary seal capacity versus depth.

The change of capillary seal capacity with depth for the different seismostratigraphic units shows a number of interesting features (Fig. 6-8). Seismostratigraphic unit **s13** is the most shallow unit of the SNS Delta sequence and its variation in depth around 400 m is minor. The capillary seal capacity of the **s13** mudstone layers (sand content < 20%) at this relatively shallow depth is still 13-16 m. The seal capacities for the mudstones in seismostratigraphic units s5 and s6 are available over a relatively large depth interval from 500 to 900 m. They show the increase in capillary seal capacity with depth within a single seismostratigraphic unit.

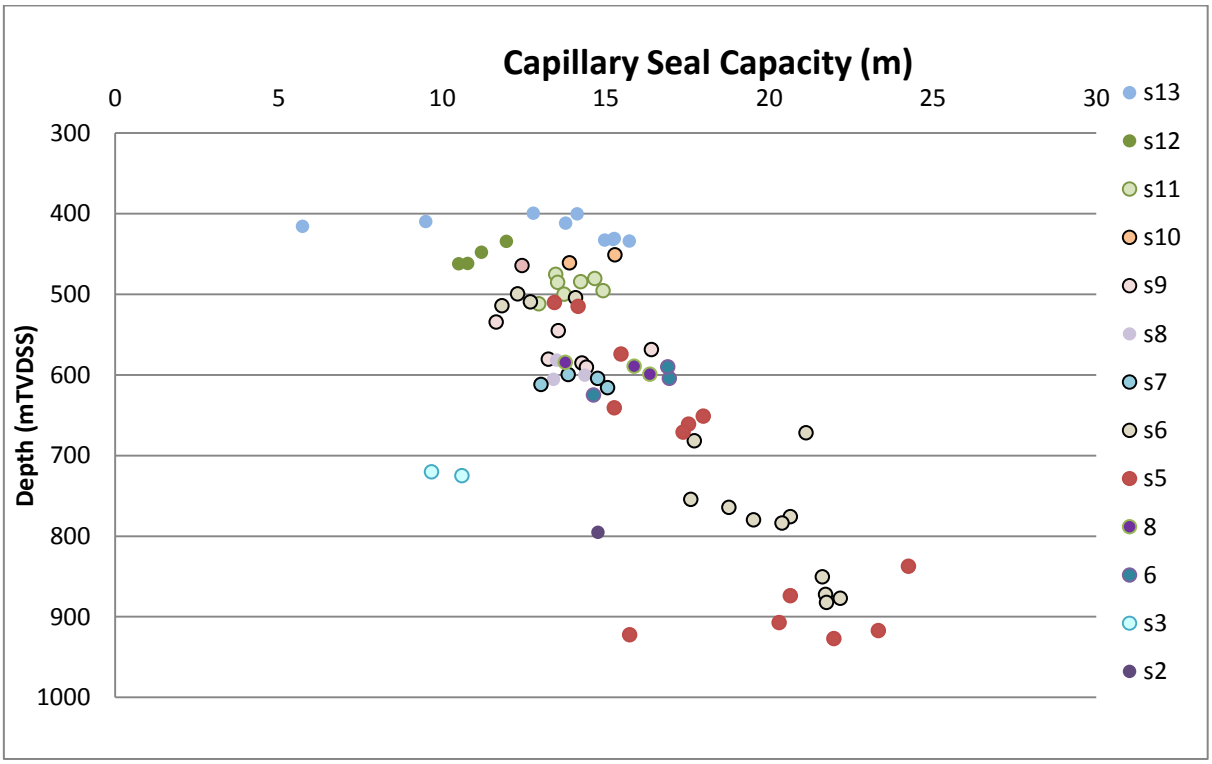

Fig. 6-8. Cross plot of capillary seal capacity with depth for the different seismostratigraphic units.

6.6 Evaluation of the grain size based method

The final step of the workflow (Appendix F) is the evaluation of the applied grain size based method to calculate capillary seal capacities. For this purpose the heights of the gas columns calculated by the grain size method are compared with those calculated from measured fluid pressures and with other indicators of gas column heights, such as the heights of gas occurrences detected from crossovers of neutron (NPHI) and density logs (RHOB) and reported gas water contacts.

The calculation of a reliable gas column height from the available RFT pressure data is not always straightforward. This is because of the small gas column heights in most of the shallow gas occurrences. Often only a limited number of pressure measurements are available for the gas phase in a certain reservoir (often only 1 pressure measurement). This small number of gas measurements in combination with the small gas column heights makes it difficult to distinguish between a pressure measurement in the gas and in the water phase if no additional information on fluid type is available. Therefore, before being able to calculate the gas column height using fluid pressure data (from RFT measurements) the type of fluid for each measurement point (gas or water) needs to be assessed using additional information. For this purpose the identified depths of gas peaks and crossovers of NPHI-RHOB from logs, and DHIs from seismic, and information from end-of well reports was used in combination with the pressure data itself. Subsequently, the pore water gradient and water density were calculated from cross plots of water pressure versus depth. The calculation procedure of the gas column height at a certain well location is outlined in detail Appendix F. The wells may not penetrate the crest of the reservoir. In that case the hydrocarbon column height at the well will be less than the maximum column height for that shallow gas reservoir.

Table 6-1 shows the availability of pressure and log information for each well. The comparison is described below for the wells A12-03, A18-02, B10-03, B13-03, B13-04, B17-06 and F02-06.

Table 6-1. Overview of data availability for evaluation of the calculated capillary seal capacities of mudrocks in 10 wells.

	RFT pressures measured in Eridanos reservoirs			Neutron and density logs		Location of well
Well name	Publicly available	RFT pressures available at reservoir depths below studied mudrock seals	RFT pressures allow calculation gas gradient at depths below studied mudrock seals	Available	NPHI-RHOB cross over at depths below studied mudrock seals	Lateral distance to crest of uppermost stacked reservoir, estimated from seismic (km)
A12-03	yes	yes	yes	yes	yes	2.6
A15-04	no	no	no	no neutron log	no	
A18-02	yes	yes	yes	yes	yes	1
B10-03	yes	yes	uncertainty of fluid type related to measured pressures	low quality neutron log	no	1.7
B13-03	yes	yes	yes	yes	yes	6.6
B13-04	yes	yes	pressures reported as supercharged	low quality logs	no	11.2
B17-05	yes	gas pressure at 25 m below studied seal	only at 25 m below studied seal	yes	cross over at 25 m below studied seal	0.9
B17-06	yes	yes	yes	yes	yes	1.1
F01-01	yes	no	no		no (no resistivity logs)	0.2
F02-06	no	no	no	yes	yes	0

6.6.1 *Evaluation of the grain size-based method: A12-03*

Well A12-03 is the discovery well of shallow gas field A12-FA. The well cuts through bright spots that are classified as stacked 4WD BS, overlying a salt structure and not fault bounded (Fig. 6-9). Application of the grain sized based method using clay contents and median grain sizes derived from core samples of the sealing mudstone at 431, 432 and 432 m depth at well A12-03 resulted in a calculated gas column height of 15 m (Table 6-2). This gas column height of 15 m exceeds the 10 m height of the NPHI-RHOB crossover observed in the reservoir below the mudstone (Fig. 6-9) and the 9.5-10 m column height calculated from pressure data (Table 6-2, Fig. 6-10). Fig. 6-9 and Table 6-1 show that well A12-03 is not cutting through the crest of the reservoir. As a consequence the NPHI-RHOB crossover and the pressure-based gas column height do not correspond to the maximum seal capacity of the mudstone. The estimated maximum seal capacity according to the cross-section would be 3/2 x 10 ~15 m, which corresponds perfectly with the grain size derived gas column height.

Table 6-2. Gas column heights calculated using different methods (well A12-03).

A12-03							
Seal Depth mTVDss	Sample Depth mTVDss	Strat. Unit	Pressure measurement mTVDss	HC column height pressure-based: From point of measurement (m)	HC column height pressure-based: From base seal m	HC column height grainsize-based m	NPHI – RHOB Cross over m
422.78 – 432.78	431;432;433	s13	433.27	9.5	10	15	10
515.75 – 526.75			530.27	20.5	24	-	22

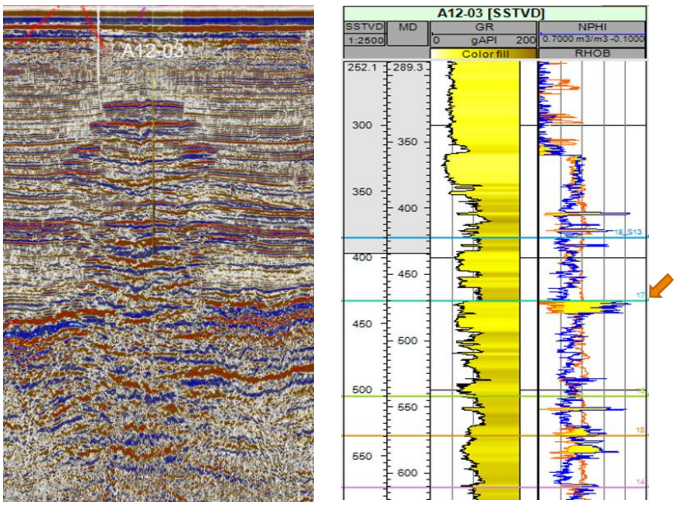

Fig. 6-9. From left to right: 1. seismic section showing location of well A12-03 cutting through stacked bright spots; 2. Gamma ray, neutron (NPHI) and density (RHOB) logs; NPHI-RHOB crossovers indicate presence of gas; arrow indicates location of mudstone samples; 3. Cross-section showing geometry of top gas reservoir/base mudstone seal; arrow indicates location of mudstone samples (figure derived from production plan A 12 field).

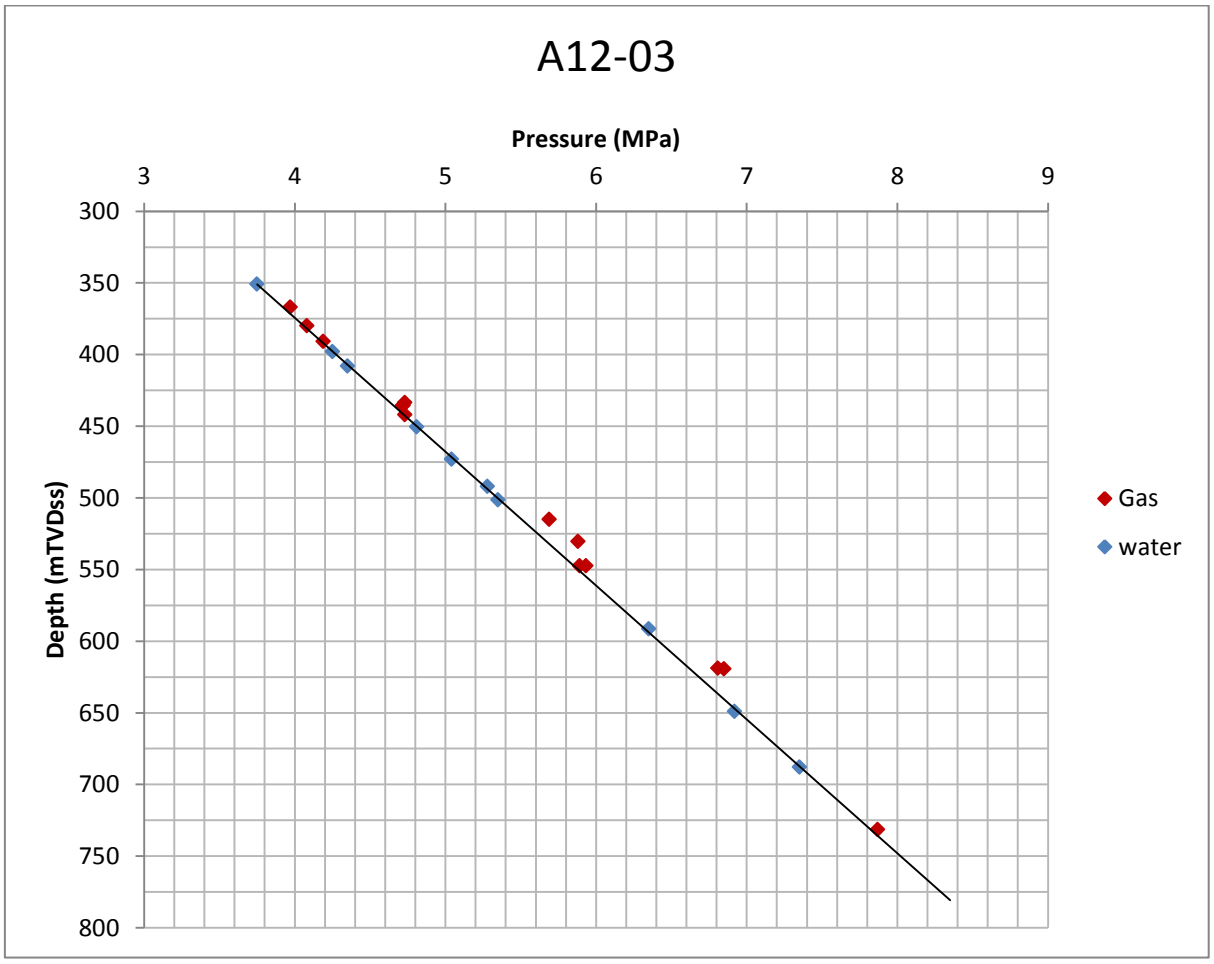

Fig. 6-10. Cross plot of gas and water pressure versus depth at well A12-03. Hydrostatic gradient through water pressures.

6.6.2 *Evaluation of the grain size-based method: A18-02*

Well A18-02 is the discovery well of shallow gas field A18-FA. The well cuts through bright spots that are classified as stacked 4WD BS, overlying a salt structure and not fault bounded (Fig. 6-11). Table 6-3 shows that 3 out of 5 gas column heights calculated with the grain size method correspond well with the pressure and the NPHI-RHOB crossover derived magnitudes of column heights (see also Fig. 6-11 and Fig. 6-12). The GWCs calculated from the pressure measurements agree with the published GWCs in the end-of-well report for A18-02. The lateral distance to crest of the uppermost stacked reservoir is approximately 1 km. The difference in depth between the crest of the reservoir and the bottom of the seal at A18-02 could not be identified reliably from seismic (probably not more than a few meters). The grain size based gas column height for the uppermost reservoir is clearly much greater than the one derived from the measured pressure. According to the BS classification the bright spot (S13 intra SG Field A18) has a size of 6.11 km^2 and seems to be filled to spill. Possibly the structural spill point of this small gas trap limits the gas column height. If so, the trap would not be filled to the maximum capillary sealing capacity of the top seal, because of lateral leakage from the structural trap. The pressure-derived gas column height of the 4th gas accumulation agrees with the NPHI-RHOB crossover but is much smaller than the grain size based gas column height. The end-of-well report indicates the presence of gas at this depth. From the available information it is not clear what causes the misfit.

Table 6-3. Gas column heights calculated using different methods (well A18-02).

A18-02							
Seal	Sample	Strat. Unit	Pressure	HC column height pressure-based		HC column height	NPHI – RHOB
Depth	Depth		measurement	From point of	From base seal	grainsize-based	Cross over
mTVDss	mTVDss		mTVDss	measurement (m)	m	m	m
393.16 – 404.16	400	s13	406.67	0.9	3.5	14	4
489.16 – 498.16	495	s11	503.12	7.4	12.4	15	11
540.16 – 555.16	545	s9	556.62	14.7	16	14	16
580.16 – 591.16	585;590	s9	592.22	4.6	5.7	14	5
603.16 – 609.16	605	s8	611.12	12.9	14.9	13	15

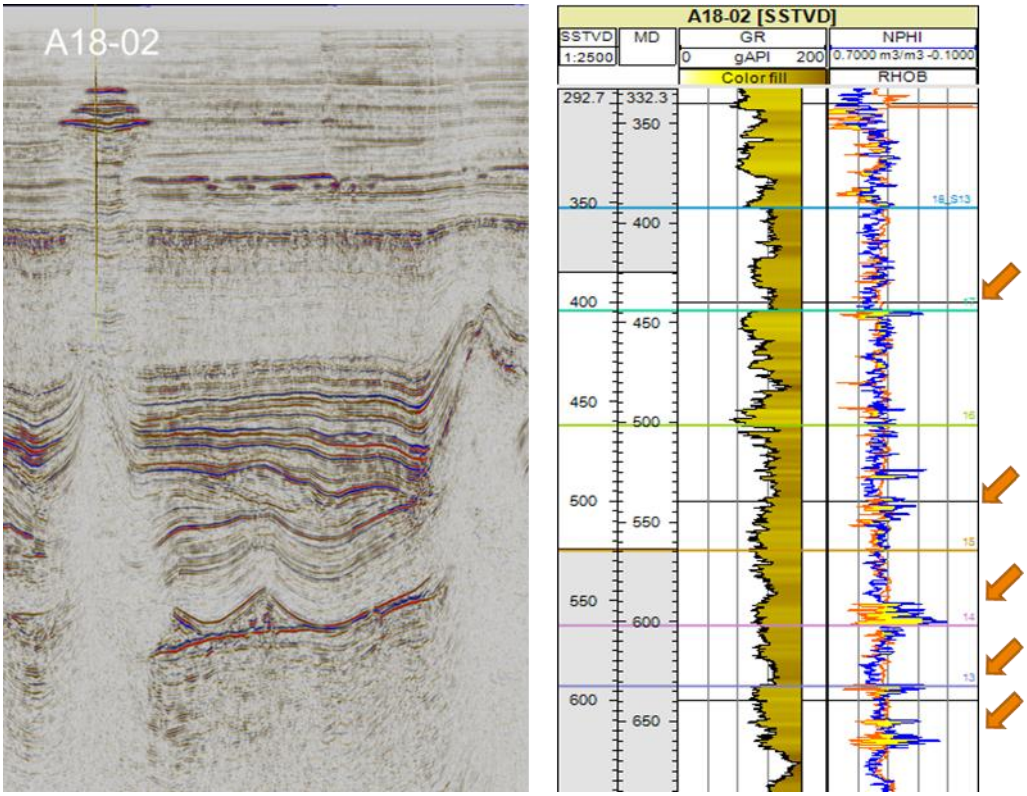

Fig. 6-11. From left to right: 1. seismic section showing location of well A18-02 cutting through stacked bright spots; 2. Gamma ray, neutron (NPHI) and density (RHOB) logs; NPHI-RHOB crossovers indicate presence of gas; arrows indicate location of mudstone samples(Table 6-3).

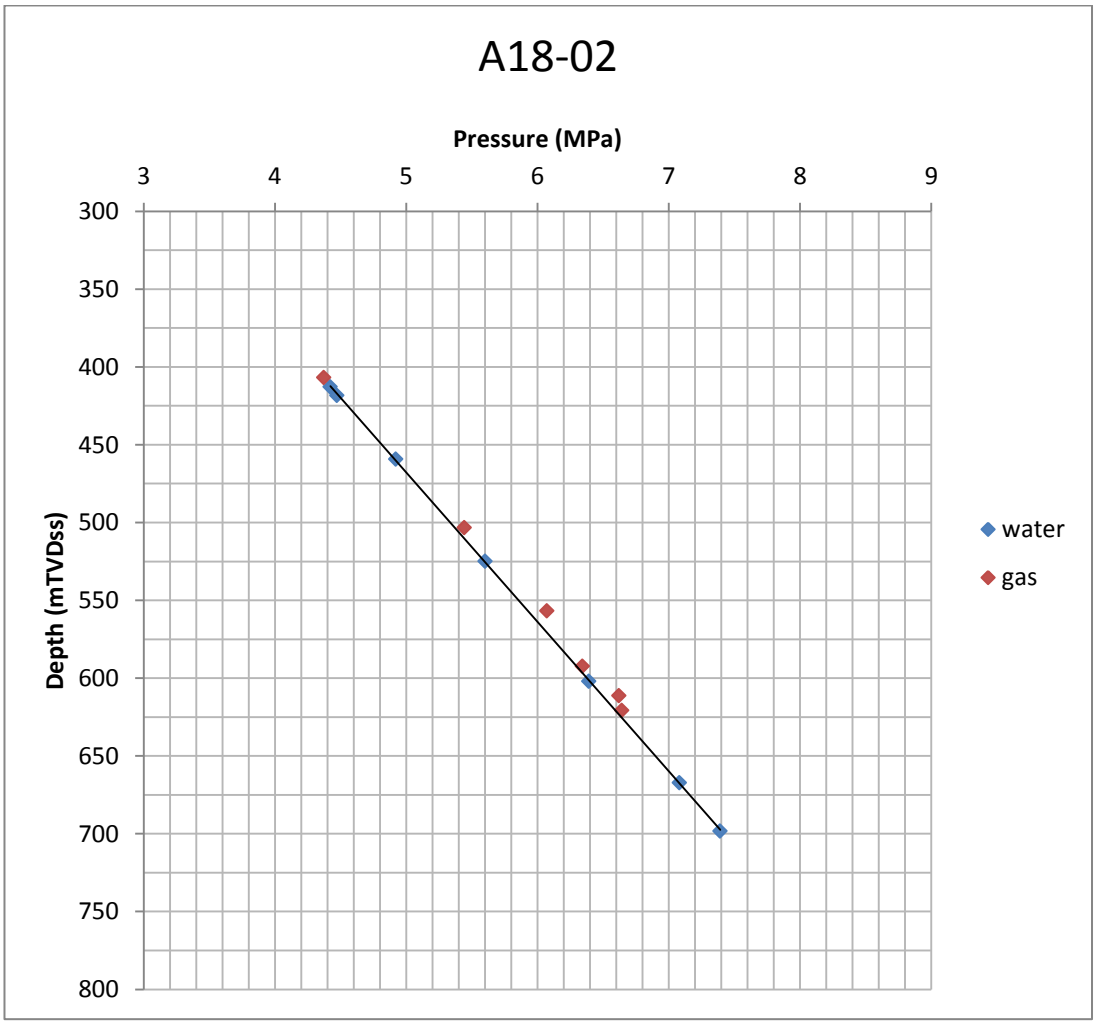

Fig. 6-12. Cross plot of gas and water pressure versus depth at well A18-02.Hydrostatic gradient through water pressures.

6.6.3 *Evaluation of the grain size-based method: B10-03*

The side track of B10-03 is the discovery well of shallow gas field B10-FA. Well B10-03 cuts through bright spots classified as stacked 4WD BS, not fault-bounded. The neutron log for his well is of poor quality and the RFT pressure distribution in the delta deposits does not show clear gas pressure gradients (Fig. 6-13). We have selected one pressure measurement corresponding to a log derived gas peak to evaluate the calculated hydrocarbon column height using the grain size based method with one derived from pressure data (Table 6-4). Please note that the calculated pressure-derived hydrocarbon column height is quite uncertain, because it was difficult to distinguish the gas and water pressures for his well. Both hydrocarbon column heights are comparable in magnitude. Also note that the lateral distance from the well location to crest of the reservoir is approximately 1.7 km (estimated from 2D seismic).

Table 6-4. Gas column heights calculated using different methods (well B10-03).

B10-03							
Seal	Sample	Strat. Unit	Pressure	HC column height pressure-based		HC column height	NPHI – RHOB
Depth	Depth		measurement	From point of	From base seal	grainsize-based	Cross over
mTVDss	mTVDss		mTVDss	measurement (m)	m	m	m
-586	582	s8	587.89	11		13	

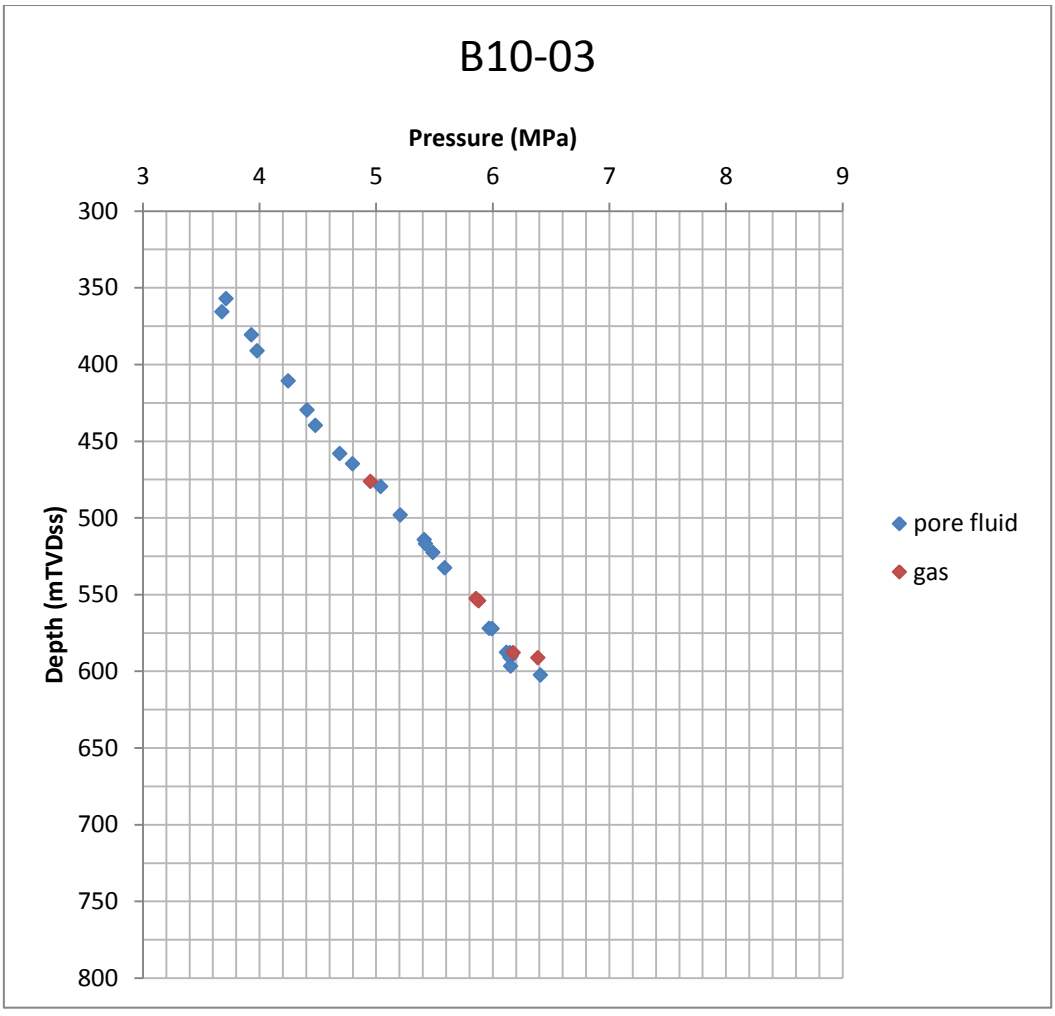

Fig. 6-13. Cross plot of gas and pore fluid pressure versus depth at well B10-03.

6.6.4 *Evaluation of the grain size-based method: B13-03*

Well B13-03 is the discovery well of shallow gas field B13-FA. The well cuts through bright spots that are classified as stacked 4WD BS, overlying a salt structure and not fault bounded (Fig. 6-14). Table 6-5 shows that the gas column height of 14 m (sample depth 484 m) calculated with the grain size method corresponds with both the pressure-derived and NPHI-RHOB crossover derived magnitudes of column heights. The capillary seal capacity of the mudstone calculated by the grain size method (12 m) at a depth of 339 m is higher than the NPHI-RHOB crossover. The water gradient at a depth around 300 m was difficult to assess from the RFT data (Fig. 6-15). The identified sealing mudstone layer at this depth is very thin (Table 6-5 and Fig. 6-14). The crossover of NPHI-RHOB logs at depths of less than 339 m shows that gas also occurs in greater or lesser extent in layers overlying the mudstone. In addition, gas plumes have been observed in the water column in the area of well B13-03 (Schroot et al., 2005). A possible explanation may be that the thin mudstone layer and/or its lithological properties and therefore its sealing capacity are not laterally continuous and may be less over the whole trap than the 12 m calculated from the grain size of the sample. In addition, Table 6-1 shows that the lateral distance between the well and the crest of the reservoir is estimated to be more than 6 km, based on 2D seismic. Hence, there will be a difference between the depth of the crest of the reservoirs and the depth of the boundary between the seal and the reservoirs in B13-03. It was not possible to derive a reliable estimate of the magnitude for this difference from the 2D seismic.

Table 6-5. Gas column heights calculated using different methods (well B13-03).

B13-03							
Seal	Sample	Strat. Unit	Pressure	HC column height pressure-based		HC column height	NPHI – RHOB
Depth	Depth		measurement	From point of	From base seal	grainsize-based	Cross over
mTVDss	mTVDss		mTVDss	measurement (m)	m	m	m
336.4 – 339.9	339	post s13	340.39	inconclusive*		12	3
393.4 – 403.4	399	s13				13	1.5
481.39 –494.39	484	s11	495.89	13.6	15	14	15
518.4 –537.4	532	s9				12	
600.4 – 609.4	604	s7	609.89	10.4	10.9	15	5.5
600.4 – 609.4	604	s7	612.89	5.1	8.6	15	5.5
			*uncertain water gradient				

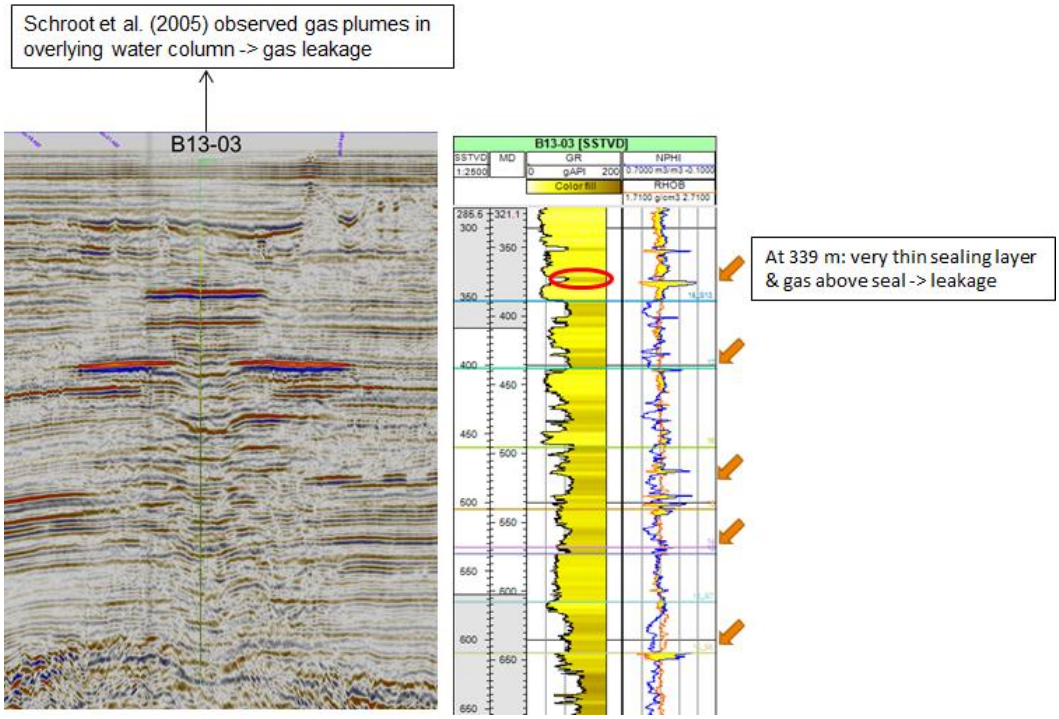

Fig. 6-14. From left to right: 1. seismic section showing location of well B13-03 cutting through stacked bright spots; 2. Gamma ray, neutron (NPHI) and density (RHOB) logs; NPHI-RHOB crossovers indicate presence of gas; arrows indicate location of mudstone samples (Table 6-5).

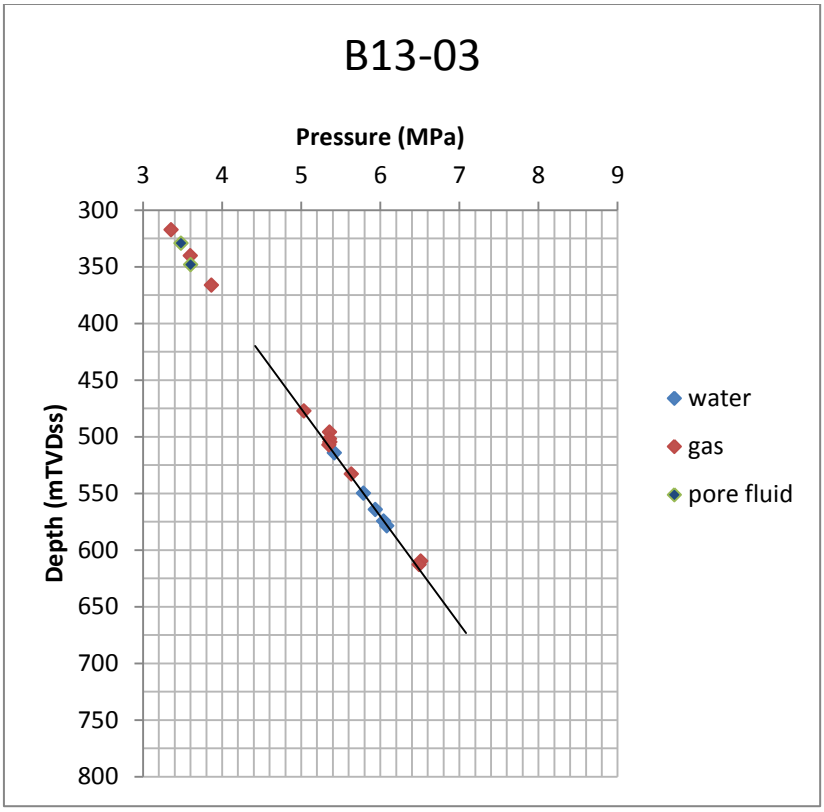

Fig. 6-15. Cross plot of water, gas and pore fluid pressure versus depth at well B13-03, showing hydrostatic gradient through the water pressures.

6.6.5 *Evaluation of the grain size-based method: B13-04*

Well B13-04 penetrates the shallow gas field B13-FA. The well cuts through bright spots that are classified as stacked 4WD BS, overlying a salt structure and not fault bounded (Fig. 6-16). Information from seismic revealed that the well is located at large distance from the crest of the reservoir (11.2 km).

The neutron and density logs for this well do not provide indicators of gas column heights related to the location of the sampled mudstone seals (Tables 6-1 and 6-6; Fig. 6-16). The samples from seismostratigraphic unit s13 (at depth of 410 and 416 m) contain > 20% sand and as a result the calculated gas column heights are less reliable. The grain size based gas column height of 14 m for unit s11 can be compared with that derived from pressure measurement at 518.9 m. The pressure measurement is reported to be related to supercharged conditions (remark on composite log of well B13-04), and as a consequence may not be representative for a gas pressure at that depth. Therefore, it is not possible to evaluate the grain size based method for the calculated column heights at this well, despite the availability of pressure data and neutron and density logs.

Table 6-6. Gas column heights calculated using different methods (well B13-04).

B13-04							
Seal	Sample	Strat. Unit	Pressure	HC column height pressure-based		HC column height	NPHI – RHOB
Depth	Depth		measurement	From point of	From base seal	grainsize-based	Cross over
mTVDss	mTVDss		mTVDss	measurement (m)	m	m	m
407.3 – 414.3	410	s13				9*	(not clear)
407.3 – 414.3	416	s13				6*	(not clear)
448 – 454.8	448	s12				11	(not clear)
495.8 – 510.8	500	s11	518.9	17	25	14	(not clear)
608.8 – 628.8	616	s7				15	(not clear)
						(* sand content > 20%)	

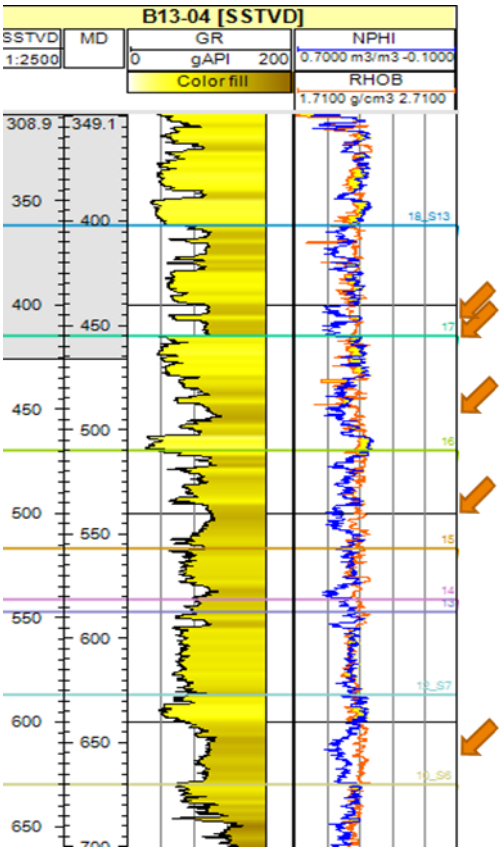

Fig. 6-16. Gamma ray, neutron (NPHI) and density (RHOB) logs for well B13-04; NPHI-RHOB crossovers indicate presence of gas; arrows indicate location of mudstone samples (Table 6-6).

6.6.6 *Evaluation of the grain size-based method: B17-06*

B17-06 cuts through bright spots classified as stacked 4WD BS overlying a salt structure and bounded by a fault. Table 6-7 (Fig. 6-17) shows that the two gas column heights calculated with the grain size method for the sealing layer at 590-630.5 m depth correspond pretty well with the NPHI-RHOB crossover derived magnitudes of column heights. The more so for the gas column height of 15 m calculated for the mudrock sample from the bottom part of the seal (sample depth of 625 m). However, the gas column heights derived by both methods are higher than that calculated using measured fluid pressures. The fluid pressures measured in the reservoir underlying the mudstone seal indicate that the reservoir may contain a number of stacked gas occurrences (Fig. 6-18). The ultimate top seal being the mudstone layer at 590-630.5 m depth. In addition, seismic interpretation revealed that the lateral distance of the well to the crest of the reservoir is 1.1 km. Hence the maximum gas column height at the crest of the reservoir will be greater than that at the well location. In addition, the hydrocarbon trap is associated with a fault. The fault may provide, or provided in the past, charging of the reservoir and/or a lateral escape way for the gas. The gas column heights calculated for samples of seismostratigraphic unit s3 (10 and 11m) are much higher than the gas presence in the underlying reservoir as indicated by the NPHI-RHOB crossovers. The s3 seal contains 32% sand, and as a consequence the calculated gas column heights can be considered to be less reliable. The high sand percentage may create a dual permeability system, creating permeable pathways for the gas (see also section 6.1.1.1).

Table 6-7. Gas column heights calculated using different methods (well B17-06).

B17-06							
Seal	Sample	Strat. Unit	Pressure	HC column height pressure-based		HC column height	NPHI – RHOB
Depth	Depth		measurement	From point of	From base seal	grainsize-based	Cross over
mTVDss	mTVDss		mTVDss	measurement (m)	m	m	m
590 - 630.5	590	6	631.25	9.3	10	17	14
590 - 630.5	625	6	631.25	9.3	10	15	14
719 - 732	720	s3		-		10*	4
719 - 732	725	s3				11*	4
						(* sand content > 20%)	

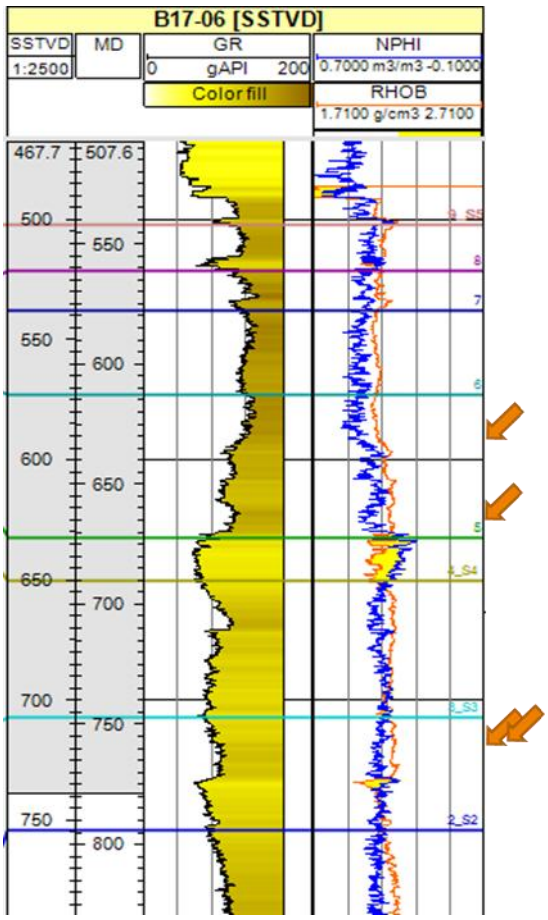

Fig. 6-17. Gamma ray, neutron (NPHI) and density (RHOB) logs for well B17-06; NPHI-RHOB crossovers indicate presence of gas; arrows indicate location of mudstone samples (Table 6-7).

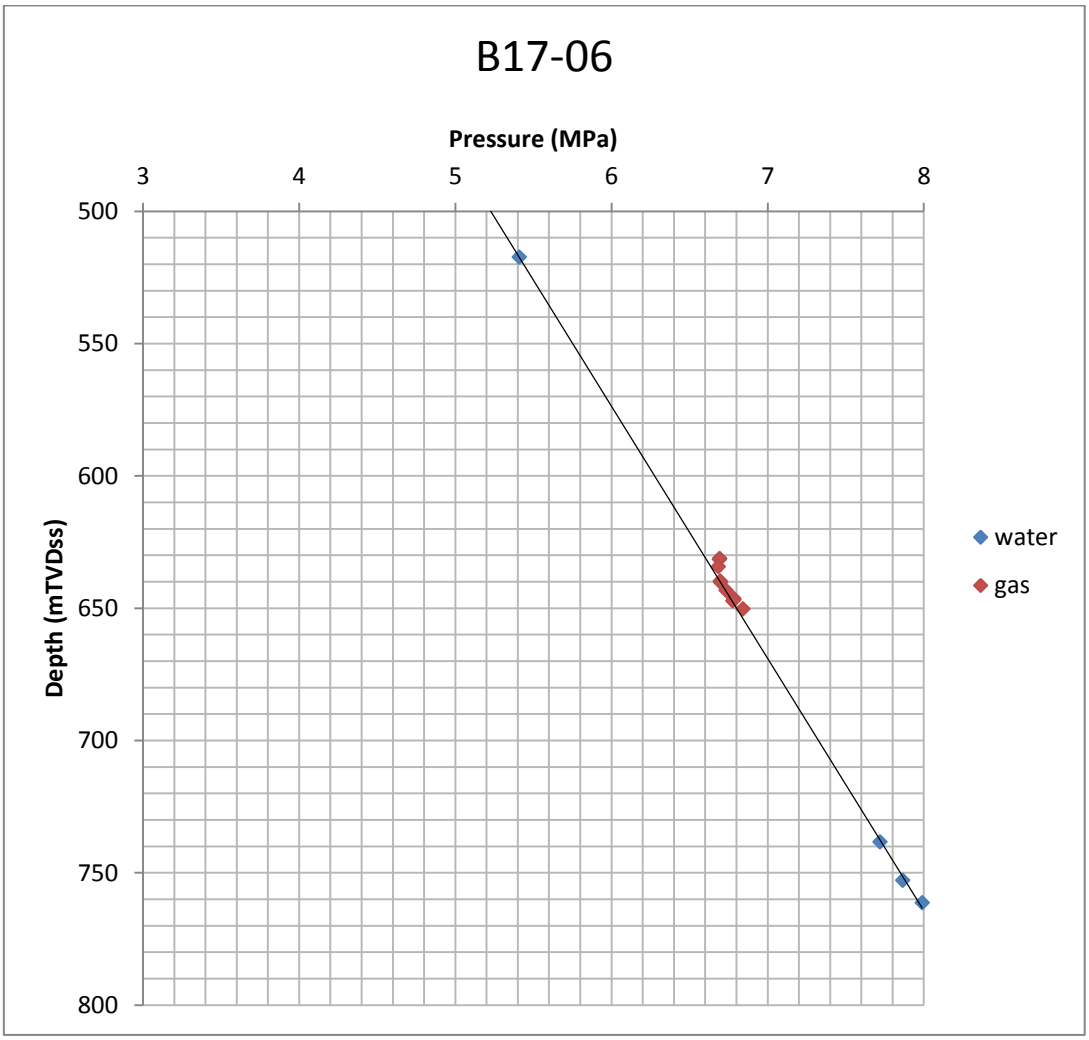

Fig. 6-18. Cross plot of gas and water pressure versus depth at well B17-06, showing hydrostatic gradient. Gas column height of 9.3 m is calculated based on measured gas pressures relative to the hydrostatic gradient. Below the gas column height of 9.3 m other smaller gas column heights seem to exist that may be separated by permeability baffles in the reservoir.

6.6.7 *Evaluation of the grain size-based method: F02-06*

Well F02-06 runs through the crest of the F2A Pliocene gas field. The gas accumulation with a gas column height of 40 m is trapped in a low relief 4W dip-closed anticline formed by the upward movement of a Zechstein salt structure that took place until Quaternary times (Winningsplan F2A, 2008). The accumulated gas is methane, as reported on the composite log of well F02-03 (well F02-03 is also penetrating the F2A gas reservoir). A prominent NW-SE running normal fault cuts through the western flank of the gas reservoir and partially offsets the reservoir sands (Winningsplan F2A, 2008; see also F02-03). The shallow gas field overlies the Hanze Oil field reservoired in the Chalk on top of the Zechstein salt structure (Fig. 6-19). This dynamic oil reservoir is highly overpressured (~7.5 MPa at 1400 m) and oil and gas shows occur in its Lower Tertiary mudrock caprock (e.g. composite logs of F02-05, F02-A-02; Price et al., 2002; Verweij et al., 2009). The normal fault that cuts through F2A Pliocene gas field extends into the Hanze oil field. Composite log of F02-03 shows a gas peak at the location where a fault is crossing the borehole at 29 m above the shallow gas field, indicating that the fault zone is or was transmitting gas.

The calculated gas column heights vary between 15 and 18 m for the mudrock seal in unit s5 (Table 6-8). The thick mudrock top seal in unit s5 was sampled between 641 and 671 m depth, well above the bottom of the seal at 690 m. Results of the grain size analysis (Appendix G and Appendix H) show that the mudrock composition of the seal varies in clay content and median grain size (see also Fig. 6-19): the bottom part of the seal may be more coarse grained and less sealing. The mudrock seal clearly holds a larger gas column (40 m) than can be explained by the capillary seal capacity calculated with the grain size method (15-18 m).

As outlined before, capillary entry pressures are not the only control on maximum column heights of mudrock top seals. Charging and top seal leakage history also control maximum and present-day column heights. The charging history of the F2A Pliocene gas field may offer an alternative explanation for the observed gas column height.

Given the dynamic nature of the Chalk oil field, the oil and gas shows in the Lower Tertiary mudstone caprock of the oil field, and the observed indicators of fault zone related gas occurrences suggest that the fault zone plays or played in the past, a role in vertical upward migration of gas from the Hanze field and charging of the F2A Pliocene gas field. Migration along fault zones is often related to specific phases of fault reactivation. Hence, charging of the F2A Pliocene gas field may have taken place in relatively short time period associated to a phase or phases of fault reactivation. Possibly this charging of original oil-related gas was added to the more gradual charging of the trap by intra-delta biogenic generated gas. A rapid fault-related charging of the trap may have increased the height of the gas column beyond the capillary seal capacity of the mudrock (estimated at 15-18 m), after which the seal started to act as a permeability seal. The migration through the mudrock seal of permeability of 1.3E-19 to 3.9 E-19 m2 by two-phase fluid flow will be very slow through this thick seal, allowing the build-up of the gas column to greater height than the maximum capillary seal capacity of 18 m.
In conclusion, assuming the mudstone seal is a capillary seal, it is clear that the grain size-based calculated gas column height underestimates its maximum capillary seal capacity. However, the F2A gas field is a special shallow gas field in the Plio-Pleistocene delta, because of its location overlying the Hanze oil field and the associated dynamic charging conditions which may have turned the mudrock seal into a permeability seal.

Table 6-8. Gas column heights calculated using different methods (well F02-06).

F02-06							
Seal	Sample	Strat. Unit	Pressure	HC column height pressure-based		HC column height	NPHI – RHOB
Depth	Depth		measurement	From point of	From base seal	grainsize-based	Cross over
mTVDss	mTVDss		mTVDss	measurement (m)	m	m	m
-690	641	s5				15	12
-690	651	s5				18	12
-690	661	s5				18	12
-690	671	s5				17	12

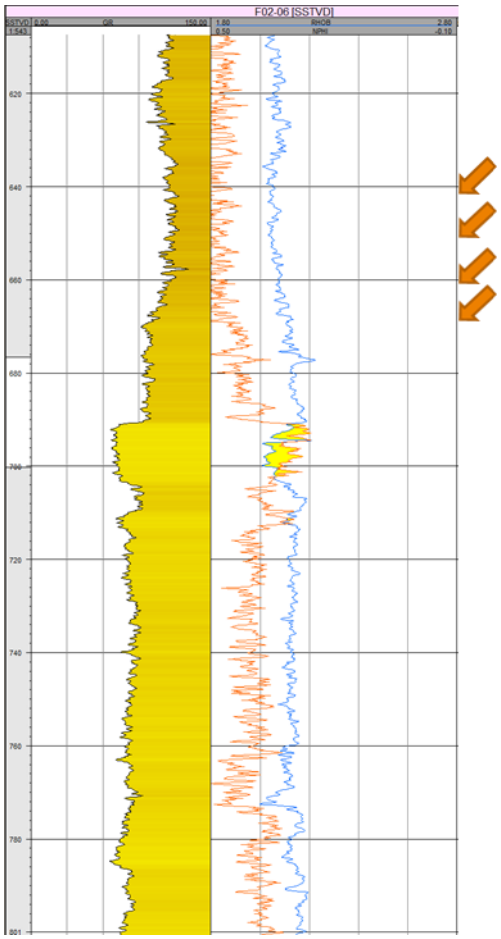

Fig. 6-19. Gamma ray, neutron (NPHI) and density (RHOB) logs for well F02-06; NPHI-RHOB crossovers indicate presence of gas; arrows indicate location of mudstone samples (Table 6-8).

6.6.8 *Discussion*

The generation of biogenic gas in the delta, the migration of gas of both biogenic and thermogenic origin and the charging and leakage of the reservoirs in the delta deposits during Pliocene to recent times developed under highly dynamic pressure, stress and temperature conditions that resulted from the combined influence of rapid sedimentary loading of the delta deposits, waxing and waning of ice sheets, and glacial-interglacial temperature fluctuations. The current presence of gas in intra-delta reservoirs is the end result of gas charging and leakage of the traps in the Plio-Pleistocene delta under these highly dynamic conditions. Current gas column heights reflect different trapping conditions, such as:

1. Trap filled to capillary seal capacity of the mudstone caprock;
2. Trap not filled to capillary seal capacity of the mudstone caprock, because:
    a. Trap is filled to structural spill point
    b. Lack of charge
    c. Leakage through dynamic/permeability mudstone caprock after charging stopped
    d. Leakage due to hydraulic failure induced by fluid pressures exceeding seal strength
    e. Leakage along permeable fault zones penetrating the reservoir
3. Trap filled to more than capillary seal capacity of the mudstone caprock, because charging exceeded the capillary seal capacity of mudstone caprock, while the ongoing charging rate was higher than the leakage rate through the mudstone caprock

The systematic approach to evaluate the porosity and permeability and the capillary seal capacity of the mudstones at shallow depths was developed, applied and tested at selected well locations cutting through bright spots. The approach is based on new grain size analysis data from mudstone layers and publicly available information, including reservoir pressure data. The samples for grain size analysis were obtained from cuttings and a core.

Porosity and permeability of mudstones
The equations developed by Yang and Aplin (2004) were used to calculate porosity. They used mudstone samples from the North Sea and Gulf of Mexico to describe the mechanical compaction and associated decrease in porosity of mudstones. The shallow Plio-Pleistocene deposits in the Dutch offshore are in the realm of mechanical compaction, not significantly affected by chemical diagenesis. The porosity-permeability equation of Yang and Aplin (2010) was used to calculate permeability. Yang and Aplin derived their equation based mainly on marine mudstones, using more than 300 samples and most of these samples were from the North Sea and Gulf of Mexico. Yang and Aplin (2010) report that for their database, an uncertainty of magnitude in permeability at a given porosity is 1 order of magnitude. The mudrock samples from the Dutch Plio-Pleistocene delta belong to one deltaic system in contrast to the samples from the Yang and Aplin (2010) study. At this time it is not known if this more homogeneous sample set reduces the uncertainty in the calculated permeability for the Dutch mudstones.

Capillary seal capacity of mudstones
The calculation of the capillary seal capacity of mudstones at shallow depths involves a number of assumptions and approximations that introduce uncertainty in the calculated capillary mudstone seal capacity. The ‘equivalent grain size method‘ published by Nakayama and Sato (2002) was used to calculate pore throat sizes. The equations involved are based on physical experiments. Input required to calculate the pore throat radius using the equivalent grain size method of Nakayama and Sato (2002) are porosity (magnitude of porosity is result of porosity calculation based on Yang and Aplin, 2004, equation) and equivalent grain diameter. For this parameter, we used the median grain size diameter (µm) resulting from the analyses of the grain size distributions.

To evaluate the applicability of the calculated properties of the mudstone seals that were obtained at lab scale, the calculated values were compared with information on reservoir scale. A reliable evaluation of the applied grain size based method to calculate capillary seal capacities requires that a number of assumptions are fulfilled, namely:

1. The mudstone top seal is a capillary seal.
2. The trap is filled to maximum capillary seal capacity.
3. Trap geometry is known.
4. The samples are homogeneous and have permeabilities and threshold capillary pressures that are controlled mainly by lithology and depth-dependent porosity.
5. Generalised conditions concerning interfacial tension, gas composition (assumed to be methane), temperature gradient (30°C/km) are representative of local conditions and allow a reliable calculation of gas column heights from the calculated pore throats.
6. The properties at the sample scale are representative for the properties of the mudstone top seal at reservoir scale.
7. The number and quality of available RFT pressure measurements in the gas and water phase of a shallow gas reservoir allow the identification of a GWC and the calculation of gas column height.

All these assumptions will seldom be fulfilled in reality, and this also applies to the investigated Plio-Pleistocene delta:

- Assumption 1. If the capillary mudstone seal is breached, or was breached in the past, the history of permeability-constrained charging and leakage control the present-day height of the hydrocarbon column, and not the capillary sealing capacity. A possible example of such a situation might exist at well F02-06.
- Assumptions 2 and 3. If the trap is filled to structural spill point, the maximum capillary seal capacity may be greater than indicated by spill point. The geometry of traps in stacked 4WD BS above salt structures changes with decreasing depths, in general towards more flat geometries of the reservoir-seal boundary at shallow depth. This is associated with decreasing distance between crest of the reservoir and spill point, which may allow lateral leakage before the capillary entry pressure related maximum gas column height has been reached. The geometry of deeper occurring traps in the stacked 4WD BS is more favorable for building-up of gas columns until the capillary seal capacity has been reached. The compiled bright spot classification includes information whether or not the bright spot reaches the structural spill point. A relatively small number of lower boundaries of bright spot could be interpreted with confidence to be clearly above structural spill point.
- Assumption 4. This is a basic assumption that was tested in the evaluation.
- Assumption 5. Generalised conditions concerning interfacial tension, gas composition (assumed to be methane), temperature gradient (30°C/km) can be considered to be representative of local conditions.
- Assumption 6. This is also a basic assumption that was tested in the evaluation.
- Assumption 7. It was often not straightforward to calculate a reliable gas column height from the available RFT pressure data. This is because of the small gas column heights and as a consequence the only limited number of pressure measurements that are available for the gas phase (often only 1 pressure measurement). In turn, this small number of pressure measurements for a gas occurrence also makes it difficult to distinguish between a gas and a water pressure measurement, if there is no additional information on fluid type.

In conclusion, selecting a good calibration location where all of the above listed assumptions are fulfilled is a challenge. The best combination of conditions occurs at wells A12-03 and B18-02 and for part of the mudstone seals at wells B10-03 and B17-06. The evaluation for these well locations shows that the applied grain size based method to calculate capillary seal capacities provides pretty good estimates of maximum gas column heights for mudstone layers at reservoir scale. Observed deviations between grain size based calculated capillary seal capacities and actual gas column heights may be due to a wide variety of causes.

The calculation of capillary seal capacity of mudstones involves, amongst other things, the use of Yang and Aplin's (2004) equation to calculate porosity and Nakayama and Sato's equations (2002) to calculate pore throats. Yang and Aplin (2004) based their equations to calculate the porosity of mudrock on a wide range of mudrock samples. Probably the main uncertainty in the calculation of the capillary seal capacity is in the use of the equivalent grain size method of Nakayama and Sato (2002) to calculate pore throats.

More rigorous testing of the calculation method of the pore throats and quantification of the uncertainty in the calculation of the capillary seal capacity covering a larger study area in the Plio-Pleistocene SNS Delta requires further more detailed research at a location or locations where the above mentioned assumptions and conditions for a reliable evaluation are known to be fulfilled to a large extent. The now available new Petrel model of the Plio-Pleistocene SNS Delta and its properties in combination with the BS classification provide the necessary information for a careful and systematic selection of new sampling locations allowing a more rigorous evaluation of the grain size-based calculation of capillary sealing of the mudstones.

6.7 New generalised method

Appendix H presents the calculated pore-throat radii, resulting from step 4 of the calculation procedure outlined Appendix F. Plotting the calculated pore throat radius against the permeability of the mudstones, omitting the samples with a sand content of less than 20 % (Fig. 6-20), reveals the following relationship:

log (r) = 0.8593 + 0.2579*log(k) (R2 = 0.8948)
Where,
r : pore throat radius (µm)
k : vertical permeability (mD)

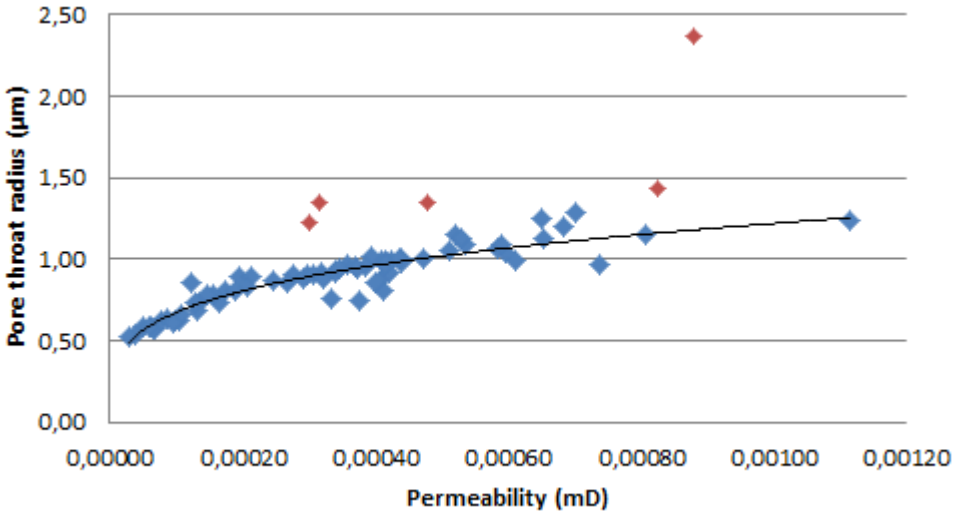

Fig. 6-20. Cross plot showing the relation between the pore throat radius and the permeability calculated for all samples of sealing layers. The red squares indicate the samples classified as sand-silt-clay (sand content > 20 %).

Using the above relationship together with the approaches for calculating porosity and permeability (given in step 2 and 3, Appendix F) was developed into a new easy-to-use generalised procedure to calculate pore throats and associated capillary seal capacities for mudstones. The generalised procedure is presented in Appendix F .

6.8 Conclusions

- **Capillary seal capacity mudstones**: The applied systematic approach using grain size analysis data (Appendix F) was found to be a promising methodology for estimating petrophysical properties (porosity, permeability, pore throat) and capillary seal capacities of the mudstones. Comparison of the gas column heights estimated from pressure data and log information with those calculated using the analysis of the grain size distribution is not straightforward and requires fulfillment of a set of subsurface conditions with regard to charging and leaking of shallow gas reservoirs and the availability of measured data (e.g. pressure data, or reported GWC). It was shown that the applied grain size based method to calculate capillary seal capacities provides pretty good estimates of maximum gas column heights for mudstone layers in the Plio-Pleistocene delta deposits for the wells A12-03 and

A18-02, and for part of the mudstone seals in wells B10-03 and B17-06. The grain size-based calculated gas column height for the mudstone seal at well F02-06 tapping the F2A shallow gas field underestimates the observed gas column height. The F2A gas field is a special shallow gas field in the Plio-Pleistocene delta, because of its location overlying the Hanze oil field and the associated dynamic charging conditions, which may have turned the mudrock seal into a permeability seal.

- **Database of relevant sealing properties**: The grain size analysis of 77 samples from 45 sealing mudrocks in 10 wells (Appendix G) in combination with the grain size based systematic approach to evaluate the porosity, permeability, pore throat size and capillary seal capacity has resulted in a database of relevant seal properties (Appendix H). The vertical permeability varies between 2.8E-20 and 1.1E-18 m^2. Most of the pore throat radii of the mudstones vary between 0.5 and 1.5 µm. The associated capillary seal capacity of the mudrocks vary between ±10-24 m (depth: 400-900 m) and increase with depth.

- **Newly developed practical workflow to estimate sealing properties of mudstones**: a new relation between pore-throat size and permeability of mudstones could be established. This new relationship in combination with the equations of Yang and Aplin (2004, 2010) for calculating porosity and permeability has resulted in a straightforward and easy to use approach to assess pore throats of mudstone seals using clay content and depth as the main input parameters.

- **Uncertainty in the application of the equivalent grain size method of Nakayama and Sato (2002) to calculate pore throats**: because of the identified uncertainty, it is recommended to carry out an additional testing of this part of the procedure to assess capillary sealing capacity of mudstones. Special attention should be paid to carefully select the location or locations where – most of – the conditions for a reliable evaluation are known to be fulfilled to a large extent.

Knowing that capillary seal capacity is a multi-scale property, and that mudstones also act as permeability seals and faulting and fracture zones crossing the mudstones influence the sealing capacity, the presented grain size-based method should be seen as a first phase of a more comprehensive approach to estimate preserved gas columns in bright spots in the Plio-Pleistocene delta in offshore Netherlands and in its distribution area outside the Netherlands.

6.9 Follow-up

The following topics are of importance in a follow-up phase of the mudstone seal study towards a more comprehensive approach to estimate preserved gas columns in bright spots in the Plio-Pleistocene delta deposits:

- **Quantification of uncertainty in calculating capillary seal capacity of mudstones**. Quantification of the uncertainty in the calculation of the capillary seal capacity requires further testing of the method over a larger study area at carefully selected locations where the previously listed conditions for a reliable evaluation are fulfilled to a large extent. This would involve new detailed sampling of mudrock seals overlying shallow gas reservoirs not filled to spill point. The now available new Petrel model of the Plio-Pleistocene delta and its properties in combination with the BS classification provide the necessary information for a careful selection of sampling locations allowing a more rigorous evaluation of the grain size-based calculation of capillary sealing of the mudstones.

- **Regional (upscaled) applicability of the grain size based method to estimate capillary seal capacity of mudstones**. The now available detailed stratigraphic model of the Plio-Pleistocene delta, including the regional facies distributions and bright spot properties provide an excellent database to investigate the wider and more regional (upscaled) applicability of the grain size based method to estimate capillary seal capacity of mudstones. The upscaling approach involves different steps, such as:
    - Additional sampling and grain size analysis. The information in the Petrel model enables systematic sampling of seals in different stratigraphic/facies positions and representing different – good as well as failed – gas reservoirs.
    - Creation synthetic geologic models for representative stratigraphic and structural trap types (based on bright spot classification).
    - Populating the sealing layer of these synthetic trap types with properties resulting from the sampling and grain size based method (porosity, permeability, pore throats, capillary pressures).
    - Calculation/simulation of equilibrium gas column heights for different trap types and different properties of sealing layers.
    - Upscaling of results.

- **Charging and leakage history of mapped traps and estimated permeability and capillary seal capacity**. History of charging was found to be important to evaluate the seal characteristics and related presence of gas accumulations: the Petrel Model provides an excellent opportunity to visualize the evolution of the Plio-Pleistocene delta in time in relation to the evolution of its properties (such as porosity, permeability, temperature) and gas charging and leakage of BS locations by using basin modeling approaches.

- **Relation clay content sample and log derived clay content.** The grain size based method to calculate properties of the mudstones depend strongly on clay content. It would be interesting to make the method more widely applicable to establish a relation between the clay content derived from grain size analysis data with log-derived clay content.

7 Bright spot classification

7.1 Introduction

Acoustic bright spots (BS) are defined as seismic reflections with anomalous high amplitudes and as such they can be easily mapped on seismic data. Bright events can be caused by many geological and physical phenomena that cause a local and anomalous impedance contrast that differs from its surrounding. This study only focuses gas filled sand layers that have the following characteristics:

- They are low Impedance layers.
- They have an anomalously high amplitude, that is not indicative for gas saturation since even low saturations give high amplitude effects (Fig. 7-1, Fig. 7-2, Fig. 7-4).
- There are two bright event of opposite nature: one representing the top of the layer, the other the base. For zero phase European polarity the top is represented by a peak and a through at the base, while zero phase American polarity is characterised by a through at the top and a peak at the base (Fig. 7-4).

7.2 Method

In selecting the BS for the ABF blocks, a preliminary study of EBN was used which provided outlines (polygons) of bright spots areas. These pre-selected (and additional) BS are mapped based upon the above mentioned criteria using the following approach:

- An auto-tracker is used to map only high amplitudes (2D / 3D).
- Stacked BS are mapped separately.
- An event is only mapped when a clear top and base anomaly are present. Only the top anomaly is mapped.
- Only low impedance layers are mapped. When an opposite amplitude top reflector is found the layer is a high impedance layer, such as shell-banks. These events are ignored.
- When bright spots are stacked it is common that the shallowest bright spot reflects most of the seismic energy back to the surface. As a consequence the events below have very low amplitudes (transmission effect; Fig. 7-3). Consequently, bright spots below other bright spots cannot meet the criteria for being an anomalously high amplitude event. Therefore, these events are not mapped. However, in most cases bright spots become larger with depth (halo shaped) and can therefore only be partially mapped.
- Based on the seismic interpretations of the bright spot, surfaces are created.
- Finally, properties from the ABF property model are extracted for all the BS surfaces and stored in the database together with other useful characteristics such as depth, size and stratigraphic interval (see chapter 6.3.).

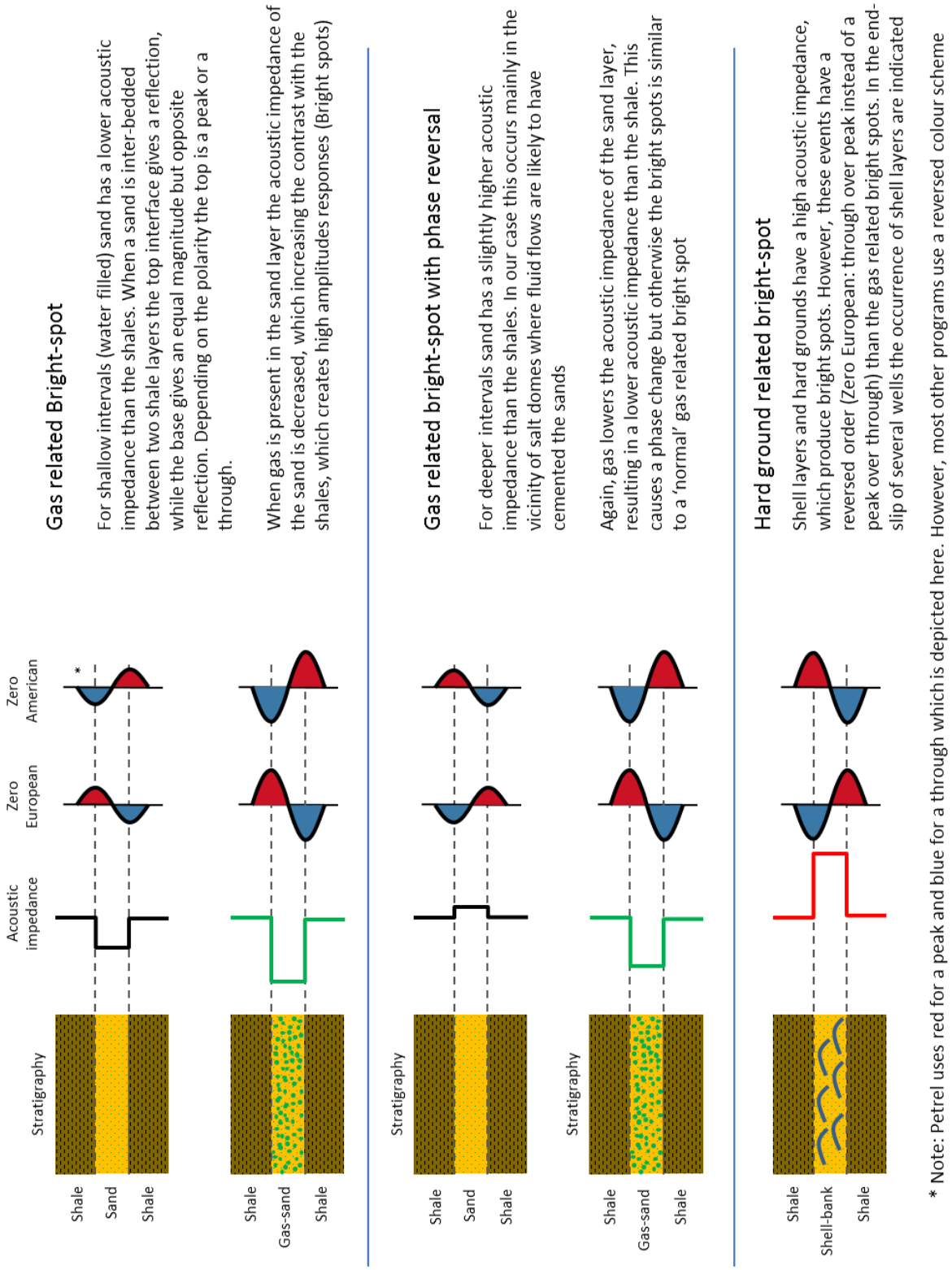

Fig. 7-1. Explanation of observed amplitude anomalies, including gas-related bright-spots, phase reversal and hard grounds.

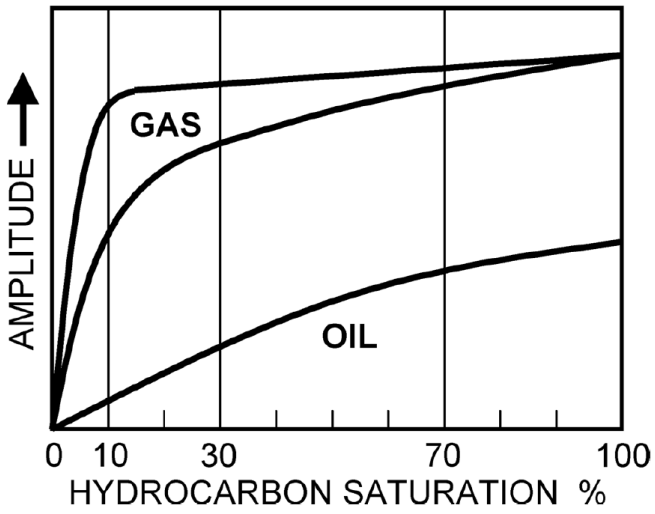

Fig. 7-2. Amplitude effect vs. HC saturation, from Brown (2010).

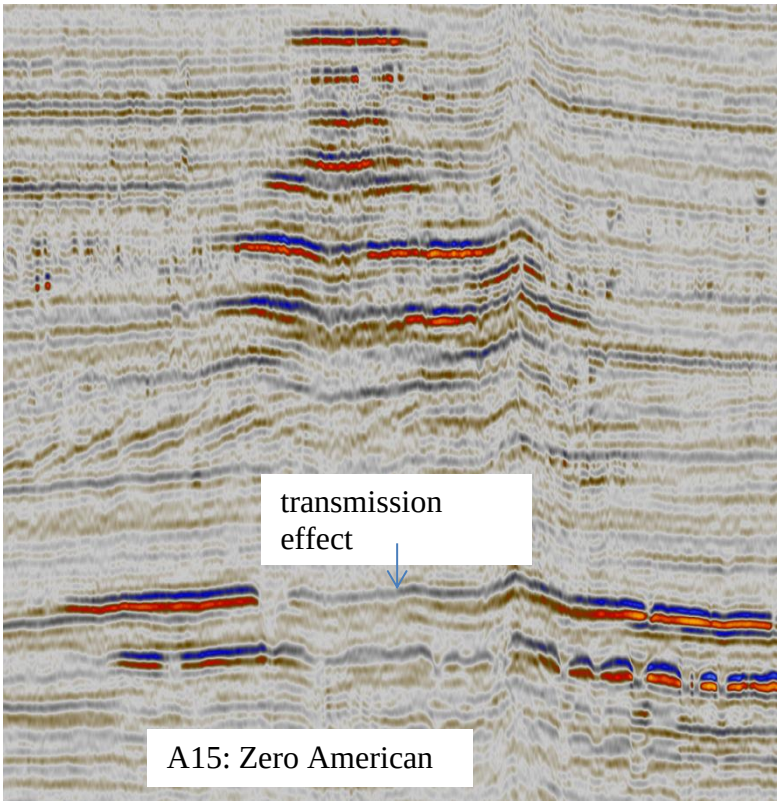

Fig. 7-3. Examples of stacked bright spots. Note the natural paring and the transmission effect.

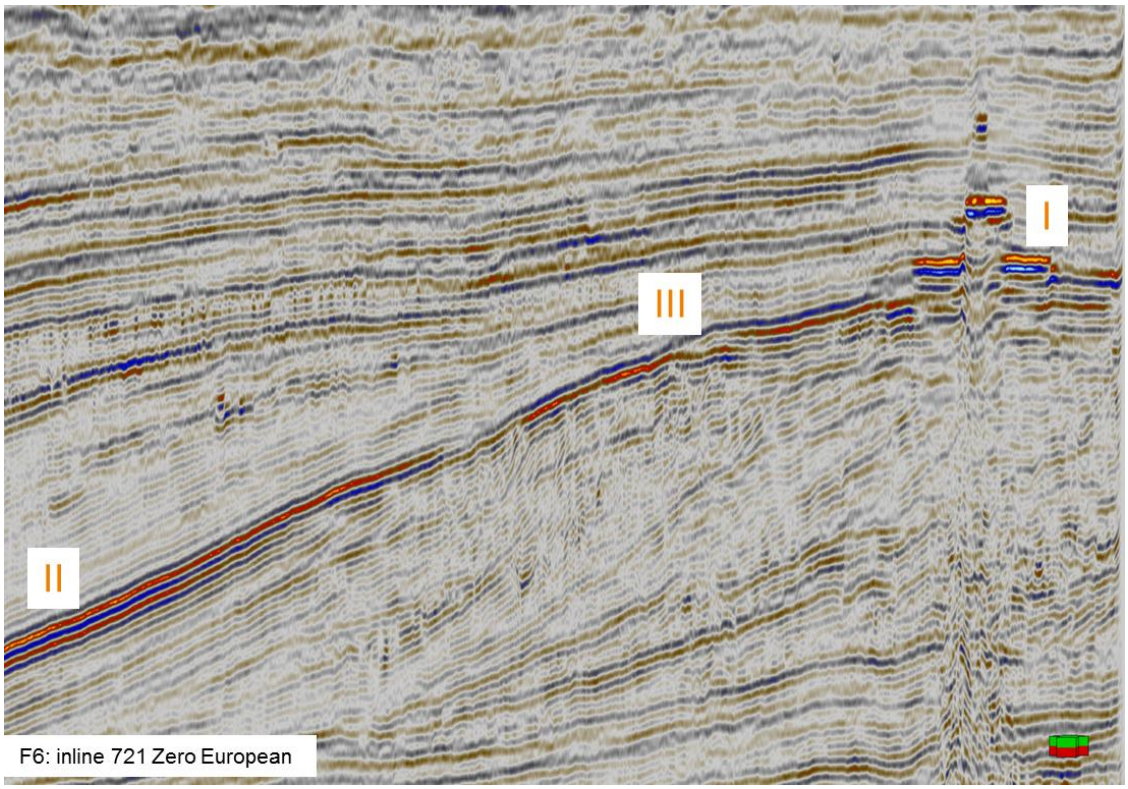

Fig. 7-4. Cross-section showing various bright spots. I) Possible gas bearing strata; all criteria are met since these events have an anomalous high amplitude and a top and base reflector are present. II) Most criteria are met but the natural paring is less pronounced and the amplitude is less high. III) Although this is a bright event, it does not represent a low-impedance gas-filled sand since it has a reversed order (blue over red). This particular case represents a hard shell bank as has been confirmed by well-log description.

7.3 Brigth spot classes

The bright spots (BS) were classified according the criteria put up by EBN (van den Boogaard and Hoetz, 2012) as far as possible. If criteria were not quantifiable, the bright spots were categorised differently. As such, six BS classes were identified:

- Stacked 4 way dip closure — anticlinal, semi-circular closure with ≥2 BS
- Small stacked — any small (< 2 km^2) BS, with ≥2 BS
- Flat medium — single, flat BS, size ≥2 km^2
- Elongated — elongated, single BS associated with sandwaves
- Foreset — BS in inclined clinoform beds
- Other — BS not representing gas sand such as shell banks, gas injectites, etc

The “fault-bounded” class, originally introduced by EBN was dismissed, because theoretically all BS types identified here can be associated with faults. Small stacked- and flat-medium-sized BS tend to occur more often in association with faults (see Chapter 8).

7.4 Name convention

BS are named according the stratigraphic level(s) and the offshore blocks they appear in. The suffix “intra” is used if the BS is within the unit, otherwise “top” is used if the BS coincides with interpreted

top horizon of the unit. Stacked BS within one stratigraphic unit are denoted alphabetically, with “a” always indicating the lowermost BS. Also, the seismic survey in which the BS has been interpreted is indicated. Very large BS that occur in many seismic surveys are not given this identifier. Occasionally, additional remarks are needed to identify the BS.
For example: *S5i_intra_F2_c_Halo_SG field: 3D_F02_F03_Z3RWE1994A* refers to a BS at surface S5i, within block F2, it is the third (“c”) BS in a series of stacked BS, the BS is a halo due to the transmission effect; the BS is within a defined shallow gas field. Examples of (almost) all BS are presented in Annex 2.

7.5 Bright spot database

Based on ABF property model, various properties are attached to the bright spot surfaces. These surfaces cover several cells of the model. Therefore, the mean cell value (or most of in case of discrete properties) of the surface is stored into the database. Other useful properties that relate to dimensions, stratigraphic position or structural settings are put into the database as well. Table 7-1 lists all parameters in the database.

Table 7-1. Bright spot properties stored in the BS database.

Name	The given name which can consist of [Depositional unit] [intra or top] + [Block] [Letter] [Seismic Survey]
TWT	The two way travel time in ms. Min, Max and Mean are provided
Model Lithofacies	1= shale, 2 = silt, 3 = (very fine) sand. Most of value is representative
depofacies with slumps	0 =delta plain fine, 1 = delta plain silt, 2 = Distr Channel, 3 = Starved Slope, 4 = Silty slope, 5 = Sandy slope, 6 = prodelta fine, 7 = Delta toeset, 8 = Delta toeset coarse, 9 = Slumps. Most of value is representative
Delta element	0 = Topset, 1 = Foreset/slope 2, prodelta/toeset. Most of value is representative
PHIE_MEAN_Arithmetic mean (P50)	Modelled effective porosity. Mean of all realisations
PHIE_P10_P90	Difference between the P10 and P90 of the Porosity. The range of the modelled porosity values is indicative for the uncertainty in modelled values
VCL_P50_mean	Modelled Volume of clay / Clay percentage. Mean of all realisations
VCLP10_P90	Difference between the P10 and P90 of the Vcl. The range of the modelled porosity values is indicative for the uncertainty in modelled values
Sw_min	Modelled Sw, Min, Max and Mean of all realisations
Block	The offshore block number
Field	Producing or planned Shallow gas field
2D /3D data	For 3D seismic: the name of the seismic survey. For 2D data: multiple surveys are used
Size	The size of the mapped surface (km2)
Size compensated for holes and transmission effect	When bright spots are stacked the lower bright spots have holes due to the transmission effect. These bright spots are compensated for that. Size in km^2
Stratigraphic interval	The stratigraphic unit (S01-S13)
Brightness	Factor that indicates how bright the bright spot is in respect to its surrounding. (Amplitude of Surrounding) x (Brightness) = (Amplitude of bright spots). Negative numbers are phase reversals
Filled to spill	Based on the seismic interpretation an estimate of the structural spill-point is made. If the BS' extent reaches the spill point it is **assumed** filled-to-spill
Stacked	Bright spots that occur above each other. #1 is the shallowest bright spot
Systems tracts	Highstand Systems tract (HST), Falling Stage Systems tract (FSST), Lowstand Systems tract (LST), Transgressive Systems tract (TST)
% Clay of seal < 8 µm	Percentage of clay as derived from grain size analysis of cuttings or cores
Porosity fraction of seal	Porosity as computed by grain size based method
Permeability (mD)	Permeability as computed by grain size based method
Pore throat radius µm	Pore throat radius computed by grain size based method
Computed Column height	Max. Column height computed by grain size based method
Fault bounded	Is the bright spot bounded at one or more side by a fault?
Above salt dome	Is the bright spot situated above a salt dome?
Chimney related	Is there a chimney below or passing along the bright spot?
Drilled	Is the bright spot drilled? The name of the well(s) are listed
Notes	Notes such as flat spots or phase reversals
EBN classification	EBN made a Bright spot classification.
TNO classification	TNO Bright spot classification
TNO #class	TNO Bright spot classification in numbers
x _	Not determined because brightspot is uninteresting (too small) Data unavailable (not drilled or analysed)

8 Bright Spot data distribution and -integration

8.1 Introduction

The suite of analysis presented in this report, and the results of which as presented in the BS database, are evaluated both graphically and spatially. The first evaluation represents data in pie- or scatters plots and allows to asses general relationships between BS properties and -characteristics. Since the Shallow Gas prospects are situated in a Late Pliocene-Pleistocene prograding deltaic system, it is foreseen that spatial trends in the BS data distribution are more insightful than a graphical representation alone. For the spatial data analysis the BS data and surfaces (polygon outlines) were combined in ArcGIS (these files can be delivered on request). It should be noted that in both methods, bias in interpretation is avoided by cross-plotting all relevant properties and characteristics. Here, only results that are meaningful for a regional assessment of shallow gas potential are presented.

8.2 Graphical BS data distribution

8.2.1 *Relationship BS size and -type and stratigraphy*

Pie-chart representations (Fig. 8-1) of BS size (as percentage of total BS size) per stratigraphic unit show that BS dominate in S5 and S12. The number of BS (as percentage of total BS number) also is highest in S5. Also S6 has a high number of BS, but the total areal extent in this unit is small, illustrating the fact that BS are relatively small compared to those in S5. S12 has a small number of large BS. The large total areal extent of BS in S5 and S12 is caused by the elongated BS type. Note that no BS occur in units S1 to S3.

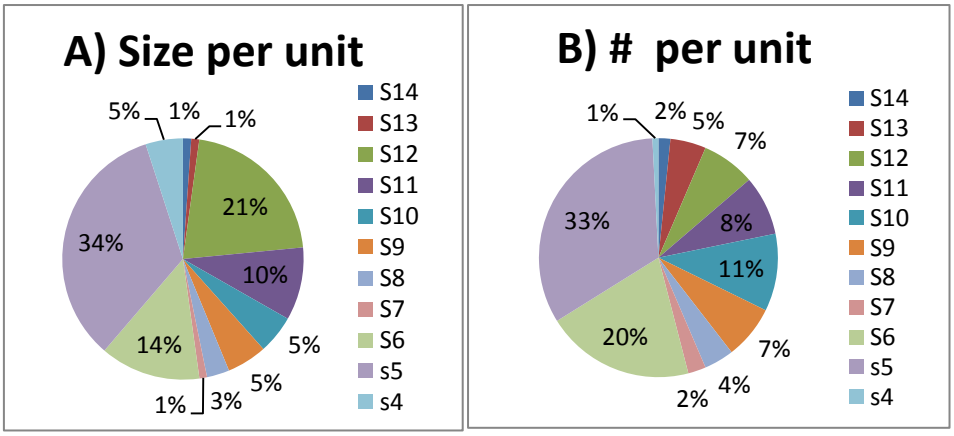

Fig. 8-1. A) Total BS size per stratigraphic unity; B) number of BS per stratigraphic unit.

8.2.2 *Relationship BS type and delta element*

Plotting the number of BS per delta element (not shown) reveals that there is an almost equal distribution, illustrating that the number of BS is not specifically linked to a setting on the delta. A representation of the areal extent of certain BS types per delta element (Fig. 8-2), however, shows that Elongated BS dominate in prodelta setting (at the palaeobasin floor), non-stacked foreset type dominate in the inclined foreset beds, and stacked 4WD BS dominate in the topset beds. Plotting the dominant BS type per stratigraphic level for each delta element reveals that stacked 4WD BS

dominate in topsets of all stratigraphic levels (Fig. 8-2), The foreset type BS, only occur in unit S5 and elongated BS only appear in the prodelta. The delta foresets contain all types of BS.

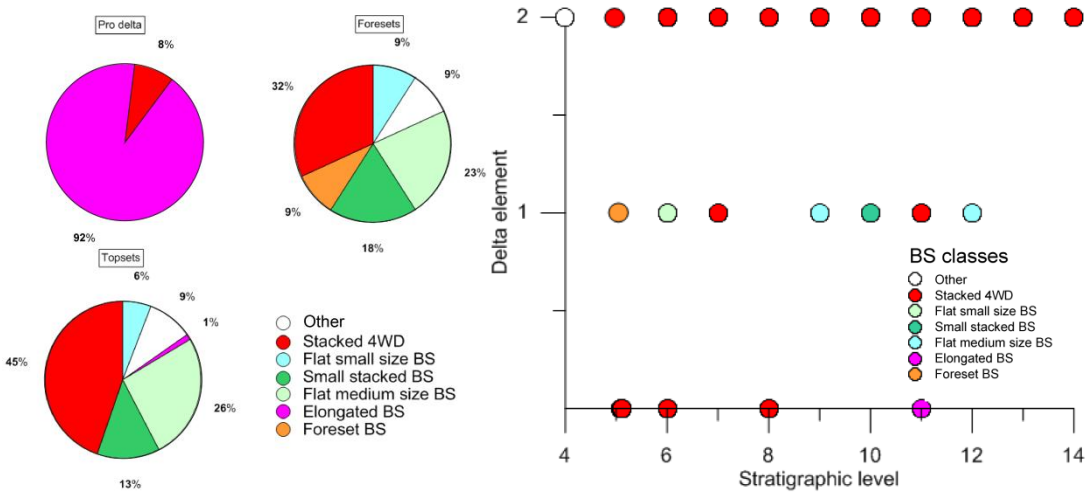

Fig. 8-2. BS type per delta element. Pie chart representation for prodelta, foresets and topsets (left) and scatter plot of delta element per stratigraphic level (right) (0 = prodelta, 2 = foreset, 3 = topset), classified according dominant BS type.

8.2.3 *Relationship BS and depositional facies*

By cross-plotting the BS size against depth and classifying the data according depositional environment enables a further subdivision of the data. First of all the general depth trend of depositional facies occurrences (as seen in the geological model, Fig. 5-12) is nicely represented. Furthermore, it can be seen that the largest BS occur in the prodelta facies (Figure 8-3); these belong to the Elongated BS class, as was also shown in the pie-chart plots of Fig. 8-2.

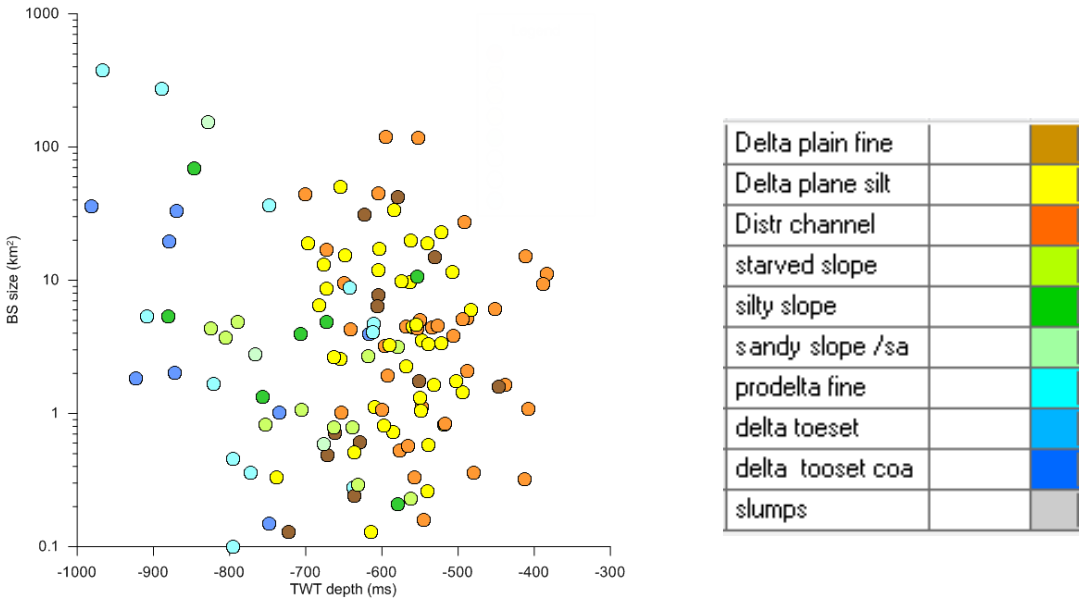

Fig. 8-3. BS size plotted against depth (TWT) classified according depositional facies (with legend).

8.2.4 *Relationship BS size and lithofacies*

If BS size is plotted against stratigraphic level and the data is classified according lithofacies (Fig. 8-4a), it shows that there is a slight tendency of the bigger BS to occur in the finer grained clay and silt lithofacies. It also shows that BS in shallower stratigraphy reside in coarser-grained lithologies whereas BS in clay and silt lithofacies dominate at deeper stratigraphic levels. Fig. 8-4 shows the relationship of BS with depth, again classified according lithofacies. It corroborates that BS at shallower depths reside in coarser sediments and that deeper BS reside in finer-grained sediments. Therefore, the main conclusions from Fig. 8-4 is that the occurrence of BS in a certain lithofacies is strongly coupled to stratigraphy and, due to the prograding and coarsening upward delta system, also to depth. It should be stressed here that BS are not exclusively related to coarser-grained strata, but can also reside in the finer-grained lithologies.

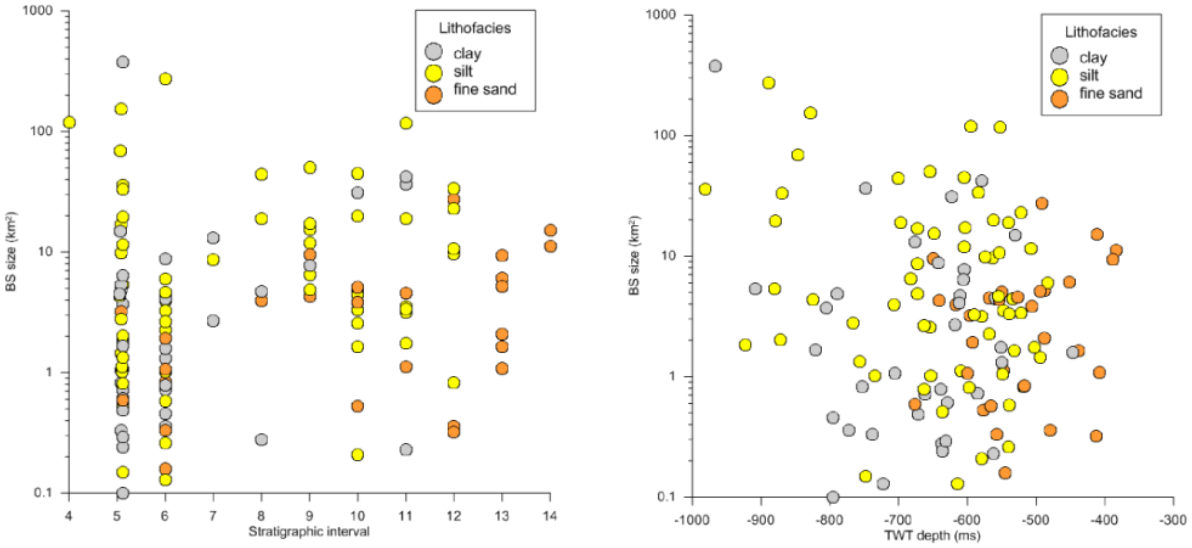

Fig. 8-4. BS plotted against stratigraphic interval (S1-S13 or above), classified by lithofacies (left). BS against depth (TWT) classified by lithofacies (right).

8.2.5 *Relationship BS and porosity (PHIE)*

For all three lithofacies classes the BS' PHIE values are plotted against stratigraphic level, which does not reveal an obvious trend (Fig. 8-5). However, if the PHIE values per BS are plotted against TWT depth (Fig. 8-5) it first of all shows a quasi-linear PHIE/depth trend that is expected to occur due to compaction. Secondly, it shows a relative large amount of (vertical) scatter of PHIE values, indicating that this PHIE-depth relation holds only partly and that lithofacies type plays an important role in the distribution of PHIE as well.

8.2.6 *Relationship BS and faults*

In the database, BS are qualified as either fault-bounded or non-fault bounded. Some fault-bounded BS are associated with salt structures as well. The data distribution shows that fault bounded BS occur especially at lower stratigraphic levels (Fig. 8-6). This trend is expected since most of the observed faults tend to terminate in upper Cenozoic strata, whereas only few reach the seabed. This attests to the fact that some faults may have seized to be active during the Quaternary, or have offsets that are below seismic resolution. Fig. 8-6 shows that flat small size, elongated and foreset BS are in general not related to faults. This is directly related to the fact that these BS types are less often coupled to salt structures and, in turn, to their associated faults.

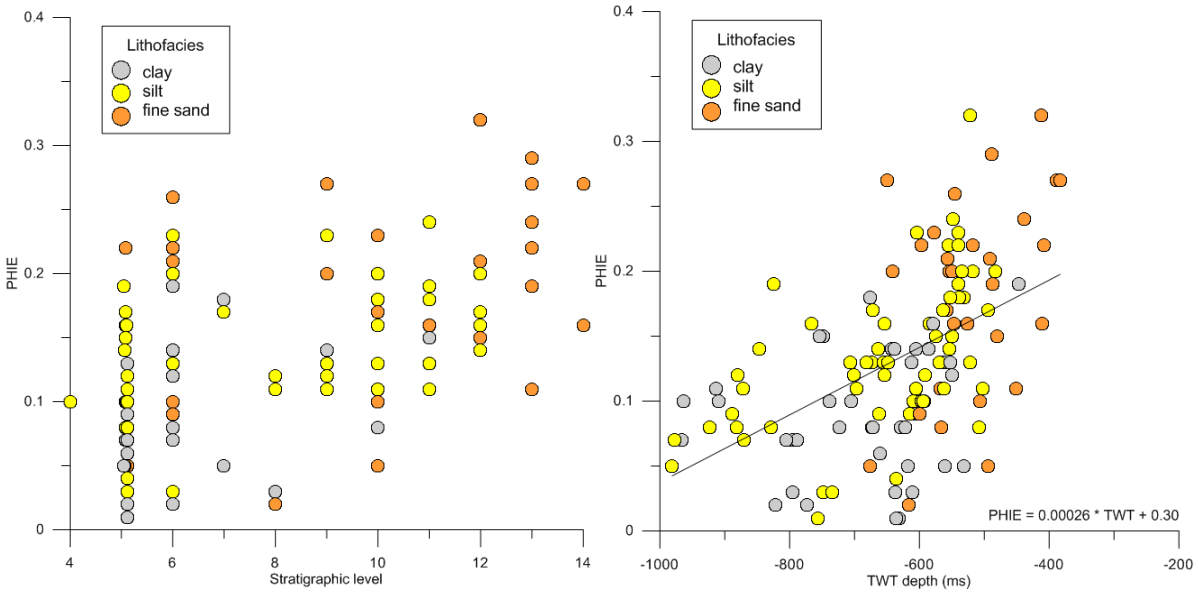

Fig. 8-5. Average PHIE for all BS against stratigraphic interval classified by lithofacies type (left) and BS against depth (TWT) classified by according lithofacies (right).

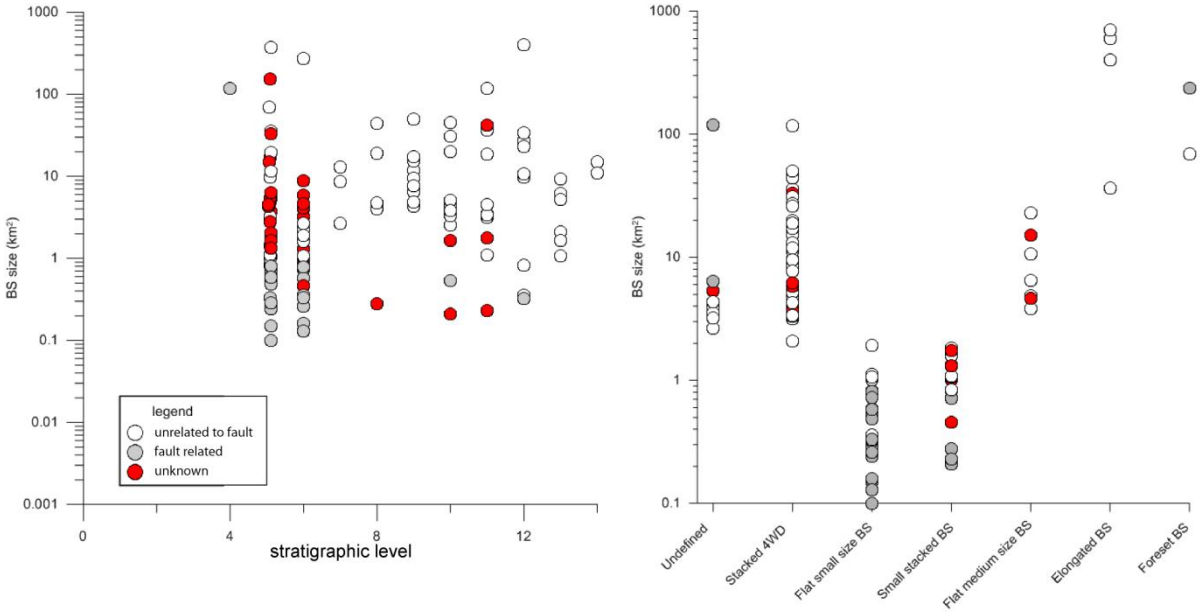

Fig. 8-6. BS size plotted against stratigraphic level, classified by fault influence (left) and BS size against TWT depth, classified by fault influence (right).

8.2.7 *BS relationship with salt*

In the database, BS are qualified as either salt-structure related or non-related. A relationship with salt means that the BS occur vertically above or in close vicinity of a salt structure. No BS have been observed adjacent to salt domes. The data distribution shows that salt-related BS occur throughout the stratigraphic sequence (Fig. 8-7) and at all depths (not shown). This attests to the fact that salt structuration played a dominant role in the formation of (anticlinal) 4WD closures during the Cenozoic. The upward weakening expression of most of these closures illustrates that salt doming occurred syn-

depositionally, i.e. during the deposition of the SNS sediments under scrutiny. Since even strata younger than S13 (referred to as S14 in the plots) show anticlinal structures it is safe to assume that most salt-related traps are very young and therefore salt-related BS potentially occur throughout the studied sequence. Fig. 8-7 shows that flat small size and foreset BS are never associated with salt structures.

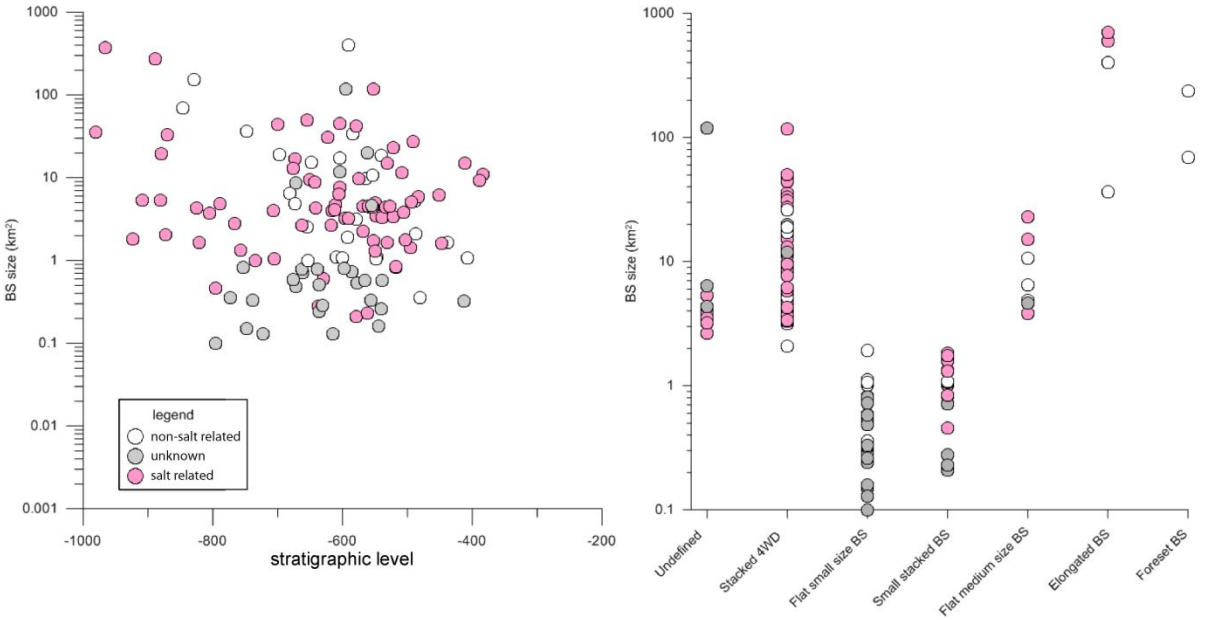

Fig. 8-7. BS size plotted against stratigraphic level, classified by salt influence (left) and BS size plotted against BS type, classified by salt influence (right).

8.2.8 *BS spillpoint*

For all BS the structural spill point has been interpreted from seismic data. Due to the very subtle expression of some of the anticlinal structures (especially in the youngest strata) spill points are sometimes unable define. For those BS that reach a clear spill point it has been assumed that the structure is filled to spill. However, this assumption is unrelated to gas presence or gas saturation and the qualification should be read as “apparent” filled-to-spill. Subsequently, the BS intensity has been plotted against TWT depth and classification was done by the argument “filled to spill” (Fig. 8-8). BS with a negative intensity, i.e. showing a phase reversal (see Fig. 7-1 for explanation), are almost all filled to spill and are associated with salt domes (not shown in graph). The phase reversal cannot be attributed to depth since at similar depths normal BS are present indicating that impedance contrast occur within the “bright-spot”. However, such local phase reversals can be attributed to impedance contrast between clay and well cemented gas-filled layers in the vicinity of salt structures, possibly due to mineral enrichment though brine water expulsion along salt domes. For the normal BS intensities there is an unclear relationship between BS intensity and the structure being filled or not. If the type of BS is considered (Fig. 8-8) it can be seen that both small and large stacked BS dominate the “filled-to-spill class, but that foreset types are not filled to spill. There is a large group, amongst which the elongated BS, for which this classification cannot be made.

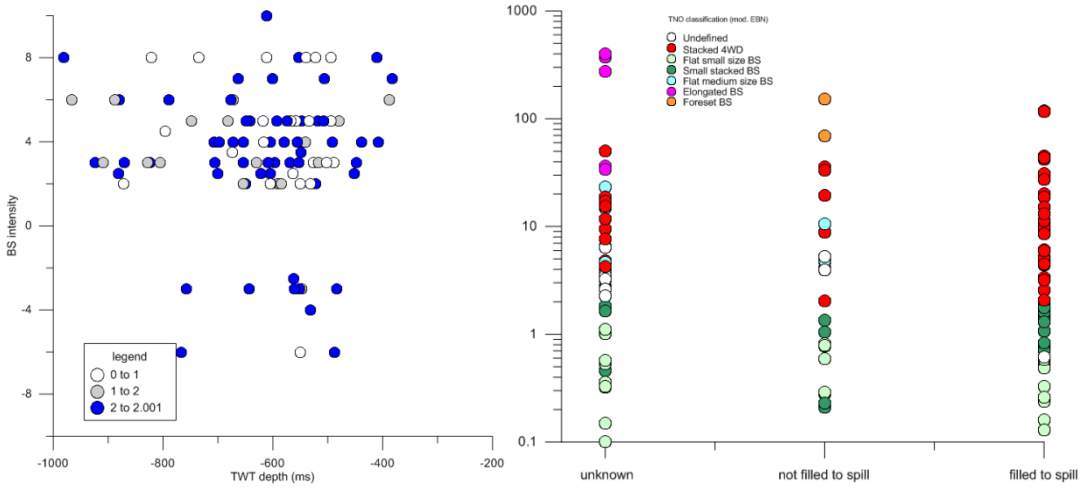

Fig. 8-8. BS intensity (neg is phase reversal) vs depth, classified by the filled to spill argument (blue = ft spill, grey is not ft spill, white is unknown) (left) and BS size vs. filled to spill argument, classified by BS type (right).

8.2.9 *Cross-correlation between BS height and grain size-based gas column height*

Although only a limited number of samples were used for the grain size based method to derive gas-column heights (Chapter 6) a positive relationship exist with the estimated height of the BS based on seismic analysis (Fig. 8-9a). The computed column heights are in reasonable good agreement with column heights derived from NPHI-RHOB cross over plots. Despite the linear trend it is also shown that BS height from seismic analysis tend to overestimate real heights. This may imply that resource estimates are too high if they are based on BS heights only. Moreover, it (once again) stresses the unknown relationship between gas saturation and BS extent or -intensity.

An important follow up suggested by the seal-capacity study is to establish a relation between the clay content derived from grain size analysis data (and indirectly the gas column height) with log derived clay content. Cross-plotting these parameters (Fig. 8-9b) of the limited data available so far, suggests a weakly positive correlation, but underlines the need for further research.

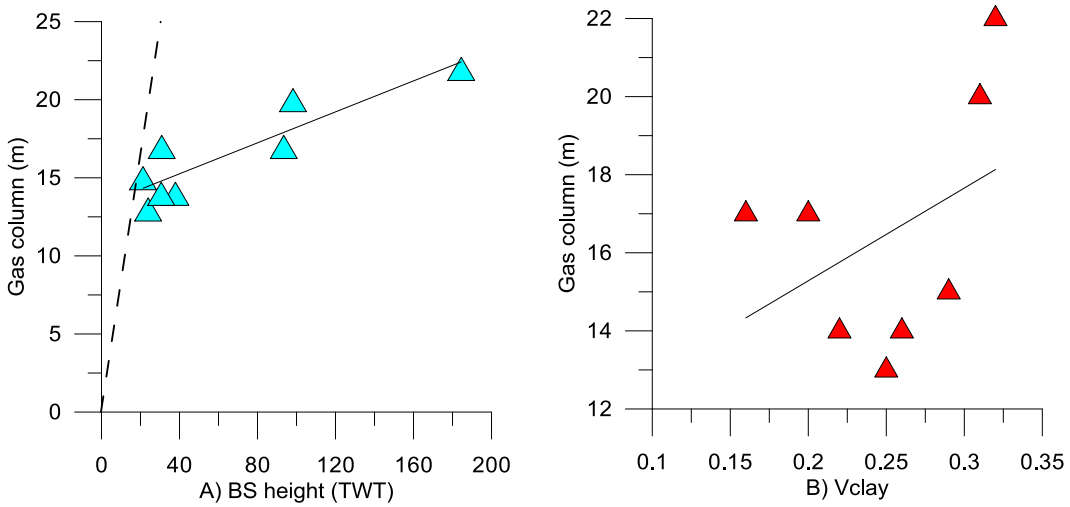

Fig. 8-9. A. BS height plotted against theoretical gas column height based on grain size method with linear fit, for reference dashed line represents Y=X. B) Vclay plotted against gas column height based on grain size method with linear fit.

8.3 Spatial Data distribution

8.3.1 *Relationship BS type and structural setting (faults and salt)*

Fig. 8-10 presents a series of maps of BS type for of all stratigraphic levels, which also show the main structural elements and salt structures of the Dutch subsurface (as presented in Kombrink et al., 2012 and ten Veen et al., 2012). Note that, within the study area, BS are not present in the units S1-S3 and that the maps also show BS in the units overlying S13 (also referred to as unit S14). From the maps it can be inferred that the spatial distributions of Stacked 4WD BS and Flat-small-stacked BS are closely related to salt domes and -ridges. Note that in map view this may not always be visible since stacked 4WD BS sometimes have a wider extent than the associated salt structure. Flat small size BS are more randomly distributed and seem, in general, unrelated to salt. A high concentration of these BS in unit S5 and S6 can be seen in strongly inverted areas across the Dutch Central Graben (DCG), i.e. those areas where parts of the Upper Mesozoic (Cretaceous) sequence is missing. Flat medium size BS can be associated with salt structures but not everywhere as is the case for unit S12 that contains this type of BS above the DCG (salt-related) and on the Elbow Split Platform (naming convention after Kombrink et al., 2012) where the Zechstein salt is virtually absent. Many of the stacked BS are not only salt-related, but also fault-related since the salt structures are delineated larger fault systems as well (Fig. 8-10). Foreset type BS are exclusively related to unit S5 in this study area, although it is known that some BS occur in older units to the east of the current study area. Elongated BS occur throughout the area in unit S5, S6, S11 and S12, and are related to BS in sandwave fields (see ten Veen et al, 2011, for explanation of this BS type). Considering that these have formed in open marine conditions with sufficient sea-bottom current activity, this corroborated the earlier suggestion (See Chapter 3) that during deposition of S11 and S12 a short-lived revival of open marine conditions was invoked by a temporal change in oceanic circulation that caused melting of the existing sea ice cap and possibly pushed the cold arctic surface waters into the proto-North Sea (see Chapter 3). The overall progradational character of the delta system is reflected by the more westward position of the sandwaves of S11 and S12 compared to those of S5 and S6. It appears that most elongated BS are also associated with salt structures: 1) because of their size they tend to overlie salt strucures in map view, but also 2) because in seismic data it is often observed that elongated BS fields are transected by chimneys that emerge from salt domes.

8.3.2 *Relationship BS delta elements and structural setting*

Figure 8-11 shows that BS occur in delta topset, foreset and prodelta environments of throughout all stratigraphic units. A large foreset type BS occurs in S5 foreset delta element in the northeastern sector of the DCG and is also associated with faults and salt structures delineating the DCG. This suggests that the structural setting may have had a large control on the formation of this potential shallow gas trap. The fact that in block F02 both Stacked 4WD and foreset type BS occur alongside (Fig. 8-10; Appendix I), may hint at a charging scenario whereby the gas migrated both vertically and laterally from below. This scenario is further explained in the synthesis of Chapter 9. In the stratigraphically higher units, i.e. S7-S10 and S13-S14, BS only occur in topset beds, whereas S11 and S12 have BS in all three delta elements. If indeed during deposition of S11 and S12 a short-lived revival of open marine conditions occurred (see Chapter 3) this would explain the reoccurrence of all three delta elements in the study area. The dominance of BS in topset beds in units S7-S10 and S13-S14 indicates that the other delta elements lay outside the study area, i.e. further west.

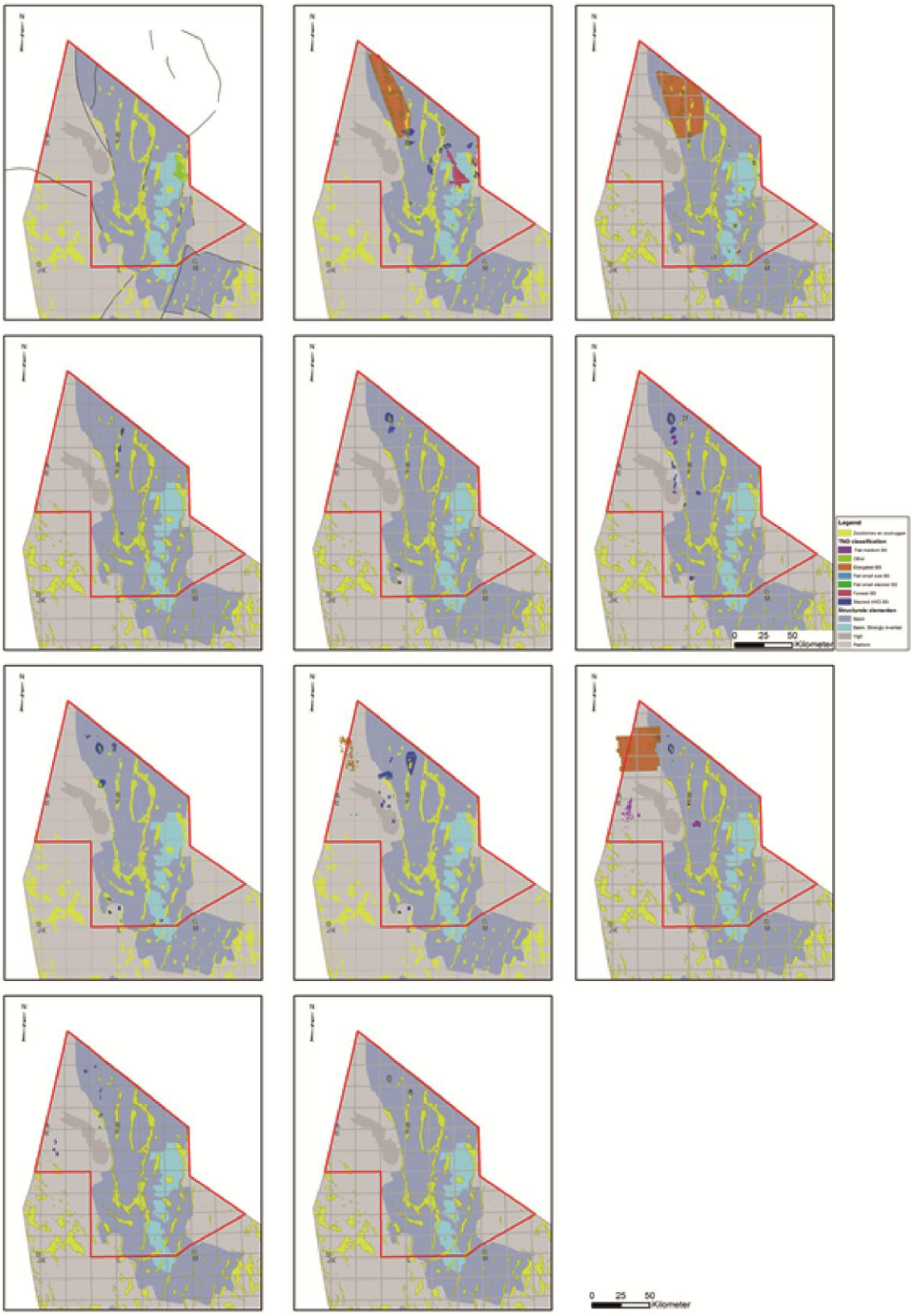

Fig. 8-10. Distribution of BS types projected on structural elements and salt structures in the Dutch, starting from S4 upper left- to supra S13 (or S14) in lower right corner. Larger scale maps are presented in Appendix I.

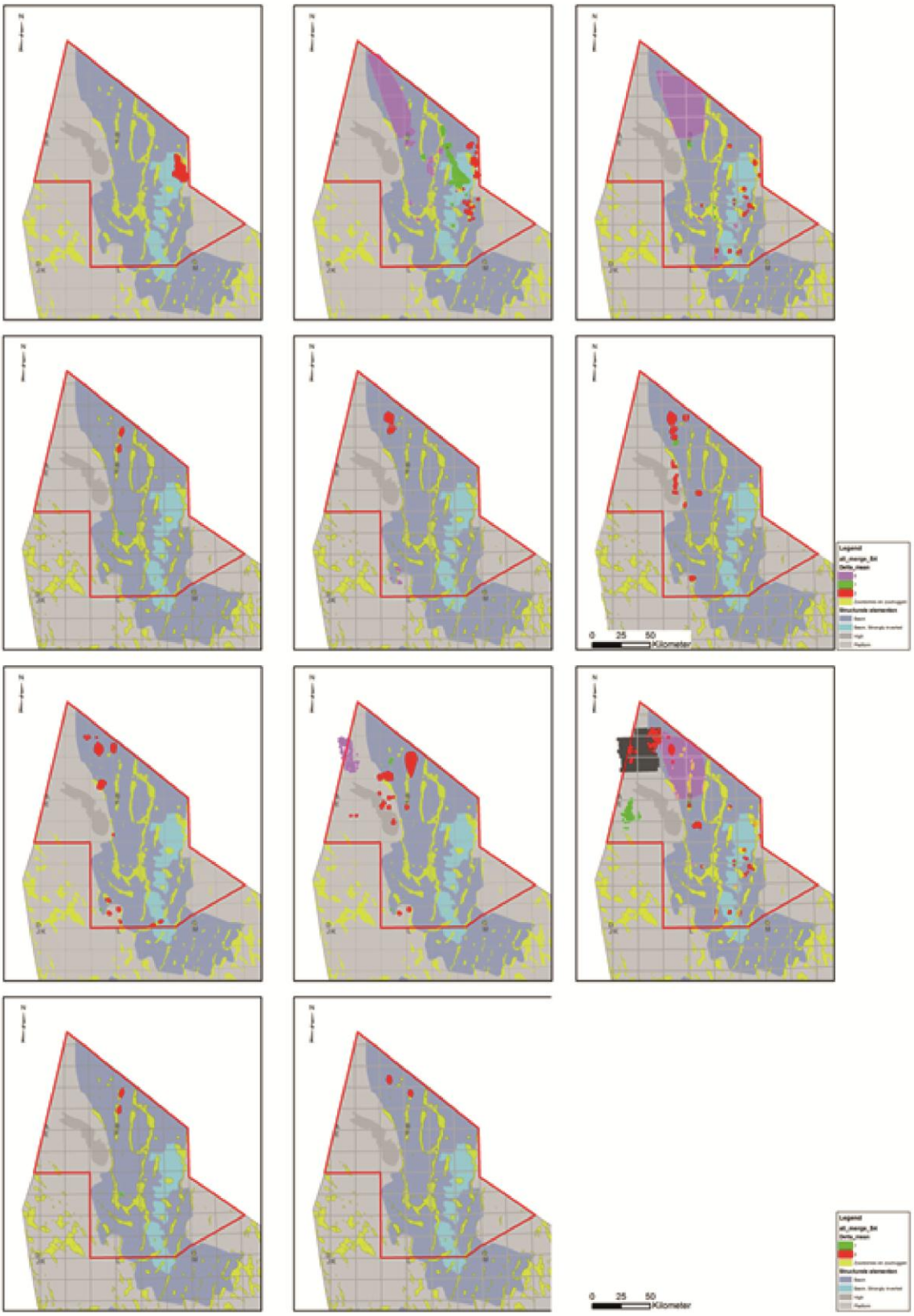

Fig. 8-11. Distribution of BS for S4-S13 indicating the associated delta element (red = top set, green = foreset, purple = prodelta. S4 upper left- to supra S13 (or S14) in lower right corner. Larger scale maps are presented in Appendix I.

8.3.3 *Relationship BS PHIE, Vcl, lithofacies and structural setting*

Figure 8-12 shows the distribution of Vcl for all BS, indicating that in general stratigraphically lower- and easternmost BS have higher clay content. A similar pattern is also shown by the distribution of lithofacies (Fig. 8-12). These observations corroborate the interpretation of the graphical data analysis, which states that the these general trends are related to the progradation and coarsening upward the delta sequence.

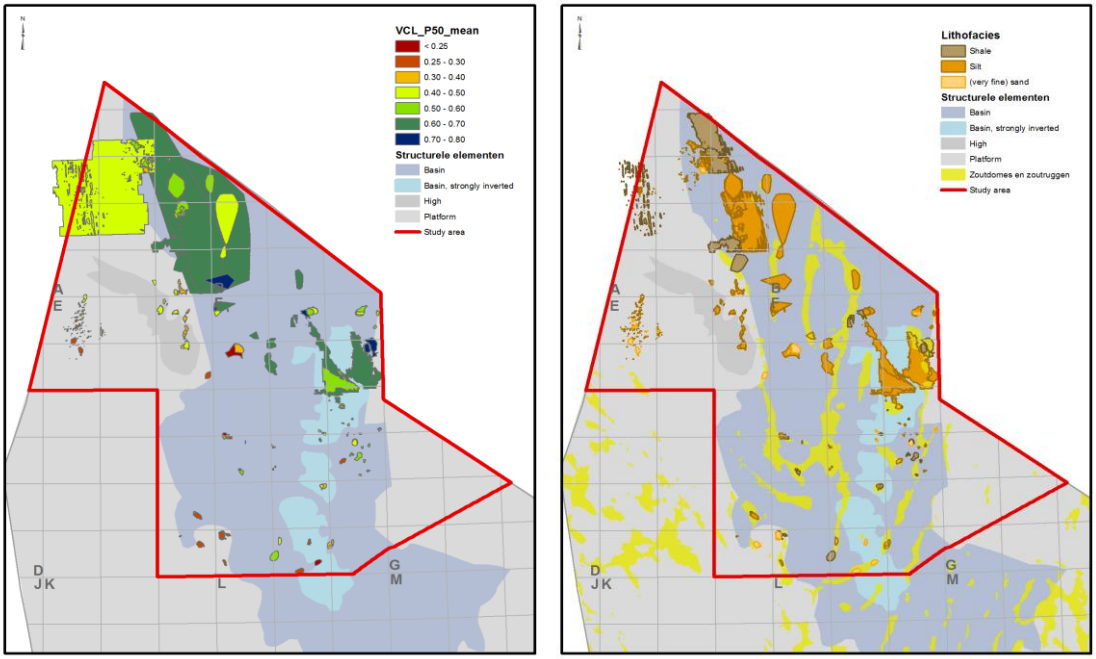

Fig. 8-12. Distribution of BS with VCl (left) and lithofacies (right). For each stratigraphic level, individual larger-scale maps are presented in Appendix I.

8.3.4 *Distribution of BS that are (apparently) filled to spill*

In spite the fact that, based on seismic data, it is difficult to determine if a structure is filled to spill (or to any other level at all), the data distribution (Fig. 8-13) shows that most of these BS occur in the AB and northern F blocks. For many of the flat small-sized BS in the southern F blocks, no inferences can be made on gas fill either.

8.3.5 *Distribution of BS with commercial gas (Sg>30 %)*

For all (data covered) BS per stratigraphic units, maps are presented that qualify the BS for its gas potential, based on gas saturation values. Normally for shallow gas, the following criteria are used:

Gas = Sg > 30 %; Fizz Gas = 30 % <Sg≤ 1.5 %; Water Sg < 1.5 %.

Under shallow, low-pressure conditions, such as apply to the SNS sediments, 5 % gas causes the fizz-water effect to reduce P-wave velocity and impedance (Han and Batzle, 2002). Other studies suggest that this percentage can be as low as 1.5 %. Since, depending on development and production issues, it is hard to state under what conditions the gas present can be considered “economic”, only maps average Sw per bright spot are presented. Figure 8-14 shows that gas saturations (Sg = 1-Sw), in general, are low but reach values up to 40 %. These highest values are reached in the Stacked 4WD BS that corresponds to the B13 gas field and in the one foreset type BS

observed in block F02 has. It should be noted that logging tools and upscaling procedures tend to smooth out high saturation streaks and that values will turn out lower. Another concern is the use of saturation estimates outside gas-bearing structures to estimate (model) the saturation within these structures. Since, a priori, it is not known which BS actually represent gas, a danger resides in averaging the saturation for one BS. This potentially leads to underestimation of values as well. This might be the reason the model Sg values derived from logs that penetrate the B13 field are lower than the actual values. All other BS in the study area plausibly represent gas filled sediment with Sg < 20 %. It would be more safe to only use those saturation values for which it in known that gas is present, for instance, based NPHI/RHOB cross over plots. Such an assessment is presented in Chapter 9.

8.4 Summary of results

- BS with a negative intensity, i.e. showing an amplitude phase reversal are almost all filled to spill (plausibly higher cementation layer above salt dome).

- Both small and large stacked BS dominate the “filled-to-spill class and many of these BS are associated with faults and reside in the AB and northern F blocks. For many of the flat small-sized BS, such as in the southern F blocks, no inferences can be made on gas fill either.

- All stacked and some flat medium-sized and elongated BS are related to salt structures

- Flat small sized BS are neither controlled by faults or salt.

- BS occur in both in delta topset, foreset and prodelta environments.

- Foreset type BS are exclusively related to unit S5 in this study area.

- The delta element is not the main player in defining the BS type and the structural setting has larger control on the formation of potential shallow gas traps.

- The fact that the Stacked 4WD BS dominate in the upper part (topset beds) of the delta sequence, may have to do with better reservoir properties, such as the overall higher PHIE values, as discussed before. The uppermost limit of these salt-related BS lies around 400 m, i.e. no gas is captured here.

- Gas saturations known from well-penetrated BS, in general, are low but reach values up to 40% especially in Stacked 4WD BS and in the one foreset type BS observed. All other BS plausibly represent gas-filled sediment with Sg < 20 %. It should be noted however that both petrophysical- and property modelling techniques applied tend to underestimate Sg.

- Gas column heights based on the grain size based method show a positive relationship with BS height based on seismic analysis. However BS tend to highly overestimate the column height suggesting that a considerable part of the BS represents very low-saturation gas (residual gas) that does not reside in the gas column. If the trap is filled to capillary seal capacity of the mudstone caprock and not to structural spill point, the filled-to-spill criterion for BS appears unreliable measure for reserve estimations.

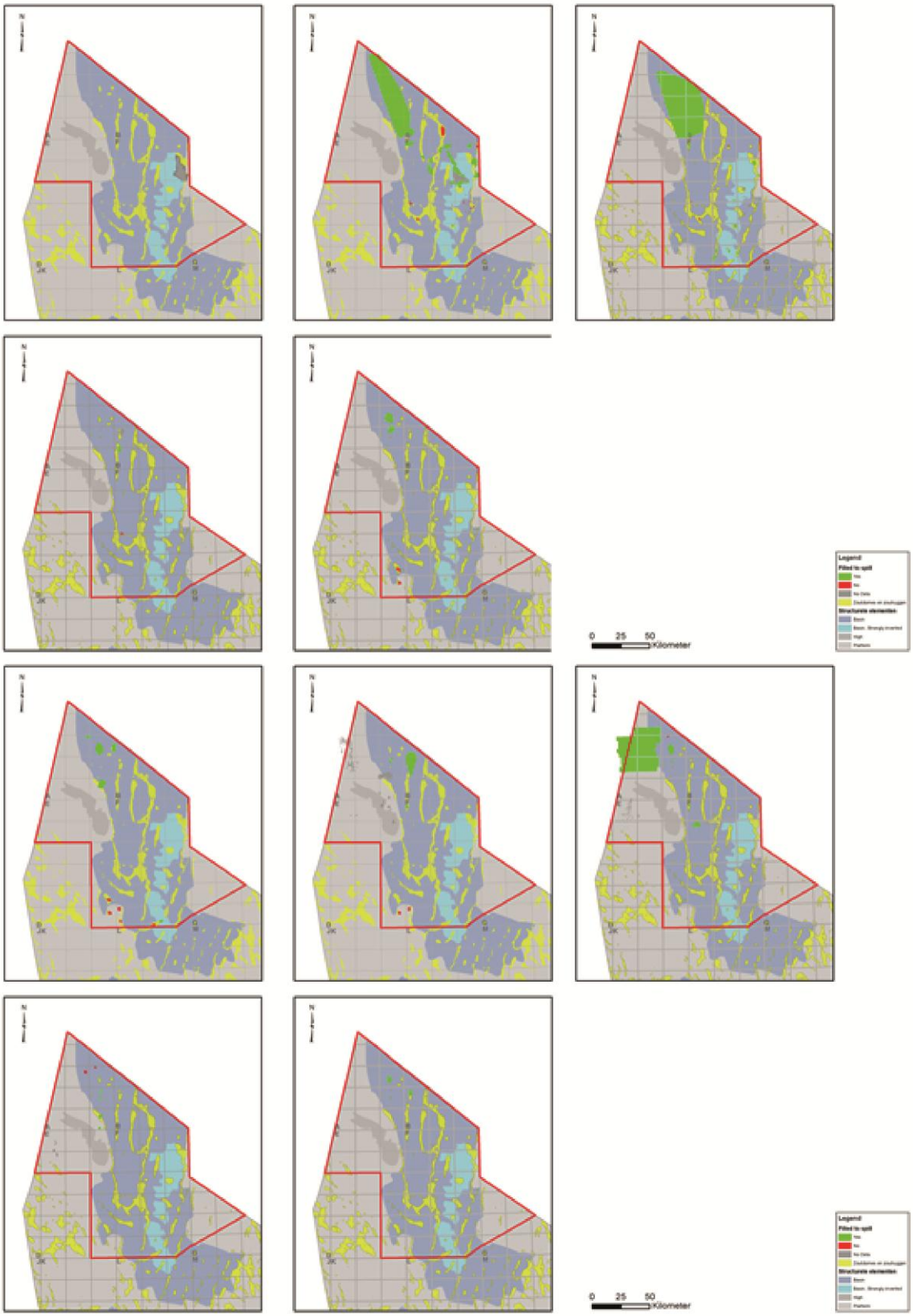

Fig. 8-13. Bright spots that are filled to spill for units S4 (upper left) to S13 (lower right). Larger scale maps are presented in Appendix I.

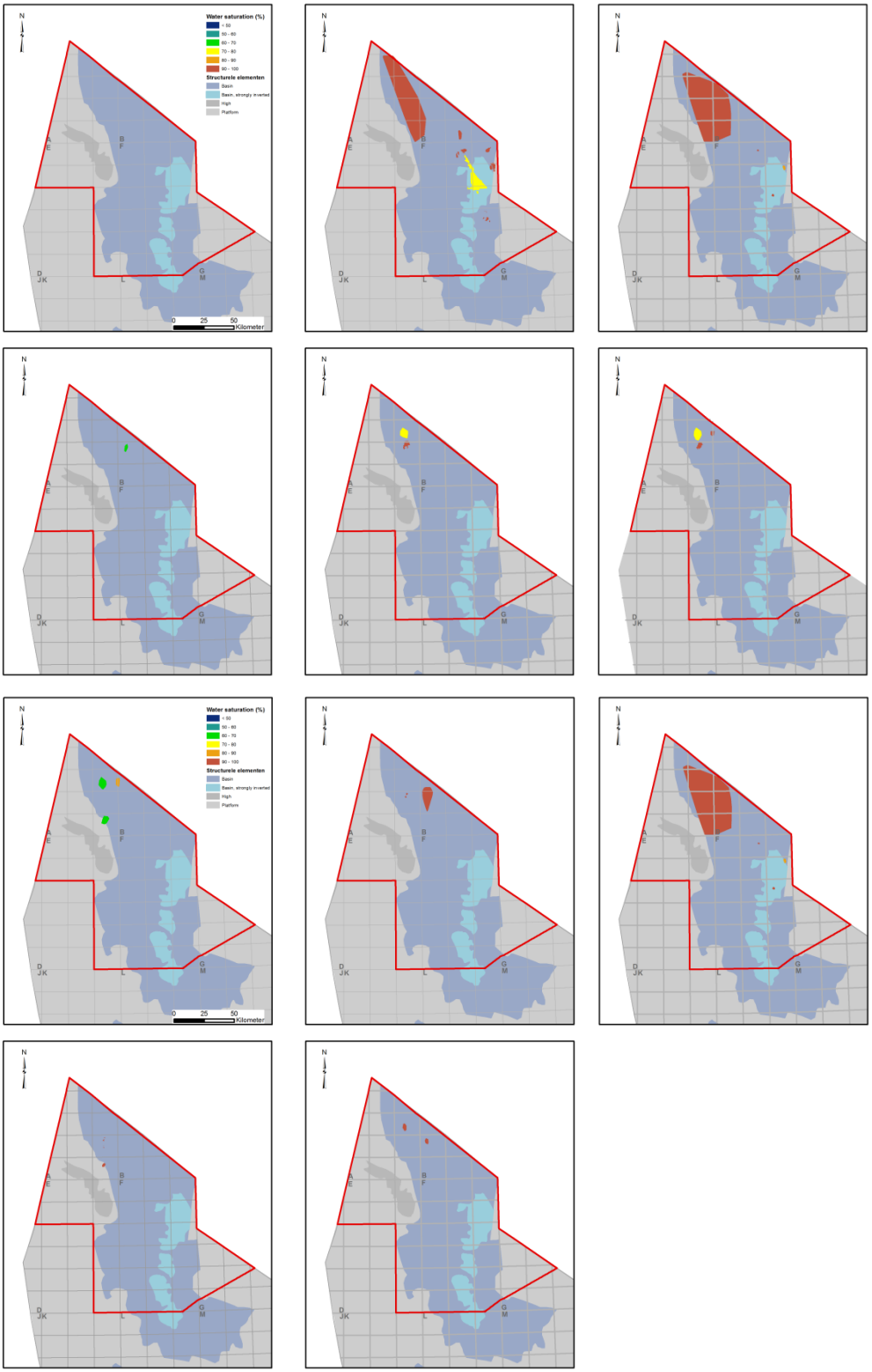

Fig. 8-14. Mean water saturation (Sw= 1-Sg) per Bright spots for units S4 (upper left) to S13 (lower right). Larger scale maps are presented in Appendix I.

8.5 Shallow gas system scenarios

Based on the data distribution presented before, the age- and palaeoclimatic framework provided, and the acquired insights in the seal-integrity of the deposits studied, a synthesis is given here which focuses on scenarios for evolution of shallow gas fields. Some of these scenarios describe the association of BS types, whereas others are described by one single BS type. The presented scenarios serve as “end-members” of a wide range of possible mixtures, which are individually not described in detail individually.

8.5.1 *Scenario 1 – 4WD stacked gas reservoirs associated with foresets*

Although this scenario is inferred for the “S5g top Onlap Extended” BS, it is crucial for understanding the relative timing of events. These very large bright spots in seismic data are interpreted as an amalgamation of foresets type BS and 4WD closures that are locally affected by salt domes and faults (relevant properties for this combined BS are present as part of this synthesis (Fig. 8-14). Based on this association, it is inferred that initial gas migration is importantly linked to chimneys (gas vents) that are associated with these salt domes and associated structures. Initially, the gas migrates upward into a predominantly silty reservoir layer (Fig. 8-14), which in this case is formed by foresets of the S5g forced-regressive wedge. The inclined nature of the foresets controls the gas migration up structure even though the average porosity is low (0.1; Fig. 8-14), up until the limit of the stratigraphic trap (pinch out) is reached and a thick shale layer (locally >100 m) is interpreted as the local permeability seal (see well-log section in Fig. 8-). This seal has been sampled for seal integrity at wells B17-6 and F02-06 to calculate gas column heights. Continued and syn-depositional salt doming is inferred from the upward waning expression of anticlinal closures above the salt domes (progressive angular unconformities or “fanning dips”; Fig. 8-16b-c).

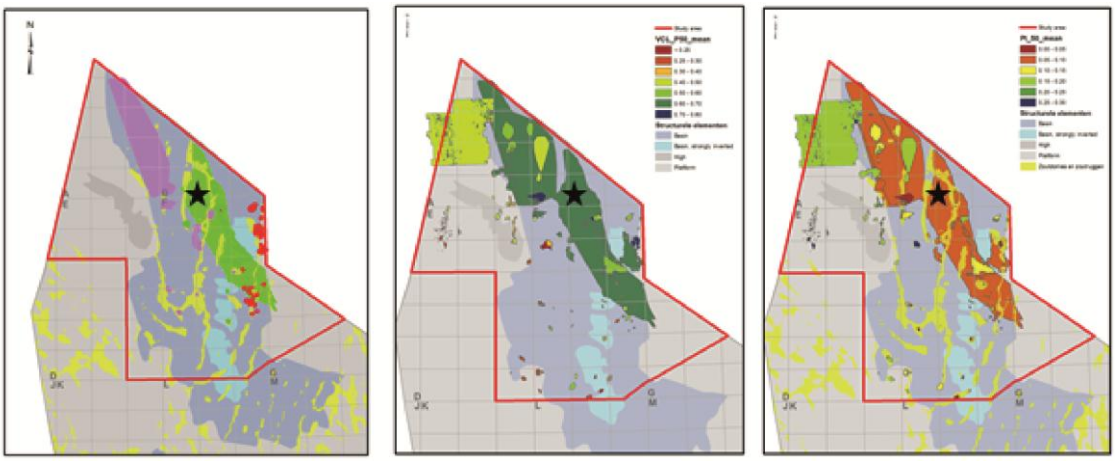

Fig. 8-15. S5g top Onlap Extended” BS (with ★) represented as amalgamation of several BS that cover ~1700 km2 area between blocks F092 and B17. a) Dominant delta element type is foreset (green), b) Mean Vcl = 0,61, c) Mean PHIE = 0,10, Individual maps for the presented BS properties per stratigraphic interval are presented in Appendix I.

Eventually, the doming of salt leads to formation of 4WD closures in the reservoir layer above, which form their own structural spill point. This leads to a disconnection of the gas already in the foreset bed and the gas which is still entering along the salt structure. Now the gas can only migrate upward in the 4WD closure till the maximum gas column height is reached that can be retained by the sealing layer. After that, the seal is breached and gas will enter a higher reservoir layer and accumulate vertically again. The alternation of seals and reservoirs in the S5 unit is strongly controlled by climatic variability at the transition from open marine interglacial- to restricted marine glacial conditions. The interplay of the structural- and palaeoclimatological conditions was essential in creating this shallow-gas field scenario with interbedded reservoirs and seals.
The presence of pockmarks (and elongated, current-transformed pockmarks) on the interpreted stratigraphic surfaces as old as S1 indicate that gas vented at the sea floor during the Plio-Pleistocene. At that time, the shallow water depths and lack of overburden favour conditions of gas leakage due to the high gas expansion factor. In other words, at shallow depths, hydrostatic and lithostatic pressures only differ very little and only very small gas column heights can be retained (stronger seals are needed) compared to conditions at greater depths. If gas migrates into the delta sediments shortly after deposition, presumable a lot of the gas has disappeared at the sea floor. Keeping the gas in a stratigraphic trap would require the thick clay layer above to prevent the gas from escaping vertically. The S5g unit is interpreted as a forced regressive parasequence (lobe) and the thick shales above (unit S5h) are related to the subsequent lowstand (glacial) period during which transport of siliciclastic is limited; Thus the S5g surface represents a correlative erosional unconformity and interfingering between sand of S5g and clay S5h is unlikely. However, lateral sealing conditions at the seismically interpreted pinchout can be easily degraded due to connectivity with sandy layers of the preceding forced regressive wedge(s). Referring to the earlier assumption that the gas must have entered shortly after deposition and the overall low gas saturations in the foreset beds (Fig. 8-17), it is suggested that a lot of gas has disappeared almost immediately after charging and therefore most probably only residual gas is present. The 4WD closures, which have a longer charging history, reached higher gas saturations (see Fig. 8-18) long after the disconnection occurred as structuration prolonged. This is corroborated when the sequential anticlinal build up is regarded, which suggests that most vertical relief was generated between deposition of S5 and S13, i.e., a considerable time after deposition and initial gas charging of the foreset beds.

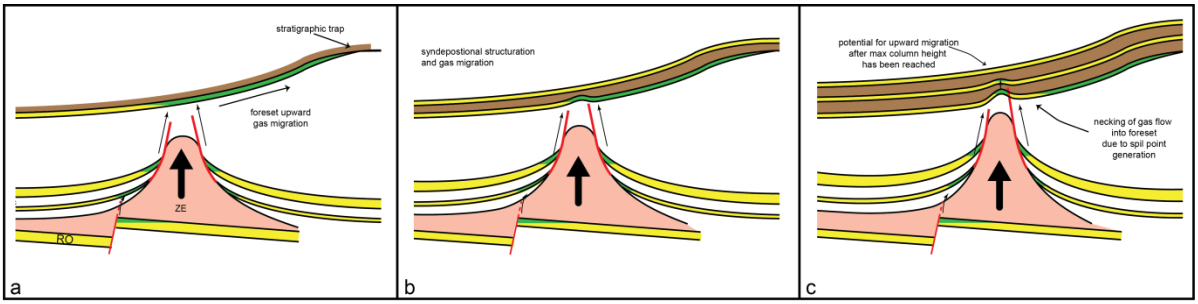

Fig. 8-16. Three-stage evolution of trapping and gas migration for scenario 1 in a roughly SW-NE cross-section. See text for explanation. (representation at approximate location of F09-01 through salt dome).

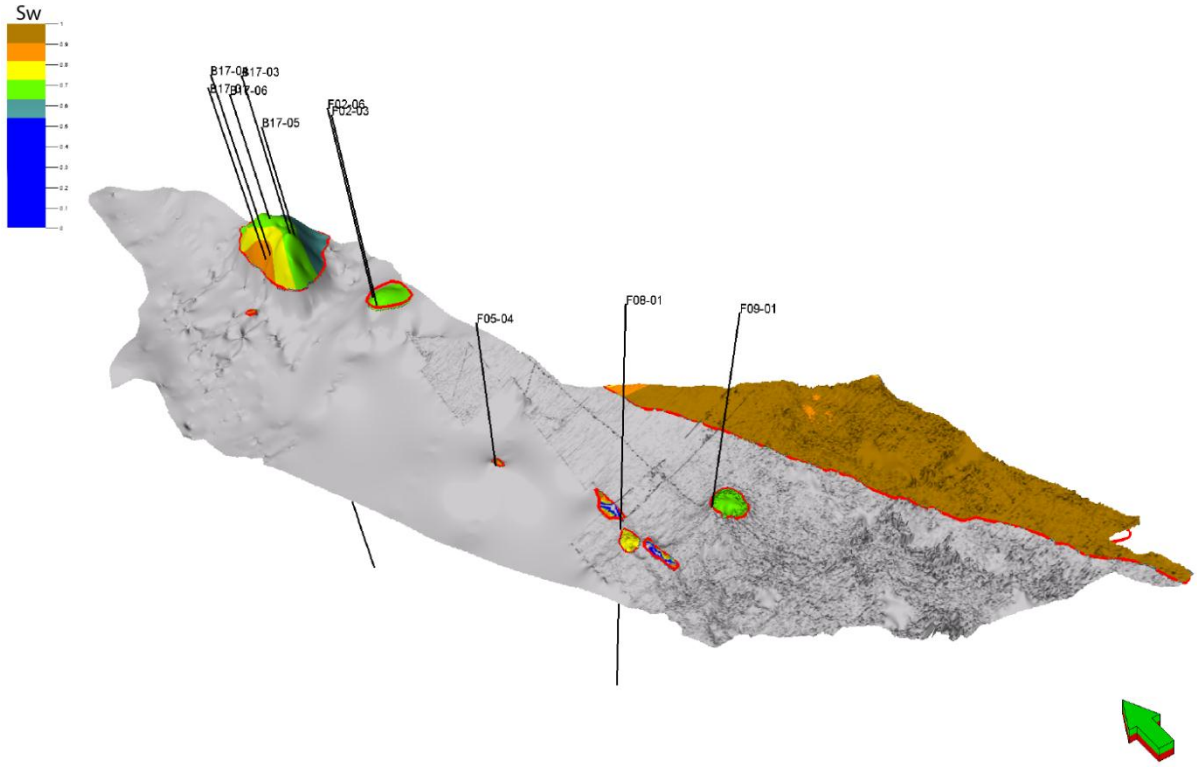

Fig. 8-17. “S5i top Onlap Extended” BS with Sw attribute. Red lines indicate structural spill points within the originally unstructured foreset reservoir bed. Where wells penetrate the structural closure, Sw values were considered representative and used for modelling within the closure; outside the closures the modelled Sw values are not representative. Sw values modelled in the large northeastern closure are not penetrated by wells either and considered unreliable as well. High gas saturation is observed near F08-01, which are fault related.

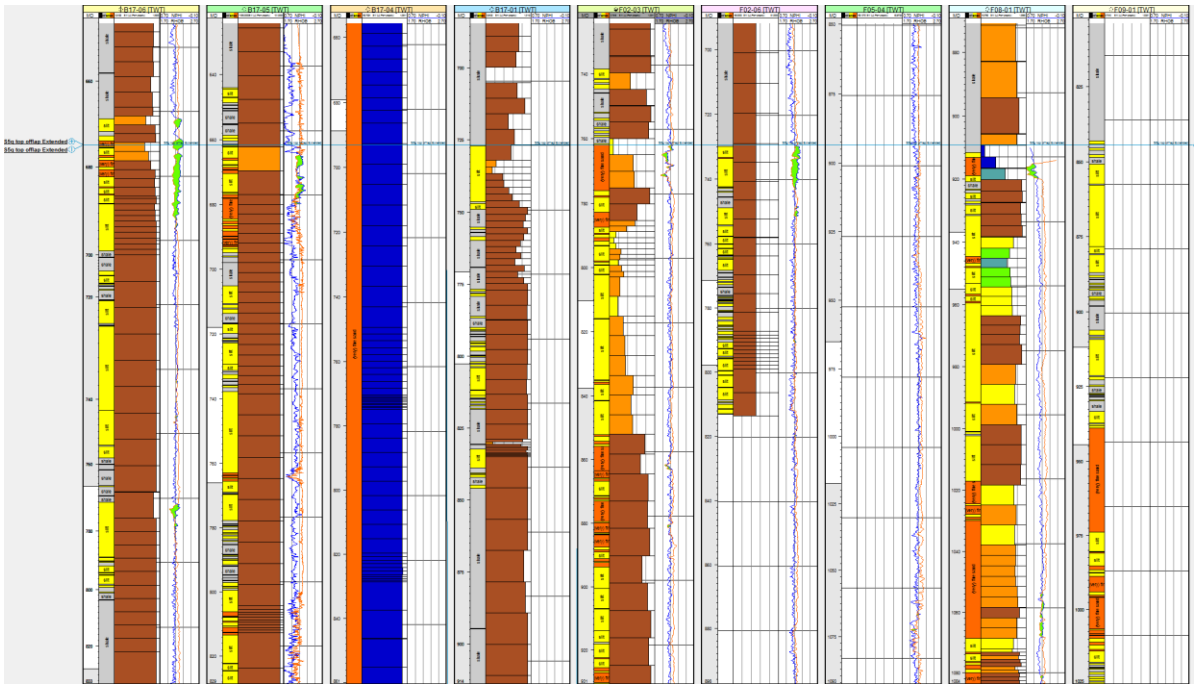

Fig. 8-18. Approximately NW-SE well section with wells penetrating the S5i top Onlap Extended" BS (on which is flattened), as represented in Fig. 8-17, clearly showing the lateral difference in lower- and higher gas saturation areas (represented as upscaled property). NPHI/RHOB crossover plot is shown indicating potential gas in green. Also note that the higher Sg (lower Sw) often occur stacked (corresponding to higher BS that are classified as "Stacked 4WD"). Anomalous low Sw values in B17-04 are due to the casing effect. Colour scale as in Fig 8-17.

8.5.2 *Scenario 2 – Elongated sandwave reservoirs*

This scenario is similar to scenario 1 in that initially the gas migrates laterally away from its structural control. Whereas in scenario 1 the trap is stratigraphically in nature (pinch out geometry), here sandwave bodies became gas filled (Fig. 8-). These traps are referred to as "depositional", since it is not the stratigraphic interrelationship but rather the depositional geometry, in combination with a sealing layer that forms the trap. As postulated earlier, the sandwaves are formed under open-marine conditions by bottom current that are able to "contour" sand into mega dunes of up to 20 m height. Alternation of glacial-interglacial conditions, especially during deposition of S5 and S11-S12, led to periods with and without major siliciclastic input (see ten Veen et al., 2011). Major sand input is association with melt-water runoff during the glacial-to-interglacial transition. During full interglacial and after waning of the main input, sand ridges are created by prevailing contour currents and prolonged winnowing due to contour currents likely produced well-sorted sands which presumably have a high (better-than average) porosity. Siliciclastic input is minor at the interglacial-glacial transition and presumably zero at the full glacial. This is the time that potential sand-wave reservoirs are sealed off by finer grained (suspension load) sediments after which a potential exists for laterally migrating gas to be trapped in the sandwaves (Fig. 8-), explaining the elongated gas BS. Note that all elongated BS are associated with salt structures or transected by chimneys associated with salt domes, making it plausible that gas is sourced from "below", rather than being of local biogenic origin (although a mixed origin cannot be excluded at the moment). As with scenario 1, continued salt doming eventually initiated the formation of an anticlinal trap and at some point the lateral migration of gas was cut off (or strongly diminished). The subsequent stages of trap development are exactly similar to those of scenario 1.

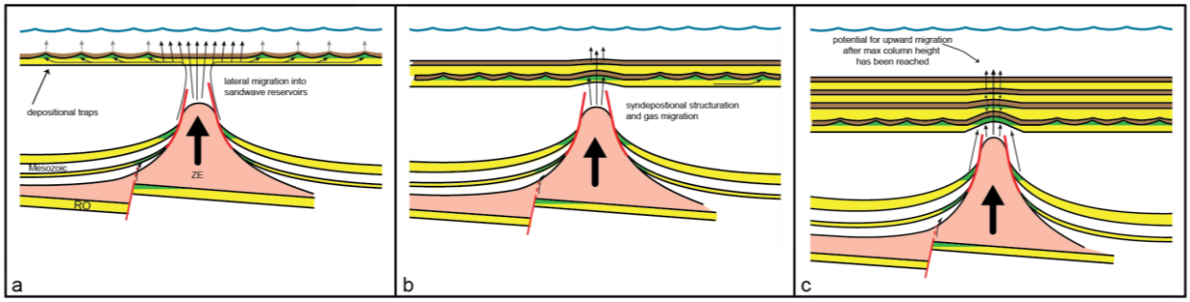

Fig. 8-19. Three-stage evolution of trapping and gas migration for scenario 3. See text for explanation.

8.5.3 *Scenario 3 – 4wd stacked gas reservoirs associated with pro-delta basin floor deposits.*
Initially, this scenario is different than the scenarios 1 and 2, since no early gas trapping in either depositional or stratigraphic traps occurred. Theoretically, any gas that is expelled before the structural trap was formed likely disappeared at the sea floor. Some gas might have been captured in reservoir layers shortly after deposition, but due 1) absence of a trapping geometry and 2) shallow burial depth most of the gas vented out and residual gas remained. This is also demonstrated by the absence of large, flat BS, i.e. BS residing in flat depositional layers. As soon as the trap geometry is formed the evolution of is similar to that of Scenario 2.

8.5.4 *Scenario 4 – pockmark and local vent related gas accumulations*
Pockmarks are a common feature throughout the studied sequence and are key in understanding the shallow gas play. In unit S1 they occur as elongated features with dimensions up to 300 wide, 15 m deep and as long as 1,25 km. Andresen et al. (2008) describe similar features (type B pockmarks) from the Oligocene and Miocene delta sequence of Denmark that also parallel the strike of the identified (shelf) clinoforms. These elongated pockmarks are thought to develop due to fluid expulsion and subsequent erosion by bottom currents. In Denmark, the pockmarks occur above gas-mature Jurassic source rocks, and thermogenic gas is suggested as the main fluid involved in the pockmark formation. The timing of gas expulsion from the Jurassic source rocks in combination with loading imposed to the basin by the progradational Miocene clinoforms are interpreted as the main factors controlling the timing and location of the pockmarks. The pockmarks observed in the S1 unit (Fig. 8-) in the Plio-Pleistocene succession in the Netherlands likely also tell a story of thermogenic gas venting to the surface and palaeocurrents scouring of the seabed. In one particular case, the pockmarks occur right above the F3-FB gas-condensate field in reservoirs of the Upper Jurassic Scuff Group. The severely faulted nature of the Cretaceous and Lower Tertiary deposits above the reservoir might form the pathway for upward fluid expulsion. The orientation of the elongated pockmarks agrees with that of the sandwaves in higher units and are likely formed and modulated by a similar bottom-current system. Also in the Netherland, progradational clinoforms formed the necessary loading that might have triggered the fluid expulsion. Moreover, the MMU consist of a vast network of polygonal faults that might be caused by fluid escape due to sediment loading. To the west, where the thickness of the onlapping units onto the MMU diminishes, this fault pattern and the pockmarks are absent. Thus the pockmarks are crucial for understanding that:

1) Fluid (water and gas) escape occurred already during the deposition of the first progradational delta units (S1).
2) The gas source is thermogenic in origin.
3) Gas was venting at the sealfoor, i.e. no sealing capacity existed initially

4) None of the pockmarks in S1 is associated with BS, suggesting that at some time after S1 deposition the pockmarks might have become sealed off. Also the fact that they are not vertically continuous supports this interpretation.

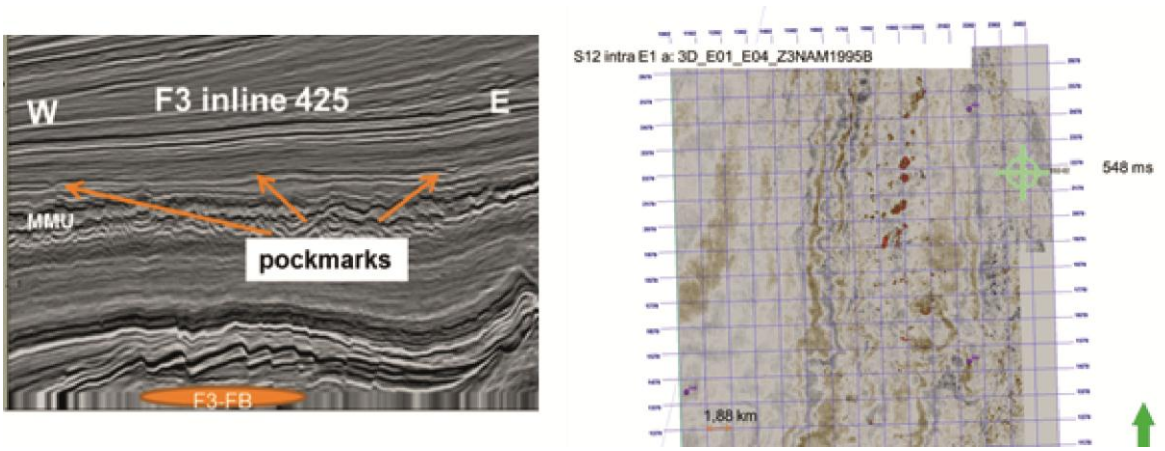

Fig. 8-20. Pockmarks at S1 as seen in seismic section (left) and pockmarks on seismic timeslice through unit S12 in westernmost part of the study area (Elbow Spit Platform) (right).

High concentrations of pockmarks are also very common in unit S11 and S12 (Fig. 8-20). They occur farther west, i.e. where they vertically are less separated from the MMU, due to the progradational westward onlap onto the MMU. The downward extent of seismic chimneys indicates that fluid escape originated as deep as the MMU and may be linked to polygonal fault pattern at this level. Occasionally, the vertical vents led to gas accumulation that are seen on seismic data as the flat medium sized BS, or as small stacked BS. Above the DCG, some small possible gas accumulations are related to salt structures.

There is a marked difference between S1 and S11/S12 pockmarks: Pockmarks in the S11/S12 delta topset beds are associated with vertical chimneys and are stacked, indicating that fluid escape at the seafloor continued for a long period. Pockmarks in S1 are sealed off by deposits of unit S2, no vertical stacking occurred.

Locally, fluid escape occurred along through-going faults and where the fault-juxtaposition or fault sealing is appropriate gas accumulation can be seen a small, flat BS. Basically the mechanism for fluid expulsion is not different than described before. Also pockmarks are commonly observed associated with linear fault, suggesting that fluid escape does not occur over the full length of a fault (e.g. Ligtenberg, 2005.)

9 Conclusions and Recommendations

9.1 Conclusions

- The geological model of the SNS delta in the Dutch ABF blocks is based on seismic horizon interpretation constrained by an excellent chronostratigraphic framework which enables precise coupling to absolute age as is derived from geomagnetic polarity data of well A15-3. The polarity intervals are coupled to the global standard by a number of well calibrated biostratigraphic events, which are traceable throughout the study area in the ABF blocks. Biostratigraphic analysis is performed both on core- and cuttings material, the results of which are considered reliable. In order to extent the biostratrigraphic coverage lower-quality literature data is incorporated, which supports the regional model but is not of high enough quality to accurately QC the seismic intepretation.

- On a regional scale the delta sequence represent a progradational and aggradational unit that progressively fills accommodation of the Plio-Pleistocene North Sea Basin and which is characterized by overall shallowing and coarsening upward. Based on paloeclimatological proxies, the delta sequence can be subdivided into three main groups that represent markedly different climatological conditions. The basal units (MMU-S4) represent a Shallowing Sequence deposited in times of Temperate Climate. The middle unit (S5-S7) marks the onset to colder conditions and is characterized by alternation of Warm and Cold Periods. The highest units (S8-S13) represent sedimentation under Arctic conditions. This is shown by the presence of well-developed clay-silt rhythms that coincide with variations in TOC and palynological indexes, which, through their link with the oxygen isotope record, are clearly linked to glacioeustasy. The glacial-interglacial cycles show a marked contrast in grain size, sea surface temperature and climate and are the key control on the presence and distribution of potential sealing clays and coarser-grained reservoir units.

- Within each of the three units identified, several parasequences are recognized based on combined seismic interpretation and biostratigrahic analysis. Individual parasequences (geomodel zones) show a strong coupling with glacial-interglacial climate cycles; this holds in particular for the middle unit (S5-S7). More importantly, these parasequences relate to specific depositional palaeoenvironments. The oldest sequences represent open marine (prodelta) conditions whereas the youngest represent fluvial conditions (delta topset), which corroborates the overall progradational geometry as observed in seismic data.

- The geological “surface” model of the SNS delta in the Dutch ABF blocks was used to construct a property model (a grid- or voxel-based model) by applying internal layering to the parasequences identified such that the model approximates the anatomy of the delta interval studied. This internal layering of delta clinoforms only appeared successful if the guidance by interpreted horizons is sufficient. To that extent, within some (S3 and S5) parasequences additional internal horizons were seismically interpreted.

- Property modelling has been performed on a number of petrophysical well logs and calculated properties. The PHIE and Vclay lithological properties obtained by petrophysical evaluation are used unchanged and have been used to define the lithofacies property. Sw/Sg values as calculated by petrophysical evalution can less straightforwardly by applied to populate the geological model, since saturations outside gas-bearing strata can never be applied to predict the saturation inside a prospect.

- Property distribution throughout the model has been performed using a combined Stochastic – Deterministic approach. Populating a regional property model with relatively low data coverage requires input of geological knowledge (the deterministic part). The stochastic part involves data distribution based on both vertical and horizontal data statistics (as expressed in variograms)

- Next to lithological properties, a delta element type is defined on the basis of horizon geometry, sequence stratigraphic interpretation and seismic attribute information of palaeomorphological features. The delta element interpretation is used to populate the entire geological model with topset, foreset and toeset elements and adequately mimics the internal organisation of the units defined.

- The prograding and coarsening upward nature of the delta interval studied is reflected by the vertical development of all properties. The (lateral) distribution of PHIE and Vclay for individual units is not that clearly related to distribution of delta elements and depositional facies. This latter observation suggests that those lithofacies classes forming potential shallow gas reservoirs and those clay-rich layers forming potential seals are not exclusively related to a certain position on the delta. This has direct implications for understanding the distribution of bright spots.

- Uncertainties in the property modelling are assessed by applying Sequential Gausssian Simulation procedures, which provides statistics for the modelled property. The calculated uncertainties (represented as P10-P90 range) only relate to the reproducibility of the property with the algorithm and input variograms applied.

- The uncertainty is importantly related to data density and tends to be high in the west of the model area (D and E blocks) where well data density is lower than in the A,B and F blocks.

- A systematic approach using grain size analysis data was found to be a promising methodology for estimating petrophysical properties (porosity, permeability, pore throat) and capillary seal capacities of the mudstones.

- The developed workflow to estimate sealing properties of mudstones provides a new relationship between pore-throat size and permeability of mudstones can be established based clay on content and depth.

- The applied grain size based method to calculate capillary seal capacities provides reasonably good estimates of maximum gas column heights for mudstone layers in the Plio-Pleistocene delta deposits, however some considerable misfits suggest the relation is not straightforward.

- Knowing that capillary seal capacity is a multi-scale property, and that mudstones also act as permeability seals and faulting and fracture zones crossing the mudstones influence the sealing capacity, the presented grain size-based method should be seen as a first phase of a more comprehensive approach to estimate preserved gas columns in bright spots in the Plio-Pleistocene delta in offshore Netherlands and in its distribution area outside the Netherlands.

- A total of 134 bright spots (BS) were mapped based on seismic amplitude anomalies. The BS can be grouped according 6 classes, i.e., 1) stacked (>2) anticlinal 4-way-dip-closures, 2) Small (< 2 km^2) stacked BS, 3) Flat medium-sized (≥ 2 km^2) single BS, 4) Elongated, single BS associated with sandwaves, 5) Foreset BS, and 6) other (non classigfiable) BS.

- All BS were assigned properties from the property model and have numerous other attributes, which are listed in a database. Based on these BS data and the position of the BS within the studied delta sequence certain rules emerge:

    1) Elongated BS dominate in prodelta setting (at the paleo basin floor), non-stacked foreset type dominate in the inclined foreset beds, and stacked 4WD BS dominate in the topset all stratigraphic levels, Foreset type BS, only occur in unit. The presence of BS seem unrelated to depostional setting, the type, however, is strongly controlled by the structural setting, which appears to have dominant control on the formation of potential shallow gas traps. The only exception to this rule is the Foreset type BS in S5.
    2) Many of the small- and large stacked BS in the ABF blocks are associated with salt structures and/or faults. These BS types often appear “filled-to-spill as the BS reaches the structural spill point. However, gas column heights, either calculated using the grain size method or measured from cross-over plots or RFT data, show that many traps are not filled to structural spill point. Trap heights generally are several tens of meters, whereas the trap can only be filled to maximum seal capacity, which does not seem to exceed 20 m, assuming the seal is a capillary seal.Thus, the filled-to-spill criterion for BS appears unreliable measure for reserve estimations since large parts of the BS may not represent high-saturation gas and a reliable relationship between gas saturation and BS intensity cannot be established yet.
    3) The occurrence of BS in a certain lithofacies is strongly coupled to stratigraphy and, due to the prograding and coarsening upward delta system, also to depth. It should be stressed here that BS are not exclusively related to coarser-grained strata, but can also reside in the finer-grained lithologies. The overall coarsening upward trend explains that the prolific stacked 4WD BS dominate in the upper part of the delta sequence, where porosities are overall higher. The uppermost limit of these salt-related BS lies around 400 mi.e. no gas is captured here.
    4) Most flat- and small-sized BS are neither controlled by faults or salt.
    5) Gas saturations known from well-penetrated BS, in general, are low but reach values up to 40 % especially in Stacked 4WD BS and in the one foreset type BS observed. All other BS plausibly represent gas-filled sediment with Sg < 20 %. It should be noted however that both petrophysical- and property modelling techniques applied tend to underestimate Sg.

- Based on several shallow gas play scenarios presented, it can be inferred that most traps are formed after 2.44 Ma (in between deposition of S5 and S13), sub-surface fluid (incl. gas) flow and –venting is active throughout the depositional history of the delta and high Plio-Pleistocene sedimentation rates quickly changed sealing capacity during burial. Therefore, the shallow gas play may be considered a highly dynamic petroleum system that has been active for at least ~ 2-3 Myrs. This inference has direct implications for the economic potential of the shallow gas occurrences, since it suggests, based on the above-mentioned conditions, a theoretical window can be defined where all conditions are favourable. Such window hints at deeper occurring structural (4WD) traps that are more favourable for building-up gas columns and where capillary seal capacity (due to depth) is sufficient.

- Where thick clays layers act as permeability seals, the depth-related capillary seal integrity plays less of a role and gas may be trapped even at shallower depths. The elongated BS, potentially representing gas-filled sandwaves, may be the example of such scenario. These only occur when sand-wave formation was followed by long-lasting clay deposition during

glacial periods of diminished coarser-grained riverine input. Such a scenario is typical for transitional climates with both glacial and interglacials alternating and as represented by S5 and S11/S12.

9.2 Recommendations for follow up

The following topics are of importance in follow-up phases of the here presented research. That should be focused on a more comprehensive approach to estimate preserved gas columns in bright spots in the Plio-Pleistocene delta deposits:

9.2.1 *Estimating gas saturation*

Problem: In derisking BS, gas saturation is the most critical parameter. Although an attempt was made to derive gas saturation values based on petrophysical analysis, the results are only to be used at the well site and cannot be extrapolated across the boundaries of potential gas-bearing structures. Nonetheless, obtained values at wells penetrating known gas fields show higher values suggesting there is value in the method applied, but it should be noted that values are generally underestimated.
Recommendation: More rigorous approaches and techniques should be sought for to estimate gas saturation values. Several techniques might be applicable:

1) As recommended by ten Veen et.al. (2011) AVO analysis should be performed on pre-stack seismic data. Whether seismic data can indeed support the estimation of high saturation versus low saturation shallow gas accumulations depends for a large part on the underlying rock physics and theoretically, this is possible through AVO analysis, but in practice this has never been tested due to the lack of pre-stack data. AVO / Elastic Impedance Inversion has the best potential for discriminating porosity from saturation effects, since substitution of hydrocarbons for water will result in a lowering of bulk density and an increase in shear-wave velocities (Vs).
2) Whereas (post-stack) seismic data is particularly good at mapping geological formation structures and volumes, gravity data is directly sensitive to density anomalies. A combined use of these two methods may turn out to be a suitable tool for discriminating between high saturation and low saturation gas occurrences at shallow to intermediate depth, up to 1.5 km.
3) Controlled-source electromagnetics, in theory, is a potential tool for detection of free gas, which is based on the relationship between gas saturation (Sg) and resistivity (Ω). The technique has the potential to detect low saturations as well, but major draw-back is the rapid decay of electromagnetic fields with depth, i.e. the deeper the gas-bearing layer the thicker it should be. Before acquisition can take place, feasibility studies should focus on generating simple systematic model to see the if CSEM method could be beneficial or not. With the property model at hand (including information on porosity, estimated gas saturation, thickness of the gas bearing layers and the layers in between, depth of the individual layers, lithology, resistivity etc.) it is relatively easy to predict the CSEM effect and thus to make recommendations future CSEM acquisition set ups.

9.2.2 *TDcon*

Problem: The presented geological model and its derivative, the property model, are presented in TWT. Main reason is that the seismic data is characterized by numerous velocity anomalies caused by shallow gas. Therefore, tying the seismic to the wells is extremely difficult. Converting the seismic surfaces to depth with VELMOD II was not considered since this model has a single velocity for the entire Upper North Sea group and is therefore too simplistic for a deltaic sequence with both vertical and lateral variations in thickness and lithology's. Therefore, it was decided to tie the wells to the seismic data and the wells are converted to time (TWT).

Recommendation: To perform a proper Time-to-depth conversion the VELMOD II approach should be extended to also include the internal layering of the SNS delta.

9.2.3 *Property modelling*

Problem: Uncertianty analysis should consist of the assessment of reproducibility (precision) and accuracy. Due to computing-time limitiations the accuracy was not calculated. Due to the relatively low data density (many well were evaluated, but average well spacing is in the order of tens of kilometres) compared to the dimensions of the constructed model it is predicted that accuracy is low. In other words, in applying a blind well-test the property modelling input parameters will be relatively unsuccessful of reproducing the well data

Recommendation: For regional models accuracy can assessed by blind-well testing using a lower density version of the property model to reduce computation time. Such approach would at least give a quantitative estimate of the accuracy. Alternatively, a small selecton of the model is used for such analysis.

9.2.4 *Capillary Seal capacity*

Problem: The uncertainty in calculating capillary seal capacity of mudstones is not quantifiable

Recommendation: Quantification of the uncertainty in the calculation of the capillary seal capacity requires further testing of the method over a larger study area at carefully selected locations where the previously listed conditions for a reliable evaluation are fulfilled to a large extent. This would involve new detailed sampling of mudrock seals overlying shallow gas reservoirs not filled to spill point. The now available new Petrel model of the Plio-Pleistocene delta and its properties in combination with the BS classification provide the necessary information for a careful selection of sampling locations allowing a more rigorous evaluation of the grain size-based calculation of capillary sealing of the mudstones.

Problem: The regional potential of upscaling the grain size based method to estimate capillary seal capacity of mudstones is currently unknown.

Recommendation: The upscaling approach should involve different steps, such as:

1) Additional sampling and grain size analysis. The information in the Petrel model enables systematic sampling of seals in different stratigraphic/facies positions and representing different – good as well as failed – gas reservoirs.
2) Creation of synthetic geologic models for representative stratigraphic and structural trap types (based on bright spot classification).
3) Populating the sealing layer of these synthetic trap types with properties resulting from the sampling and grain size based method (porosity, permeability, pore throats, capillary pressures).
4) Calculation/simulation of equilibrium gas column heights for different trap types and different properties of sealing lay ers
5) Upscaling of results

Problem: No evident relationship exists between petrophysically derived clay content (Vclay) and clay content measured from grain size analysis. To bridge this knowledge cap, it would be interesting to make the method more widely applicable to establish a relation between the clay content derived from grain size analysis data with log derived clay content.

Problem: The applied grain size based method to calculate capillary seal capacities and thus gas column heights shows some considerable misfits with measured heights.

Recommendation: This requires fulfilment of a set of subsurface conditions with regard to charging and leaking of shallow gas reservoirs and the availability of measured data (e.g. pressure data, or reported GWC).

9.2.5 *Shallow gas system scenarios*

Problem: The charging and leakage history of mapped traps as represented in several shallow gas system scenarios and the estimated permeability and capillary seal capacity was found to be important to evaluate the seal characteristics and related presence of gas accumulations. However, this history is largely unknown.

Recommendation: The Petrel Model provides an excellent opportunity to visualize the evolution of the Plio-Pleistocene delta in time in relation to the evolution of its properties (such as porosity, permeability, temperature) and gas charging and leakage of BS locations by using basin modelling approaches.

10 References

Andresen, K.J., Huuse, M., Clausen, O.R., 2008. Morphology and distribution of Oligocene and Miocene pockmarks in the Danish North Sea - implications for bottom current activity and fluid migration. Basin Research 20, 445-466.

Anell, I., Thybo, H., Rasmussen, E., 2012. A synthesis of Cenozoic sedimentation in the North Sea. Basin Research 24, 154-179.

Aplin, A.C., Macquaker, H., 2011. Mudstone diversity: origin and implications for source, seal, and reservoir properties in petroleum systems. AAPG Bulletin 95, 2031-2059.

Baumann, K.-H., Huber, R., 1999. Sea-surface gradients between the North Atlantic and the Norwegian Sea during the last 3.1 M.y.: comparison of sites 982 and 985. In: M.E. Raymo, E. Jansen, P. Blum, T.D. Herbert (Eds.). Proceedings of the Ocean Drilling Program, Scientific Results 162, 179-190.

Benvenuti, A., Kombrink, H., ten Veen, J.H., Munsterman, D.M., Bardi, F., Benvenuti, M., 2012. Late Cenozoic shelf delta development and mass transport deposits in the Dutch offshore area – results of 3D seismic interpretation. Netherlands journal of Geosciences 91, 591-608.

Berg, R.R., 1975. Capillary pressures in stratigraphic traps. AAPG Bulletin 59, 939-956.

Bernard, B., Brooks, J.M., Sackett, W.M., 1978. Light hydrocarbons in recent Texas continental shelf and slope sediments. Journal of Geophysical Research 83, 4053-4061.B.M.

Bernard, B.B., Brooks, J.M., Sackett, W.M., 1976. Natural gas seepage in the Gulf of Mexico. Earth Planetary Science Letters 31, 48-54.

Bijlsma, S., 1981. Fluvial sedimentation from the Fennoscandian area into the north-west European basin during the late Cenozoic. Geologie en Mijnbouw 60, 337-345.

Boreham, C.J., Hope, J.M., Hartung-Kagi, B., 2001. Understanding source, distribution and preservation of Australian natural gas: A geochemical perspective. APPEA Journal 41, 523-547.

Brown, 2010. Interpretation of Three-Dimensional Seismic data, 7th Edition, AAPG Memoir 42, SEG Investigations in Geophysics, No.9 pp 646.

Bujak, J.P., Mudge, D.C., 1994. A high-resolution North Sea Eocene dinocyst zonation. Journal of the Geological Society of London 151, 449-462.

Cameron, T.D.J, Bulat, J., Mesdag, C.S. 1993. High resolution seismic profile through a Late Cenozoic delta complex in the southern North Sea. Marine and Petroleum Geology 10, 591-599.

Cameron, T.D.J., Stoker, M.S., Long, D., 1987. The history of Quaternary sedimentation in the Uk sector of the North Sea Basin. Journal of the Geological Society 144, 43-58.

Clausen, O.R., Gregersen, U., Michelsen, O., Sorensen, J.C., 1999. Factors controlling the Cenozoic sequence development in the eastern parts of the North Sea. Journal of the Geological Society, London 156, 809-816.

Claypool, G.E., Magoon, L.B., Lorenson, Th.D., Lillis, P.G., Kaplan, I.R., 2001. Natural gas in the Great Valley of California – Geochemical characterization and petroleum systems. Paper 8902. AAPG Annual meeting 2001.

Costa, L., Davey, R., 1992. Dinoflaggelate cysts of the Cretaceous system. In: A.J. Powell (ed.). A stratigraphic index of dinoflaggelate cysts. Chapman & Hall, London, 99-153.

Daza Cajigal, V., 2012. Sampling and particle size analysis by Laser Diffraction technique. Internship report. Politecnico di Torino, Department of Environment, Land and Infrastructure_ DIATA, 24 p.

De Gans, W., 2007. Quaternary. In: T.E. Wong, D.A.J. Batjes, J. De Jager (eds.). Geology of the Netherlands. Royal Netherlands Academy of Arts and Sciences, Amsterdam, 173-196.

De Haan, H., Godderij, R., van Hulten, F., Scheffer, B., 2010. Unconventional gas in the Netherlands. PGK lecture, 21. April 2010, (abstract: http://www.pgknet.nl/archive/past_lectures/3).

De Schepper, S., Head, M.J., S. Louwye, S., 2009b. Pliocene dinoflagellate cyst stratigraphy, palaeoecology and sequence stratigraphyof the Tunnel-Canal Dock, Belgium. Geol.ogical Magazine 146, 92-112.

De Schepper, S., Head, M.J., 2009a. Pliocene and Pleistocene dinoflagellate cyst and acritarch zonation of DSDP Hole 610A, eastern North Atlantic. Palynology 33, 179-218.

Dolfing, J., Larter, S.R., Head, I.M., 2008. Thermodynamic constraints on methanogenic crude oil biodegradation. The International Society for Microbial Ecology (ISME) Journal 2, 442-452.

Donders, T.H., Weijers, J.W.H., Munsterman, D.K., Kloosterboer-van Hoeve, M.L., Buckles, L., Pancost, R.D., Sinninghe Damsté, J.S., Brinkhuis, H., 2009. Strong climate coupling of terrestrial and marine environments in the Miocene of northwest Europe. Earth and Planetary Science Letters 281, 215-225.

Downey, M.W., 1984. Evaluating seals for hydrocarbon accumulations. AAPG Bulletin 68, 1752-1763.

Fensome, R.A., Williams, G.L., 2004. The Lentin and Williams index of fossil dinoflagellates. College Park: American Association of Stratigraphic Palynologists.

GCA-Geochemische analysen, 1997. Analyses of adsorbed gases from cuttings of well B17-06. (report available at www.nlog.nl; retrieved June 2011) .

Gibbard, P.L., West, R.G., Zagwijn, W.H., Balson, P.S., Burger, A.W., Funnel, B.M., Jeffery, D.H., de Jong, J., van Kolfschoten, T., Loster, A.M., Meijer, T., Norton, P.E.P., Treece, R.C., Rose, J., Stuart, A.J., Whiteman, C.A., Zalasiewicz, J.A., 1991. Early and Early Middle Pleistocene correlations in the southern North Sea Basin. Quaternary Science Reviews 10, 23-52.

Gradstein, F., Ogg, J., Smith, A., 2004. A geologic time scale, Cambridge University Press, 589 pp.

Han, D., Batzle, M., 2002. Fizz water and low gas-saturated reservoirs (in offshore technology). Leading Edge (Tulsa, OK), 21, 395-398.

Head, I.M., Jones, D.M., Larter, S.R., 2003. Biological activity in the deep subsurface and the origin of heavy oil. Nature Vol 426, 344-352.

Heilmann-Clausen, C., 1985. Dinoflaggelate stratigraphy of the uppermost Danian to Ypresian in the Viborg 1 borehole, central Jylland, Denmark. C.A. Reitzels, Copenhagen, 69 p.

Horstad, I., Larter, S.R., 1997. Petroleum migration, alteration and remigration within Troll field, Norwegian North Sea. AAPG Bulletin 81, 222-248.

Huisman, D.J., Klaver, G.T.H., 2007. Heavy minerals in the subsurface: Tracking sediment sources in three dimensions. Developments in Sedimentology 58, 869-885.

Huuse, M., 2002. Cenozoic uplift and denudation of southern Norway: Insights from the North Sea basin. Geological Society, London, Special Publications 196, 209-233.

Huuse, M., Clausen, O.R., 2001. Morphology and origin of major Cenozoic sequence boundaries in the eastern North Sea Basin: top Eocene, Near-top Oligocene and the mid-Miocene unconformity. Basin Research 13, 17-41.

Huuse, M., Lykke-Andersen, H., Michelsen, O., 2001. Cenozoic evolution of the eastern North Sea Basin – new evidenc from high-resolution and conventional seismic data. Marine Geology 177, 243-269.

Ingram, G.M., Urai, J.L., Naylor, M.A., 1997. Sealing processes and top seal assessment. In: Møller-Pedersen, P., Koestler, A.G. (eds). Hydrocarbon seals: Importance for exploration and production. NPF Special Publication 7, 165-174.

James, A.T., Burns, B.J., 1984. Microbial alteration of subsurface natural gas accumulations. The AAPG Bulletin 68 (8), 957-960.

Knox, R.W.O.B., Bosch, J.H.A., Rasmussen, E.S., Heilmann-Clausen, C., Hiss, M., De Lugt, I.R., Kasińksi, J., King, C., Köthe, A., Słodkowska, B., Standke, G., Vandenberghe, N., 2010. Cenozoic. In: J.C. Doornenbal, A.G. Stevenson, (Eds.), Petroleum Geological Atlas of the Southern Permian Basin Area. EAGE Publications, 211-223.

Kombrink, H., Doornenbal, J.C., Duin, E.J.T., den Dulk, M., van gessel, S.F., ten Veen, J.H., Witmans, N., 2012. New insights into the geological structure of the Netherlands; results of a detailed mapping project. Netherlands Journal of Geosciences, 91: 419-446.

Konert, M., Vandenberghe, J., 1997. Comparison of laser grain size analysis with pipette and sieve analysis: a solution for the underestimation of the clay fraction. Sedimentology 44, 523-535.

Köthe, A., 2003. Dinozysten-Zonierung im Tertiär Norddeutschlands. Revue Paläobiologie 22, 895-923.

Kuhlmann, G., 2004. High resolution stratigraphy and palaeoenvironmental changes in the southern North Sea during the Neogene — an integrated study of Late Cenozoic marine deposits from the northern part of the Dutch offshore area. Ph.D. thesis, Utrecht University, Geologica Ultraiectina, Mededelingen van de Faculteit Aardwetenschappen, No. 245, 205 pp.

Kuhlmann, G., de Boer, P.L., Pedersen, R.B., Wong, Th.E., 2004. Provenance of Pliocene sediments and paleoenvironmental changes in the southern North Sea region using Samarium–Neodymium (Sm/Nd) provenance ages and clay mineralogy. Sedimentary Geology 171, 205-226

Kuhlmann, G., Langereis, C., Munsterman, D., van Leeuwen, R.J., Verreussel, R., Meulenkamp, J., Wong, T., 2006. Chronostratigraphy of Late Neogene sediments in the southern North Sea Basin and palaeoenvironmental interpretations. Palaeogeography, Palaeoclimatology, Palaeoecology 239, 426-455.

Kuhlmann, G., Langereis, C.G., Munsterman, D., van Leeuwen, R.-J., Verreussel, R., Meulenkamp, J.E., Wong, T.E., 2006b. Integrated chronostratigraphy of the Pliocene–Pleistocene interval and its relation to the regional stratigraphical stages in the southern North Sea region. Netherlands Journal of Geosciences 85, 19-35.

Kuhlmann, G., Wong, T.E., 2008. Pliocene palaeoenvironmental evolution as interpreted from 3D-seismic data in the southern North Sea, Dutch offshore sector. Marine and Petroleum Geology 25, 173-189.

Kurtev, K.D., Böker, U., Drews, M., Abrakasa, S., Aplin, A.C., 2012. Leaky top seals – Evidence, rates and mechanisms. Extended Abstract. 3rd International conference on fault and top seals – From characterization to modelling, Montpellier, France, 1-3 October 2012.

Larter, S.R., Di Primio, R., 2005. Effects of biodegradation on oil and gas field PVT properties and the origin of oil rimmed gas accumulations. Organic geochemistry 36, 299-310.

Larter, S.R., Head, I.M., Huang, H., Bennett, B., Jones, M., Aplin, A.C., Murray, A., Erdmann, M., Wilhelms, A., Di Primio, R., 2005. Biodegradation, gas destruction and methane generation in deep subsurface petroleum reservoirs: an overview. In: Doré, A.G. and Vining, B.A. (eds).

Petroleum geology: North-West Europe and Global perspectives – Proceedings of the 6th Petroleum Geology Conference. Published by the Geological Society London, 633-639.

Ligtenberg, H., 2005. Detection of fluid migration pathways in seismic data: implications for fault seal analysis. Basin Research 17, 141-153.

Lourens, L., Hilgen, F., Shackleton, N.J., Laskar, J., Wilson, D., 2004. The Neogene Period. In: F. Gradstein, J. Ogg, A. Smith (Eds.), A geologic time scale, Cambridge University Press, 409-440.

Luterbacher, H.P., Ali, J.R., Brinkhuis, H., Gradstein, F.M., Hooker, J.J., Monechi, S., Ogg, J.G., Powell, J., Röhl, U., Sanfilippo, A., Schmitz, B., 2004. The Paleogene Period. In: F.M. Gradstein, J.G. Ogg, A.G. Smith (eds.), A Geological Timescale 2004. Cambridge University Press, United Kingdom, 384-408.

Maystrenko, Y.P., Bayer, U., Scheck-Wenderoth, M., 2012. Regional scale structural role of Permian salt within the Central European Basin System. Geological Society London Special Publication. 363, 409-430.

Miller, K.G., Kominz, M.A., Browning, J.V., Wright, J.D., Mountain, G.S., Katz, M.E., Sugarman, P.J., Cramer,B.S., Christie-Blick, N., Pekar, S.F., 2005. The Phanerozoic record of global sea level change. Science 310, 1293-1298.

Møller, L.K., Rasmussen, E.S., Clausen, O.R., 2009. Clinoformmigration patterns of a Late Miocene delta complex in the Danish Central Graben; implications for relative sea level changes. Basin Research 21, 704-720.

Munsterman, D.K. and Brinkhuis, H., 2004. A southern North Sea Miocene dinoflagellate cyst zonation. Netherlands Journal of Geosciences 83, 267-285.

Muntendam-Bos, A.G., Abbink, O.A., Wassing, B.B.T., van Bergen, F.M., 2009. Inventory non-conventional gas. TNO report TNO-034-UT-2009-00774/B, 188 p.

Nakayama, N., Sato, D., 2002. Prediction of sealing capacity by the equivalent grain size method. In: Koestler, A.G. and Hunsdale, R., 2002 (Eds.). Hydrocarbon seal quantification. NPF (Norwegian Petroleum Society) Special Publication no.11, Elsevier Science B.V., Amsterdam, 51-60.

Nordgård Bolås, H.M., Hermanrud, Chr., Teige, G.M.G., 2005. Seal capacity estimation from subsurface pore pressures. Basin Research 17, 583-599.

Overeem, I., Weltje, G.J., Bishop-Kay, C., Kroonenberg, S.B., 2001. The Late Cenozoic Eridanos delta system in the Southern North Sea Basin: a climate signal in sediment supply? Basin Research 13, 293-312.

Powell, A.J., 1992. Dinoflagellate cysts of the Tertiary System, In: A.J. Powell (Ed.), A stratigraphic index of dinoflagellate cysts, 155 – 272.

Price, A., Hofmann, A., Van Dalen, E., McKellar, D., Kaffenberger, G. 2002. Hanze field in the Dutch North Sea. Oil Gas European Magazine 2/2002, 15-20.

Prinzhofer, A., Battani, A., 2003. Gas isotopes tracing: an important tool for hydrocarbons exploration. Oil & Gas Science and Technology – Rev. IFP Vol 58 (2), 299-311.

Prinzhofer, A., Pernaton, E., 1997. Isotopically light methane in natural gas: bacterial imprint or diffusive fractionation? Chemical Geology 142, 193-200.

Rasmussen, E.S., 2005. Late Cenozoic depositional history of the Danish North Sea Basin: implications for the petroleum systems in the Kraka, Halfdan, Siri and Nini basins. Petroleum Geology Conference Series 6, 1347-1358.

Remmelts, G., 1996. Salt tectonics in the southern North Sea, the Netherlands. In: H.E. Rondeel, D.A.J. Batjes, W.H. Nieuwenhuijs (Eds.), Geology of gas and oil under the Netherlands. Kluwer Academic Publishers (Dordrecht), 143-158.

Rijsdijk, K.F., Passchier, S., Weerts, H.J.T., Laban, C., van Leeuwen, R.J.W., Ebbing, J.H.J., 2005. Revised Upper Cenozoic stratigraphy of the Dutch sector of the North Sea Basin: towards an integrated lithostratigraphic, seismostratigraphic and allostratigraphic approach, Netherlands Journal of Geosciences 84-2, 129-146.

Robertson Group – Petroleum Division, July 1990. Geochemical evaluation of the interval 500' to 6420' in the Arco F/1-1 well, Dutch North Sea. Robertson Group Report no. 6773/Ic) (report available at www.nlog.nl; retrieved June 2011).

Schloemer, S., Krooss, B.M., 2004. Molecular transport of methane, ethane and nitrogen and the influence of diffusion on the chemical and isotopic composition of natural gas accumulations, Geofluids 4, 81-108.

Schneider, J., Flemings, P.B., Day-Stirrat, R.J., Germaine, J.T., 2011. Insights into pore scale controls on mudstone permeability through re-sedimentation experiments. Geology 39, 1011-1014.

Schoell, M., 1983. Genetic characterization of natural gases. AAPG Bulletin 67, 2225-2238.

Schoell, M., 1988. Multiple origins of methane in the earth. Chemical Geology 71, 1-10.

Schowalter, T.T., 1979. Mechanics of secondary hydrocarbon migration and entrapment: AAPG Bulletin 63, 723-760.

Schroot, B.M., Klaver, G.T., Schüttenhelm, R.T.E., 2005. Surface and subsurface expressions of gas seepages to the seabed – examples from the Southern North Sea. Marine and Petroleum Geology 22, 499-515.

Shepard, F.P., 1954. Nomenclature based on sand-silt-clay ratios. Journal of Sedimentary Petrology. 24, 151-158.

Sørensen, J.C., Gregersen, U., Breiner, M., Michelsen, O., 1997. High-frequency sequence stratigraphy of Upper Cenozoic deposits in the central and southeastern North Sea areas. Marine and Petroleum Geology 14, 99-123.

Steeghs, P., Overeem, I., Tigrek, S., 2000. Seismic volume attribute analysis of the Cenozoic succession in the L08 block (Southern North Sea). Global and Planetary Change 27, 245-262.

Stuart, J.Y., Huuse, M., 2012. 3D seismic geomorphology of a large Plio-Pleistocene delta – 'Bright spots' and contourites in the Southern North Sea. Marine and Petroleum Geology 38, 143-157.

Sweeney, R.E., 2001. Methanogenesis during biodegradation of petroleum in groundwater and oil/gas reservoirs. Paper 6492. AAPG Annual meeting 2001.

Sylta, Ø., 2005. On the dynamics of capillary gas trapping: implications for the charging and leakage of gas reservopirs. In: Doré, A.G., Vining, B.A. (eds.). Petroleum Geology: North West Europe and global perspectives – Proceedings of the 6th Petroleum Geological Conference, Geological Society, London, 625-631.

Ten Veen, J.H., Geel, C.R., Kunakbayeva, G., Donders, T.H., Verreussel, R.M.C.H., 2011. Property prediction of Plio-Pleistocene sediments in the A15 shallow gas system. TNO Report TNO-060-UT-2011-01184/C12.

Van den Boogaard, M., Hoetz, H.L.J.G., 2012. Shallow Gas Play in the Netherlands takes off. Extended abstract: 74th EAGE Conference & Exhibition, Copenhagen.

Van Helmond, N.A.G.M., 2010. Palynological and organic geochemical characterization of marine and terrestrial Early Pleistocene climate in northwest Europe. Unpublished MSc thesis, Utrecht University, 78 p.

Verweij, J.M, Simmelink, H.J., Underschultz, J., Witmans, N., 2012a. Pressure and fluid dynamic characterization of the Dutch subsurface. Netherlands Journal of Geosciences 91-4, 465-490.

Verweij, J.M., 2011. Preliminary report on 'Origin and composition of shallow gas in offshore Netherlands'. TNO report, 12 p. *(also available in Appendix E of this shallow gas study).*

Verweij, J.M., Souto Carneiro Echternach, M., Nelskamp, S., Witmans, N. 2009. New findings with respect to key conditions controlling the Jurassic-Cretaceous Petroleum System, Dutch Central Graben. Oral presentation at the 71st EAGE Conference and Exhibition Amsterdam, 8-11 June 2009.

Verweij, J.M., ten Veen, J.H., De Bruin, G., Nelskamp, S.N., Donders, T., Kunakbayeva, G., Geel, K., 2012b. Shallow gas migration and trapping in the Cenozioc Eridanos delta deposits, Dutch offshore. Extended abstract. 74th EAGE Conference & Exibition Copenhagen, Denmark, June 2012.

Whiticar, M.J., 1994. Correlation of natural gases with their sources. In: Magoon, L.B. and Dow, W.G. The petroleum system from source to trap. AAPG Memoir 60, 261-283.

Whiticar, M.J., 1999. Carbon and hydrogen isotope systematics of bacterial formation and oxidation of methane. Chemical Geology 161, 291-314.

Whiticar, M.J., Faber, E., Schoell, M., 1986. Biogenic methane formation in marine and freshwater environments: CO2 reduction vs. acetate fermentation – isotope evidence. Geochimica et Cosmochimica Acta 50, 693-709.

Wong., Th.E., de Lugt, I.R., Kuhlmann, G., Overeem, I., Herngreen, G.F.W., 2007. Tertiary. In: T.E. Wong, D.A.J. Batjes, J. De Jager (Eds.). Geology of the Netherlands. Royal Netherlands Academy.

Wood, G.D., Gabriel, A.M., Lawson, J.C., 1996. Palynological techniques — processing and microscopy. In: J. Jansonius, D.C. McGregor, (eds.), Palynology: principles and applications. AASP, Salt Lake City, 29-50.

Yang, Y., Aplin, A.C., 2004. Definition and practical application of mudstone porosity-effective stress relationships. Petroleum Geoscience 10, 153-162.

Yang, Y., Aplin, A.C., 2010. A permeability-porosity relationship for mudstones. Marine and Petroleum Geology 27, 1692-1697

Zhang, T., Krooss, B.M., 2001. Experimental investigation on the carbon isotope fractionation of methane during gas migration by diffusion through sedimentary rocks at elevated temperatures and pressures. Geochimica et Cosmochimica Acta 65 (16), 2723-2742.

Ziegler, P.A., 1990. Geological Atlas of Western and Central Europe (3rd edition). Shell International Petroleum Maatschappij B.V., 239pp.

11 Signature

Utrecht,

R. Peters
Head of department

J. ten Veen
Author

Appendices

The following documents are included to this report:

Appendix A	Sample List A15-03 and A15-04
Appendix B	Sample list of F-blocks wells
Appendix C	Overview of used seismic surveys
Appendix D	Data analysis of reservoir properties
Appendix E	Origin and composition of shallow gas in offshore Netherlands
Appendix F	Approach to estimate the capillary seal capacity of mudstones
Appendix G	Results of grain size analysis I
Appendix H	Results of grain size analysis II
Appendix I	BS distribution maps
Appendix J	Petrel project guide

Digital annexes

The following documents are presented as digital annex:

Annex 1	Well overview (Excel document)
Annex 2	BS classification
Annex 3	BS picture database (Powerpoint document)
Annex 4	Petrel project (Shallow_GAS_ABF_Model)

Appendix A. Sample list A15-03 and A15-04

Table AA-1. Sample list A15-03 and A15-04.

Nr.	TNO label	Core	Depth (mbsl)	Splice depth (mbsl) to core A15-3	Box
1	1 CO	A15-3	890.8	890.8	
2	2 CO	A15-3	891.75	891.75	
3	6 CO	A15-3	892.8	892.8	
4	8 CO	A15-3	893.8	893.8	
5	12 CO	A15-3	896.8	896.8	
6	13 CO	A15-3	897.8	897.8	
7	15 CO	A15-3	898.8	898.8	
8	17 CO	A15-3	899.8	899.8	6-1
9	20 CO	A15-3	901.8	901.8	6-4
10	23 CO	A15-3	903.85	903.85	6-6
11	24 CO	A15-3	904.8	904.8	6-7
12	32 CO	A15-4	925.45	907.8	
13	36 CO	A15-4	926.8	908.97	
14	38 CO	A15-4	927.45	909.53	
15	40 CO	A15-4	928	910.01	
16	42 CO	A15-4	928.75	911.06	
17	44 CO	A15-4	929.55	912.19	
18	45 CO	A15-4	930.25	913.21	
19	48 CO	A15-3	917.55	917.55	8-1
20	49 CO	A15-3	918.15	918.15	8-2
21	51 CO	A15-3	920	920	8-4
22	55 CO	A15-3	921.95	921.95	8-6
23	57 CO	A15-3	924	924	8-8
24	60 CO	A15-3	925	925	8-10
25	62 CO	A15-3	926.7	926.7	9-1
26	67 CO	A15-3	929.95	929.95	9-5
27	68 CO	A15-3	935.9	935.9	10-2
28	69 CO	A15-3	936.9	936.9	10-3
29	72 CO	A15-3	938.9	938.9	10-5
30	75 CO	A15-3	940.9	940.9	10-7
31	77 CO	A15-3	942.9	942.9	10-9
32	79 CO	A15-3	943.85	943.85	10-10
33	80 CO	A15-3	944.9	944.9	11-1
34	81 CO	A15-3	945.9	945.9	11-2
35	85 CO	A15-3	946.91	946.91	11-3
36	86 CO	A15-3	953.25	953.25	12-1
37	87 CO	A15-3	954.15	954.15	12-2
38	89 CO	A15-3	956.18	956.18	12-4
39	92 CO	A15-3	957.3	957.3	12-5
40	94 CO	A15-3	958.25	958.25	12-6
41	97 CO	A15-3	960.33	960.33	12-9
42	101 CO	A15-3	962.2	962.2	13-1
43	103 CO	A15-3	963.17	963.17	13-2
44	104 CO	A15-3	964.02	964.02	13-3

45	126 CO	A15-4	975.1	960.1
46	129 CO	A15-4	976.1	961.1
47	131 CO	A15-4	976.8	961.8
48	133 CO	A15-4	977.45	962.45
49	136 CO	A15-4	978.3	963.3
50	137 CO	A15-4	978.85	963.85
51	143 CO	A15-4	980.8	965.8
52	146 CO	A15-4	981.8	966.8
53	151 CO	A15-4	983.5	968.5
54	154 CO	A15-4	984.5	969.5
55	158 CO	A15-4	986.15	971.06
56	161 CO	A15-4	987.15	972
57	CO	A15-4	997.8	981.91
58	CO	A15-4	999.8	983.77
59	CO	A15-4	1003.8	987.49
60	CO	A15-4	1008.35	991.72
61	CO	A15-4	1011.3	994.47
62	CO	A15-4	1014.3	997.26
63	SC	A15-4	937.8	922.8
64	SC	A15-4	938.45	923.45
65	SC	A15-4	1008.05	991.44
66	SC	A15-4	1008.75	992.09
67	SC	A15-4	1064	1037.69
68	SC	A15-4	1067	1040
69	SC	A15-4	1070	1042.31
70	SC	A15-4	1073	1044.62
71	SC	A15-4	1076	1046.92
72	SC	A15-4	1079	1049.23
73	SC	A15-4	1082	1051.54
74	SC	A15-4	1084	1053.08
75	SC	A15-4	1085	1053.85
76	SC	A15-4	1086	1054.62
77	SC	A15-4	1088	1056.15
78	SC	A15-4	1089.9	1057.62

Appendix B. Sample list of F-block wells

Table AB-1. Sample list of F-block wells.

F01-01		F02-06		F06-02		F12-03	
Depth (m)	**Type**	**Depth (m)**	**Type**	**Depth (m)**	**Type**	**Depth (m)**	**Type**
600	CU	450	CU	300	CU	620	CU
690	CU	525	CU	400	CU	700	CU
780	CU	595	CU	460	CU	740	CU
870	CU	670	CU	500	CU	800	CU
960	CU	750	CU	540	CU	890	CU
1020	CU	835	CU	580	CU	980	CU
1050	CU	930	CU	600	CU	1070	CU
1140	CU	1020	CU	620	CU	1130	CU
		1150	CU	665	CU		
				760	CU		
				820	CU		
				850	CU		
				880	CU		
				915	CU		
				950	CU		
				1040	CU		
				1130	CU		

Appendix C. Overview of used seismic surveys

Table AC-1. Seismic surveys used for seismic interpretation. Highlighted surveys were used for construction of ABF model. All others are used (or consulted) for ABCDEFG regional model.

Block	Type	Name
AB	2D	A15_Z2WES1988B
AB	2D	A15B15B17_Z2NAM1990A
AB	2D	B16_B17_A15_B13_F02_Z2NAM1990A
AB	2D	B17_Z2WES1985C
FG	2D	F_Z2GTM1998A
FG	2D	F01-Z2ARC1988C
FG	2D	F05_Z2REW1996A
FG	2D	F13_Z2CGG1985A
northern offshore	2D	SNST83
northern offshore	2D	SNST87
AB	3D	A15_Z3WIN2000A
AB	3D	A08_A09_Z3NAM1993a
AB	3D	A10_A11_A13_A14_Z3NAM1998C
AB	3D	A13_A14_Z2NAM1998C
AB	3D	A15_A12_A14_A13_A18_A11_Z3WIN2000A
DE	3D	D06_D09_Z3PGS1999A
DE	3D	D09_D12_E07_E10_E11_Z3GEC1997A
DE	3D	D12_D15_D18_E13_Z3WIN1994A
DE	3D	D12_D15_D18_Z3NAM1991C
DE	3D	E01_E04_Z3NAM1995B
DE	3D	E01_Z3NAM1995B
DE	3D	E02_E03_Z3NAM1998B
DE	3D	E02_Z3NAM1998B
DE	3D	E10_Z3WIN1997C
DE	3D	E10B_Z3PET1995B
DE	3D	E12_E09_Z3PET1999B
DE	3D	E14_E15_Z3PGS1999B
DE	3D	E16_E13_D18_Z3NAM1998A
DE	3D	E16_E17_Z3NAM1993B
DE	3D	E18_F16_Z3WIN1997A
FG	3D	F02_F03_F05_F06_Z3NAM1989E
FG	3D	F02_F03_Z3RWE1994A
FG	3D	F02_Z3RWE1994E
FG	3D	F03_B18_Z3NAM1982A
FG	3D	F06_Z3PET1992F
FG	3D	F08_F09_Z3OXY1994A

Block	Type	Name
JK	3D	K07_K10_Z3NAM1992C
JK	3D	K08_K11_Z3NAM1987A
JK	3D	K08_K11_Z3NAM1989F
JK	3D	K09_L07_Z3PLA1989A
JK	3D	K09_Z3OXY1996B
JK	3D	K09_Z3PLA1991A
JK	3D	K10_K13_Z3WIN1989A
JK	3D	K10_K13_Z3WIN1990C
JK	3D	K11_K12_K14_K15_L13_K17_K18_Z3NAM1989A
JK	3D	K11_K12_K14_K15_Z3NAM1988B
JK	3D	K11_K14_Z3NAM1990C
JK	3D	K12_K15_L10_Z3PLA1992A
JK	3D	K12_K15_Z3PLA1983A
JK	3D	K12_L10_Z3PLA1988B
JK	3D	K12_Z3OXY1997A
JK	3D	K13_Z3WIN1990D
JK	3D	K14_K17_K18_Z3NAM1982B
JK	3D	K15_K18_L13_L16_Z3NAM1984A
JK	3D	K15_L10_L13_L16_Z3NAM1986A
JK	3D	K15_L13_K18_L16_Z3CON1989A
JK	3D	K15_L13_Z3NAM1996B
JK	3D	K15_Z3NAM1981A
JK	3D	K17_K18_Z3NAM1990A
LMN	3D	L01_L02_Z3NAM1991E
LMN	3D	L02_F17_Z3NAM1985A
LMN	3D	L02_L03_F17_F18_G16_M01_L05_L06_M04_Z3NAM1994B
LMN	3D	L04_L05_L07_L08_Z3WIN2003A
LMN	3D	L04_L05_Z3NAM1990B
LMN	3D	L04_L07_Z3PET1992A
LMN	3D	L04_Z3PET1991D
LMN	3D	L05_L06_L08_L09_Z3NAM1990G
LMN	3D	L05_L06_L09_M04_Z3NAM1990F
LMN	3D	L06_Z3NAM1995A
LMN	3D	L07_L08_Z3WIN1995A
LMN	3D	L07_L10_Z3PET1990A
LMN	3D	L07_Z3PET1985A

FG	3D	F10_Z3PET1994B	LMN	3D	L08_Z3PEN1985A
FG	3D	F11_F12_Z3WES2003A	LMN	3D	L08_Z3WIN1992A
FG	3D	F12_G10_Z3PET1991A	LMN	3D	L09_L08_Z3NAM1988D
FG	3D	F14_Z3STA1985A	LMN	3D	L10_L07_L13_Z3PLA1991B
FG	3D	F15_F18_Z3PET1987A	LMN	3D	L10_L11_L13_L14_Z3PLA1991D
FG	3D	F15_F18_Z3PET1994A	LMN	3D	L10_Z3PLA1989C
FG	3D	F16_F17_L01_Z3WIN2003B	LMN	3D	L10_Z3PLA1992C
FG	3D	F16_Z3WIN2003B	LMN	3D	L11_L08_L12_Z3OXY1996A
FG	3D	F17_F18_Z3NAM1992A	LMN	3D	L11_L12_M10_L14_L15_Z3NAM1988A
FG	3D	F18_G16_Z3NAM1993C	LMN	3D	L11_Z3UNC1987A
FG	3D	F18_Z3WES1983A	LMN	3D	L13_L14_L16_L17_Z3NAM1988C
FG	3D	G13_G14_G17_Z3NAM1997A	LMN	3D	L13_Z3NAM1984B
FG	3D	G17_Z3CLY1998A	LMN	3D	L13_Z3NAM1991F
JK	3D	J03_J06_K01_K04_Z3ULT1988A	LMN	3D	L14_Z3PLA1992B
JK	3D	J03_K01_K02_K03_K05_Z3NAM1992B	LMN	3D	L16_Q01_Z3CON1984A
JK	3D	K02_K07_K09_Z3PET1990B	LMN	3D	M01_Z3NAM1990E
JK	3D	K03_K09_L01_I07_Z3PET1991C	LMN	3D	M02_Z3NAM1991A
JK	3D	K03_K13_L01_L10_Z3PET1992A	LMN	3D	M04_Z3NAM1991D
JK	3D	K04_J06_Z3PET1993B	LMN	3D	M05_M04_Z3PET1991B
JK	3D	K04_Z3BPE1985B	LMN	3D	M05_M08_Z3NAM1996A
JK	3D	K06_K03_K09_Z3PET1988A	LMN	3D	M07_L09_Z3NAM1994A
JK	3D	K06_K09_Z3PLA1989B	LMN	3D	M09_Z3NAM1989B
JK	3D	K07_K08_K10_K11_Z3NAM1989F	LMN	3D	M09_Z3NAM1989C
JK	3D	K07_K08_Z3NAM1991B	LMN	3D	N04_N05_N07_N08_Z3NAM1994C

Appendix D. Data analysis of reservoir properties

Data analysis and variograms of properties

Before the up-scaled properties can be distributed throughout the model, data analysis should provide rules for this distribution. These rules should give information on the horizontal and vertical ranges that describe, respectively, how data is dependent on surrounding data points, or to data points above or below. The anisotropy in the data distribution gives information on the geometrical shape of the geological element in which the data should be distributed.

Since most facies and continuous properties are related to PHIE, horizontal and vertical variograms for PHIE are determined and applied to other (continuous) logs such as VCL as well.

Analysis of Horizontal variograms and anisotropy

Using the standard automated variogram functionality of Petrel, the following input was used for sample variogram computation:

Orientation:	based on progradation direction and paleo shelf orientation (N330E).
Search radius (Long axis):	70% of entire model (200x200km) = 140 km, this value corresponds to the size of the prograding shelf edge delta system.
Search radius (short axis):	80 km, based on the average clinoform size. This assumes that lithofacies, PHIE, Vcl trends exist in a direction perpendicular to the paleo shelf orientation.
Average well spacing:	~5 km
#legs = 140000/5000:	28

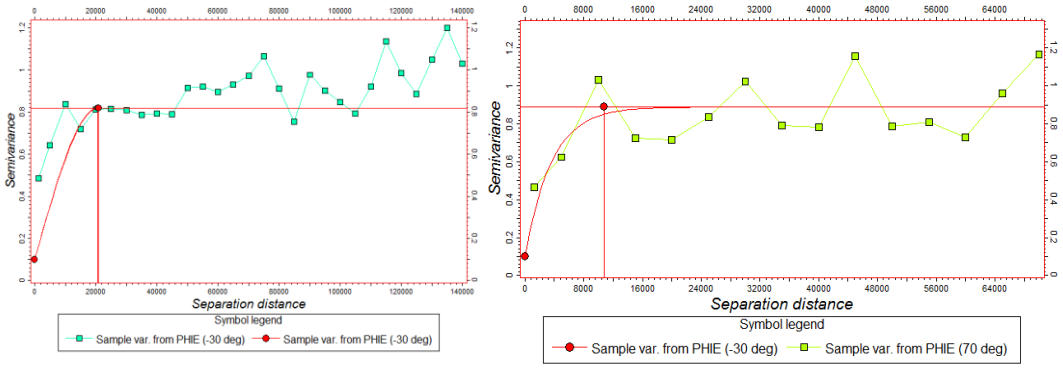

Fig. AD-1. Horizontal sample variogram of upscaled PHIE, in major and minor direction.

The results of the sample variogram analysis in major and minor direction (Fig. AD-1) indicate: Nugget = 0.1; sill = 0.9; major range = 25 km), minor range = 12 km, suggesting that beyond this range the data is not correlating anymore. Note that this is a measure corresponding to the size of individual delta lobes, rather than the whole shelf delta system. Applying these values in property modelling tend to focus on the small-scale data variability rather than on regional trends. This regional trend is well represented by the anisotropy of the entire shelf-edge delta (also used as search radii). The rhythmic variation around the sill may indicate a spatial trend that might also be related to presence of smaller delta lobes (lateral repetition of time-equivalent facies that bear similar porosity characteristics) as explained in Fig. AD-2, Fig. AD-3, Fig. AD-4.

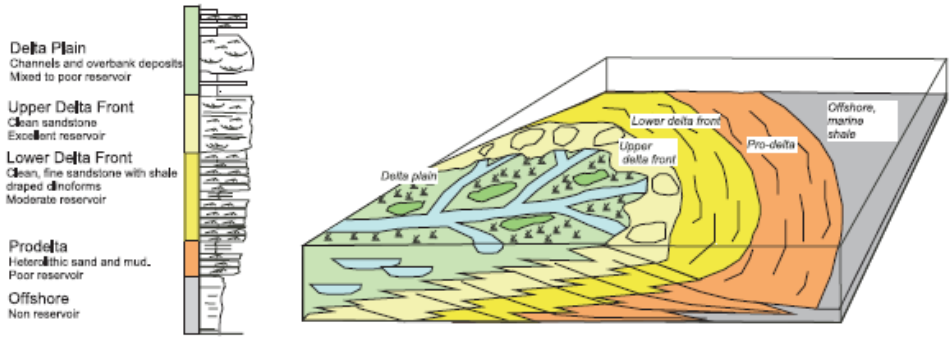

Fig. AD-2. Input facies vs PHIE concept (from Howell et al., 2008) showing general trend and superposition of individual smaller lobes.

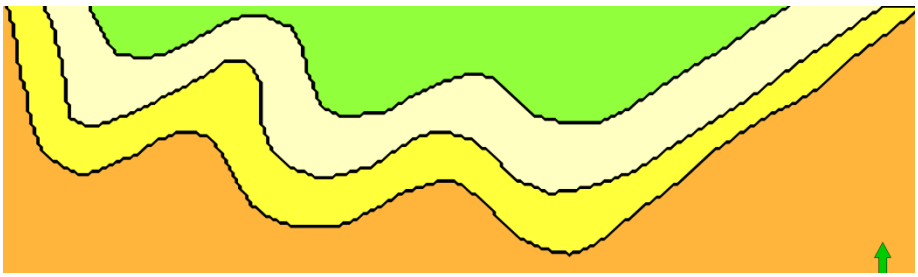

Fig. AD-3. Distribution of PHIE in a horizontal slice through the delta depicted in AD-2.

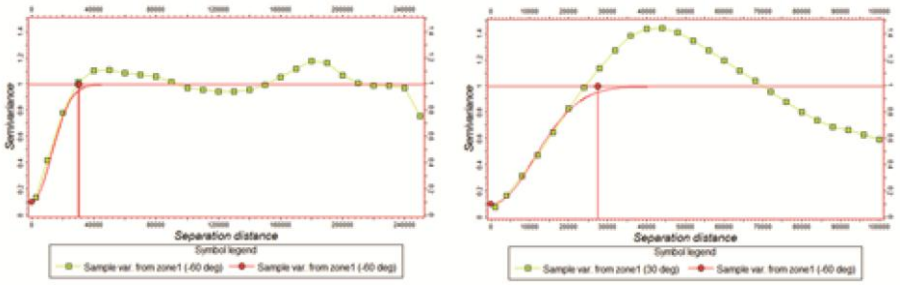

Fig. AD-4. Left: Major direction (left) and Minor direction (right variogram of PHIE distribution through above described delta, showing rhythmic variation around the sill due to superposition of delta lobes.

Analysis on vertical well logs and upscaled continuous properties

This analysis should be done to see if the chosen vertical grid spacing (min layer thickness) of 1 m is small enough to capture the vertical variability (generally ½ of the vertical range on raw data is taken as measure for layer thickness). The vertical range of the up-scaled (i.e. averaged) data should be larger than that of the raw data.

First a vertical variogram is generated from all the raw PHIE data, which gives the following values: sill = 0.5, nugget = 0.1; range is 22 m, which is the average vertical distance (thickness) beyond which the data are unrelated and gives an idea of average PHIE clusters.

Secondly a vertical variogram is generated from the up-scaled PHIE data, which gives the following values: sill = 0.7, nugget = 0.08; range is 22 m.
The 22 m vertical range of the raw data suggests that the layer thickness should not exceed 11 m. The minimum 1 m layer thickness used to mimic the internal stratification of the delta properly, is thus appropriate. The vertical range of the up-scaled cells is similar to the raw data, meaning that no averaging effect of up-scaling took place.

Both vertical and (regional) horizontal data analysis results are used in property modelling of vertical range and anisotropy respectively, as shown in Fig. AD-5 and Fig. AD-6 (the automatically chosen sill of 1.0 does not influence the modelling result). For facies modelling the vertical range is set by the conditioning facies properties.

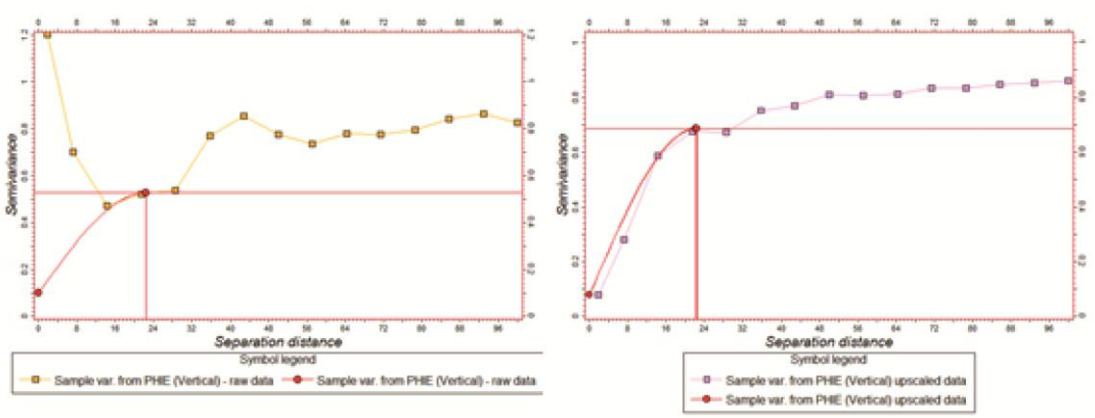

Fig. AD-5. Vertical variogram for raw (left) and upscaled (right) PHIE values.

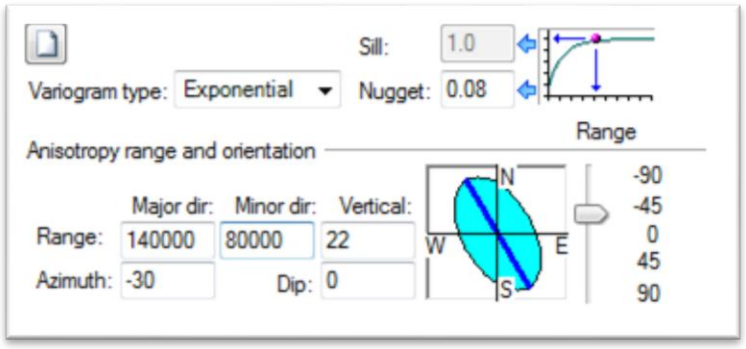

Fig. AD-6. Horizontal and Vertical anisotropy settings used in property modelling.

Data analysis on core-measured properties

Measured properties often have an irregular sample interval. For instance SD, TOC, CaCO3 are based on core material and sampling largely depend on quality and availability of the core material. For this reason the same horizontal variograms have been applied, but vertical variograms have been calculated separately. The vertical range for the SD data (123 m; Fig. AD-7), for example, is 10 times as high as for PHIE (22 m).

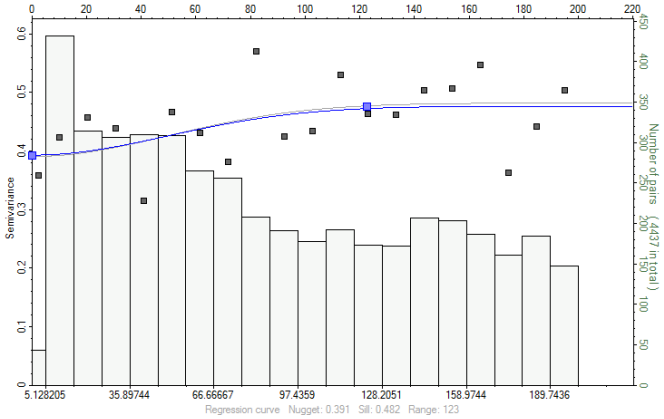

Fig. AD-7. Vertical variogram for SD values, showing a vertical range of 123 m, which is much higher than for continuously sampled data.

Appendix E. Origin and composition of shallow gas in offshore Netherlands

Introduction

An important requirement for understanding the shallow gas system in the offshore Netherlands concerns knowledge on the origin and geochemical characteristics of the shallow gas accumulations.

This report gives a brief general outline on origins of gas and how to assess the origin of gas and provides a preliminary overview on geochemical compositions of natural shallow gas occurrences in the northern part of the Dutch offshore.

Types and origins of shallow gas

Origin of shallow gas

Natural gases can be grouped into those that are generated directly by a sole source of organic matter, and those that no longer represent a single, original gas type but have been mixed or altered (Whiticar, 1994).

The different types of origins of hydrocarbons in natural gas accumulations include (Schoell, 1988; Whiticar, 1994, 1999; Larter et al., 2005)**:**

1. Biogenic origin
    a. Primary biogenic origin: biogenic (microbiological) decay of organic matter. The microbial decay involves methanogenesis, an anaerobic process by methanogens (archae) that use substrates, such as acetate and bicarbonates to form methane;
    b. Secondary biogenic origin: biodegradation of oil accumulations (Head et al., 2003; Larter et al., 2005; Claypool et al., 2001; Sweeney, 2001); Biodegradation by methanogenesis is commonly associated with biodegraded petroleum reservoirs that are free of abundant sulphate (Head et al., 2003).
2. Thermogenic origin
    a. Primary thermogenic origin: thermal decay of organic matter
        i. Gas from late primary cracking of kerogen and gas from secondary cracking of liquid hydrocarbons in source rocks (dry gas);
        ii. Oil and gas are generated simultaneously: primary cracking of kerogen producing early gas (oil-associated gas);
    b. Secondary thermogenic origin: cracking of oil in oil accumulations.

3. Deep origin (degassing mantle, metamorphic reactions, e.g. Schoell, 1988).

The main origins of hydrocarbons in natural gas accumulations in the subsurface are organic (that is biogenic and thermogenic origins).

In addition there are a number of processes that may influence the composition of gas from the time of generation to the accumulation of the gas in a reservoir, for example:

- Phase separation during migration (increasing the GOR of gas in relation to decreasing temperatures and pressures);
- Bacterial decay of gas during migration or in the reservoir (James and Burns, 1984; Horstad and Larter, 1997; Boreham et al., 2001; Larter et al., 2005). Extensive biodegradation of C2-C5 hydrocarbons, with propane being degraded most rapidly, appears to be capable of removing all but traces of the wet gas components, resulting in

a dry gas that could be confused with overmature dry gas whose wet components have undergone extensive thermal cracking (James and Burns, 1984);
- Chemical oxidation of gas during migration;
- Release of gas from formation water;
- Release of hydrocarbons adsorbed on e.g. organic matter in source rocks, or on coals during uplift and erosion (and associated decrease in pressure and temperature);

General geochemical characteristics of biogenic and thermogenic gas
Gases of microbial origin are almost exclusively methane, i.e. biogenic gas is dry. In contrast, thermogenic gas can be dry (such as dry, post-mature thermogenic gas), or can contain significant concentrations of wet gas components (ethane, propane, butanes) and condensate (C5+ hydrocarbons).

Stable isotope ratios (13C/12C and D/H) represent, besides compositional data (concentration, wetness, non-hydrocarbon components, noble gases) the fundamental parameters for the assessment of the sources and origins of natural gases (Whiticar, 1994; Zhang and Krooss, 2001). There is a set of widely-used classification schemes (Bernard et al., 1976; Schoell, 1983, 1988; Whiticar et al., 1986; Whiticar, 1994, 1999) available to distinguish microbial gas from gas generated by thermal decay of organic matter. These schemes are based on the assumption that microbial genesis of gas give gas enriched in methane, isotopically light (more depleted in the heavy isotope of carbon,13C) compared to a thermal generation. Gases with intermediate compositions are interpreted to be of mixed biogenic and thermogenic end members.

A correct interpretation of the data is sometimes delicate (Prinzhofer and Pernaton, 1997; Prinzhofer and Battani, 2003). For example, Prinzhofer and Pernaton, 1997 ascribe large changes (> 5 promille) in d13C/C1 to migration effects, while others have largely discounted the effects of migration on d13C/C1 values (see Zhang and Krooss, 2001). Schloemer and Krooss (2004) showed that diffusive transport results in strong fractionation processes along the diffusive front. However, because methane losses by molecular diffusion through caprocks are small in comparison with contents of commercial size gas accumulations strong fractionation effects are only observed for relatively small portions of gas (Zhang and Krooss, 2001). Hence, secondary effects can obscure the signature of sources under certain conditions. The isotopic abundances of the heavy isotope of carbon (^{13}C) of hydrocarbons play an important role in studying the sources of hydrocarbons in natural gas accumulations. The ratio difference (δ) between ^{13}C and ^{12}C in parts per thousand (‰), relative to standard:
$D13C = [\{(13C/12C)_{sample}/(13C/12C)_{standard}\}-1]*1000$ (the standard is a belemnite from the Peedee Formation in South Carolina (PDB)).

A usual way of distinguishing a microbial imprint versus a thermogenic one in natural gases is the use of the carbon isotopes of methane, the biogenic gas being generally isotopically lighter (d13C/C1< -50 ‰ PDB, e.g. Whiticar, 1999) than gases generated through thermal cracking. Thermogenic CH4 is generally enriched in 13C compared with biogenic CH4, with a d13C/C1 ranging from roughly -50‰ to -20‰ (Whiticar, 1999). The d13C/C1 of thermogenic gases becomes progressively enriched in 13C with increasing maturity, eventually approaching the 13C/12C of the original organic matter or kerogen (Schoell, 1988; Whiticar, 1994). Hydrogen-rich organic matter (i.e. kerogen types I and II) can often generate CH4 at lower levels of thermal stress and with more negative d13C/C1 values than for example type III kerogen (Whiticar, 1999). Carbon isotopic composition of methane associated with subsurface oil biodegradation frequently seems to be in the range of -45 ‰ to -55 ‰ d13C/C1 (e.g. Head et al., 2003; Larter and Di Primio, 2005; Dolfing et al., 2008).

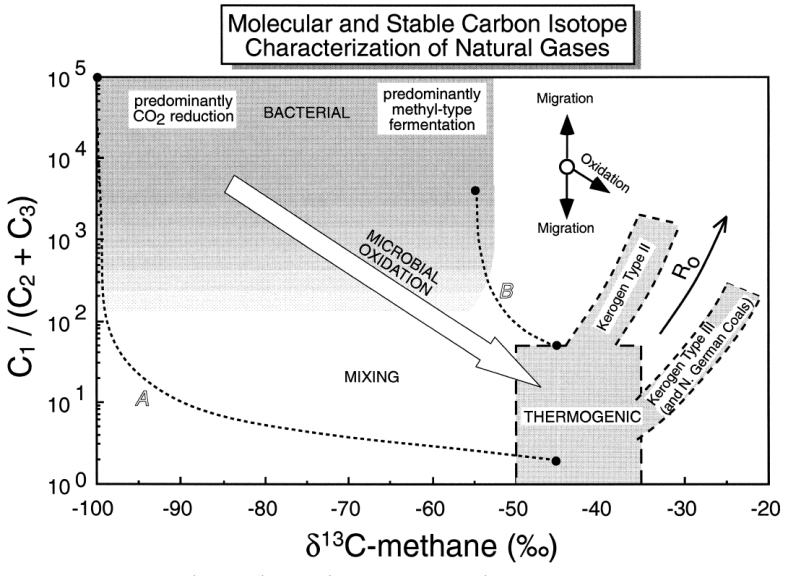

Fig. AE-1. Widely used natural gas interpretive 'Bernard' diagram to delineate gas types (from Whiticar, 1999; after Bernard et al., 1978). It combines the molecular {(vol%) ratio C1/(C2+C3)} of a natural gas and isotope information (d13C/C1). The lines (A) and (B) are calculated mixing lines for possible mixtures of biogenic and thermogenic gas with end-members isotope (d13C/C1) and molecular {C1/(C2 + C3)} compositions of -100 ‰, 105; -45 ‰, 2 (A), and -55 ‰, 5000; -45 ‰, 50 (B), respectively. The relative compositional effects of migration or oxidation are also indicated (Whiticar, 1999).

The heavy isotope of hydrogen is deuterium (D or 2H). The standard for D is mean ocean water (SMOW). Hydrogen isotope ratios are given in $^{o}/_{oo}$ SMOW. The hydrogen isotope ratios of thermogenic CH4 range from -275‰ to -100‰ dD/C1, and biogenic CH4 varies from -400 ‰ to -150 ‰ dD/C1 (Whiticar, 1999).

In combination, the carbon and hydrogen isotope signatures are frequently adequate to reliably characterize biogenic or thermogenic natural gas types (Whiticar, 1999).

Geochemical characteristics gas of shallow gas in the offshore Netherlands

Tables 11.8-1 and 11.8-2 present the geochemical compositions of natural shallow gas in offshore Netherlands, based on public information available at TNO.

Measured geochemical compositions of shallow gas from the Upper North Sea Group in the A and B blocks show that the gas is very dry at wells A12-03, A15-02, A18-02, A18-02-S2 and B16-01 (%C1 methane of > 99%) and B17-05 (98-99%C1 methane). The isotopic composition of methane measured at well B16-01 (-70.3 ‰ d13C/C1), F01-01 (-70.5 ‰ d13C/C1; Robertson Group – Petroleum Division, July 1990) suggests a biogenic origin of the methane gas.

The geochemical composition and the isotopic composition of the gas (measured on samples of adsorbed gases from cuttings) at B17-06 (GCA-Geochemische analysen, 1997) deviate from the above locations, being less dry and less depleted in C13/C1. The observed %C1 and the ‰ d13C/C1 are outside the typical range for a biogenic origin of gas, and are indicative of a thermogenic origin.

The geochemical analysis of a gas sample from the North Sea Group taken at a depth of 683 m in well F01-01 indicates that this gas is of biogenic origin. In the same well samples were taken for airspace gas hydrocarbon analysis from depths between c. 152 to 1957 m (Table 11.8- 2; Robertson Group – Petroleum Division, July 1990). The geochemical compositions of the gas samples in the

North Sea Group from depths < 1311 m are dominated by methane, while at greater depth in the lowermost parts of the North Sea Group and in the underlying Rijnland Group and Scruff Group, the percentage of methane decreases and concentration of wet gases increases, suggesting a thermogenic origin of the gas.

Schroot et al (2005) measured the gas content of 86 seabed samples and carbon stable isotope ratios of methane in the northern Dutch offshore. They found carbon isotope ratios range from -88.9 to -30.5 ‰ d13C/C1 in samples taken above a Jurassic condensate field (in block F3) and suggested that this may result from a leakage of a mixture of thermogenic and biogenic hydrocarbons to the seabed.

Conclusion
Most analyses from shallow gas in the northern offshore Netherlands show typical characteristics of biogenic gas: the gas is very dry (at wells A12-03, A15-02, A18-02, A18-02-S2, B16-01 and B17-05); the gas is depleted in 13C/C1 (at wells B16-01 and F01-01). In addition, there are gas analyses from 3 locations with observed methane content (%C1) and/or a carbon isotopic composition of methane (‰ d13C/C1) that are outside the typical range for a biogenic origin of gas, indicating that also gas from thermogenic origins has entered the North Sea Group sediments.

The origin of the very dry gas in the shallow gas accumulations is unknown. In theory there are different possible origins:

- primary biogenic origin (biogenic decay of organic matter in e.g. the Plio-Pleistocene SNS Delta deposits);
- secondary biogenic origin (biodegradation of oil accumulations in Jurassic or Chalk reservoirs);
- biogenic decay of (originally thermogenic) gas during migration or in the reservoir;
- phase separation of (originally thermogenic) gas during migration;
- water washing of oil or (originally thermogenic) gas during migration or in the reservoir.

Table AE-1. Geochemical composition of natural gases in the Upper North Sea Group.

Well Name	Depth m AHRT	Depth m AHRT	Stratigraphy	Unit	C1	C2	C3	i-C4	n-C4	i-C5	n-C5	C6	C7+	CO2	N2+	H2S	Total	d13C/C1 ‰PDB	dD/C1 ‰SMOW	d13C/C2 ‰PDB	d13C/C3 ‰PDB
A12-03	404	472,5	NU	mol%	99,48	0,02	0,01	0	0	0	0	0	0	0,02	0,46	0	100,0				
A12-03	404	472,5	NU	mol%	99,256	0	0,001	0,001	0,001	0	0	0	0	0,046	0,695	0	100,0				
A15-02			NU	mol%	99,2	0,075	0,018	0,0085	0,0096	0,00026	0,00033	0,000056	0	0,014	0,67	0	100,0				
A18-02	600	610	NU	mol%	99,5666	0,01	0	0	0	0	0	0	0	0,025	0,398203	0	100,0				
A18-02	446	738	NU	mol%	99,6008	0	0	0	0	0	0	0	0	0	0,399202	0	100,0				
A18-02	446	738	NU	mol%	99,21	0,01	0	0	0	0	0	0	0	0,01	0,76	0	100,0				
A18-02	446	738	NU	mol%	98,86	0,01	0	0	0	0	0	0,02	0	0,01	1,12	0	100,0				
A18-02-S2	600	610	NU	mol%	99,57	0,01	0	0	0	0	0	0	0	0,03	0	0	99,6				
B10-03	592	596	NU	mol%	99,655	0	0	0	0	0	0	0	0	0,075	0,27	0	100,0				
B10-03	592	596	NU	mol%	99,632	0	0	0	0	0	0	0	0	0,073	0,295	0	100,0				
B16-01			NU	mol%	99,6	0	0	0	0	0	0	0	0	0,04	0,33	0	100,0	-70,3	-183		
B17-05			NU	mol%	98	1	0	0	0	0	0	0	0	0,4	0,6	0	100,0				
B17-05			NU	mol%	98,966	0,034	0,015	0	0	0,001	0	0	0	0,161	0,823	0	100,0				
B17-05	664	677	NU	mol%	98,822	0,034	0,015	0	0	0,001	0	0	0	0,161	0,967	0	100,0				
B17-06	300		NU	vol%	66,86	4,52	2,81	0	0,73	0	0	0	24,64	0	0	0	99,6	-41,4		-33,8	
B17-06	475		NU	vol%	86,63	3,42	1,74	0	0,47	0	0	0	7,75	0	0	0	100,0	-39,8		-30,1	
B17-06	515		NU	vol%	78,54	3,23	1,43	0	0,45	0	0	0	16,36	0	0	0	100,0	-60,1		-34,8	
B17-06	625		NU	vol%	91,1	5,37	2,01	0,52	0,74	0	0,05	0	0	0	0	0	99,8	-44,2		-28,9	-26,6
B17-06	675		NU	vol%	88,9	3,7	1,54	0	0,61	0	0	5,25	0	0	0	0	100,0	-53,5		-33,6	
B17-06	700		NU	vol%	82,75	10,41	3,25	1,28	1,25	0	0,62	0,16	0	0	0	0	99,7	-44,9		-27,5	-27,4
B17-06	750		NU	vol%	74,66	7,72	2,65	0,76	1,7	0	0	12,37	0	0	0	0	99,9	-49,6		-24,8	-21,7
B17-06	775		NU	vol%	77,35	7,58	3,08	0,65	2,3	0	0	8,84	0	0	0	0	99,8	-51,9		-26,5	-25,8
B17-06	800		NU	vol%	80,85	7,09	2,58	0	0,71	0	0	8,58	0	0	0	0	99,8	-53,9		-26,5	-23,5
F01-01	683,4		N	mol%	99,22	0,02	0	0	0	0	0	0	0,09	0,14	0,01	0,52	0	100	-70,5	-187	

Table AE-2. Geochemical composition of airspace gas samples from different depths at well F01-01.

Well Name	Depth mAHRT	Stratigraphy	C1 %	C2 %	C3 %	i-C4 %	n-C4 %	i-C5 %	n-C5 %	C6 %	C7+ %	Total %	Total abundance gas ppm
F01-01	152.4	N	97.1				0.1			2.8		100	560
F01-01	213.36	N	93.7	0.7						5.6		100	140
F01-01	274.32	N	50.6	3.8						45.6		100	60
F01-01	335.28	N	99.7	0.1						0.2		100	3280
F01-01	365.76	N	99.4	0.2	0.1		0		0	0.3		100	5260
F01-01	396.24	N	99.6	0.1						0.3		100	5495
F01-01	426.72	N	99.6	0.1	0		0		0	0.3		100	7040
F01-01	457.2	N	99.9	0.1								100	5620
F01-01	487.68	N	99.6	0.1	0.1		0	0	0	0.3		100.1	4910
F01-01	518.16	N	99.7	0.1						0.2		100	12200
F01-01	548.64	N	99.4	0.1	0			0		0.4		99.9	9935
F01-01	579.12	N	99.5	0.1						0.4		100	9200
F01-01	609.6	N	99.1	0.1	0		0			0.8		100	9320
F01-01	640.08	N	99.5	0.1						0.4		100	9180
F01-01	701.04	N	98.1	0.2						1.7		100	4420
F01-01	762	N	82.8							17.2		100	260
F01-01	822.96	N	97.9	0.2						1.9		100	2585
F01-01	883.92	N	99.1							0.9		100	3480
F01-01	944.88	N	98.7	0.1						1.2		100	3700
F01-01	1005.84	N	98.3	0.2						1.6		100.1	2940
F01-01	1066.8	N	94.6	0.2	0.7	0.6		0.1		3.8		100	950
F01-01	1127.76	N	95.9	0.8	1.3	0.3	0.1		0.1	1.5		100	2200
F01-01	1188.72	N	96.9	1.6	0.6					0.9		100	2490
F01-01	1249.68	N	95.2	0.8	0.6					3.4		100	790
F01-01	1310.64	N	93.8	1.4	0.7					4.1		100	800
F01-01	1371.6	N	61.9	2.2						34.9		99	85
F01-01	1432.56	N								100		100	30
F01-01	1493.52	N	52.9	4.5	5.3					37.3		100	75
F01-01	1554.48	N	64.8	9.3	10.3	3.8	2.5	0.2		9.1		100	330
F01-01	1615.44	CKGR	57.3	2.9	2.8	1.1				35.9		100	90
F01-01	1676.4	CKGR	50.4	4						45.6		100	35
F01-01	1908.048	KNNC	43.1	8.6	18.8	12.4	13.3			30.5		126.7	495
F01-01	1932.432	SGK	24.1	6.1	17.3	7.9	12			32.6		100	390
F01-01	1956.816	SGK	47.5	10.3	16	3.7	7			14.9		99.4	1220

SAMPLE TYPE: airspace gas; canned cuttings
SOURCE: The Robertson Group (July 1990): Geochemical evaluation of the interval; 500' to 6420' in the ARCO F/1-1 well, Dutch North Sea (retrieved from NLOG June 2011)

References

Boreham, C.J., Hope, J.M., Hartung-Kagi, B., 2001. Understanding source, distribution and preservation of Australian natural gas: A geochemical perspective. APPEA Journal 41, 523-547.

Bernard, B.B., Brooks, J.M., Sackett, W.M., 1976. Natural gas seepage in the Gulf of Mexico. Earth Planetary Science Letters 31, 48-54.

Bernard, B., Brooks, J.M., Sackett, W.M., 1978. Light hydrocarbons in recent Texas continental shelf and slope sediments. Journal of Geophysical Research 83, 4053-4061.B.M.

Claypool, G.E., Magoon, L.B., Lorenson, Th.D., Lillis, P.G., Kaplan, I.R., 2001. Natural gas in the Great Valley of California – Geochemical characterization and petroleum systems. Paper 8902. AAPG Annual meeting 2001.

Dolfing, J., Larter, S.R., Head, I.M., 2008. Thermodynamic constraints on methanogenic crude oil biodegradation. The International Society for Microbial Ecology (ISME) Journal 2, 442-452.

GCA-Geochemische analysen, 1997. Analyses of adsorbed gases from cuttings of well B17-06. (report available at www.nlog.nl; retrieved June 2011) .

Head, I.M., Jones, D.M., Larter, S.R., 2003. Biological activity in the deep subsurface and the origin of heavy oil. Nature Vol 426, 344-352.

Horstad, I., Larter, S.R., 1997. Petroleum migration, alteration and remigration within Troll field, Norwegian North Sea. AAPG Bulletin 81, 222-248.

James, A.T., Burns, B.J., 1984. Microbial alteration of subsurface natural gas accumulations. The AAPG Bulletin 68 (8), 957-960.

Larter, S.R., Di Primio, R., 2005. Effects of biodegradation on oil and gas field PVT properties and the origin of oil rimmed gas accumulations. Organic geochemistry 36, 299-310.

Larter, S.R., Head, I.M., Huang, H., Bennett, B., Jones, M., Aplin, A.C., Murray, A., Erdmann, M., Wilhelms, A., Di Primio, R., 2005. Biodegradation, gas destruction and methane generation in deep subsurface petroleum reservoirs: an overview. In: Doré, A.G. and Vining, B.A. (eds). Petroleum geology: North-West Europe and Global perspectives – Proceedings of the 6th Petroleum Geology Conference. Published by the Geological Society London, 633-639.

Prinzhofer, A., Battani, A., 2003. Gas isotopes tracing: an important tool for hydrocarbons exploration. Oil & Gas Science and Technology – Rev. IFP Vol 58 (2), 299-311.

Prinzhofer, A., Pernaton, E., 1997. Isotopically light methane in natural gas: bacterial imprint or diffusive fractionation? Chemical Geology 142, 193-200.

Robertson Group – Petroleum Division, July 1990. Geochemical evaluation of the interval 500' to 6420' in the Arco F/1-1 well, Dutch North Sea. Robertson Group Report no. 6773/Ic) (report available at www.nlog.nl; retrieved June 2011).

Schloemer, S., Krooss, B.M., 2004. Molecular transport of methane, ethane and nitrogen and the influence of diffusion on the chemical and isotopic composition of natural gas accumulations, Geofluids 4, 81-108.

Schoell, M., 1983. Genetic characterization of natural gases. AAPG Bulletin 67, 2225-2238.

Schoell, M., 1988. Multiple origins of methane in the earth. Chemical Geology 71, 1-10.

Schroot, B.M., Klaver, G.T., Schüttenhelm, R.T.E., 2005. Surface and subsurface expressions of gas seepages to the seabed – examples from the Southern North Sea. Marine and Petroleum Geology 22, 499-515.

Sweeney, R.E., 2001. Methanogenesis during biodegradation of petroleum in groundwater and oil/gas reservoirs. Paper 6492. AAPG Annual meeting 2001.

Whiticar, M.J., 1994. Correlation of natural gases with their sources. In: Magoon, L.B. and Dow, W.G. The petroleum system from source to trap. AAPG Memoir 60, 261-283.

Whiticar, M.J., 1999. Carbon and hydrogen isotope systematics of bacterial formation and oxidation of methane. Chemical Geology 161, 291-314.

Whiticar, M.J., Faber, E., Schoell, M., 1986. Biogenic methane formation in marine and freshwater environments: CO2 reduction vs. acetate fermentation – isotope evidence. Geochimica et Cosmochimica Acta 50, 693-709.

Zhang, T., Krooss, B.M., 2001. Experimental investigation on the carbon isotope fractionation of methane during gas migration by diffusion through sedimentary rocks at elevated temperatures and pressures. Geochimica et Cosmochimica Acta 65 (16), 2723-2742.

Appendix F. Approach to estimate the capillary seal capacity of mudstones

Introduction
The evaluation of the sealing capacity of the mudstones is based on the following assumptions:

- The mudstone seals are capillary seals (~membrane seals);
- The mudstone seals are water-wet;
- The contact angle is zero for gas-water systems (i.e. the wetting phase completely wets the solid grain surfaces);
- There is equilibrium between capillary forces resisting displacement of the water phase in the seal and buoyancy force of the hydrocarbon column;
- The hydrocarbons are gas; the gas is composed of methane.

Capillary seal theory
Any lithostratigraphic unit whose minimum displacement pressures of the largest connecting pore throats is greater than the buoyancy forces of the hydrocarbon column below it can, in principle, act as a capillary seal for hydrocarbons (e.g., Berg, 1975; Downey, 1984). Effective seals are typically laterally continuous, homogeneous, and fairly ductile (such that fractures do not crosscut the unit) (Downey, 1984). For an underlying more porous and permeable lithostratigraphic unit (reservoir) to define as a trap there must be closure (Schowalter, 1979; Downey, 1984).

Capillary seal capacity of a water-wet rock corresponds to the height of a hydrocarbon column that a seal may retain prior to leaking and is a function of :

- Capillary entry pressure of a water-wet seal (P_{ce}), and thus on:
- Seal properties: Pore throat size distribution (along largest interconnected pore throat path through seal) (d=diameter of the critical pore throat in seal)
- Interfacial tension between hydrocarbon and water
- Density hydrocarbons (ρ_{hc})
- Density formation water (ρ_w)
- Formation water pressure (P_w)

The capillary entry pressure of a water-wet seal is (e.g. Berg, 1975):

$P_{ce} = 2\ \Upsilon \cos\theta / r$
where,
P_{ce} :capillary entry pressure of a water-wet seal
Υ : interfacial tension between hydrocarbon and water
θ :contact angle between hydrocarbon and water in seal. When a breakthrough of hydrocarbons occurs, this angle is zero ($\cos\theta=1$).
r :radius of pores in seal.

The capillary entry pressure of a water-wet seal, when breakthrough of hydrocarbons occurs, is given by:

$P_{ce} = 4\ Y/d$
where,
d :diameter of the critical pore throat in seal

Under equilibrium conditions, just prior to breakthrough of the hydrocarbons into the seal:

$(\rho w-\rho hc)gh = P_{ce}$
where,
ρ_w :density pore water
ρ_{hc} :density hydrocarbon
g :acceleration due to gravity
h :maximum height of a hydrocarbon column that a seal may retain prior to leaking

If measured values of P_{ce} are available the maximum height of a hydrocarbon column can be calculated from the density difference between the hydrocarbons and the pore water and acceleration due to gravity.

The maximum height of a hydrocarbon column (h) that a seal may retain prior to leaking can also be described by (see e.g. Nordgård Bolås et al., 2005).

$h = 4\ Y/[(\rho_w-\rho_{hc})gd]$
Calculation of the maximum height of the hydrocarbon column (~ capillary seal capacity) thus requires the assessment of the following parameters:

- Diameter of the pore throats in seal (d)
- Interfacial tension between hydrocarbon and water (Y)
- Density of pore water (ρ_w)
- Density of hydrocarbons (ρ_{hc})

The estimation of the fluid densities and interfacial tensions for the mudstones at different locations and depths is rather straightforward. The challenge lies in estimating the pore throat size.
In case the hydrocarbon density is known or can be estimated, the pore water gradient is known or can be estimated, and the gas pressure is known for a certain depth in a hydrocarbon accumulation, the hydrocarbon column can also be calculated from the following equation:

$h = (P_{hc} -\rho_w gz)/(\rho_w g-\rho_{hc} g)$ [Note: $(P_{hc} -\rho_w gz)$ =overpressure at depth z]

Step-wise approach to estimate capillary sealing capacity
We developed and applied a systematic approach to evaluate the porosity and permeability and the seal capacity of mudstones at shallow depths in the Dutch northern offshore based on new grain size analysis data and publicly available pressure data. After evaluating different approaches we selected equations developed by Yang & Aplin (2004) and Yang & Aplin (2010) for calculating mudstone porosity and permeability, respectively. These equations include clay content as important steering parameter. The pore throats are calculated from approaches that use the calculated porosities and median grain size, published by Nakayama & Sato (2002). Knowing the pore throats, the seal capacity could be determined by estimating the water densities from RFT pressure measurements, and gas densities and gas-water interfacial tensions from established relations using known

temperature and pressure changes with depth (NIST Chemistry WebBook: http://webbook.nist.gov/chemistry/fluid/; Nordgråd Bolås et al., 2005, respectively).
Grain size, especially the clay fraction and median grain size, are basic parameters needed to assess the capillary seal capacity. The grain size based workflow includes the following steps:

1. Selection clay fraction and median grain size from grain size data base
2. Calculation porosity
3. Calculation permeability
4. Calculation pore throat diameter
5. Calculation hydrocarbon column height

Finally the results of the grain size based calculations of the gas column heights (capillary seal capacity) are compared with those calculated from measured pressures and the height of crossovers of neutron and density logs.

Assessment capillary seal capacity from grain size distribution

Step 1: Selection clay fraction and median grain size from grain size data base
The clay fraction and median grain size of the mudstone layers are derived from newly analysed grain size distributions of 77 samples of mudstones at 10 well locations. Samples were analysed at the Sedimentary Laboratory of the Vrije Universiteit, Amsterdam (using Laser Particle Sizer Helos KR Sympatec/Windox5.6). The Laser clay fraction is of grain size < 8µm.

Step 2: Calculation porosity
Porosity is calculated using the following equation for void ratio developed by Yang and Aplin (2004):

$e = e100 – \beta \ln[(\sigma_v - P_w)/100]$
where,
$e100 = 0.3024 + 1.6867clay + 1.9505clay^2$
e100 : void ratio at 100 kPa effective stress
clay : clay content (fraction)
$\beta = 0.0407 + 0.2479clay + 0.3684clay^2$
$e = \theta/(1 - \theta)$
e : void ratio
θ : porosity (fraction)
$\sigma_v - P_w$: effective stress (kPa)
σ_v : vertical stress (kPa)
P_w : formation water pressure (kPa)

The effective stress for the upper part of the North Sea Group is estimated from the following relation:
$\sigma_v – P_w = 11.1*z$
where,
z : depth (mTVDss)

The vertical stress σ_v in the upper part of the North Sea Group is derived from the RHOB log at well B18-02 for depths between 400-1200m (R2 = 0.997):

$\sigma_v = 21.6*z$ (z in mTVDss; σ_v = vertical stress in kPa).

The following generalised equation to calculate the formation water pressure (P_w) in the upper part of the North sea Group is based on pressure gradients derived from measured RFT pressures at 9 wells (A12-03, A15-02, A15-03, A18-02, B10-03, B13-03, B13-04, B16-01, B17-05):

$P_w = 10.5*z$ (z in mTVDss; P_w in kPa)

Input required to calculate the porosity using the Yang and Aplin equation (2004):

- Clay content (fraction < 8 µm; result step 1)
- Depth (z)

Step 3. Calculation permeability
Permeability is calculated using the relationship published by Yang and Aplin (2010):

$Ln\ (k) = -69.59-26.79*clay+44.07*clay^{0.5}+(-53.61-80.03*clay+132.78*clay^{0.5})*e + (86.61+81.91*clay-163.61*clay^{0.5})*e^{0.5}$
where,
k : bedding perpendicular permeability (m2)
clay : clay content (fraction)
e : void ratio= θ/(1- θ)

Input required to calculate the porosity using the Yang and Aplin equation (2010):

- Clay content (fraction < 8 µm; result step 1)
- Porosity (result step 2)

Step 4. Calculation pore throat
The ‘equivalent grain size method‘ published by Nakayama and Sato (2002) is used to calculate pore-throat size. This method is based on the assumption that a seal consists of equalized grains and the pore throat can be regarded as a function of grain size and porosity if the geometrical ratio of pore-throat and grain size is considered. Although porosity does not change as grain size changes, it does change according to the packing. The relation between the ratio of pore-throat size to grain size (COEF) and porosity for theoretical types of packing is given by (Nakayama and Van Siclen in: Nakayama and Sato, 2002):

$COEF = 1.92*\theta^2 - 0.0882*\theta$
and
$r = (½)(COEF)d_e$
where,
r : pore-throat radius (µm)
COEF : ratio of pore throat to grain size
θ : porosity (fraction)
d_e : equivalent grain diameter (µm)

Hence, the pore-throat radius can be obtained from:
$r = ½\ (1.92*\theta^2 - 0.0882*\theta)d_e$
Input required to calculate the pore-throat radius using the equivalent grain size method of Nakayama and Sato (2002):

- Porosity (result step 2)
- Equivalent grain diameter. For this parameter, we use the median grain size diameter (µm) resulting from the analysis of the grain size distribution (result step 1)

Step 5. Calculation gas column height

The height of a gas column (h) that a seal for shallow gas may retain prior to leaking can be derived from (see e.g. Nordgård Bolås et al., 2005).

$h = 2\,\Upsilon/[(\rho wg-\rho gasg)r]$

where,

h : height of gas column (m)

Υ : interfacial tension between gas and water (N/m)

ρ_w : density pore water (kg/m3)

ρ_{gas} : density gas (kg/m3)

g : acceleration due to gravity (m/s2)

r : pore-throat radius (m)

Input parameters required to calculate of height of the gas column (~ capillary seal capacity):

- Interfacial tension between gas and water (Υ)
- Density of pore water (ρ_w), or pore water gradient ($\rho_w g$)
- Density of gas (ρ_{gas}), or gas gradient ($\rho_{gas} g$)
- Radius of the pore throats in seal (r)

<u>Interfacial tension between gas and water</u>

The variations in interfacial tension of water-hydrocarbon systems with depth (with temperature and pressure) can be estimated from published information (Nordgård Bolås et al., 2005, and references therein).

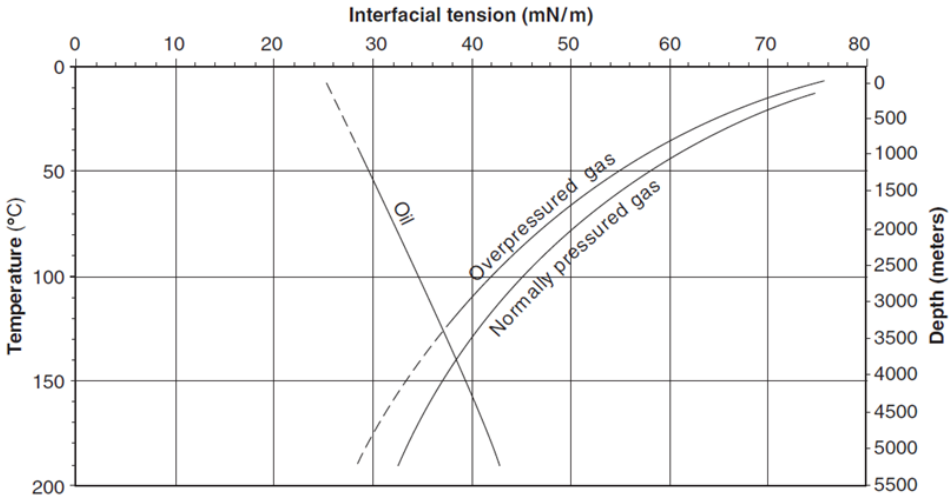

Fig. AF-1. Cross plot showing oil and gas interfacial tensions versus depth (from Nordgård Bolås et al., 2005).

Fig. AF-1 was used to derive a new linear relation between interfacial tension and depth for shallow depths. This new relation is used to estimate interfacial tensions for normally pressured shallow gas-water systems at different depths:

$\Upsilon = (5222.2 - z)/69.44$
where,
Υ : interfacial tension (mN/m)
z : depth (mTVDss)

Density of pore water
This can be estimated from water pressure gradients derived from measured RFT pressures in wells. The following generalised water density in the upper part of the North Sea Group is based on pressure gradients derived from measured RFT pressures at 9 wells (A12-03, A15-02, A15-03, A18-02, B10-03, B13-03, B13-04, B16-01, B17-05). This pore-water density is also used for wells without pressure measurements.

ρ_w = 1070 kg/m3 (or $\rho_w g$ = 10500 Pa/m)
Density of gas
The subsurface density of gas can be calculated by one of the following three methods, depending on data availability:

- The subsurface density can be estimated from gas pressure gradients, provided that the number and quality of the measured pressure data allow this.
- The subsurface density of the gas can also be estimated from known or assumed hydrocarbon composition (for shallow gas we assume that the hydrocarbon composition is methane), pressure and temperature conditions at a certain depth. We used the following website to calculate the gas density at a certain depth: http://webbook.nist.gov/chemistry/fluid/.

Required input parameters are pressure and temperature at a certain depth. A pressure gradient of 10500 Pa/m is used to calculate the pressure (same gradient is used for determining the effective stress). Temperature data for the Dutch northern offshore show some spatial variations in geothermal gradient (about 0.025 – 0.030°C/m). For this study we selected the following relation to calculate the temperature at a certain depth:

$T = 0.030 (z) + 10$
where,
T : temperature (°C)
Z : depth (mTVDss)

- In addition the subsurface density of gas can be calculated from published well information, including specific gravity of the gas at standard conditions, and gas formation volume factor (see for example production plan for well B18-02).

Radius of pore throat

The radius of the pore throat is available from the results of Step 4 of the work flow.

11.1.1 *Assessment capillary seal capacity from measured fluid pressures*

The following equation is used to calculate the height of the gas column:

$h = (P_{gas} - \rho_w gz)/(\rho_w g - \rho_{gas} g)$

h : height of the gas column (m)
P_{gas} : pressure of gas at depth z (Pa)
$\rho_w gz$: pore-water pressure at depth z (Pa)
$P_{gas} - \rho_w gz$: overpressure at depth z (Pa)
ρ_w : density pore water (kg/m3)
ρ_{gas} : density gas (kg/m3)
g : acceleration due to gravity (m/s2)

Before being able to calculate the gas column height using fluid pressure data (from e.g. RFT measurements), the type of fluid for each measurement point (gas or water) needs to be assessed. For this purpose the identified depths of gas peaks and crossovers of NPHI-RHOB from logs, and DHIs from seismic can be used in combination with the pressure data itself using pressure depth plots. The pore water gradient and water density can be calculated from cross plots of water pressure versus depth.

The gas column height can be calculated provided the density of gas, the pore water gradient, and gas pressure is known for a certain depth in the shallow gas reservoir. The calculation procedure is as follows:

- Pgas is measured at a certain depth (z)
- The density of gas ρ_{gas} can be estimated at depth of P_{gas} measurement (knowing measured P_{gas} at depth z and the calculated temperature at depth z assuming a temperature gradient of 0.03°C/m) from http://webbook.nist.gov/chemistry/fluid/
- Pore-water density ρ_w can be estimated from water pressure gradients derived from measured RFT pressures in wells
- Calculate gas column height h; h= height between the depth of measurement of the gas pressure (z) and depth of GWC

The point of measurement of P_{gas} in the gas accumulation may be at some distance below the base of the seal. If the depth of the base of the seal can be derived from logs or seismic, it is possible to calculate the height of the gas column with respect to the base of the seal at the well location. In addition, the well may not be located at the geometrical top of the reservoir: if so, the calculated gas column height at the well location will be less than the maximum gas column height.

Comparison of seal capacities calculated from grain size distribution and measured fluid pressures

The final step of the workflow is the evaluation of the applied grain size based method to calculate capillary seal capacities. For this purpose the heights of the gas columns calculated by the grain size method are compared with those calculated from measured fluid pressures and with other indicators of gas column heights, such as the heights of gas occurrences detected from cross overs of neutron (NPHI) & density logs (RHOB).

New generalised method

The application of the above outlined workflow on the samples of mudstones of the Plio-Pleistocene delta resulted in a database of permeability and pore throat magnitudes. Plotting the calculated pore

throat radius against the permeability of the mudstones, omitting the samples with a sand content of less than 20% (Fig. AF-2), revealed the following relationship:

*log (r) = 0.8593 + 0.2579*log(k) (R2 = 0.8948)*

Where,
r : pore throat radius (μm)
k : vertical permeability (mD)

The above relationship together with the approaches for calculating porosity and permeability (given in step 2 and 3) was developed into a new easy-to-use generalised procedure to calculate pore throats and associated capillary seal capacities for mudstones. The generalised procedure is illustrated below.

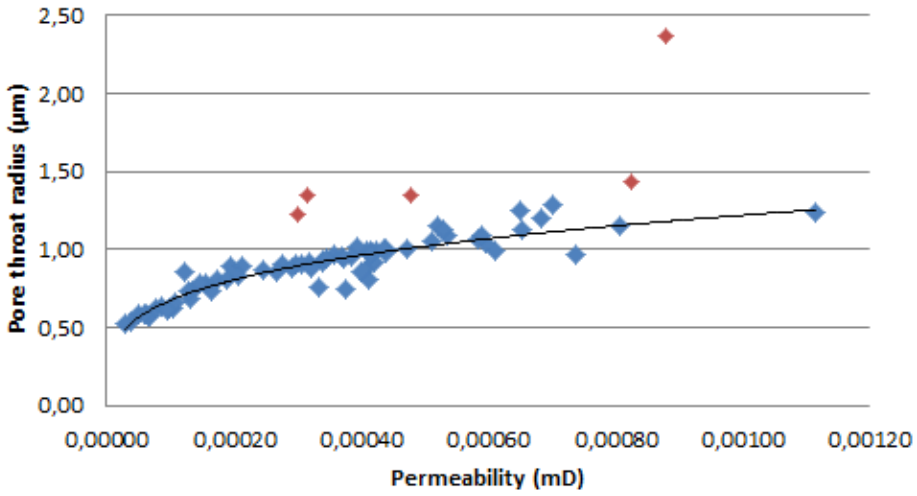

Fig. AF-2. Cross plot showing the relation between the pore throat radius and the permeability calculated for all samples of sealing layers. The red squares indicate the samples classified as sand-silt-clay (sand content > 20%).

Fig. AF-3. Step 1 of generalised method: From clay percentage to pore throat radius and capillary seal capacity of mudstones.

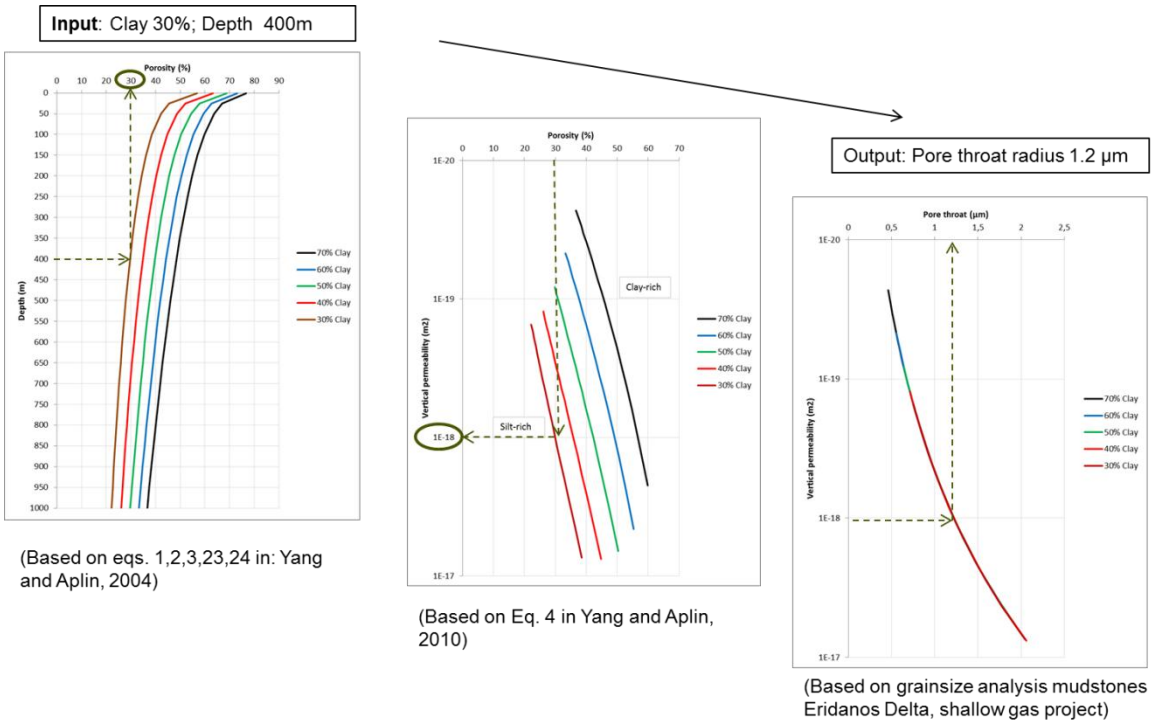

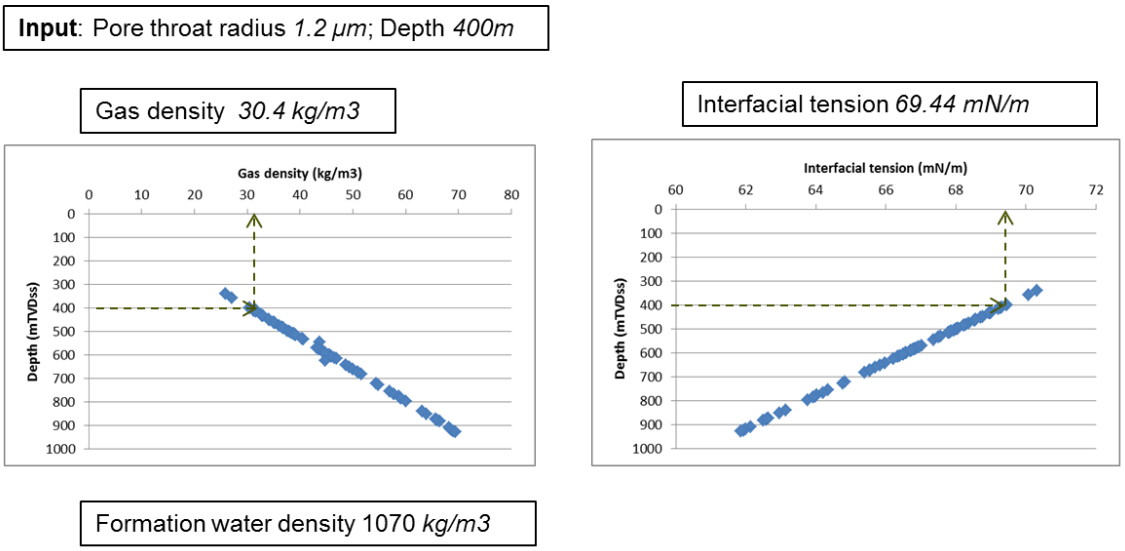

*Gas column height h = (2γ/r)/ [(ρ_w - ρ_{gas})g] = [2*69.44/1.2*1000]/[(1070 - 30.4)*9.81] = 11 m*

Fig. AF-4. Step 2 of generalised method: From clay percentage to pore throat radius and capillary seal capacity of mudstones.

References

Berg, R.R., 1975. Capillary pressures in stratigraphic traps. The AAPG Bulletin 59, 939-956.

Downey, M.W., 1984. Evaluating seals for hydrocarbon accumulations. AAPG Bulletin 68, 1752-1763.

Nakayama, N., Sato, D., 2002. Prediction of sealing capacity by the equivalent grain size method. In: Koestler, A.G., Hunsdale, R., 2002 (eds.), Hydrocarbon seal quantification. NPF (Norwegian Petroleum Society) Special Publication no.11, Elsevier Science B.V., Amsterdam, 51-60.

Nordgård Bolås, H.M., Hermanrud, Chr., Teige, G.M.G., 2005. Seal capacity estimation from subsurface pore pressures. Basin research 17, 583-599.

Schowalter, T.T., 1979. Mechanics of secondary hydrocarbon migration and entrapment: AAPG Bulletin 63, 723-760.

Yang, Y., Aplin, A.C., 2004. Definition and practical application of mudstone porosity-effective stress relationships. Petroleum Geoscience 10, 153-162.

Yang, Y., Aplin, A.C., 2010. A permeability-porosity relationship for mudstones. Marine and Petroleum Geology 27, 1692-1697.

Appendix G. Results of grain size analysis I

Table AG-1. Grain size analysis was conducted by Laser Particle Sizer Helos KR Sympatec/Windox5.6 at the sedimentology laboratory of the Vrije Universiteit Amsterdam.

Well	Sample depth		Strat. Unit	Clay (< 8 µm)	Silt (8-63 µm)	Sand (63-2000 µm)	Median Grain Size	Sample
Name	MD (m)	mTVDss		%	%	%	µm	Type
A12-03	468	431	s13	66.61	33.39	0	4.78	Core
A12-03	469	432	s13	65.4	34.56	0.04	4.91	Core
A12-03	470	433	s13	61.67	36.48	1.86	5.38	Core
A12-03	471	434	s13	72.09	27.91	0	4.22	Core
A15-04	910	872	s6	64.03	35.93	0.05	5.17	Cutting
A15-04	915	877	s6	59.6	36.66	3.74	5.6	Cutting
A15-04	920	882	s6	60.87	38.01	1.12	5.57	Cutting
A15-04	945	907	s5	51.09	46.57	2.34	7.69	Cutting
A15-04	955	917	s5	66.89	32.15	0.96	4.7	Cutting
A15-04	960	922	s5	34.45	56.41	9.14	16.71	Cutting
A15-04	965	927	s5	57.94	40.1	1.96	6.1	Cutting
A18-02	440	400	s13	60.13	38.11	1.76	5.69	Cutting
A18-02	515	475	s11	47.35	46.94	5.71	8.75	Cutting
A18-02	520	480	s11	55.63	41.95	2.42	6.57	Cutting
A18-02	525	485	s11	37.24	59.02	3.74	11.93	Cutting
A18-02	535	495	s11	55.79	39.44	4.76	6.53	Cutting
A18-02	585	545	s9	42.6	49.77	7.63	10.71	Cutting
A18-02	615	575	s9	39.57	55.57	4.86	11.19	Cutting
A18-02	620	580	s9	36.64	54.96	8.4	13.7	Cutting
A18-02	625	585	s9	44.84	48.34	6.82	9.87	Cutting
A18-02	630	590	s9	36.81	58.94	4.25	12.64	Cutting
A18-02	640	600	s8	43.31	49.73	6.95	10.41	Cutting
A18-02	645	605	s8	35.09	56.14	8.76	14.63	Cutting
A18-02	890	850	s6	62.45	33.67	3.88	5.28	Cutting
B10-03	395	357	post s13	34.43	52.4	13.17	13.81	Cutting
B10-03	450	412	s13	56.78	39.65	3.57	6.35	Cutting
B10-03	500	462	s12	38.57	46.84	14.59	13.97	Cutting
B10-03	550.1	512	s11	23.95	68.1	7.95	21.62	Cutting
B10-03	606.9	569	s9	17.23	67.65	15.12	25.53	Cutting
B10-03	620	582	s8	36.27	51.57	12.16	13.63	Cutting
B10-03	650.6	612	s7	36.77	54.04	9.19	14.29	Cutting
B10-03	710	672	s6	62.35	32.93	4.72	4.68	Cutting
B10-03	720	682	s6	57.54	39.82	2.64	6.26	Cutting
B13-03	375	339	post s13	50.37	45.45	4.19	7.9	Cutting
B13-03	435	399	s13	50.6	39.28	10.12	7.81	Cutting
B13-03	470	434	s12	42.88	45.11	12	10.7	Cutting
B13-03	520	484	s11	53.58	41.41	5.01	7.13	Cutting
B13-03	570	534	s9	36.12	45.22	18.66	15.14	Cutting
B13-03	635	599	s7	40.85	47.95	11.2	11.62	Cutting
B13-03	640	604	s7	44.64	46.45	8.92	9.78	Cutting
B13-03	790	754	s6	49.34	43.92	6.74	8.21	Cutting
B13-03	800	764	s6	53.2	40.65	6.15	7.03	Cutting
B13-04	448	410	s13	37.77	30.26	31.97	15.37	Cutting
B13-04	456	416	s13	31.35	23.87	44.78	32.19	Cutting
B13-04	488	448	s12	38.95	43.73	17.33	13.08	Cutting
B13-04	540	500	s11	47.88	42.57	9.55	8.68	Cutting
B13-04	656	616	s7	46.17	45.21	8.62	9.27	Cutting
B13-04	816	776	s6	62.09	35.09	2.81	5.25	Cutting
B13-04	820	780	s6	56.16	39.87	3.97	6.37	Cutting
B13-04	824	784	s6	59.6	37.63	2.77	5.65	Cutting
B17-05	500	464	s9	42.12	47.04	10.84	10.87	Cutting
B17-05	535	499	s6	40.57	48.61	10.81	11.95	Cutting
B17-05	540	504	s6	49.56	44.04	6.4	8.13	Cutting
B17-05	545	509	s6	40.75	45.82	13.43	11.64	Cutting
B17-05	550	514	s6	38.76	47.59	13.65	13.38	Cutting
B17-05	610	574	s5	51.58	39.82	8.6	7.52	Cutting
B17-05	620	584	8	38.53	42.42	19.05	12.42	Cutting
B17-05	625	589	8	55.57	41.51	2.93	6.74	Cutting
B17-05	635	599	8	56.58	40.44	2.97	6.45	Cutting
B17-05	640	604	6	59.75	38.23	2.02	5.82	Cutting
B17-06	550	510	s5	45.63	46.5	7.86	9.53	Cutting
B17-06	555	515	s5	49.3	45.58	5.12	8.23	Cutting
B17-06	630	590	6	61.24	35.96	2.8	5.58	Cutting
B17-06	665	625	6	44.03	47.3	8.66	10.21	Cutting
B17-06	760	720	s3	26.14	42.07	31.78	32.05	Cutting
B17-06	765	725	s3	22.78	44.78	32.44	34.28	Cutting
B17-06	835	795	s2	32.91	50.98	16.11	17.02	Cutting
F01-01	502.9	462	s12	34.44	49.29	16.27	16.51	Cutting
F01-01	877.8	837	s5	72.62	27.23	0.15	3.81	Cutting
F01-01	914.4	874	s5	53.72	43.34	2.91	6.89	Cutting
F02-06	490	451	s10	57.78	36	6.22	5.83	Cutting
F02-06	500	461	s10	27.36	65.15	7.49	16.4	Cutting
F02-06	570	531		40.18	36.41	23.41	15.47	Cutting
F02-06	680	641	s5	26.88	52.38	20.75	18.31	Cutting
F02-06	690	651	s5	60.1	33.3	6.59	5.67	Cutting
F02-06	700	661	s5	27.94	62.05	10.01	15.52	Cutting
F02-06	710	671	s5	35.74	59.8	4.46	11.73	Cutting

Appendix H. Results of grain size analysis II

Table AH-1. This table summarizes the results of grain size analysis and the porosities, permeabilities, pore throats and gas column heights calculated using the approach outlined in Appendix F.

	Sample depth			Results grain-size analysis				Calcuted properties			
Well	MD	TVDss	Strat. Unit	Clay (<8 µm)	Silt (8-63 µm)	Sand (63-2000 µm)	Median Grain Size	Porosity	Permeability	Pore-throat radius	Gas column height
	m	m		%	%	%	µm	fraction	m2	µm	m
A12-03	468	431	s13	66.61	33.39	0	4.78	0.4632	1.94E-14	0.89	15
A12-03	469	432	s13	65.4	34.56	0.04	4.91	0.458	2.11E-15	0.89	15
A12-03	470	433	s13	61.67	36.48	1.86	5.38	0.442	2.73E-15	0.9	15
A12-03	471	434	s13	72.09	27.91	0	4.22	0.4845	1.20E-14	0.86	16
A15-04	910	872	s6	64.03	35.93	0.05	5.17	0.3669	4.98E-15	0.58	22
A15-04	915	877	s6	59.6	36.66	3.74	5.6	0.3501	6.60E-15	0.57	22
A15-04	920	882	s6	60.87	38.01	1.12	5.57	0.3539	6.00E-15	0.58	22
A15-04	945	907	s5	51.09	46.57	2.34	7.69	0.3141	9.82E-15	0.62	20
A15-04	955	917	s5	66.89	32.15	0.96	4.7	0.3697	3.60E-15	0.54	23
A15-04	960	922	s5	34.45	56.41	9.14	16.71	0.2475	1.72E-15	0.8	16
A15-04	965	927	s5	57.94	40.1	1.96	6.1	0.3365	6.40E-15	0.57	22
A18-02	440	400	s13	60.13	38.11	1.76	5.69	0.4434	3.52E-14	0.96	14
A18-02	515	475	s11	47.35	46.94	5.71	8.75	0.3686	4.66E-14	1	13
A18-02	520	480	s11	55.63	41.95	2.42	6.57	0.405	3.14E-15	0.92	15
A18-02	525	485	s11	37.24	59.02	3.74	11.93	0.3184	6.02E-14	0.99	14
A18-02	535	495	s11	55.79	39.44	4.76	6.53	0.4025	2.92E-14	0.9	15
A18-02	585	545	s9	42.6	49.77	7.63	10.71	0.3335	4.19E-14	0.99	14
A18-02	615	575	s9	39.57	55.57	4.86	11.19	0.3144	4.10E-14	0.91	15
A18-02	620	580	s9	36.64	54.96	8.4	13.7	0.2999	4.32E-15	1	13
A18-02	625	585	s9	44.84	48.34	6.82	9.87	0.3368	3.36E-14	0.93	14
A18-02	630	590	s9	36.81	58.94	4.25	12.64	0.2992	4.16E-15	0.92	14
A18-02	640	600	s8	43.31	49.73	6.95	10.41	0.3274	3.36E-14	0.92	14
A18-02	645	605	s8	35.09	56.14	8.76	14.63	0.2889	4.10E-14	0.99	13
A18-02	890	850	s6	62.45	33.67	3.88	5.28	0.3647	5.90E-15	0.59	22
B10-03	395	357	post s13	34.43	52.4	13.17	13.81	0.3289	1.10E-13	1.23	11
B10-03	450	412	s13	56.78	39.65	3.57	6.35	0.4258	4.04E-14	0.99	14
B10-03	500	462	s12	38.57	46.84	14.59	13.97	0.3292	6.43E-14	1.25	11
B10-03	550.1	512	s11	23.95	68.1	7.95	21.62	0.2474	5.90E-14	1.03	13
B10-03	606.9	569	s9	17.23	67.65	15.12	25.53	0.2062	4.05E-15	0.81	16
B10-03	620	582	s8	36.27	51.57	12.16	13.63	0.298	4.33E-14	0.98	13
B10-03	650.6	612	s7	36.77	54.04	9.19	14.29	0.2958	3.88E-14	1.01	13
B10-03	710	672	s6	62.35	32.93	4.72	4.68	0.395	1.02E-14	0.62	21
B10-03	720	682	s6	57.54	39.82	2.64	6.26	0.3741	1.33E-14	0.74	18
B13-03	375	339	post s13	50.37	45.45	4.19	7.9	0.4141	7.96E-14	1.16	12
B13-03	435	399	s13	50.6	39.28	10.12	7.81	0.4004	5.77E-14	1.06	13
B13-03	470	434	s12	42.88	45.11	12	10.7	0.3557	6.45E-14	1.13	12
B13-03	520	484	s11	53.58	41.41	5.01	7.13	0.3951	3.42E-14	0.94	14
B13-03	570	534	s9	36.12	45.22	18.66	15.14	0.3046	5.13E-14	1.15	12
B13-03	635	599	s7	40.85	47.95	11.2	11.62	0.3164	3.64E-14	0.95	14
B13-03	640	604	s7	44.64	46.45	8.92	9.78	0.3327	3.17E-14	0.9	15
B13-03	790	754	s6	49.34	43.92	6.74	8.21	0.3291	1.63E-14	0.73	18
B13-03	800	764	s6	53.2	40.65	6.15	7.03	0.3431	1.31E-14	0.69	19
B13-04	448	410	s13	37.77	30.26	31.97	15.37	0.3352	8.14E-15	1.43	9
B13-04	456	416	s13	31.35	23.87	44.78	32.19	0.3009	8.67E-15	2.37	6
B13-04	488	448	s12	38.95	43.73	17.33	13.08	0.3337	6.75E-14	1.21	11
B13-04	540	500	s11	47.88	42.57	9.55	8.68	0.3662	4.13E-14	0.98	14
B13-04	656	616	s7	46.17	45.21	8.62	9.27	0.3376	2.88E-14	0.88	15
B13-04	816	776	s6	62.09	35.09	2.81	5.25	0.3756	7.48E-15	0.62	21
B13-04	820	780	s6	56.16	39.87	3.97	6.37	0.3523	1.07E-14	0.66	20
B13-04	824	784	s6	59.6	37.63	2.77	5.65	0.3649	8.58E-15	0.63	20
B17-05	500	464	s9	42.12	47.04	10.84	10.87	0.346	5.81E-14	1.08	12
B17-05	535	499	s6	40.57	48.61	10.81	11.95	0.332	5.27E-14	1.09	12
B17-05	540	504	s6	49.56	44.04	6.4	8.13	0.373	3.79E-14	0.95	14
B17-05	545	509	s6	40.75	45.82	13.43	11.64	0.3311	5.05E-14	1.05	13
B17-05	550	514	s6	38.76	47.59	13.65	13.38	0.3207	5.21E-15	1.13	12
B17-05	610	574	s5	51.58	39.82	8.6	7.52	0.3686	2.65E-14	0.86	15
B17-05	620	584	8	38.53	42.42	19.05	12.42	0.3081	4.08E-14	0.96	14
B17-05	625	589	8	55.57	41.51	2.93	6.74	0.3828	2.05E-14	0.83	16
B17-05	635	599	8	56.58	40.44	2.97	6.45	0.3852	1.87E-15	0.81	16
B17-05	640	604	6	59.75	38.23	2.02	5.82	0.3973	1.52E-14	0.78	17
B17-06	550	510	s5	45.63	46.5	7.86	9.53	0.3539	4.32E-14	1	13
B17-06	555	515	s5	49.3	45.58	5.12	8.23	0.3697	3.67E-14	0.95	14
B17-06	630	590	6	61.24	35.96	2.8	5.58	0.4062	1.46E-14	0.78	17
B17-06	665	625	6	44.03	47.3	8.66	10.21	0.3266	3.02E-14	0.9	15
B17-06	760	720	s3	26.14	42.07	31.78	32.05	0.2332	3.12E-14	1.34	10
B17-06	765	725	s3	22.78	44.78	32.44	34.28	0.2173	2.97E-14	1.22	11
B17-06	835	795	s2	32.91	50.98	16.11	17.02	0.2549	2.44E-14	0.87	15
F01-01	502.9	462	s12	34.44	49.29	16.27	16.51	0.3085	6.92E-15	1.28	11
F01-01	877.8	837	s5	72.62	27.23	0.15	3.81	0.403	2.81E-15	0.53	24
F01-01	914.4	874	s5	53.72	43.34	2.91	6.89	0.3287	9.36E-15	0.61	21
F02-06	490	451	s10	57.78	36	6.22	5.83	0.421	3.18E-14	0.88	15
F02-06	500	461	s10	27.36	65.15	7.49	16.4	0.2724	7.29E-14	0.97	14
F02-06	570	531		40.18	36.41	23.41	15.47	0.3246	4.73E-14	1.34	10
F02-06	680	641	s5	26.88	52.38	20.75	18.31	0.2455	3.94E-14	0.86	15
F02-06	690	651	s5	60.1	33.3	6.59	5.67	0.3899	1.26E-14	0.73	18
F02-06	700	661	s5	27.94	62.05	10.01	15.52	0.2481	3.71E-14	0.75	18
F02-06	710	671	s5	35.74	59.8	4.46	11.73	0.2827	3.29E-14	0.75	17

Appendix I. BS distribution maps

10.1 Bright spot distribution and delta elements

S4

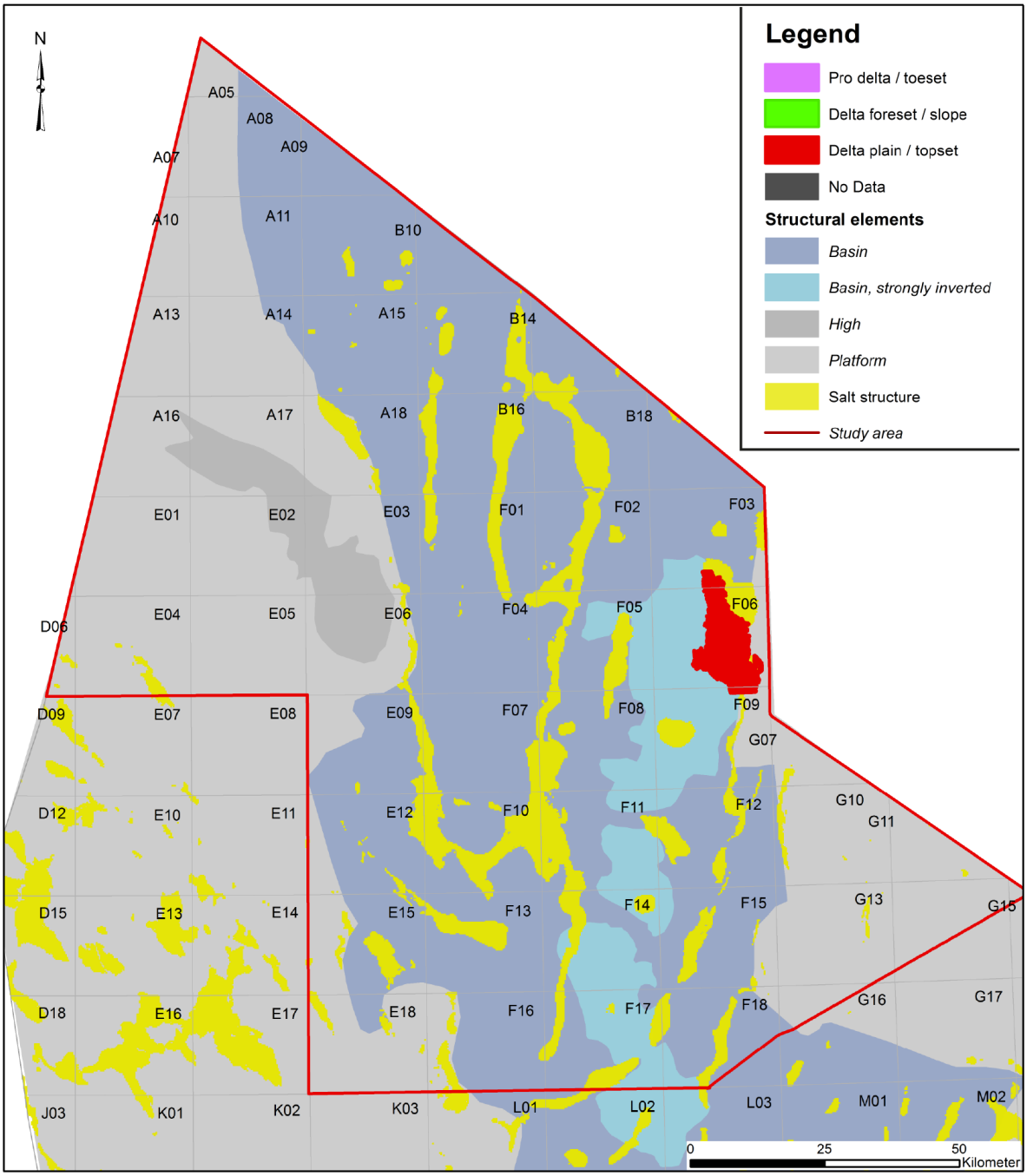

S5

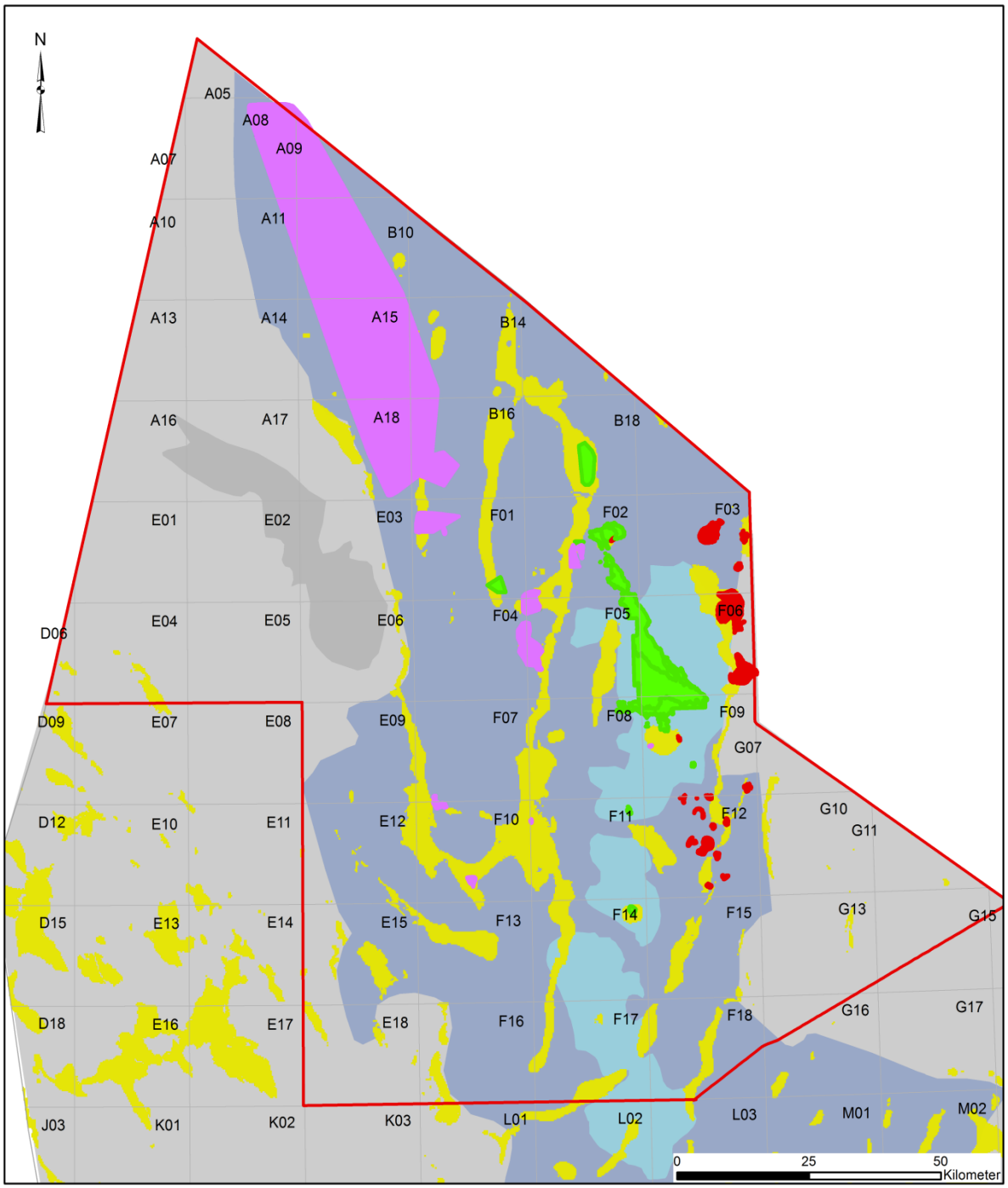
N
A05
A08
A09
A07
A10
A11
B10
A13
A14
A15
B14
A16
A17
A18
B16
B18
E01
E02
E03
F01
F02
F03
D06
E04
E05
E06
F04
F05
F06
D09
E07
E08
E09
F07
F08
F09
G07
D12
E10
E11
E12
F10
F11
F12
G10
G11
D15
E13
E14
E15
F13
F14
F15
G13
G15
D18
E16
E17
E18
F16
F17
F18
G16
G17
J03
K01
K02
K03
L01
L02
L03
M01
M02
0
25
50
Kilometer

S6

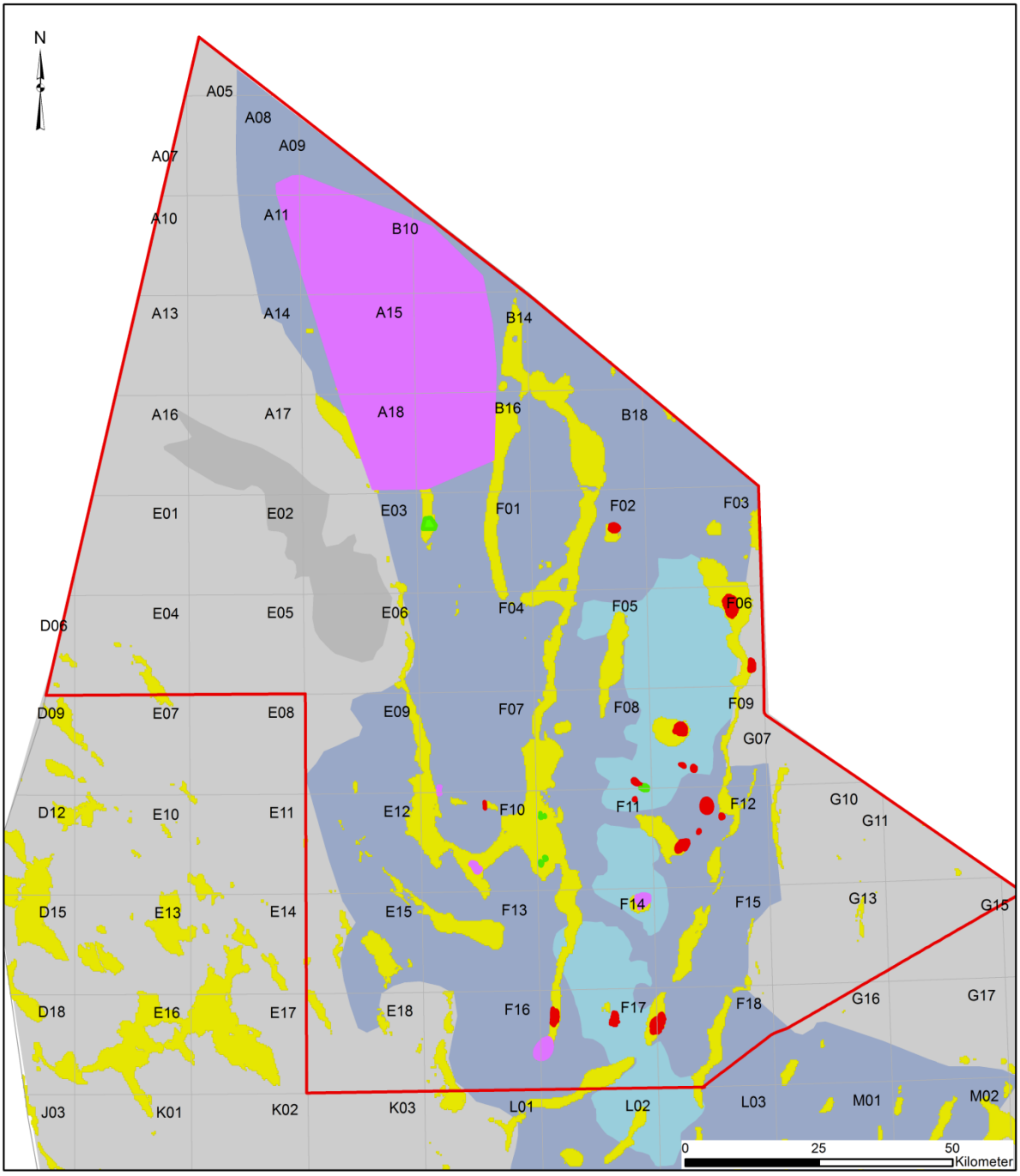
N
A05
A08
A09
A07
A10
A11
B10
A13
A14
A15
B14
A16
A17
A18
B16
B18
E01
E02
E03
F01
F02
F03
D06
E04
E05
E06
F04
F05
F06
D09
E07
E08
E09
F07
F08
F09
G07
D12
E10
E11
E12
F10
F11
F12
G10
G11
D15
E13
E14
E15
F13
F14
F15
G13
G15
D18
E16
E17
E18
F16
F17
F18
G16
G17
J03
K01
K02
K03
L01
L02
L03
M01
M02
0
25
50
Kilometer

S7

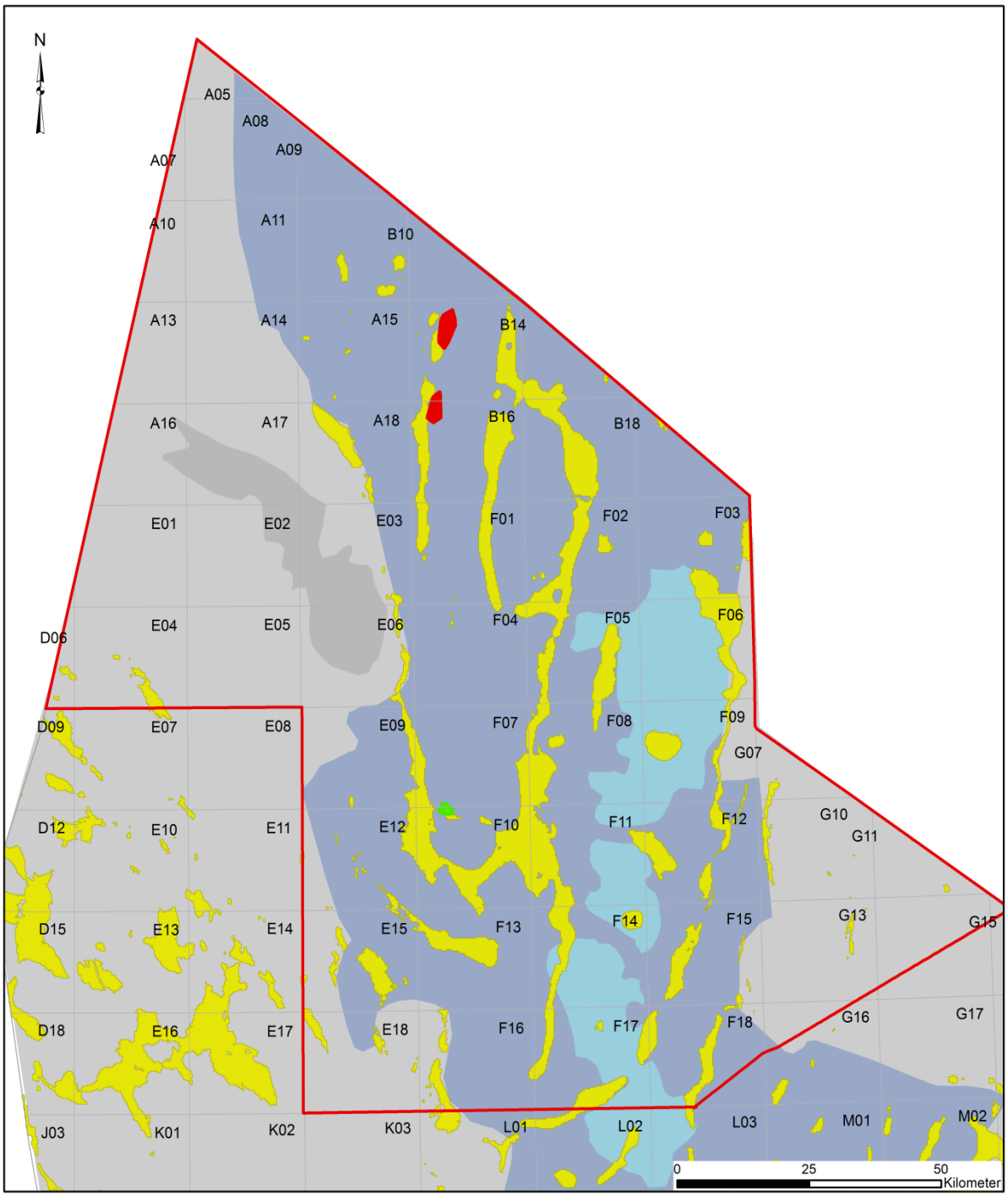
N
A05
A08
A09
A07
A10
A11
B10
A13
A14
A15
B14
A16
A17
A18
B16
B18
E01
E02
E03
F01
F02
F03
D06
E04
E05
E06
F04
F05
F06
D09
E07
E08
E09
F07
F08
F09
G07
D12
E10
E11
E12
F10
F11
F12
G10
G11
D15
E13
E14
E15
F13
F14
F15
G13
G15
D18
E16
E17
E18
F16
F17
F18
G16
G17
J03
K01
K02
K03
L01
L02
L03
M01
M02
0
25
50
Kilometer

S8

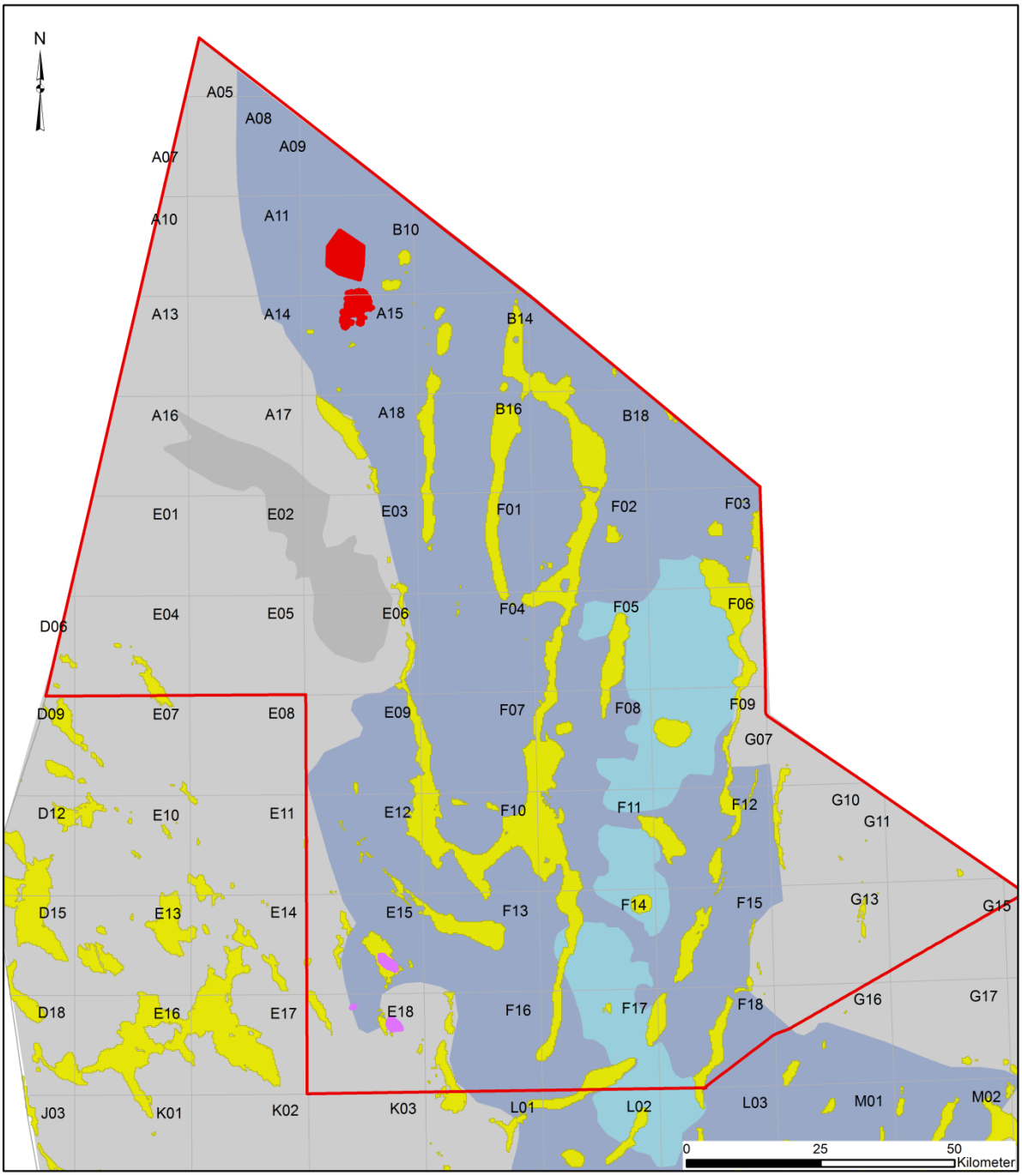
N
A05
A08
A09
A07
A10
A11
B10
A13
A14
A15
B14
A16
A17
A18
B16
B18
E01
E02
E03
F01
F02
F03
D06
E04
E05
E06
F04
F05
F06
D09
E07
E08
E09
F07
F08
F09
G07
D12
E10
E11
E12
F10
F11
F12
G10
G11
D15
E13
E14
E15
F13
F14
F15
G13
G15
D18
E16
E17
E18
F16
F17
F18
G16
G17
J03
K01
K02
K03
L01
L02
L03
M01
M02
0
25
50
Kilometer

S9

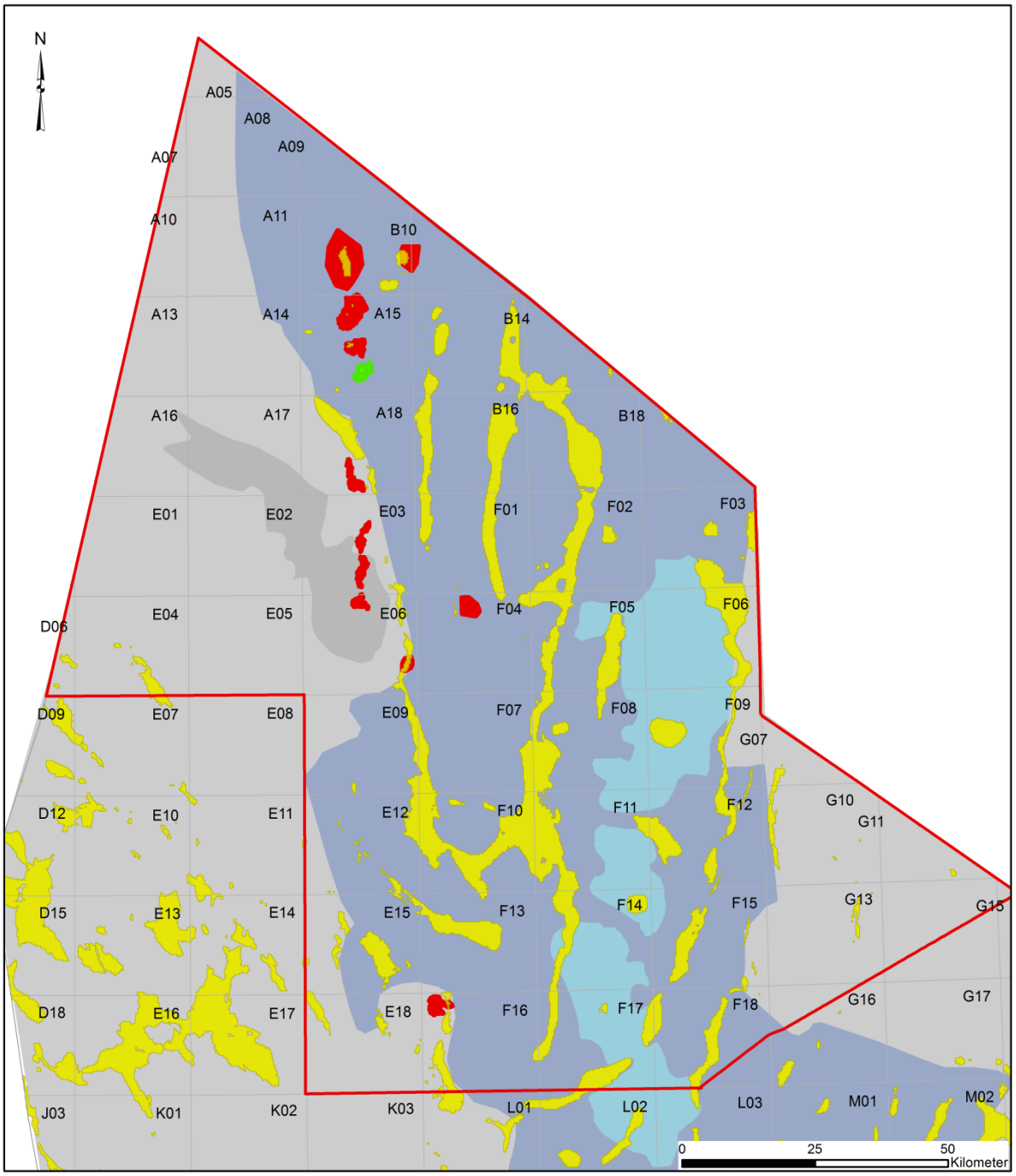
N
A05
A08
A09
A07
A10
A11
B10
A13
A14
A15
B14
A16
A17
A18
B16
B18
E01
E02
E03
F01
F02
F03
D06
E04
E05
E06
F04
F05
F06
D09
E07
E08
E09
F07
F08
F09
G07
D12
E10
E11
E12
F10
F11
F12
G10
G11
D15
E13
E14
E15
F13
F14
F15
G13
G15
D18
E16
E17
E18
F16
F17
F18
G16
G17
J03
K01
K02
K03
L01
L02
L03
M01
M02
0
25
50
Kilometer

S10

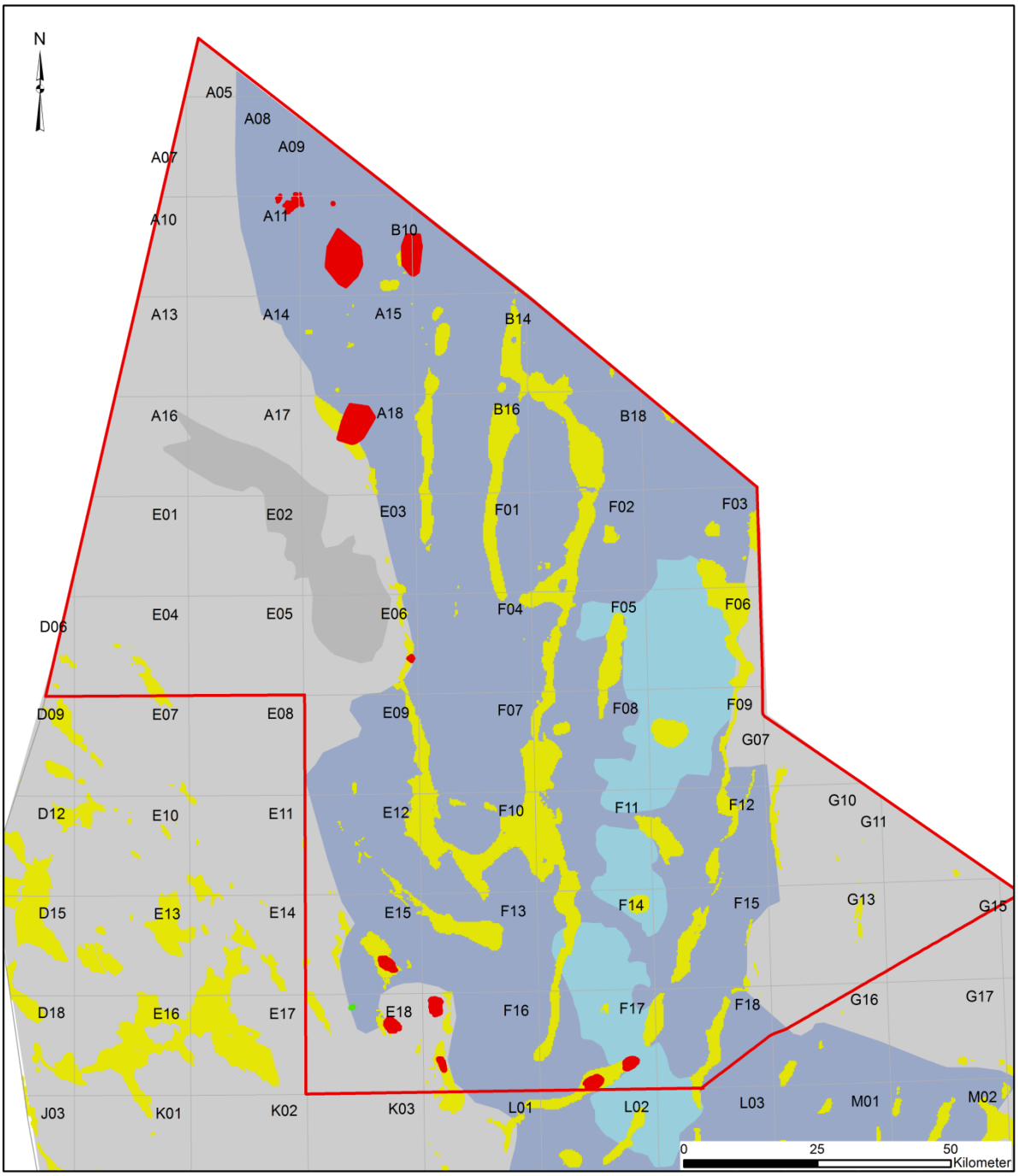
N
A05
A08
A09
A07
A10
A11
B10
A13
A14
A15
B14
A16
A17
A18
B16
B18
E01
E02
E03
F01
F02
F03
D06
E04
E05
E06
F04
F05
F06
D09
E07
E08
E09
F07
F08
F09
G07
D12
E10
E11
E12
F10
F11
F12
G10
G11
D15
E13
E14
E15
F13
F14
F15
G13
G15
D18
E16
E17
E18
F16
F17
F18
G16
G17
J03
K01
K02
K03
L01
L02
L03
M01
M02
0
25
50
Kilometer

S11

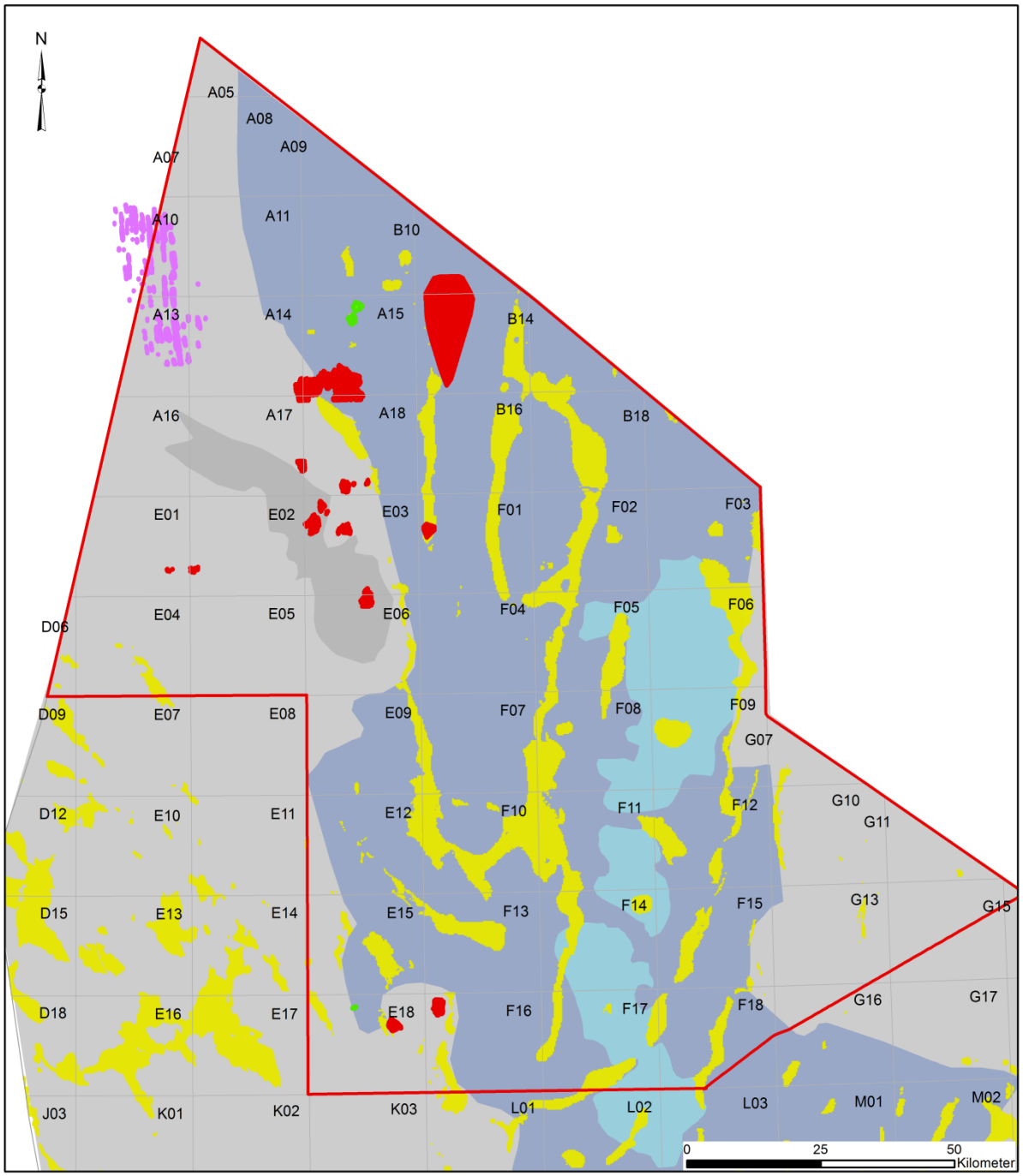
N
A05
A08
A09
A07
A10
A11
B10
A13
A14
A15
B14
A16
A17
A18
B16
B18
E01
E02
E03
F01
F02
F03
E04
E05
E06
F04
F05
F06
D06
D09
E07
E08
E09
F07
F08
F09
G07
D12
E10
E11
E12
F10
F11
F12
G10
G11
D15
E13
E14
E15
F13
F14
F15
G13
G15
D18
E16
E17
E18
F16
F17
F18
G16
G17
J03
K01
K02
K03
L01
L02
L03
M01
M02
0
25
50
Kilometer

S12

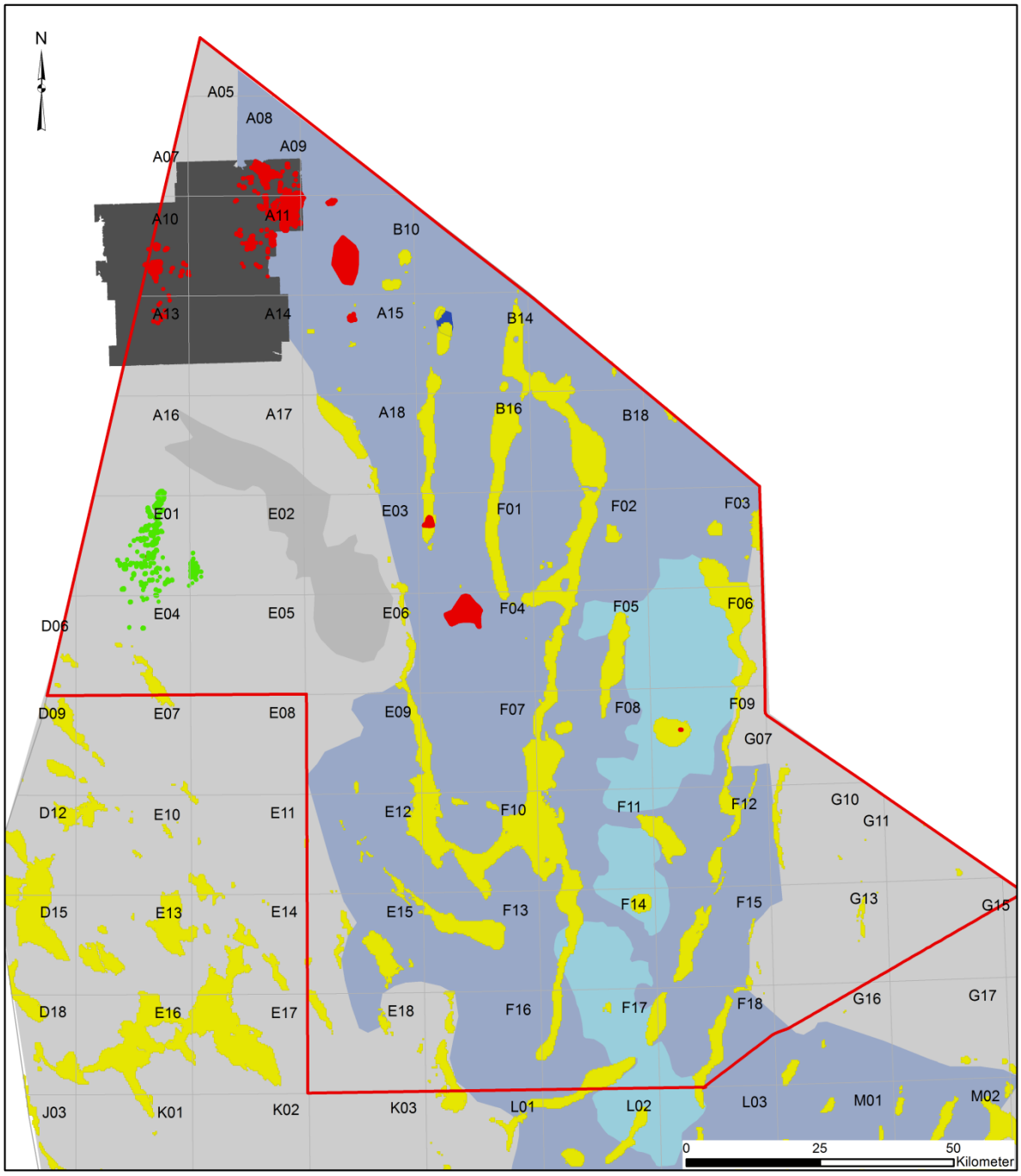
N
A05
A08
A09
A07
A10
A11
B10
A13
A14
A15
B14
A16
A17
A18
B16
B18
E01
E02
E03
F01
F02
F03
D06
E04
E05
E06
F04
F05
F06
D09
E07
E08
E09
F07
F08
F09
G07
D12
E10
E11
E12
F10
F11
F12
G10
G11
D15
E13
E14
E15
F13
F14
F15
G13
G15
D18
E16
E17
E18
F16
F17
F18
G16
G17
J03
K01
K02
K03
L01
L02
L03
M01
M02
0
25
50
Kilometer

S13

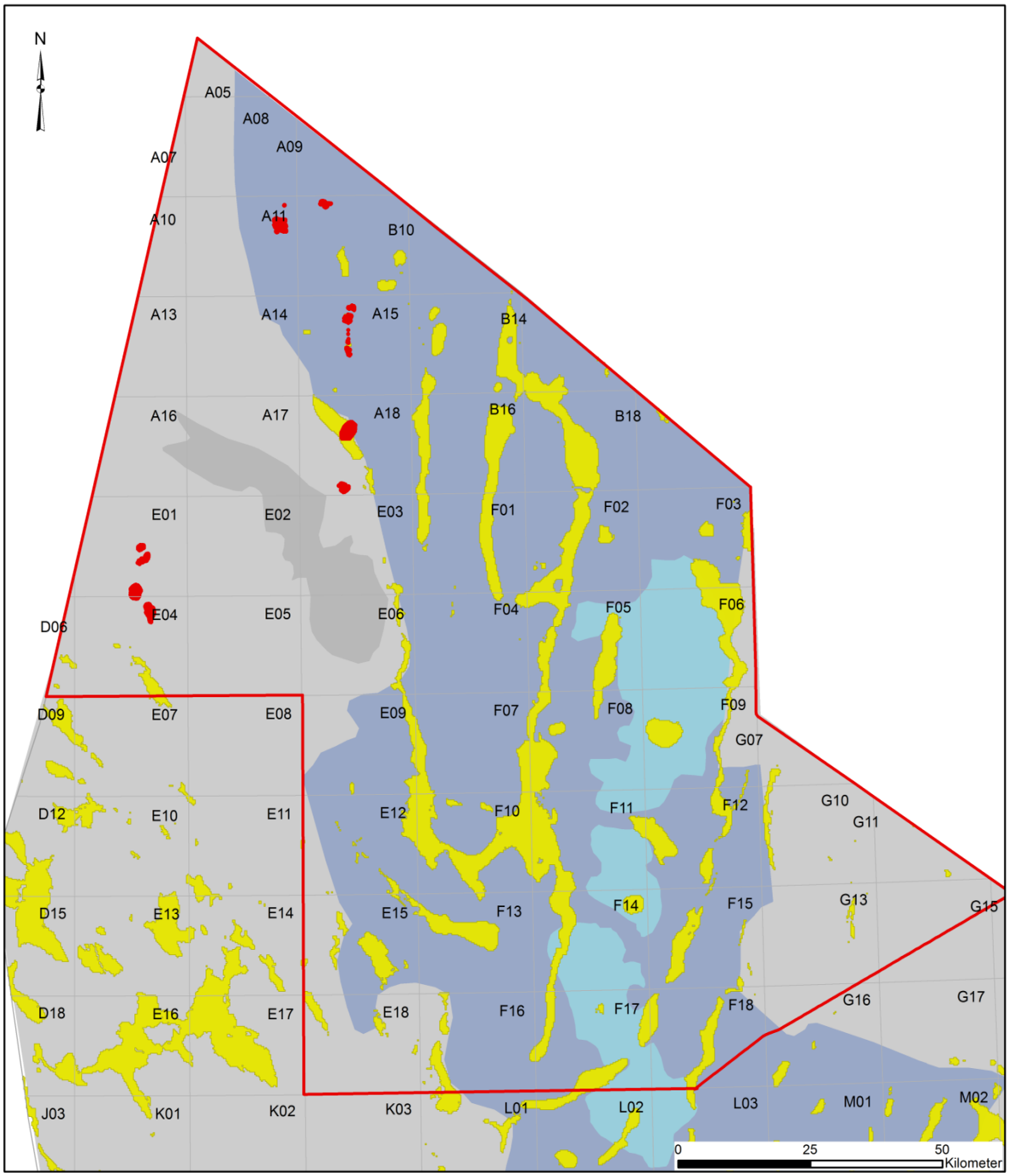
N
A05
A08
A09
A07
A10
A11
B10
A13
A14
A15
B14
A16
A17
A18
B16
B18
E01
E02
E03
F01
F02
F03
D06
E04
E05
E06
F04
F05
F06
D09
E07
E08
E09
F07
F08
F09
G07
D12
E10
E11
E12
F10
F11
F12
G10
G11
D15
E13
E14
E15
F13
F14
F15
G13
G15
D18
E16
E17
E18
F16
F17
F18
G16
G17
J03
K01
K02
K03
L01
L02
L03
M01
M02
0
25
50
Kilometer

10.2 Distribution of Bright spot types

S4

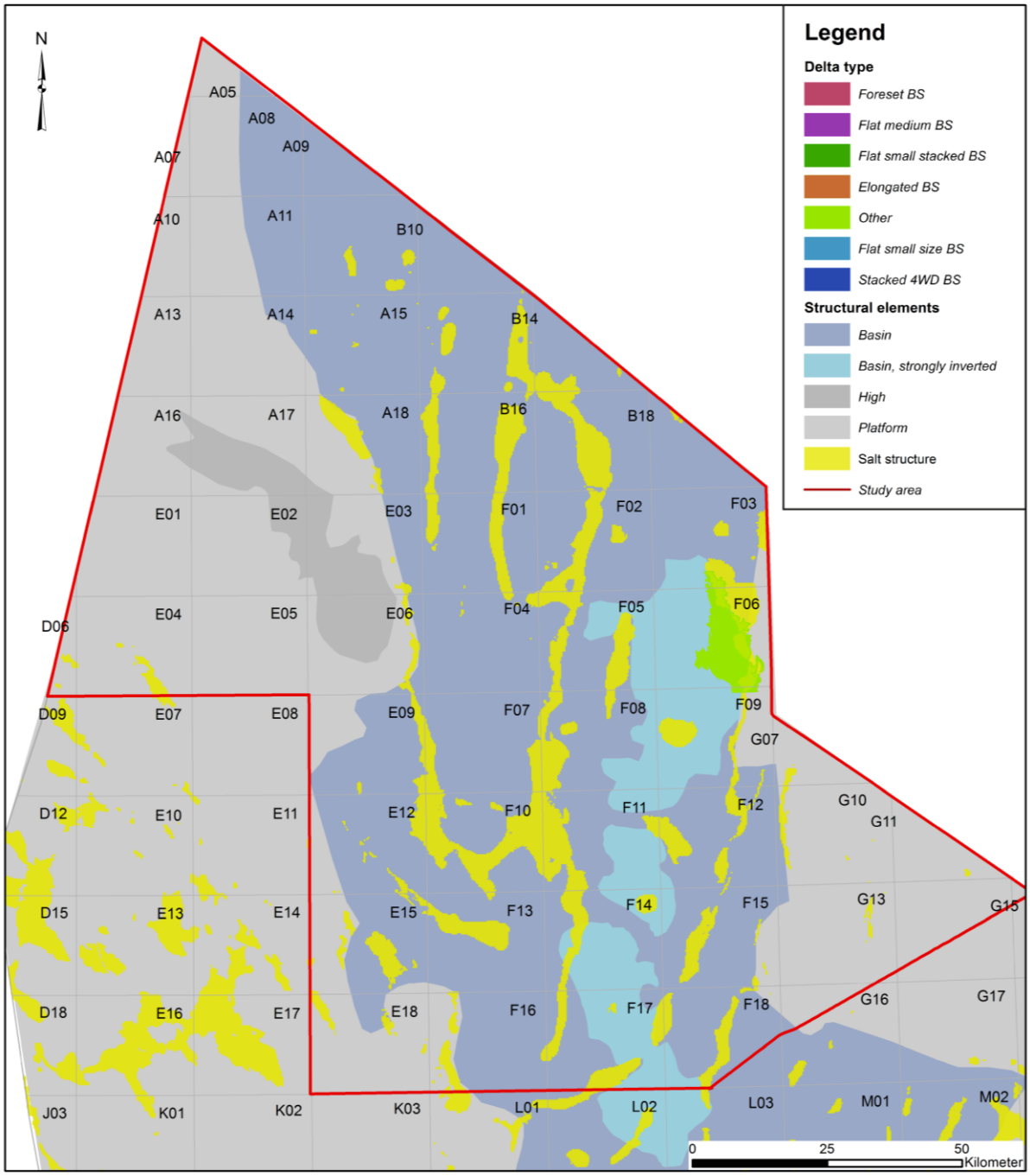

S5

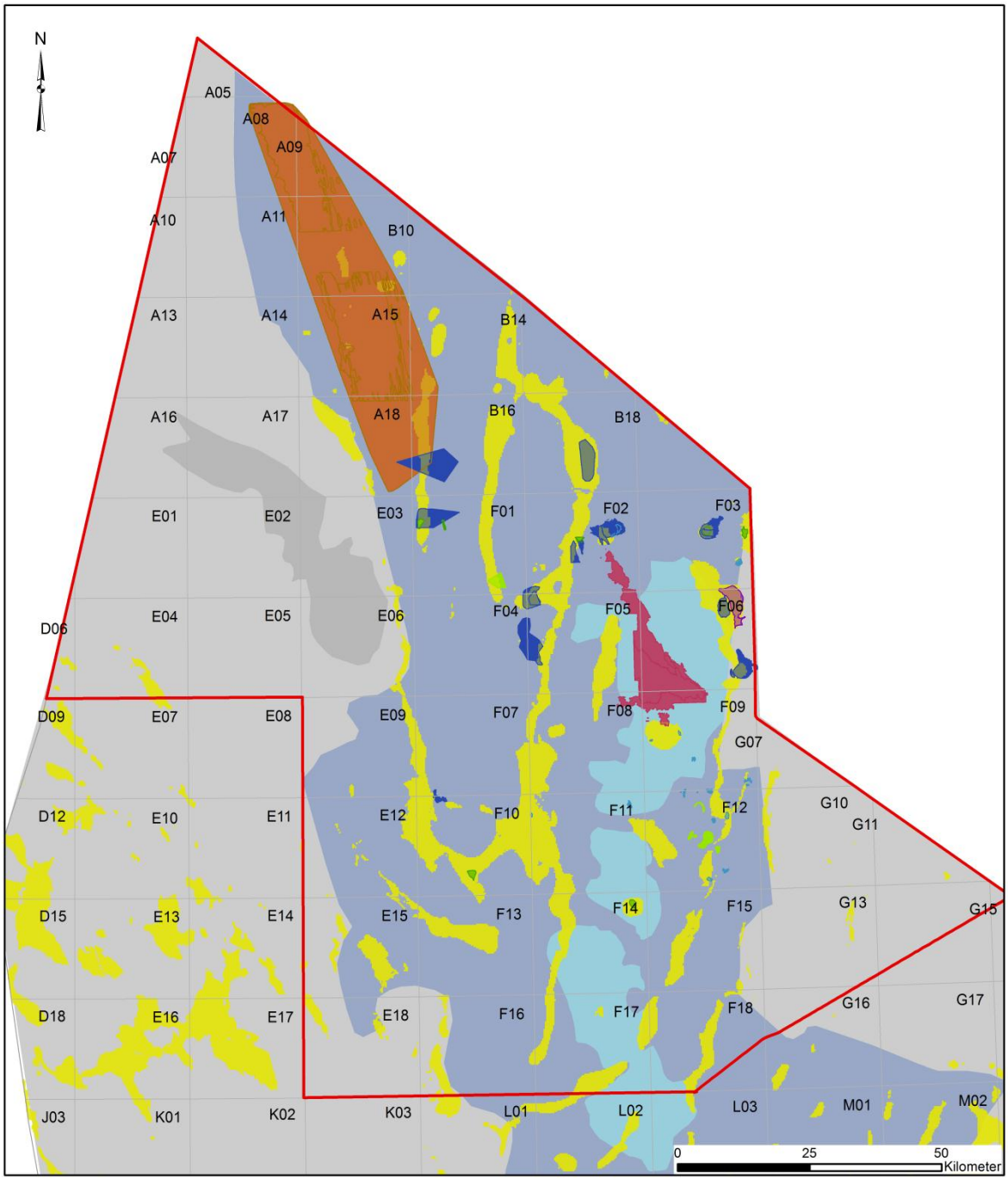
N
A05
A08
A09
A07
A10
A11
B10
A13
A14
A15
B14
A16
A17
A18
B16
B18
E01
E02
E03
F01
F02
F03
D06
E04
E05
E06
F04
F05
F06
D09
E07
E08
E09
F07
F08
F09
G07
D12
E10
E11
E12
F10
F11
F12
G10
G11
D15
E13
E14
E15
F13
F14
F15
G13
G15
D18
E16
E17
E18
F16
F17
F18
G16
G17
J03
K01
K02
K03
L01
L02
L03
M01
M02
0
25
50
Kilometer

S6

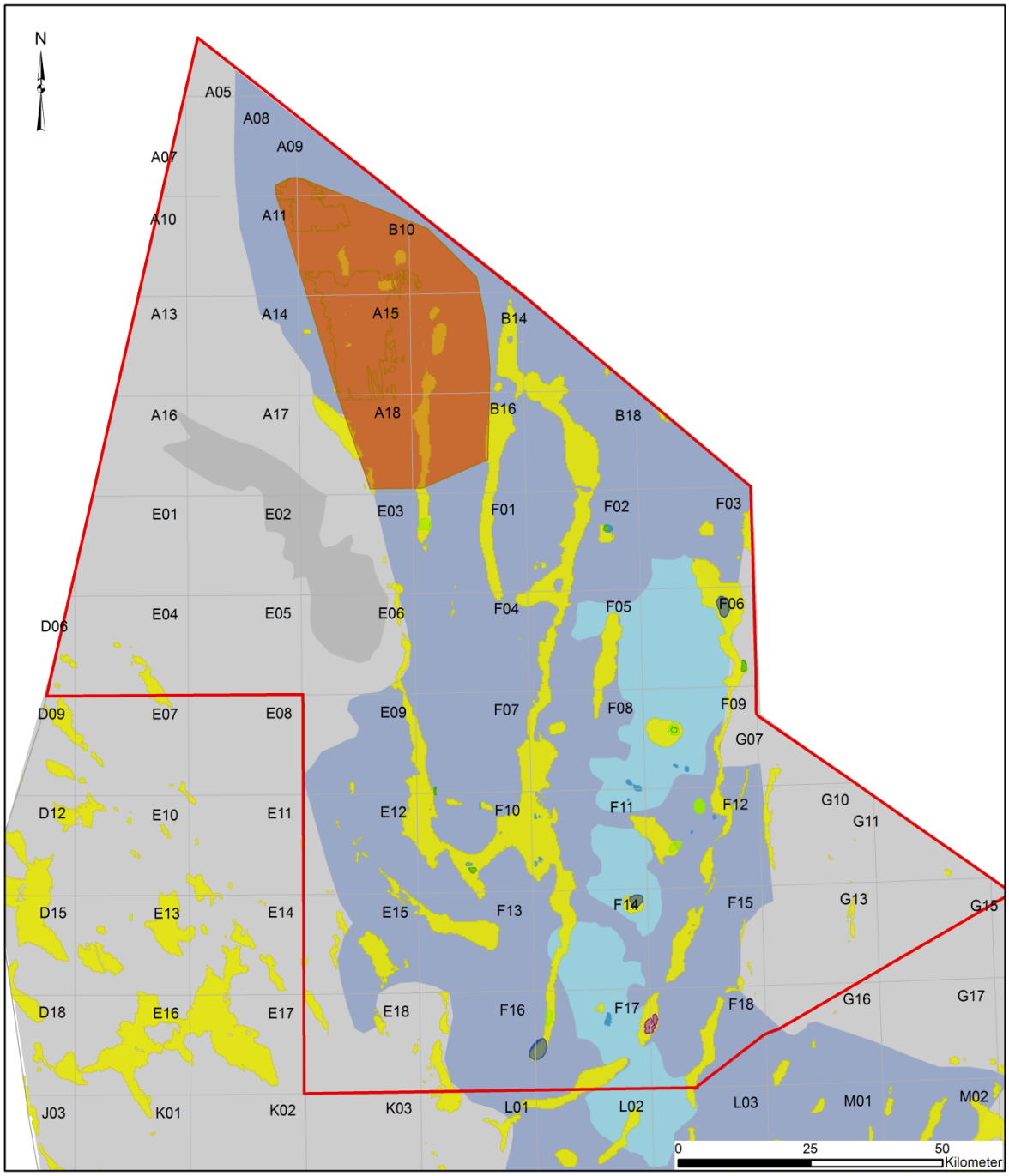
N
A05
A08
A09
A07
A10
A11
B10
A13
A14
A15
B14
A16
A17
A18
B16
B18
E01
E02
E03
F01
F02
F03
D06
E04
E05
E06
F04
F05
F06
D09
E07
E08
E09
F07
F08
F09
G07
D12
E10
E11
E12
F10
F11
F12
G10
G11
D15
E13
E14
E15
F13
F14
F15
G13
G15
D18
E16
E17
E18
F16
F17
F18
G16
G17
J03
K01
K02
K03
L01
L02
L03
M01
M02
0
25
50
Kilometer

S7

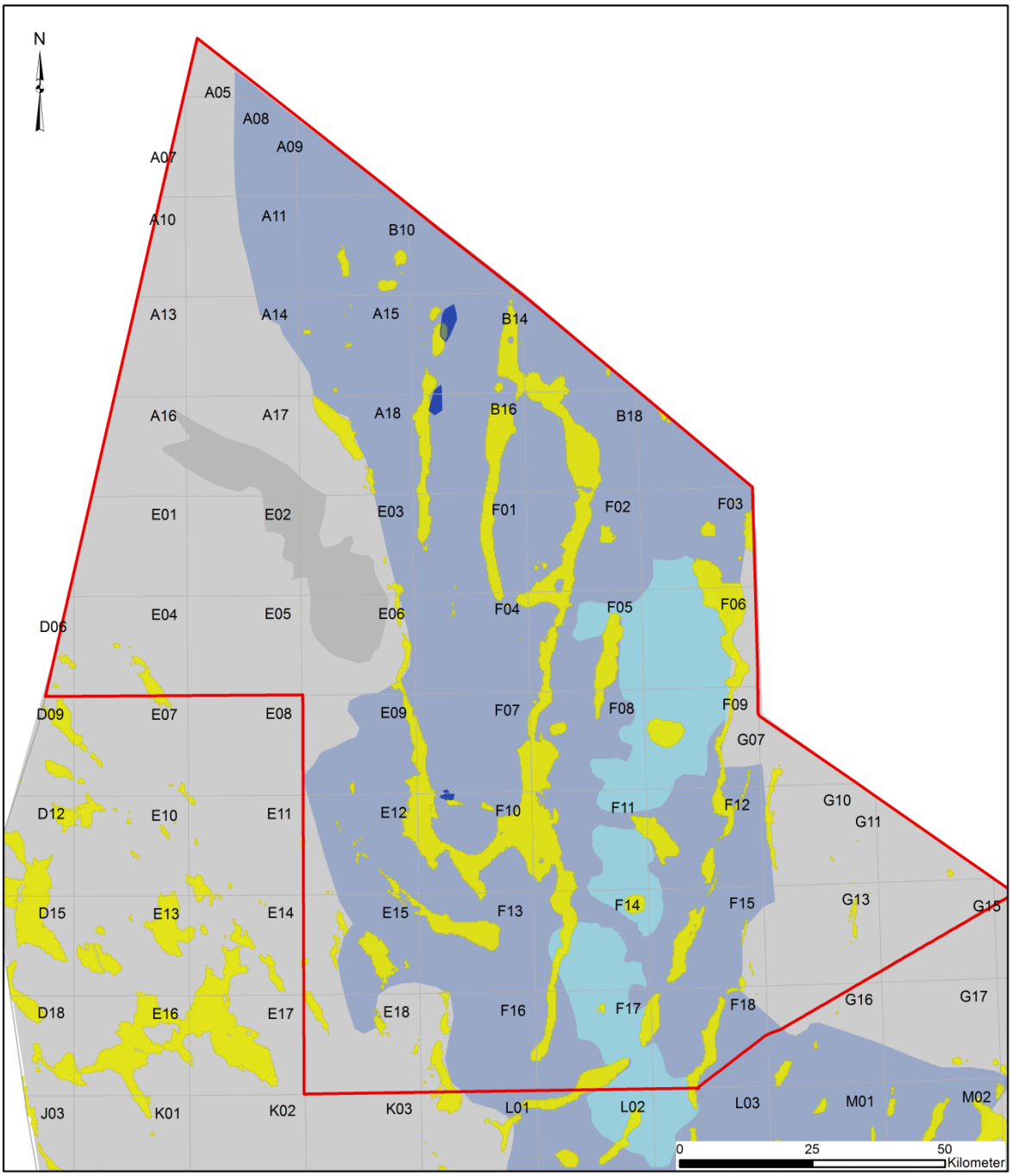
N
A05
A08
A09
A07
A10
A11
B10
A13
A14
A15
B14
A16
A17
A18
B16
B18
E01
E02
E03
F01
F02
F03
D06
E04
E05
E06
F04
F05
F06
D09
E07
E08
E09
F07
F08
F09
G07
D12
E10
E11
E12
F10
F11
F12
G10
G11
D15
E13
E14
E15
F13
F14
F15
G13
G15
D18
E16
E17
E18
F16
F17
F18
G16
G17
J03
K01
K02
K03
L01
L02
L03
M01
M02
0
25
50
Kilometer

S8

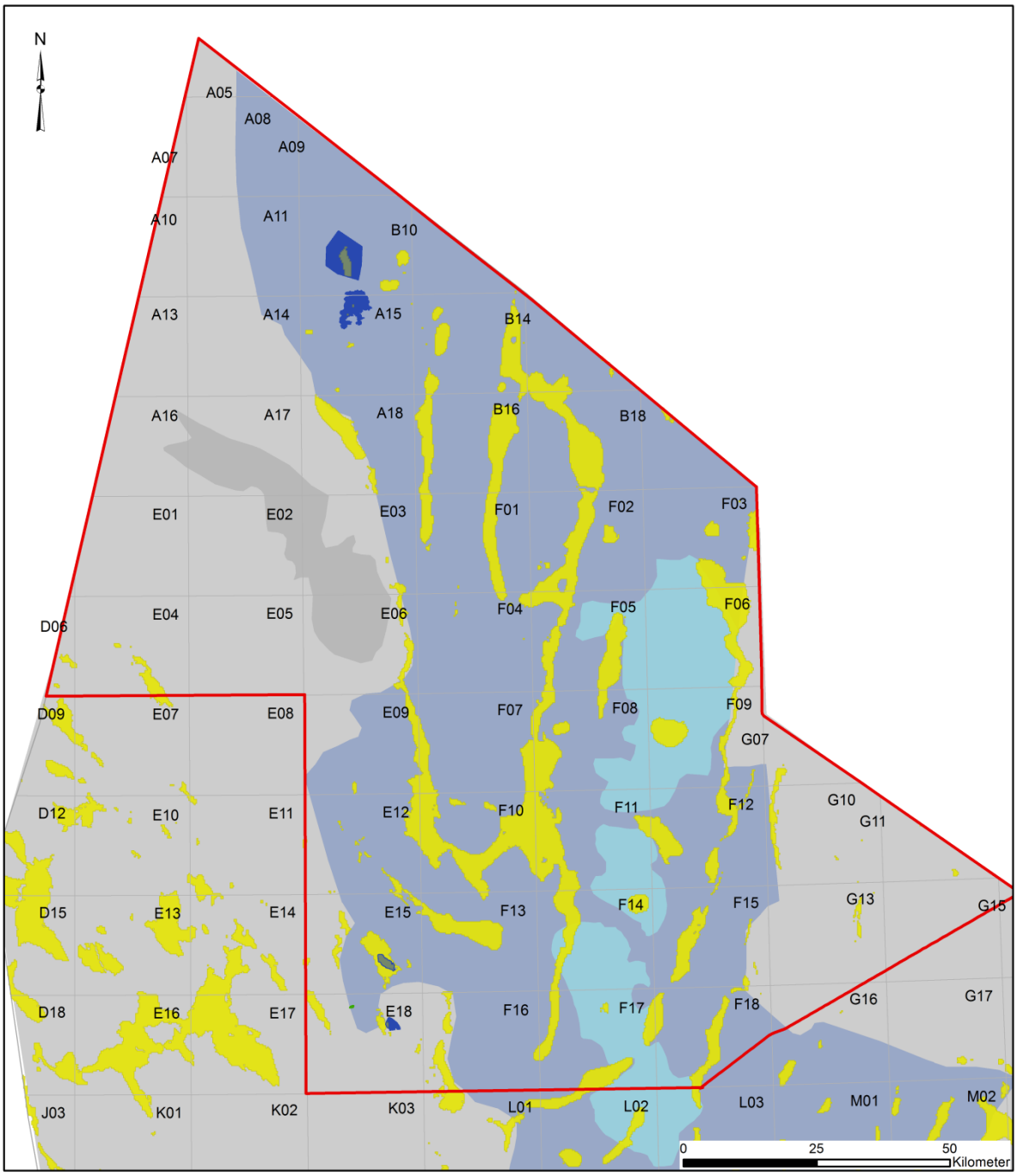
N
A05
A08
A09
A07
A10
A11
B10
A13
A14
A15
B14
A16
A17
A18
B16
B18
E01
E02
E03
F01
F02
F03
D06
E04
E05
E06
F04
F05
F06
D09
E07
E08
E09
F07
F08
F09
G07
D12
E10
E11
E12
F10
F11
F12
G10
G11
D15
E13
E14
E15
F13
F14
F15
G13
G15
D18
E16
E17
E18
F16
F17
F18
G16
G17
J03
K01
K02
K03
L01
L02
L03
M01
M02
0
25
50
Kilometer

S9

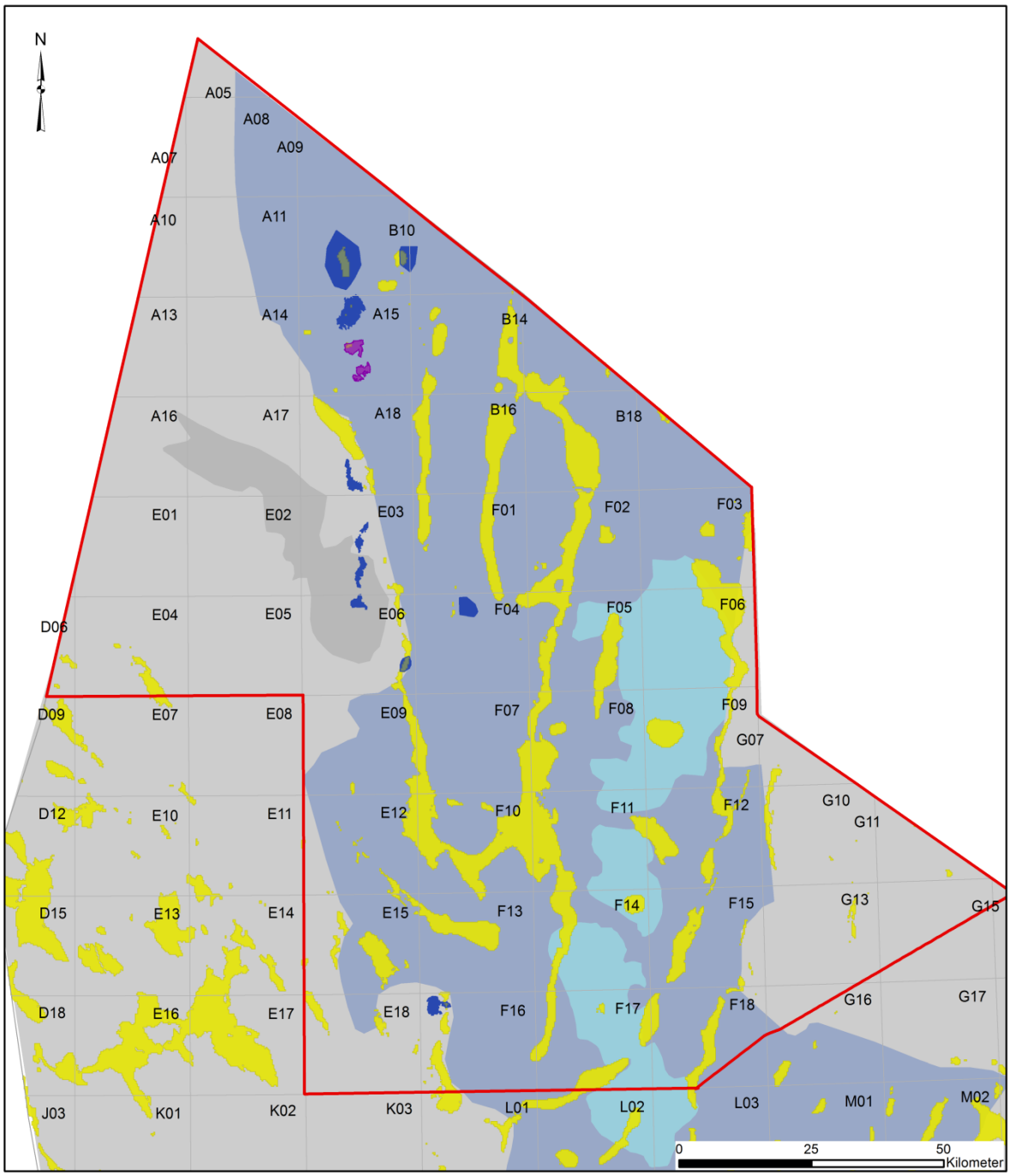
N
A05
A08
A09
A07
A10
A11
B10
A13
A14
A15
B14
A16
A17
A18
B16
B18
E01
E02
E03
F01
F02
F03
D06
E04
E05
E06
F04
F05
F06
D09
E07
E08
E09
F07
F08
F09
G07
D12
E10
E11
E12
F10
F11
F12
G10
G11
D15
E13
E14
E15
F13
F14
F15
G13
G15
D18
E16
E17
E18
F16
F17
F18
G16
G17
J03
K01
K02
K03
L01
L02
L03
M01
M02
0
25
50
Kilometer

S10

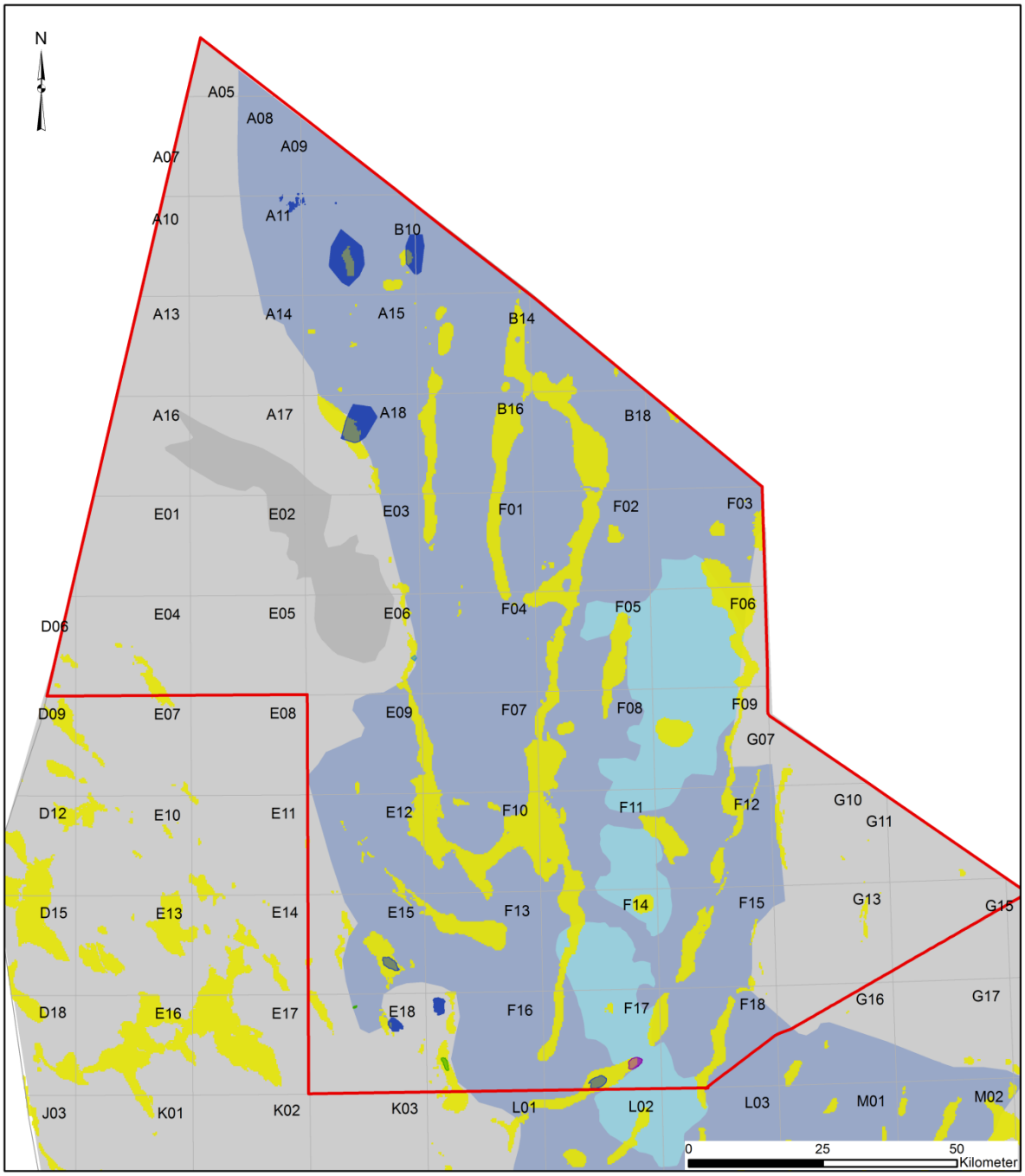
N
A05
A08
A09
A07
A10
A11
B10
A13
A14
A15
B14
A16
A17
A18
B16
B18
E01
E02
E03
F01
F02
F03
D06
E04
E05
E06
F04
F05
F06
D09
E07
E08
E09
F07
F08
F09
G07
D12
E10
E11
E12
F10
F11
F12
G10
G11
D15
E13
E14
E15
F13
F14
F15
G13
G15
D18
E16
E17
E18
F16
F17
F18
G16
G17
J03
K01
K02
K03
L01
L02
L03
M01
M02
0
25
50
Kilometer

S11

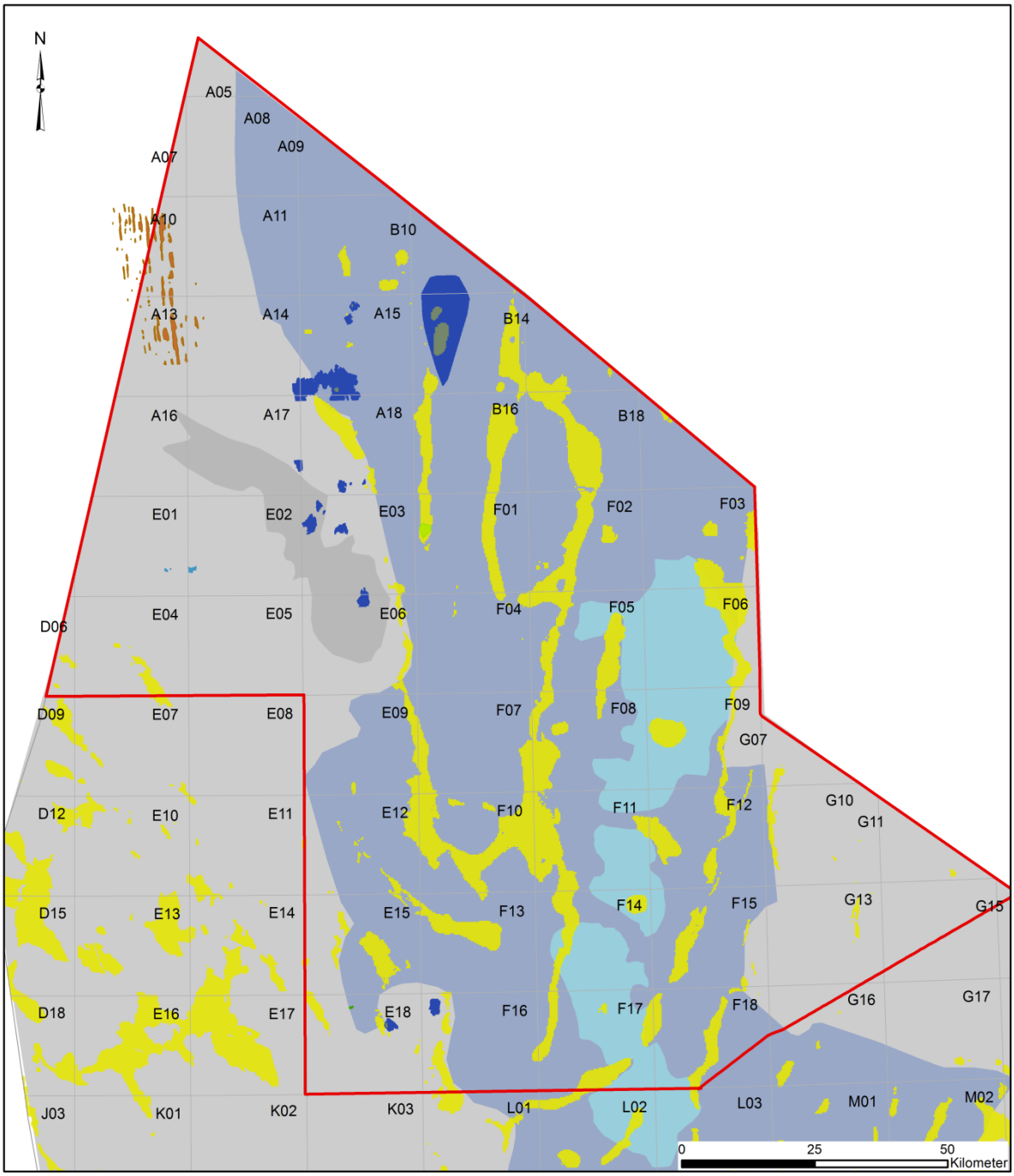
N
A05
A08
A09
A07
A10
A11
B10
A13
A14
A15
B14
A16
A17
A18
B16
B18
E01
E02
E03
F01
F02
F03
D06
E04
E05
E06
F04
F05
F06
D09
E07
E08
E09
F07
F08
F09
G07
D12
E10
E11
E12
F10
F11
F12
G10
G11
D15
E13
E14
E15
F13
F14
F15
G13
G15
D18
E16
E17
E18
F16
F17
F18
G16
G17
J03
K01
K02
K03
L01
L02
L03
M01
M02
0
25
50
Kilometer

S12

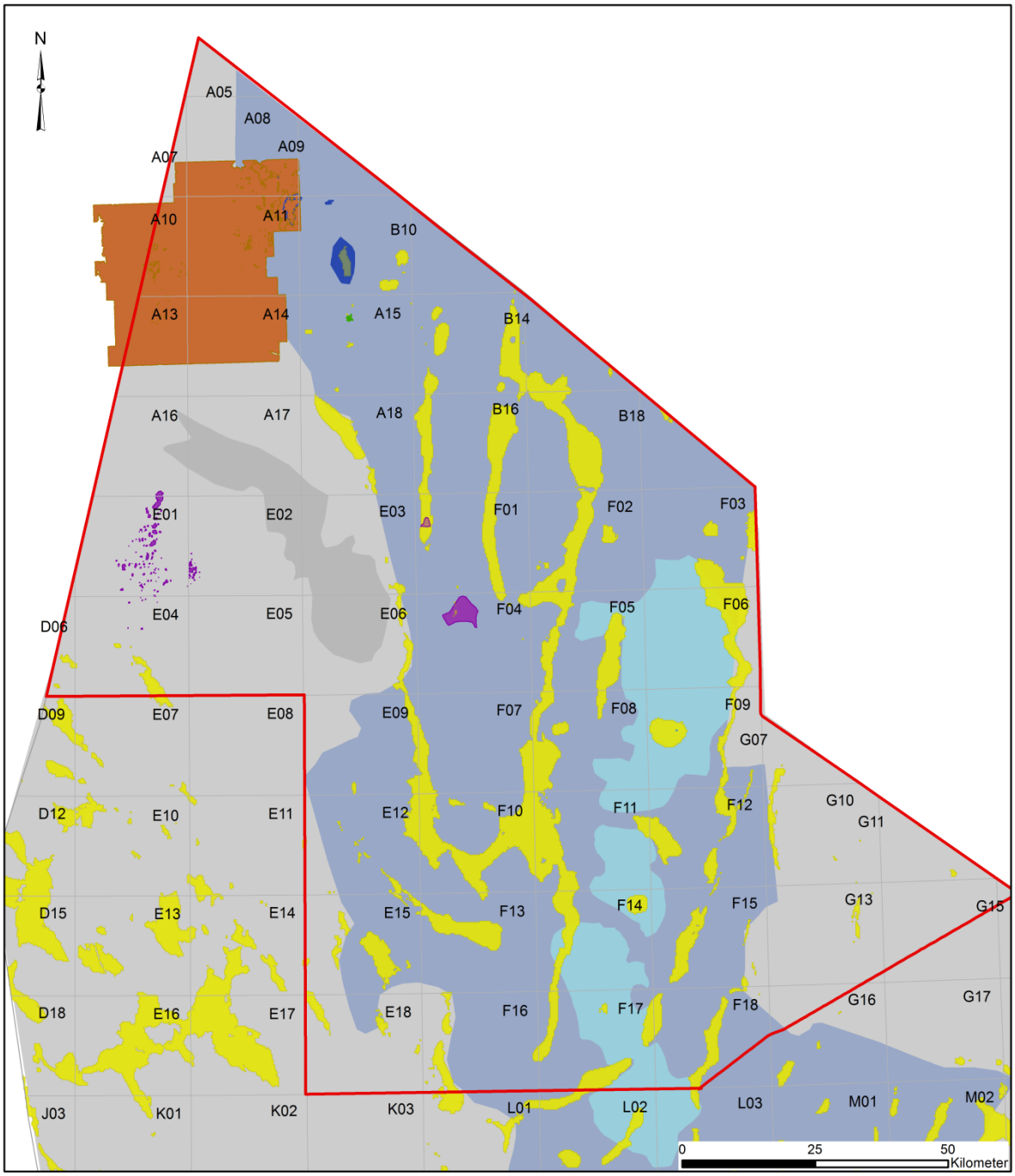
N
A05
A08
A09
A07
A10
A11
B10
A13
A14
A15
B14
A16
A17
A18
B16
B18
E01
E02
E03
F01
F02
F03
D06
E04
E05
E06
F04
F05
F06
D09
E07
E08
E09
F07
F08
F09
G07
D12
E10
E11
E12
F10
F11
F12
G10
G11
D15
E13
E14
E15
F13
F14
F15
G13
G15
D18
E16
E17
E18
F16
F17
F18
G16
G17
J03
K01
K02
K03
L01
L02
L03
M01
M02
0
25
50
Kilometer

S13

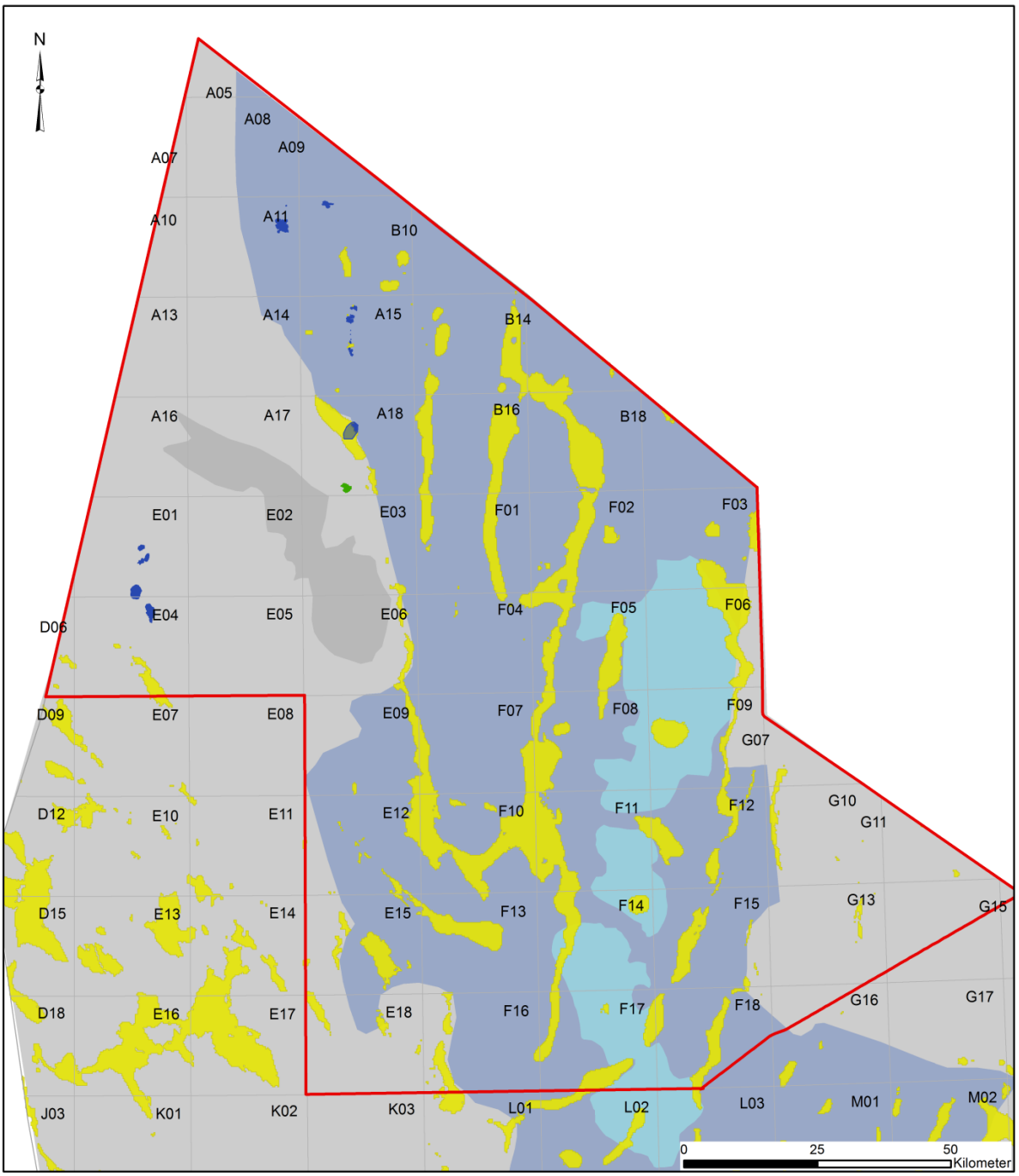
N
A05
A08
A09
A07
A10
A11
B10
A13
A14
A15
B14
A16
A17
A18
B16
B18
E01
E02
E03
F01
F02
F03
D06
E04
E05
E06
F04
F05
F06
D09
E07
E08
E09
F07
F08
F09
G07
D12
E10
E11
E12
F10
F11
F12
G10
G11
D15
E13
E14
E15
F13
F14
F15
G13
G15
D18
E16
E17
E18
F16
F17
F18
G16
G17
J03
K01
K02
K03
L01
L02
L03
M01
M02
0
25
50
Kilometer

10.3 Bright spot distribution and lithofacies

S4

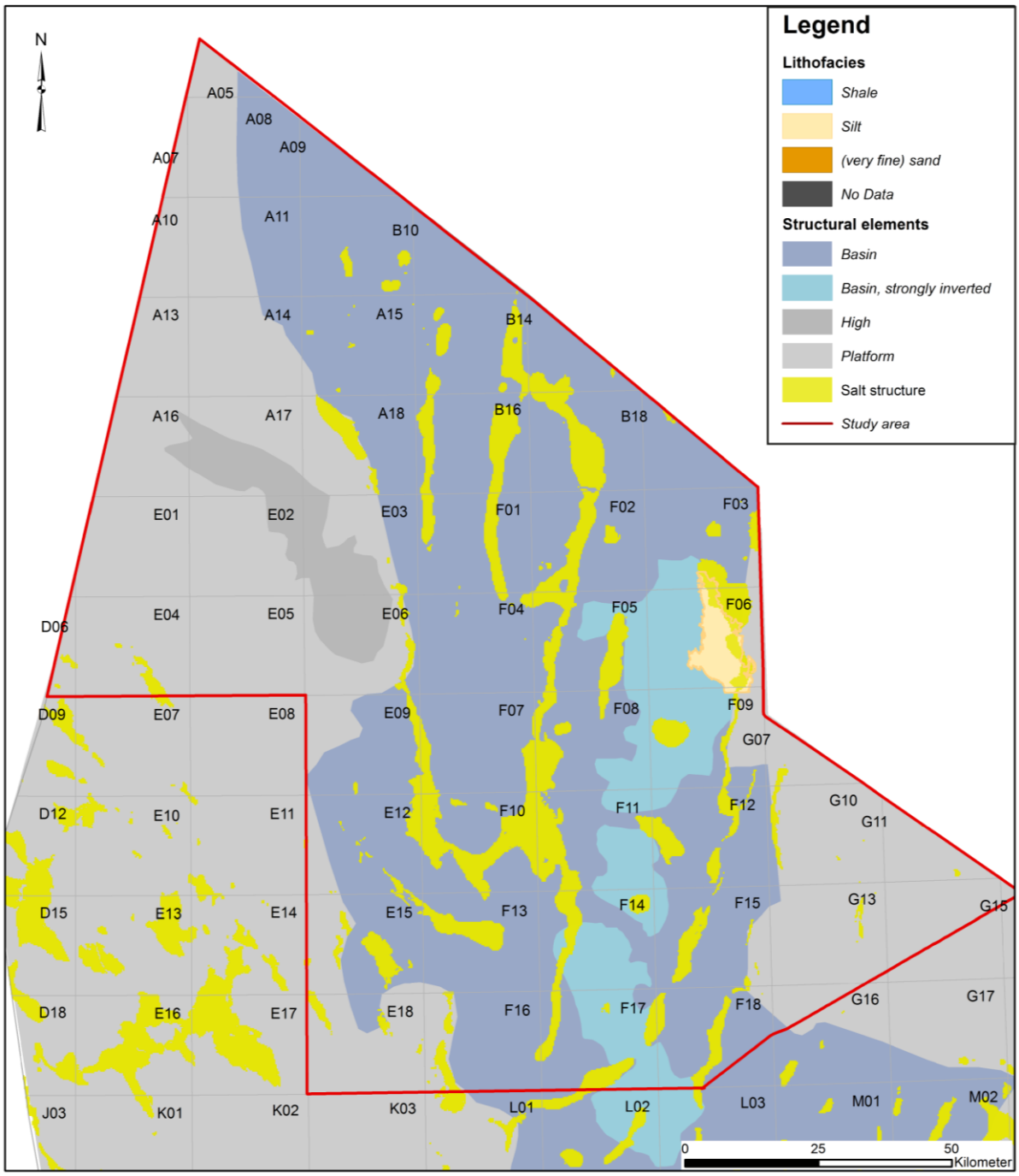

S5

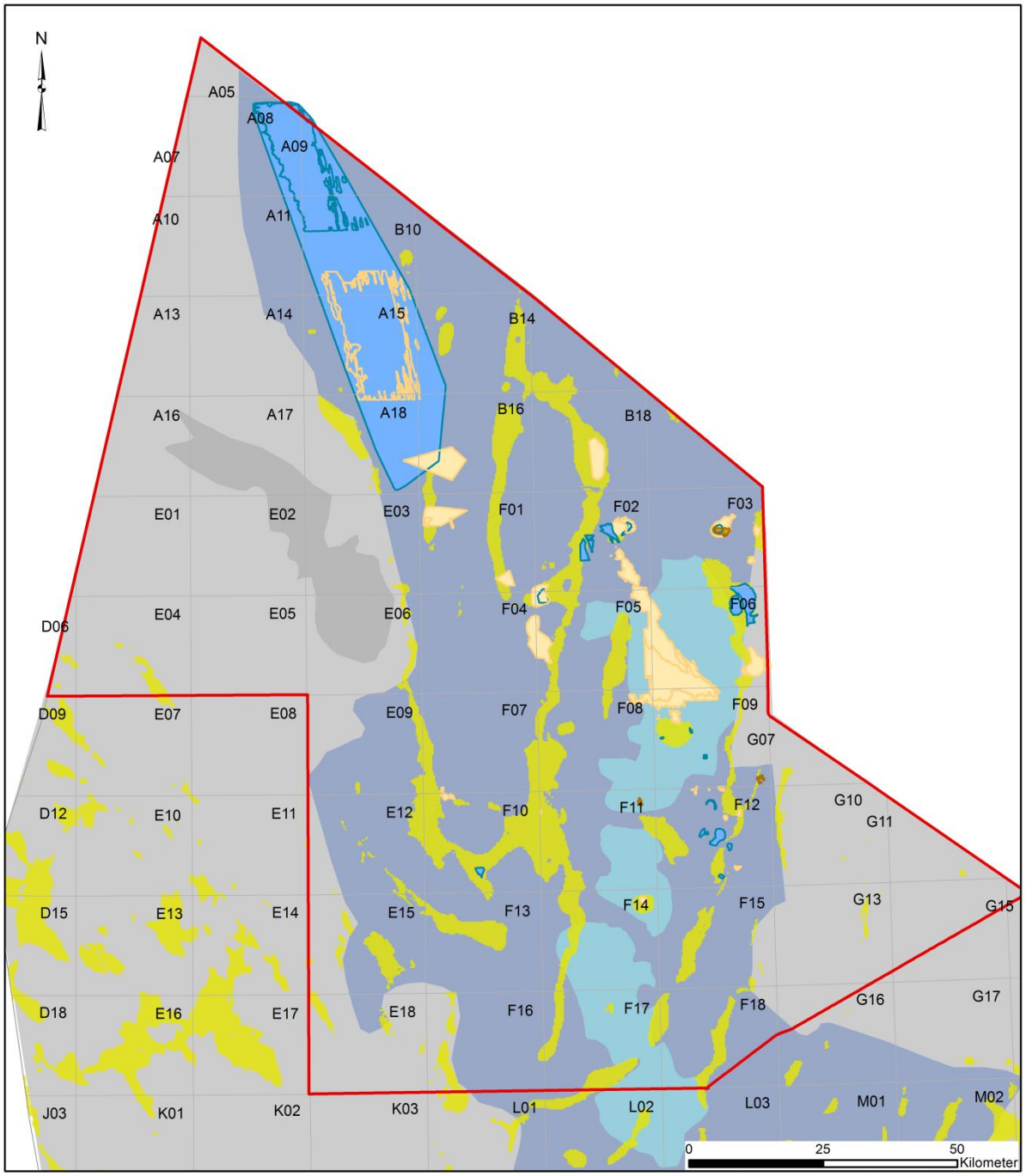
N
A05
A08
A09
A07
A10
A11
B10
A13
A14
A15
B14
A16
A17
A18
B16
B18
E01
E02
E03
F01
F02
F03
D06
E04
E05
E06
F04
F05
F06
D09
E07
E08
E09
F07
F08
F09
G07
D12
E10
E11
E12
F10
F11
F12
G10
G11
D15
E13
E14
E15
F13
F14
F15
G13
G15
D18
E16
E17
E18
F16
F17
F18
G16
G17
J03
K01
K02
K03
L01
L02
L03
M01
M02
0
25
50
Kilometer

S6

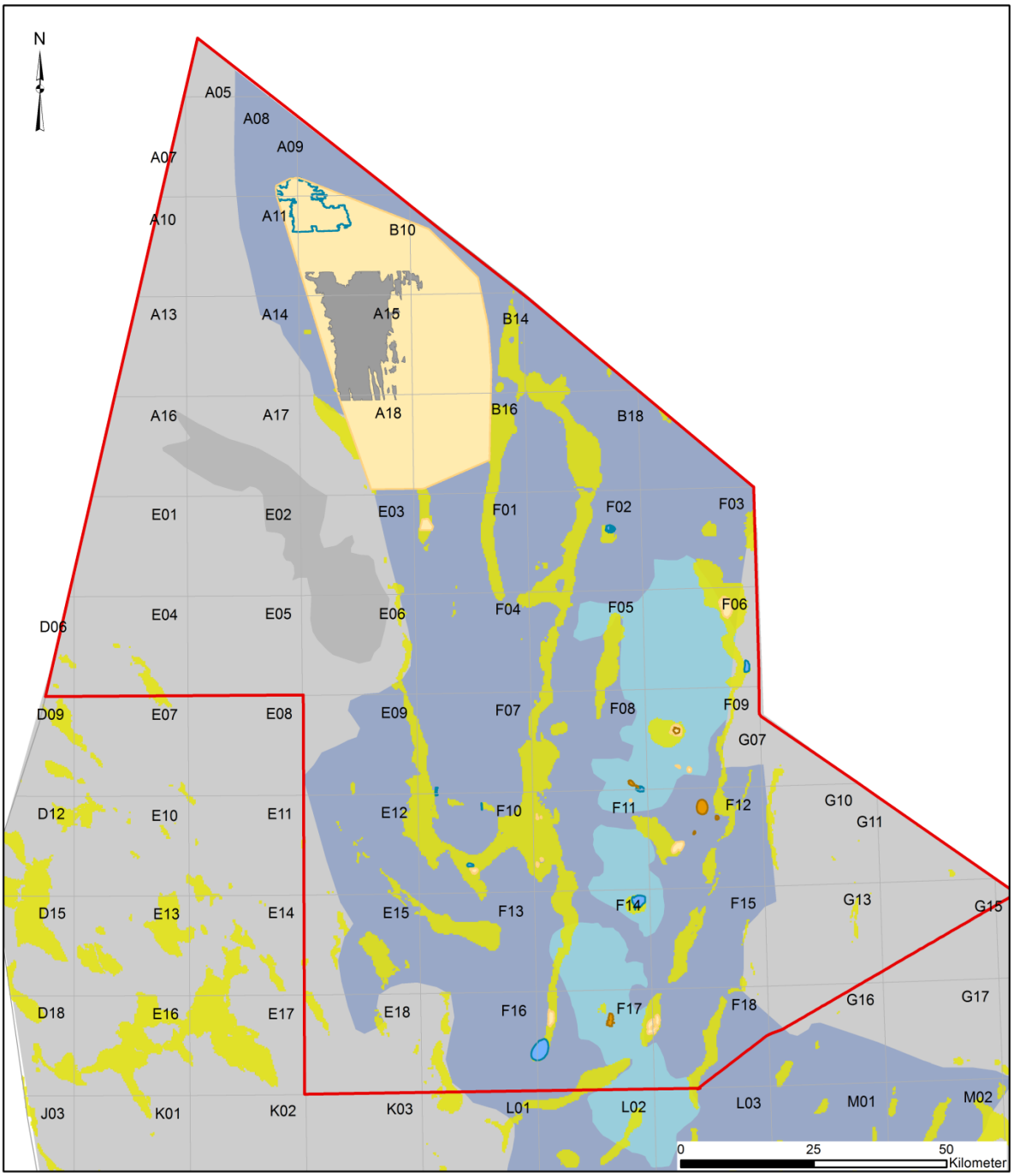
N
A05
A08
A09
A07
A10
A11
B10
A13
A14
A15
B14
A16
A17
A18
B16
B18
E01
E02
E03
F01
F02
F03
D06
E04
E05
E06
F04
F05
F06
D09
E07
E08
E09
F07
F08
F09
G07
D12
E10
E11
E12
F10
F11
F12
G10
G11
D15
E13
E14
E15
F13
F14
F15
G13
G15
D18
E16
E17
E18
F16
F17
F18
G16
G17
J03
K01
K02
K03
L01
L02
L03
M01
M02
0
25
50
Kilometer

S7

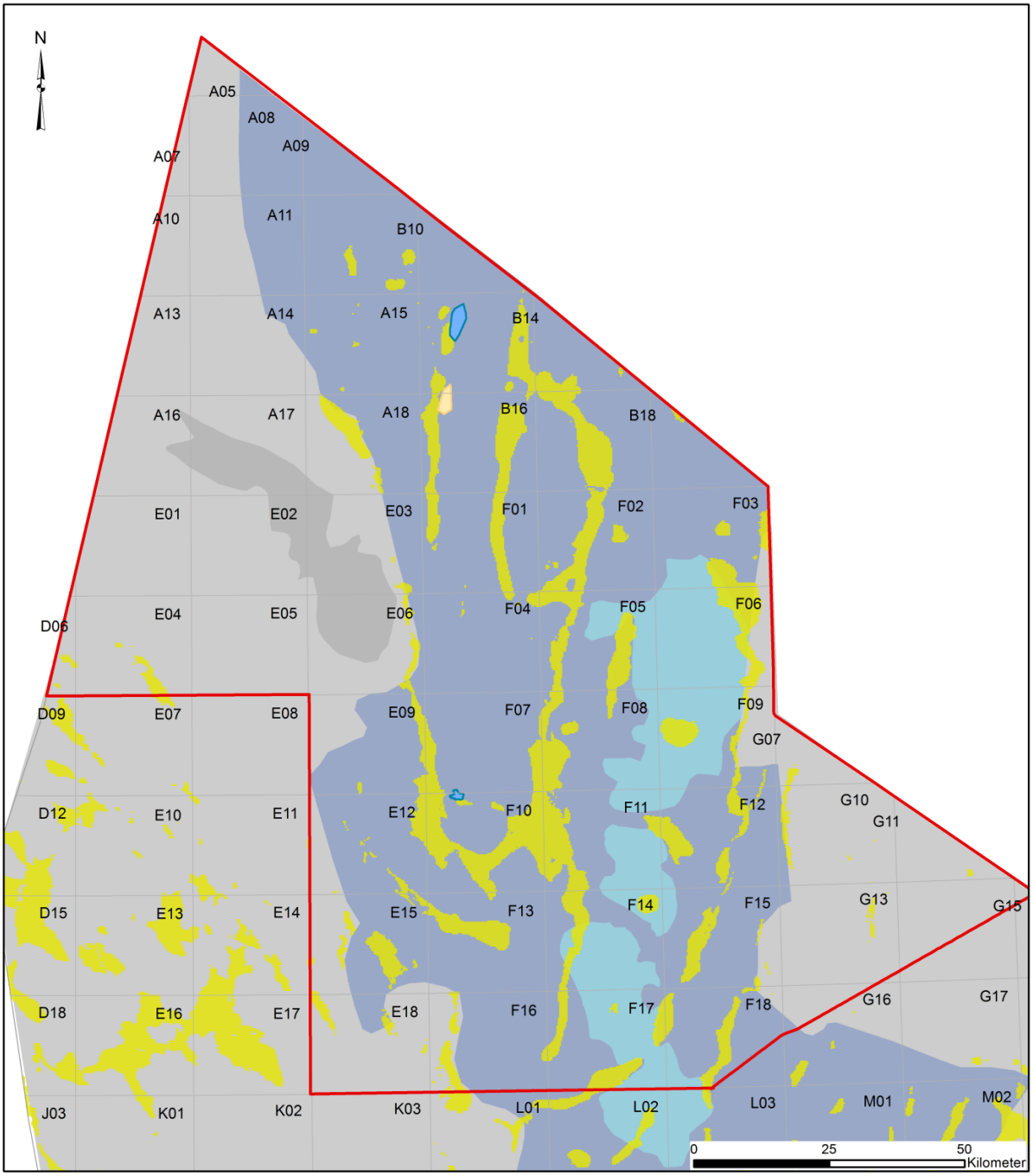
N
A05
A08
A09
A07
A10
A11
B10
A13
A14
A15
B14
A16
A17
A18
B16
B18
E01
E02
E03
F01
F02
F03
D06
E04
E05
E06
F04
F05
F06
D09
E07
E08
E09
F07
F08
F09
G07
D12
E10
E11
E12
F10
F11
F12
G10
G11
D15
E13
E14
E15
F13
F14
F15
G13
G15
D18
E16
E17
E18
F16
F17
F18
G16
G17
J03
K01
K02
K03
L01
L02
L03
M01
M02
0
25
50
Kilometer

S8

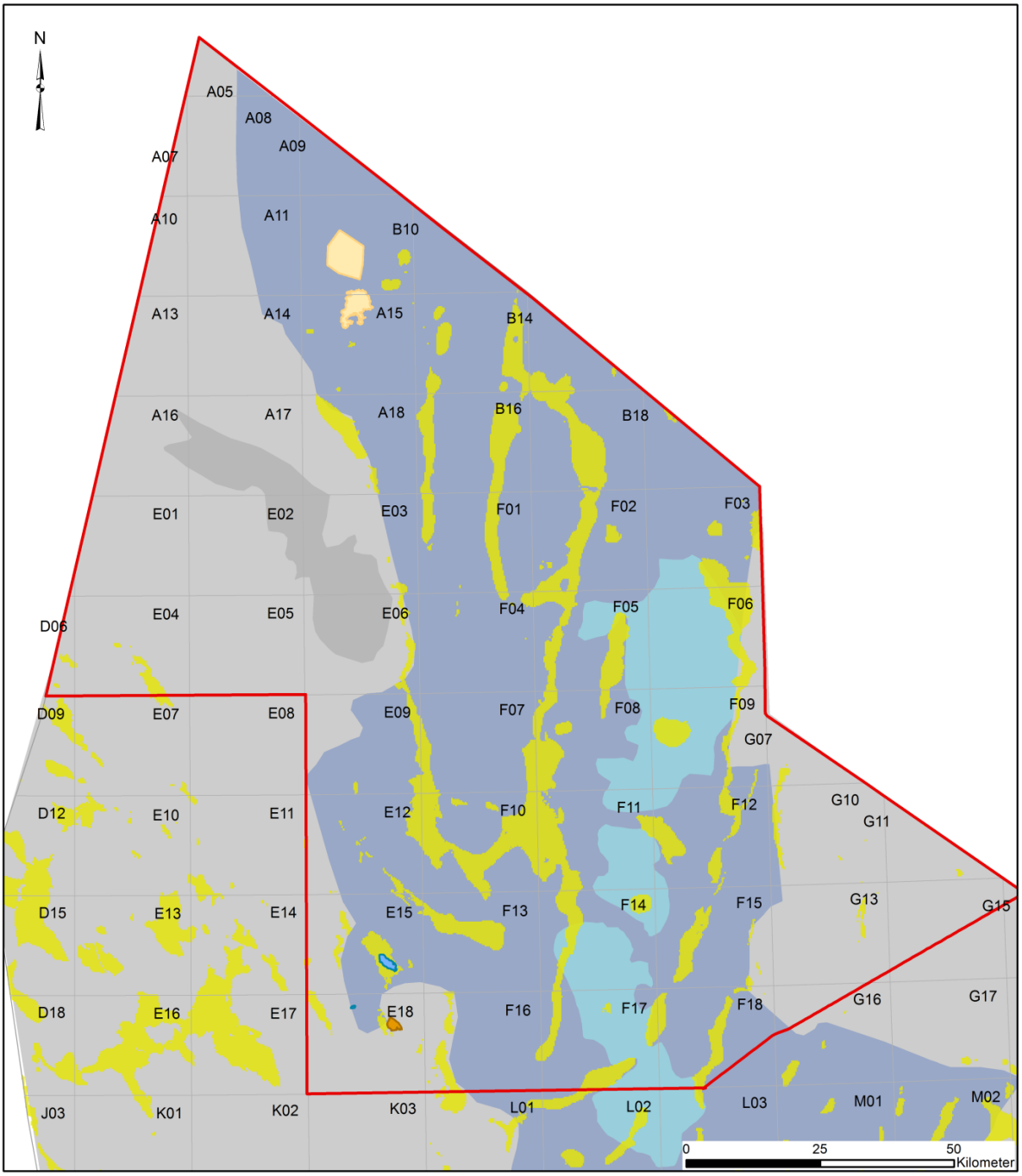
N
A05
A08
A09
A07
A10
A11
B10
A13
A14
A15
B14
A16
A17
A18
B16
B18
E01
E02
E03
F01
F02
F03
D06
E04
E05
E06
F04
F05
F06
D09
E07
E08
E09
F07
F08
F09
G07
D12
E10
E11
E12
F10
F11
F12
G10
G11
D15
E13
E14
E15
F13
F14
F15
G13
G15
D18
E16
E17
E18
F16
F17
F18
G16
G17
J03
K01
K02
K03
L01
L02
L03
M01
M02
0
25
50
Kilometer

S9

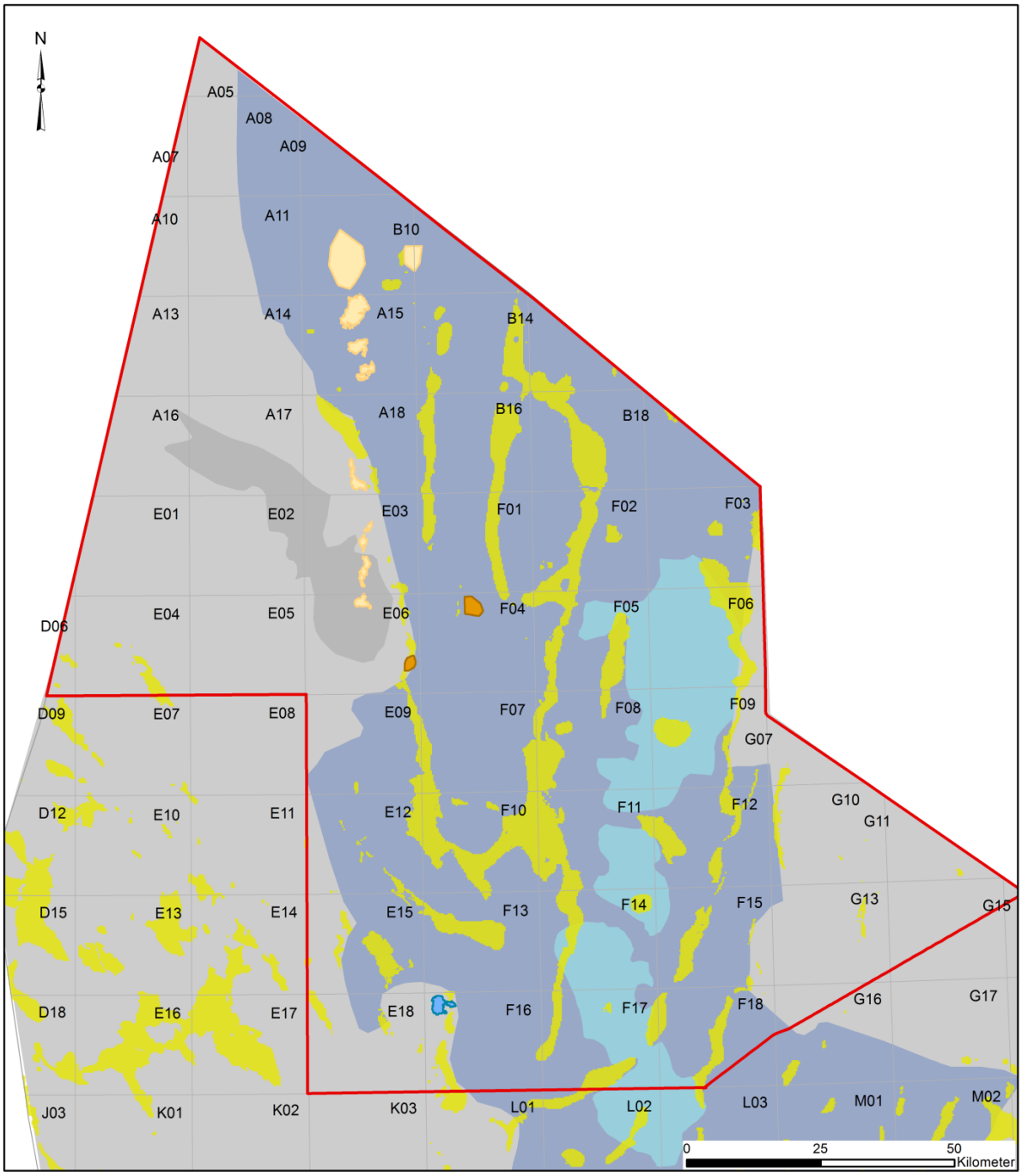
N
A05
A08
A09
A07
A10
A11
B10
A13
A14
A15
B14
A16
A17
A18
B16
B18
E01
E02
E03
F01
F02
F03
D06
E04
E05
E06
F04
F05
F06
D09
E07
E08
E09
F07
F08
F09
G07
D12
E10
E11
E12
F10
F11
F12
G10
G11
D15
E13
E14
E15
F13
F14
F15
G13
G15
D18
E16
E17
E18
F16
F17
F18
G16
G17
J03
K01
K02
K03
L01
L02
L03
M01
M02
0
25
50
Kilometer

S10

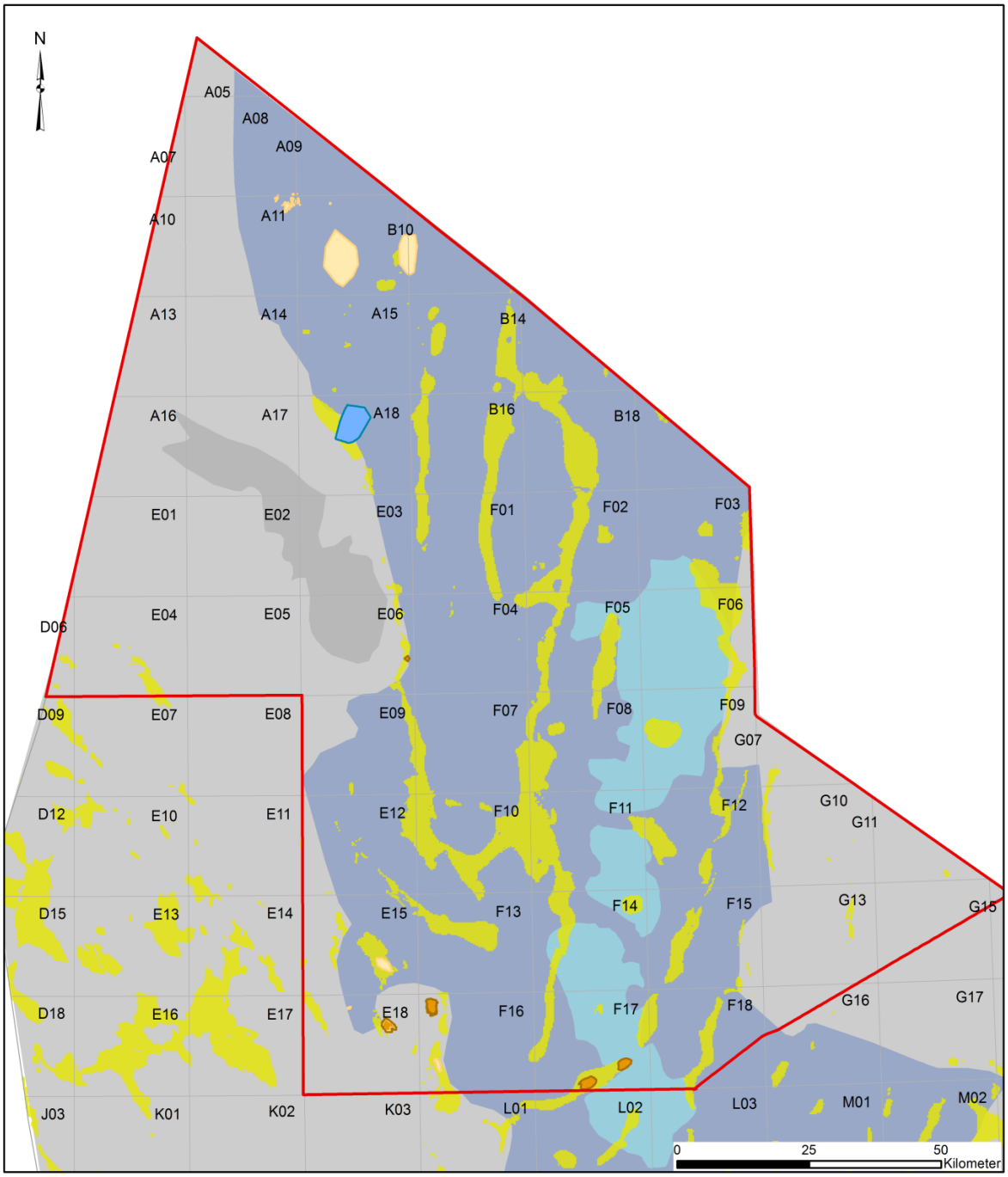
N
A05
A08
A09
A07
A10
A11
B10
A13
A14
A15
B14
A16
A17
A18
B16
B18
E01
E02
E03
F01
F02
F03
D06
E04
E05
E06
F04
F05
F06
D09
E07
E08
E09
F07
F08
F09
G07
D12
E10
E11
E12
F10
F11
F12
G10
G11
D15
E13
E14
E15
F13
F14
F15
G13
G15
D18
E16
E17
E18
F16
F17
F18
G16
G17
J03
K01
K02
K03
L01
L02
L03
M01
M02
0
25
50
Kilometer

S11

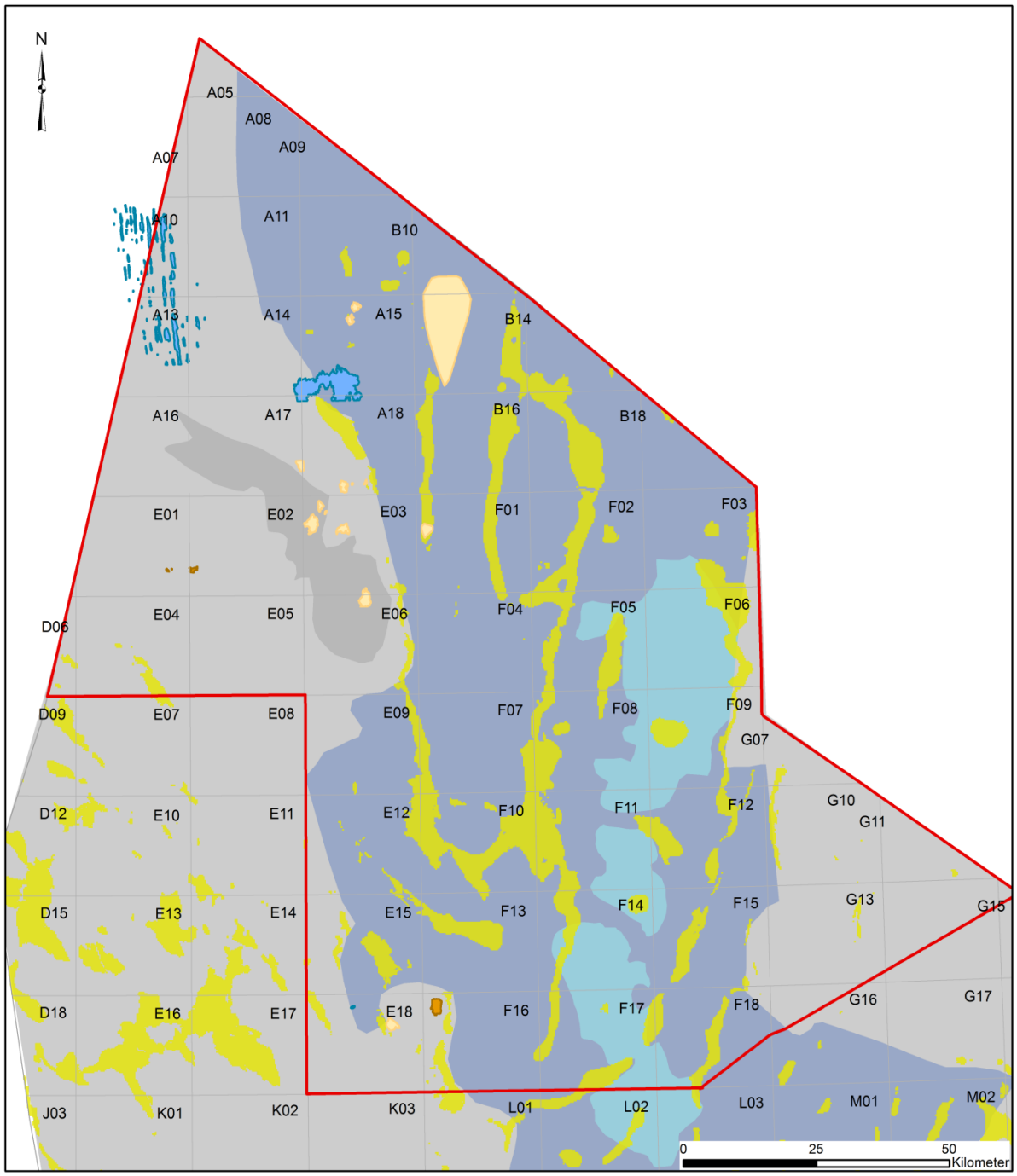
N
A05
A08
A09
A07
A10
A11
B10
A13
A14
A15
B14
A16
A17
A18
B16
B18
E01
E02
E03
F01
F02
F03
D06
E04
E05
E06
F04
F05
F06
D09
E07
E08
E09
F07
F08
F09
G07
D12
E10
E11
E12
F10
F11
F12
G10
G11
D15
E13
E14
E15
F13
F14
F15
G13
G15
D18
E16
E17
E18
F16
F17
F18
G16
G17
J03
K01
K02
K03
L01
L02
L03
M01
M02
0
25
50
Kilometer

S12

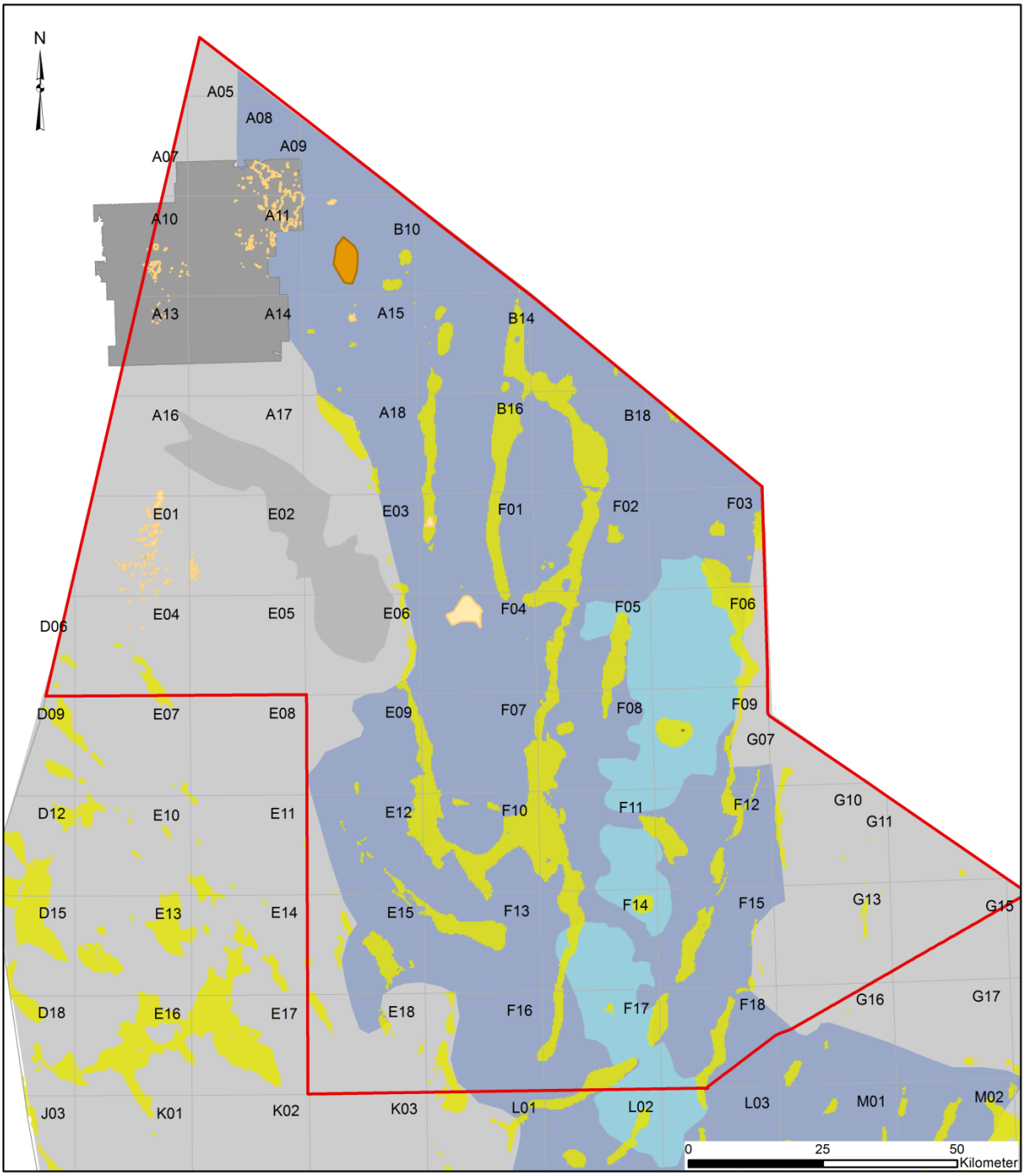
N
A05
A08
A09
A07
A10
A11
B10
A13
A14
A15
B14
A16
A17
A18
B16
B18
E01
E02
E03
F01
F02
F03
D06
E04
E05
E06
F04
F05
F06
D09
E07
E08
E09
F07
F08
F09
G07
D12
E10
E11
E12
F10
F11
F12
G10
G11
D15
E13
E14
E15
F13
F14
F15
G13
G15
D18
E16
E17
E18
F16
F17
F18
G16
G17
J03
K01
K02
K03
L01
L02
L03
M01
M02
0
25
50
Kilometer

S13

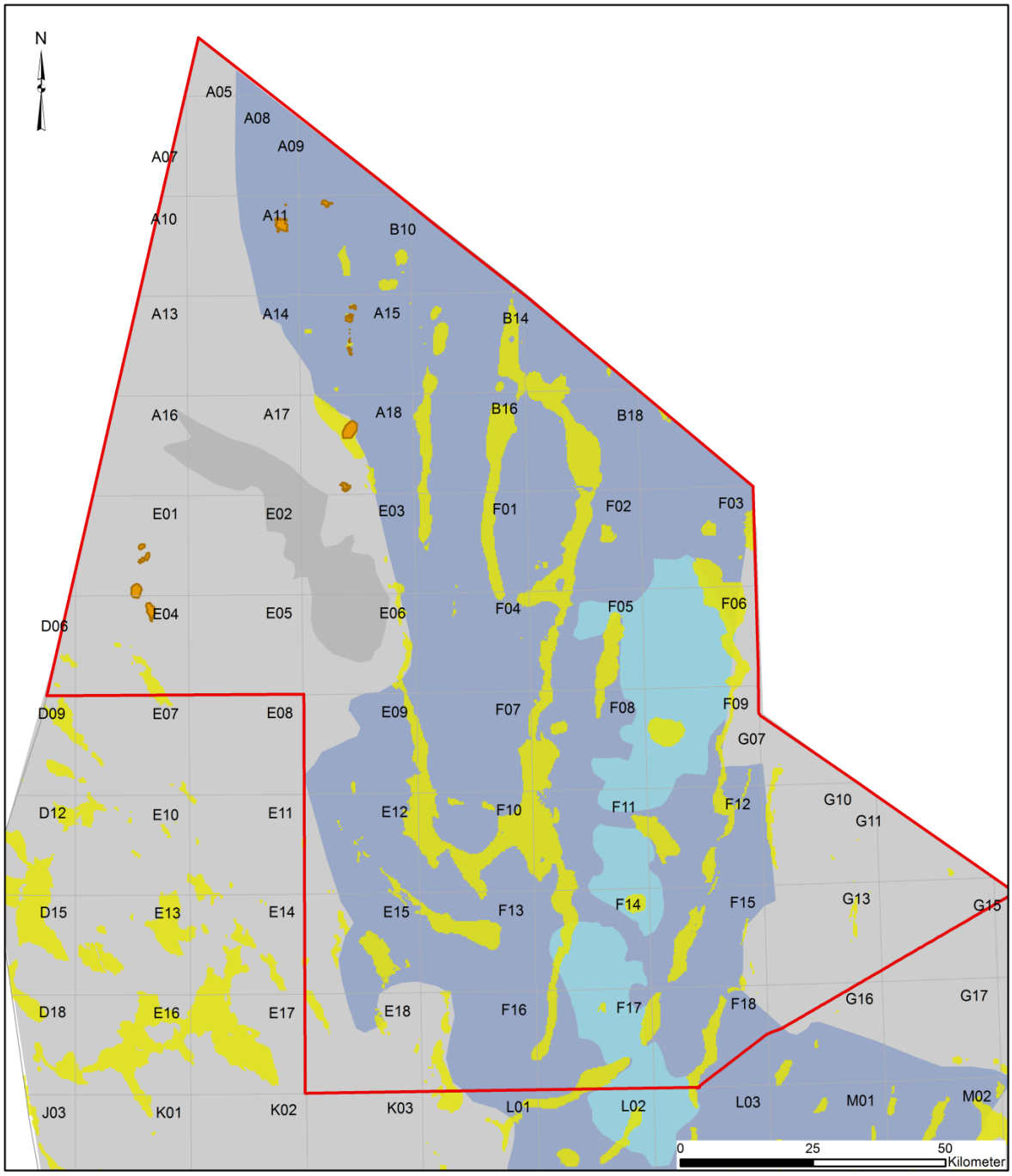
N
A05
A08
A09
A07
A10
A11
B10
A13
A14
A15
B14
A16
A17
A18
B16
B18
E01
E02
E03
F01
F02
F03
D06
E04
E05
E06
F04
F05
F06
D09
E07
E08
E09
F07
F08
F09
G07
D12
E10
E11
E12
F10
F11
F12
G10
G11
D15
E13
E14
E15
F13
F14
F15
G13
G15
D18
E16
E17
E18
F16
F17
F18
G16
G17
J03
K01
K02
K03
L01
L02
L03
M01
M02
0
25
50
Kilometer

10.4 Bright spot distribution and Vclay

S4

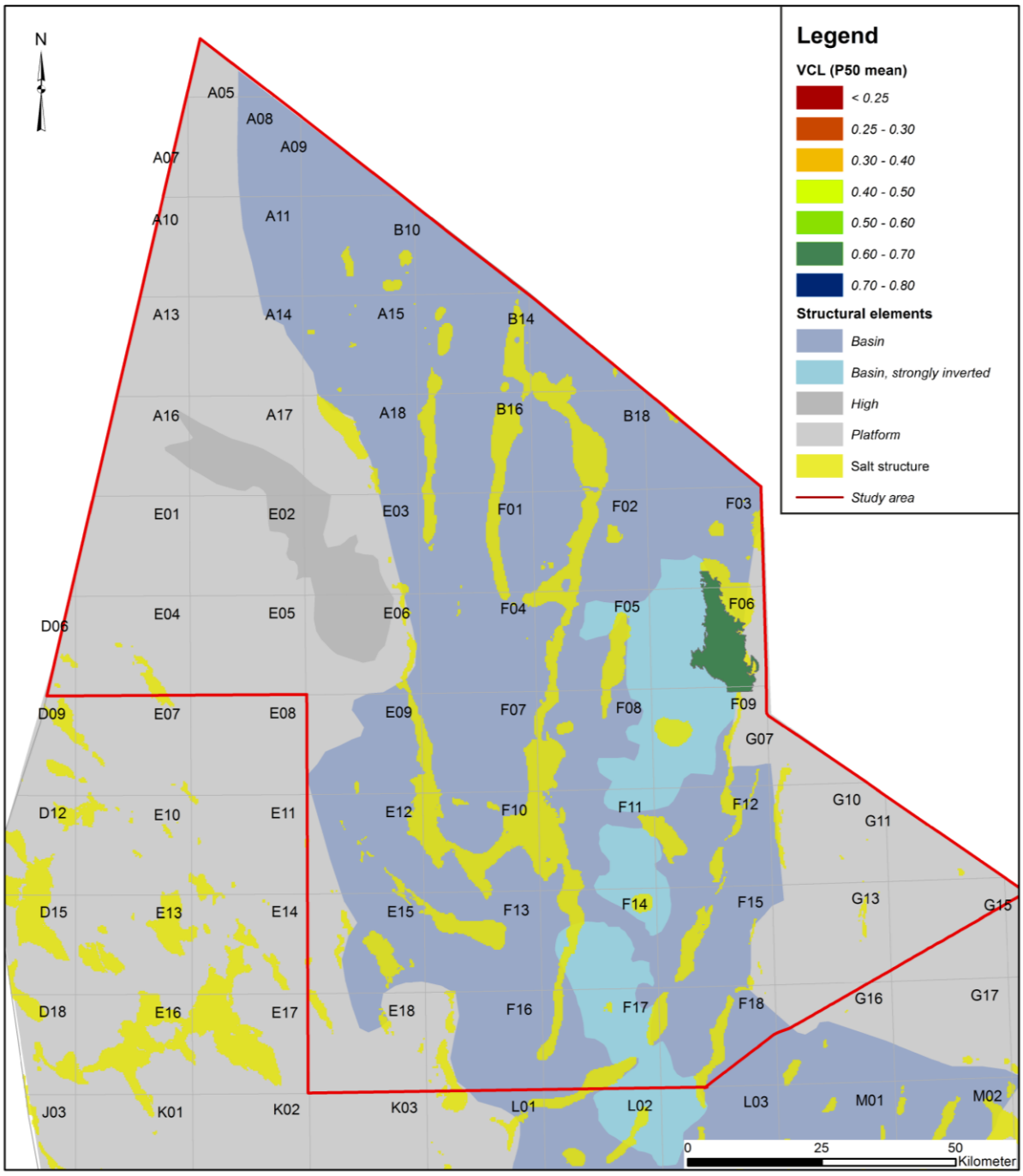

S5

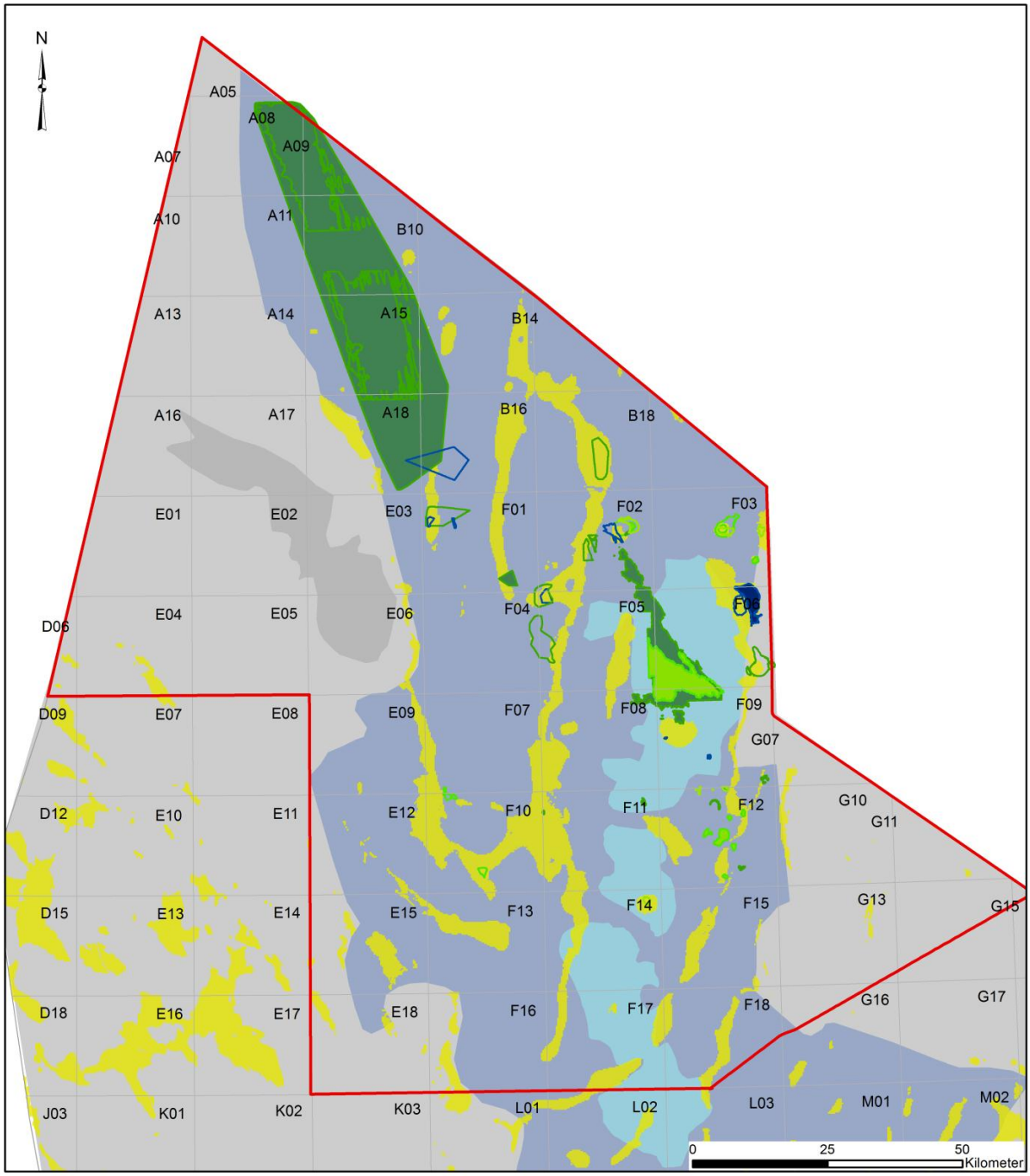
N
A05
A08
A09
A07
A10
A11
B10
A13
A14
A15
B14
A16
A17
A18
B16
B18
E01
E02
E03
F01
F02
F03
D06
E04
E05
E06
F04
F05
D09
E07
E08
E09
F07
F08
F09
G07
D12
E10
E11
E12
F10
F11
F12
G10
G11
D15
E13
E14
E15
F13
F14
F15
G13
G15
D18
E16
E17
E18
F16
F17
F18
G16
G17
J03
K01
K02
K03
L01
L02
L03
M01
M02
0
25
50
Kilometer

S6

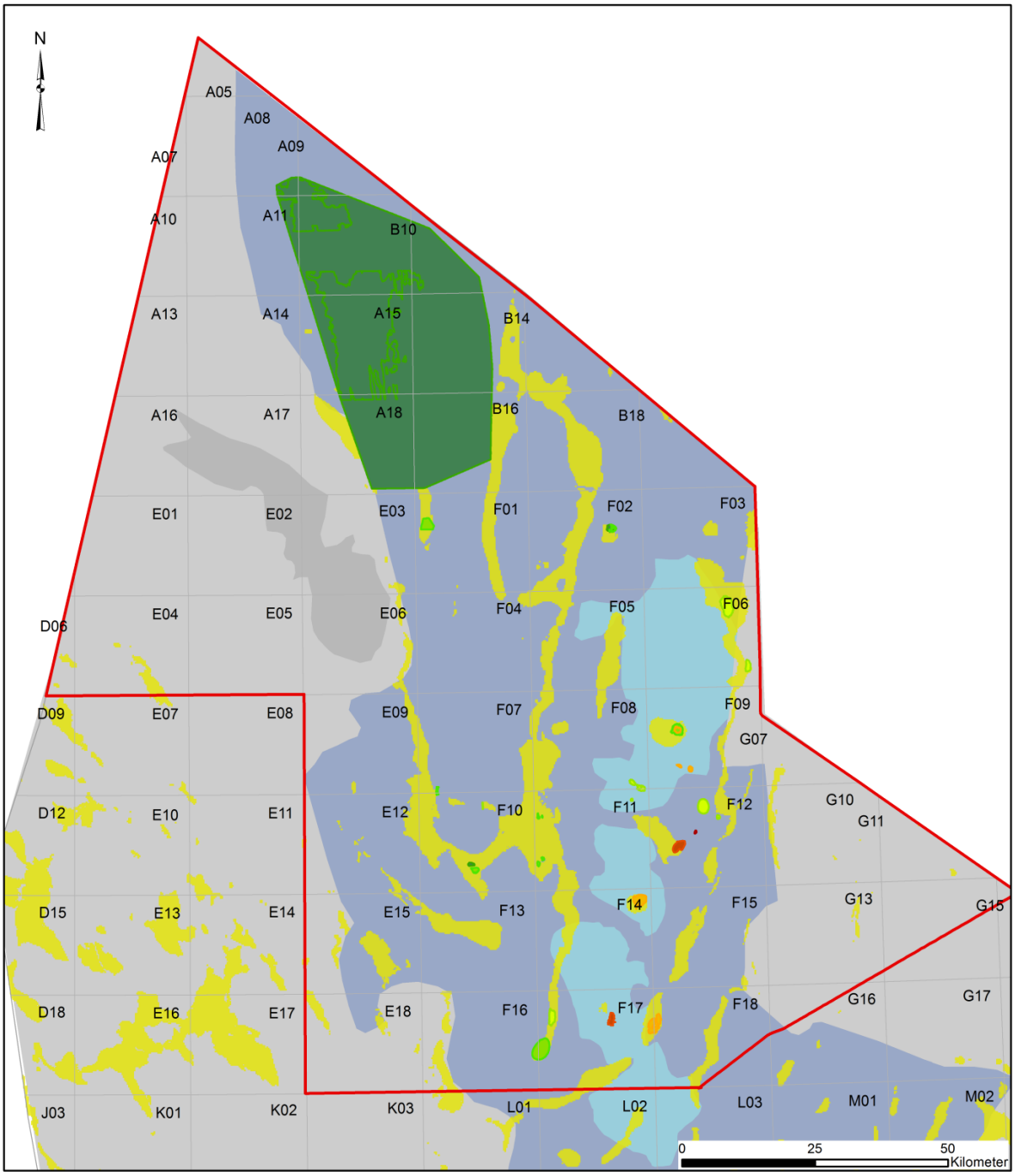
N
A05
A08
A09
A07
A10
A11
B10
A13
A14
A15
B14
A16
A17
A18
B16
B18
E01
E02
E03
F01
F02
F03
D06
E04
E05
E06
F04
F05
F06
D09
E07
E08
E09
F07
F08
F09
G07
D12
E10
E11
E12
F10
F11
F12
G10
G11
D15
E13
E14
E15
F13
F14
F15
G13
G15
D18
E16
E17
E18
F16
F17
F18
G16
G17
J03
K01
K02
K03
L01
L02
L03
M01
M02
0
25
50
Kilometer

S7

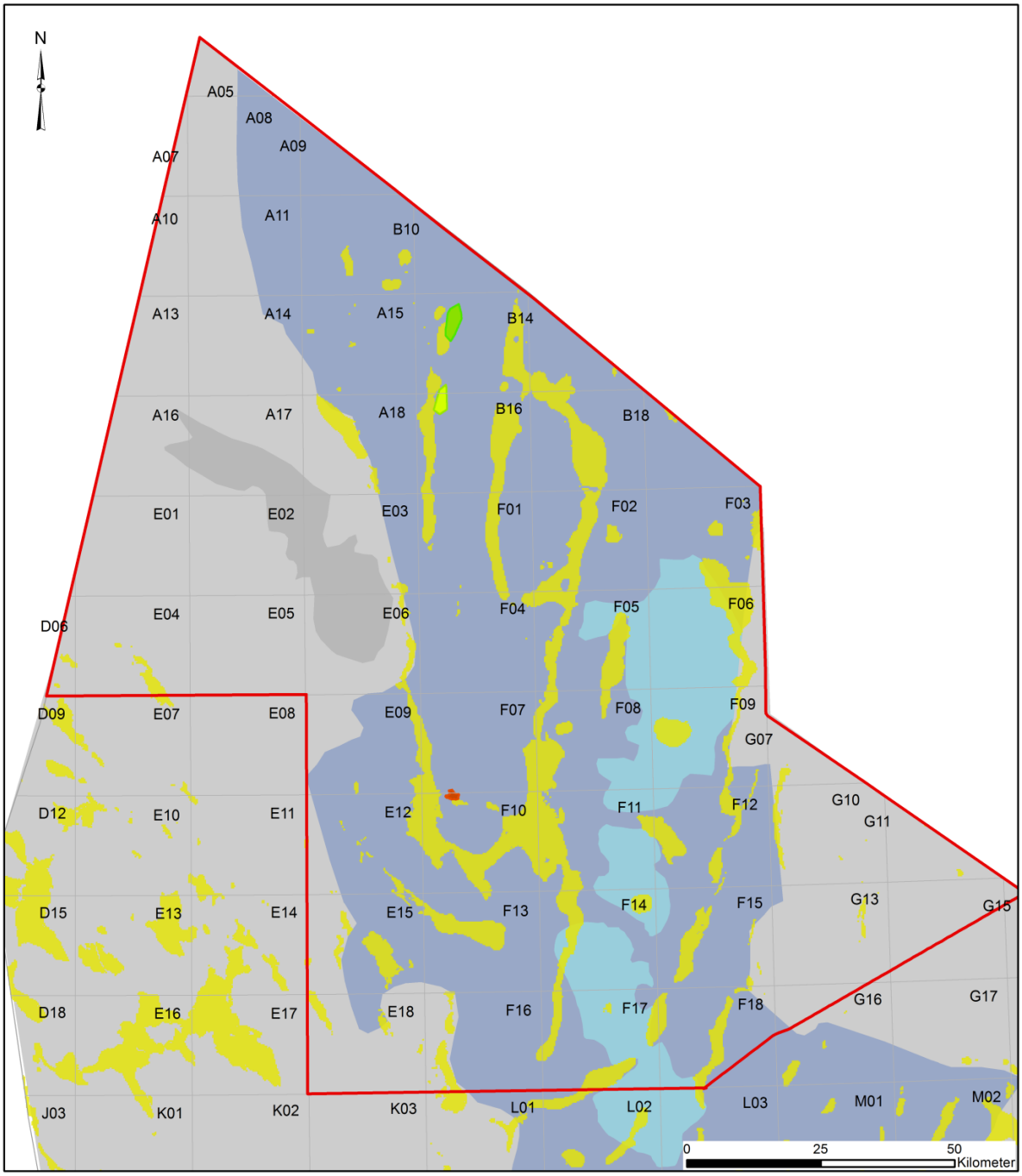
N
A05
A08
A09
A07
A10
A11
B10
A13
A14
A15
B14
A16
A17
A18
B16
B18
E01
E02
E03
F01
F02
F03
D06
E04
E05
E06
F04
F05
F06
D09
E07
E08
E09
F07
F08
F09
G07
D12
E10
E11
E12
F10
F11
F12
G10
G11
D15
E13
E14
E15
F13
F14
F15
G13
G15
D18
E16
E17
E18
F16
F17
F18
G16
G17
J03
K01
K02
K03
L01
L02
L03
M01
M02
0
25
50
Kilometer

S8

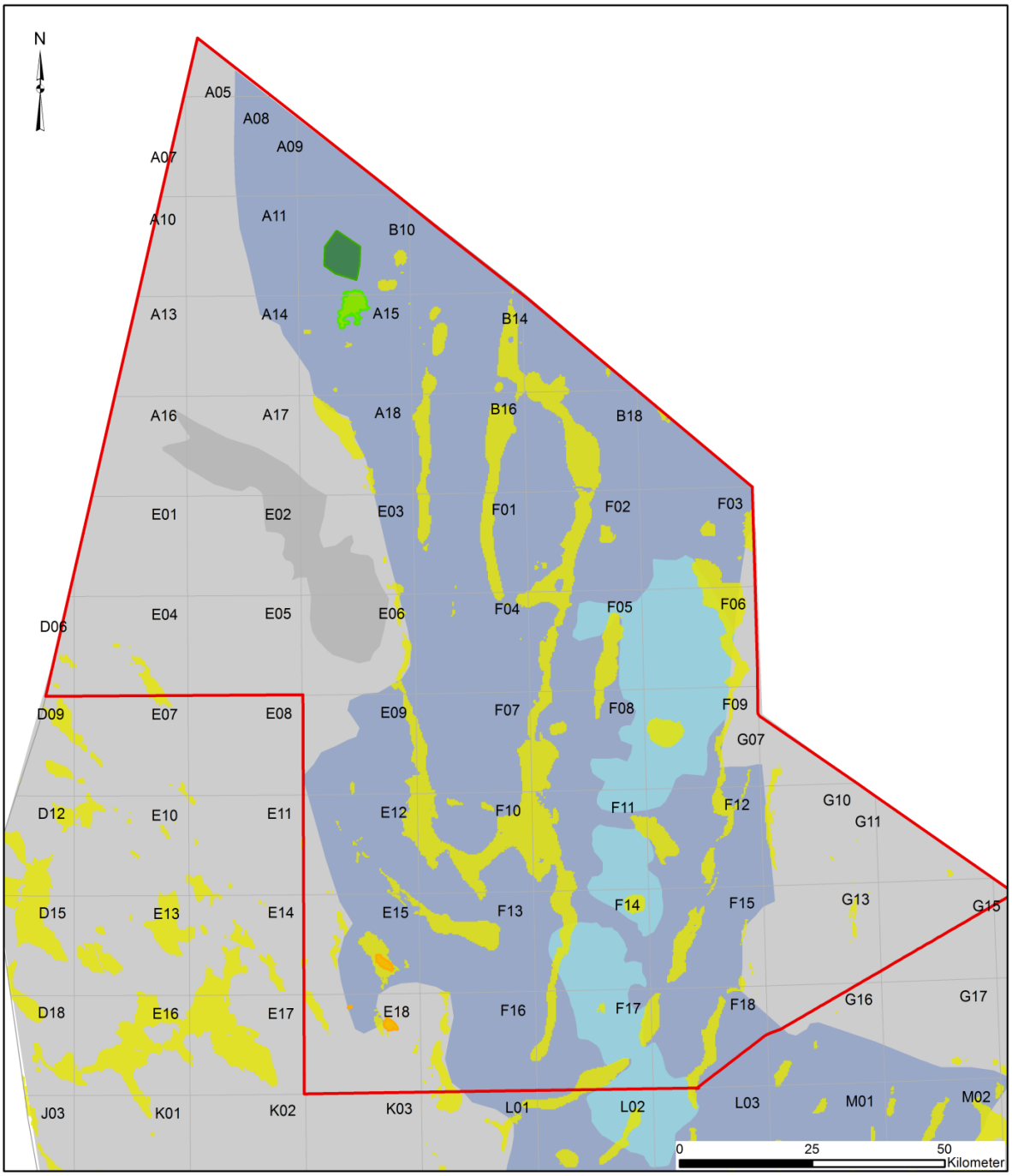
N
A05
A08
A09
A07
A10
A11
B10
A13
A14
A15
B14
A16
A17
A18
B16
B18
E01
E02
E03
F01
F02
F03
D06
E04
E05
E06
F04
F05
F06
D09
E07
E08
E09
F07
F08
F09
G07
D12
E10
E11
E12
F10
F11
F12
G10
G11
D15
E13
E14
E15
F13
F14
F15
G13
G15
D18
E16
E17
E18
F16
F17
F18
G16
G17
J03
K01
K02
K03
L01
L02
L03
M01
M02
0
25
50
Kilometer

S9

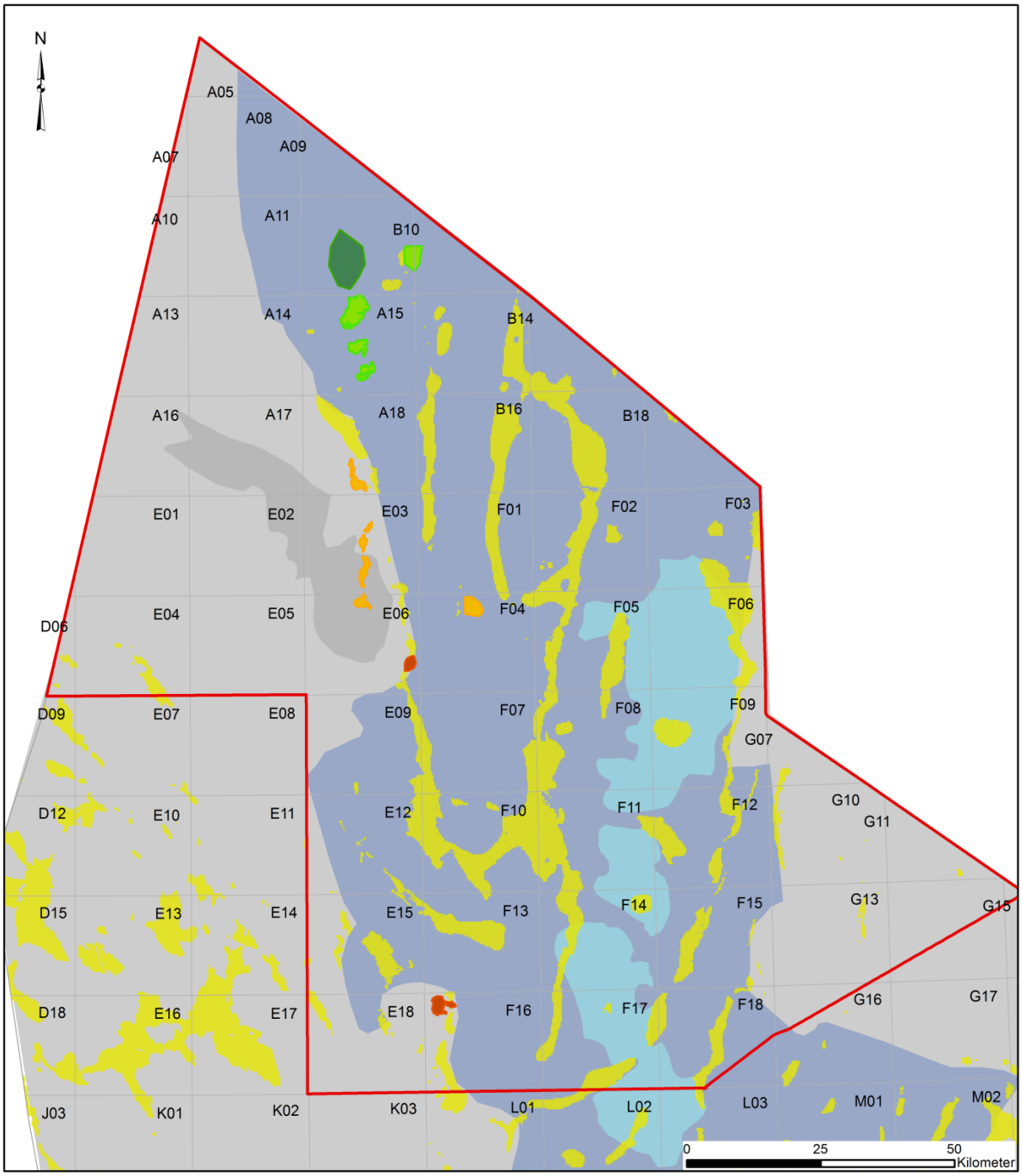
N
A05
A08
A09
A07
A10
A11
B10
A13
A14
A15
B14
A16
A17
A18
B16
B18
E01
E02
E03
F01
F02
F03
D06
E04
E05
E06
F04
F05
F06
D09
E07
E08
E09
F07
F08
F09
G07
D12
E10
E11
E12
F10
F11
F12
G10
G11
D15
E13
E14
E15
F13
F14
F15
G13
G15
D18
E16
E17
E18
F16
F17
F18
G16
G17
J03
K01
K02
K03
L01
L02
L03
M01
M02
0
25
50
Kilometer

S10

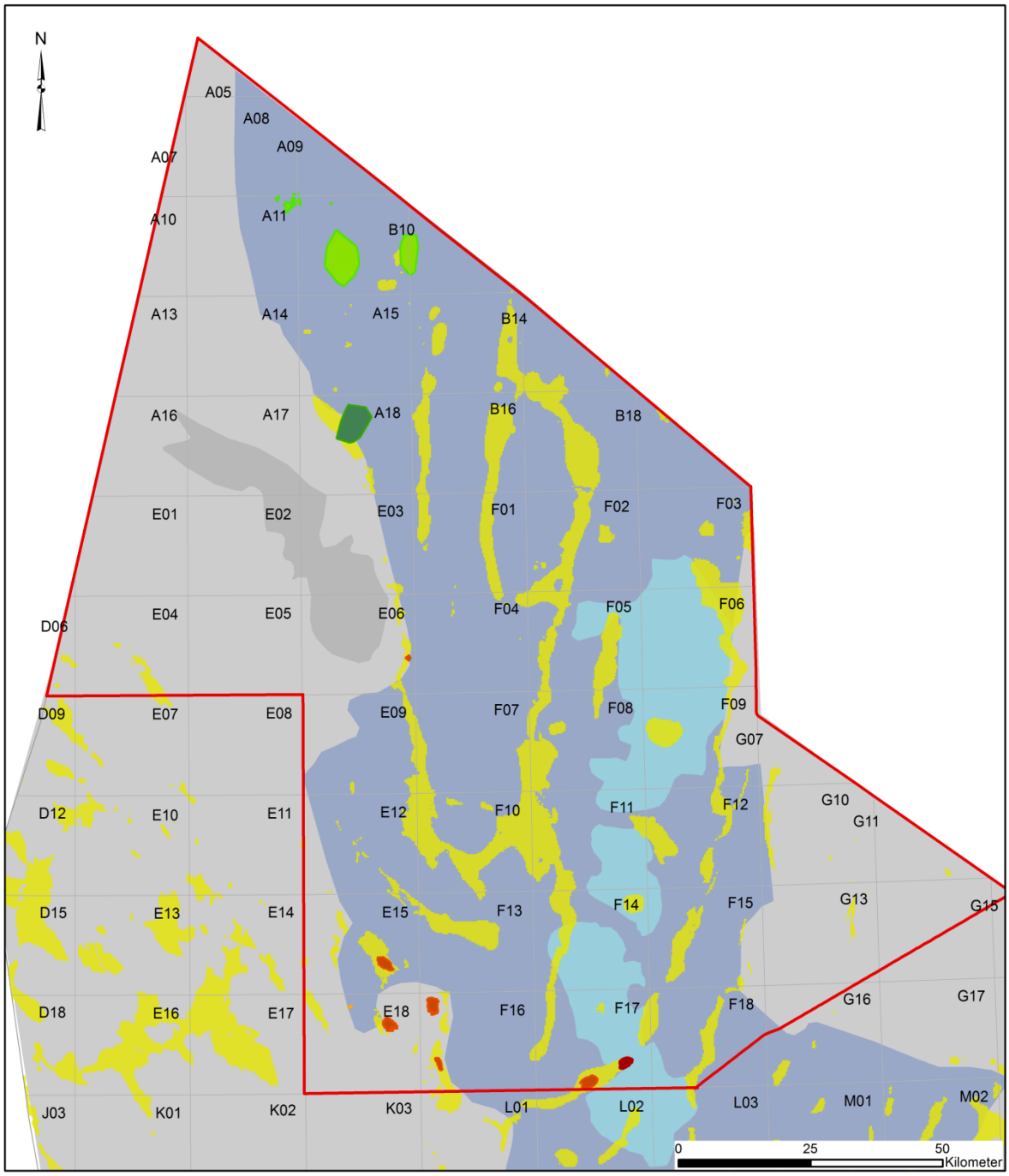
N
A05
A08
A09
A07
A10
A11
B10
A13
A14
A15
B14
A16
A17
A18
B16
B18
E01
E02
E03
F01
F02
F03
D06
E04
E05
E06
F04
F05
F06
D09
E07
E08
E09
F07
F08
F09
G07
D12
E10
E11
E12
F10
F11
F12
G10
G11
D15
E13
E14
E15
F13
F14
F15
G13
G15
D18
E16
E17
E18
F16
F17
F18
G16
G17
J03
K01
K02
K03
L01
L02
L03
M01
M02
0
25
50
Kilometer

S11

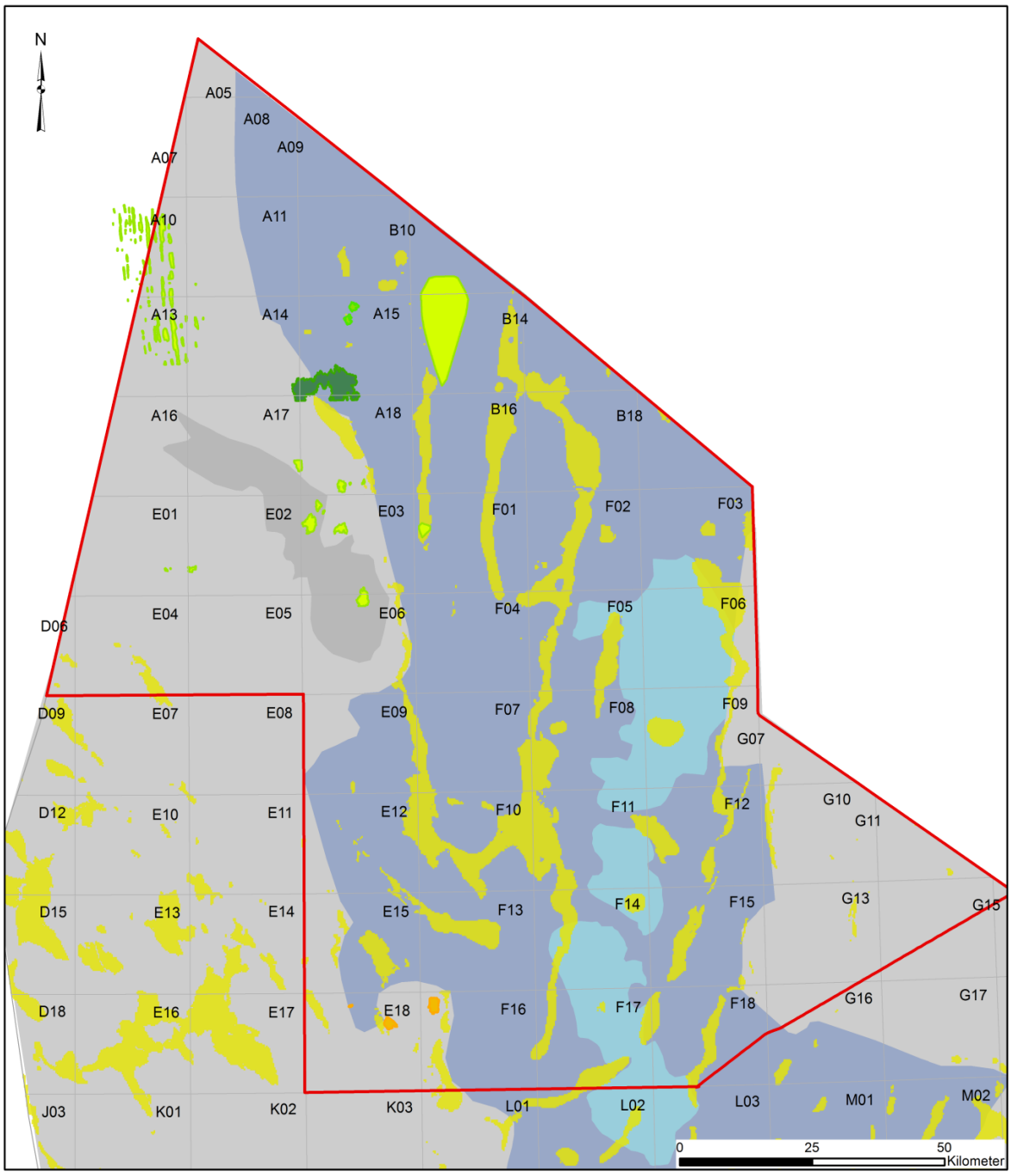
N
A05
A08
A09
A07
A10
A11
B10
A13
A14
A15
B14
A16
A17
A18
B16
B18
E01
E02
E03
F01
F02
F03
D06
E04
E05
E06
F04
F05
F06
D09
E07
E08
E09
F07
F08
F09
G07
D12
E10
E11
E12
F10
F11
F12
G10
G11
D15
E13
E14
E15
F13
F14
F15
G13
G15
D18
E16
E17
E18
F16
F17
F18
G16
G17
J03
K01
K02
K03
L01
L02
L03
M01
M02
0
25
50
Kilometer

S12

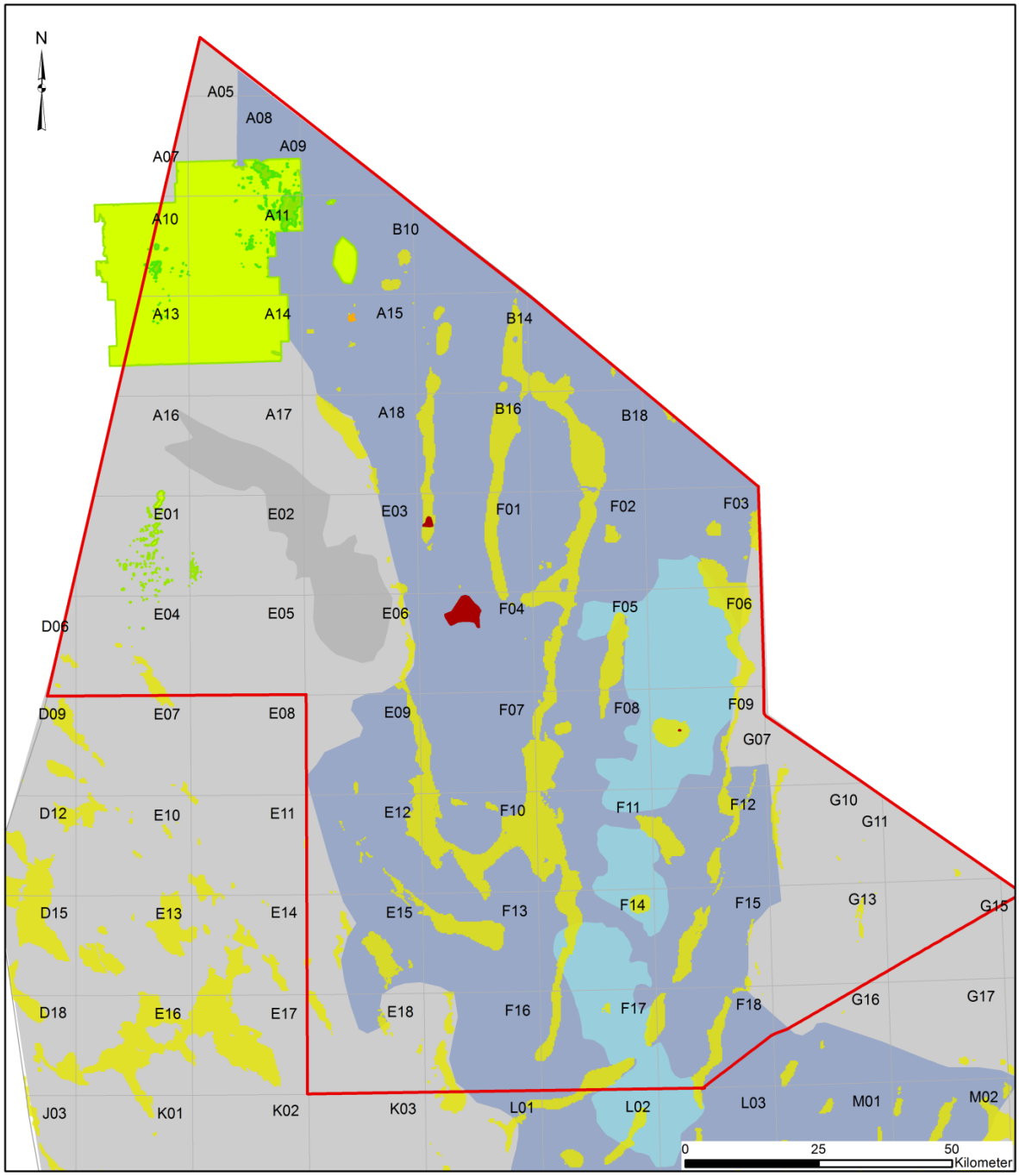
N
A05
A08
A09
A07
A10
A11
B10
A13
A14
A15
B14
A16
A17
A18
B16
B18
E01
E02
E03
F01
F02
F03
D06
E04
E05
E06
F04
F05
F06
D09
E07
E08
E09
F07
F08
F09
G07
D12
E10
E11
E12
F10
F11
F12
G10
G11
D15
E13
E14
E15
F13
F14
F15
G13
G15
D18
E16
E17
E18
F16
F17
F18
G16
G17
J03
K01
K02
K03
L01
L02
L03
M01
M02
0
25
50
Kilometer

S13

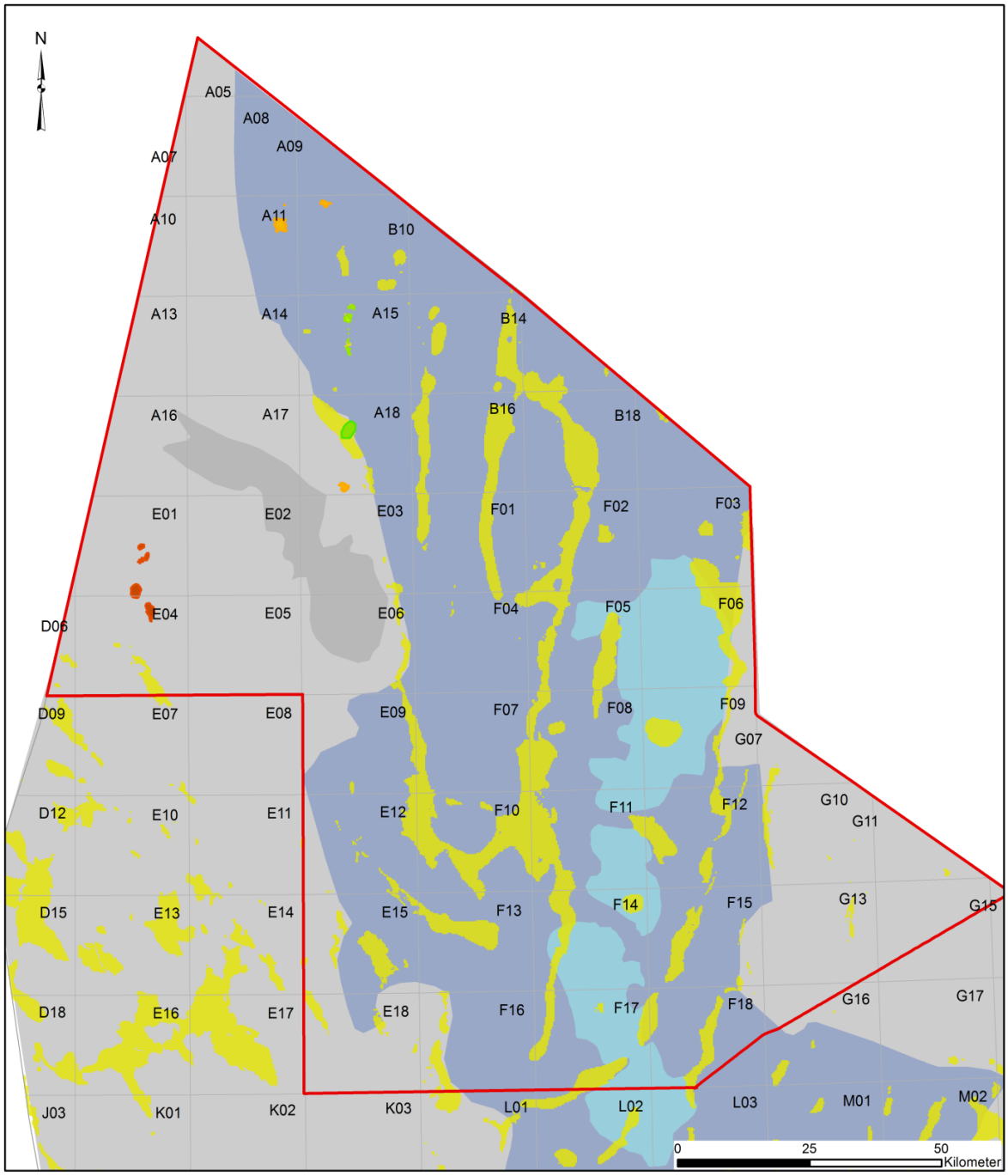
N
A05
A08
A09
A07
A10
A11
B10
A13
A14
A15
B14
A16
A17
A18
B16
B18
E01
E02
E03
F01
F02
F03
D06
E04
E05
E06
F04
F05
F06
D09
E07
E08
E09
F07
F08
F09
G07
D12
E10
E11
E12
F10
F11
F12
G10
G11
D15
E13
E14
E15
F13
F14
F15
G13
G15
D18
E16
E17
E18
F16
F17
F18
G16
G17
J03
K01
K02
K03
L01
L02
L03
M01
M02
0
25
50
Kilometer

Appendix J. Petrel project guide

For the use of this guide it is assumed that the reader is familiar with basic functionality of Petrel© version 10.2. Details of all modelling steps and discussion of results are presented in the main text of the report.

General Data structure

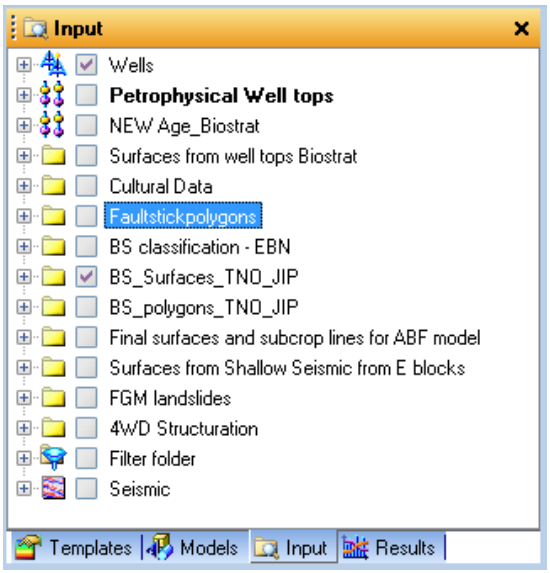

The input pane of the project contains basically all input for the Property model (which resides under the “Model” pane). This input includes well data, well tops, surfaces constructed from seismic horizon interpretation. A seismic folder is automatically added to the project; this folder is empty since no seismic data is included.

Well data

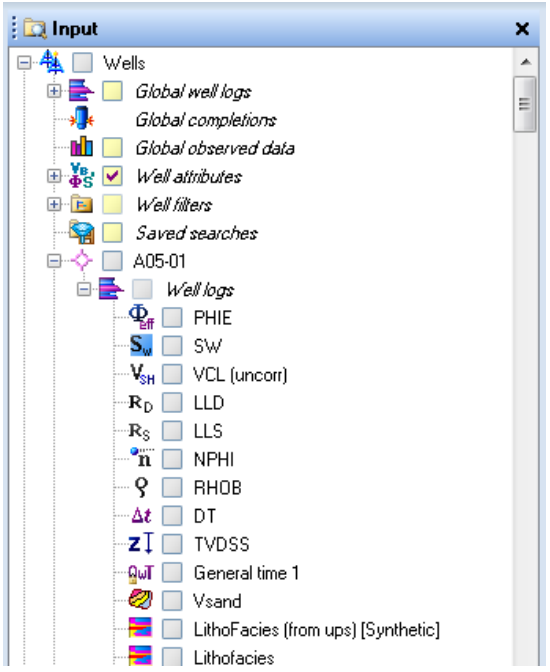

The wells folder contains well logs of all wells used in the project. Availability of logs is documented in Appendix G. Available well logs are also listed for each individual well. These logs include 1) raw well logs (e.g. RHOB, NPHI), 2) petrophysical estimations (Vcl, PHIE), and facies (discrete) logs that are calculated in Petrel and which are based on 1) and/or 2).

Well tops

Petrophysical Well tops

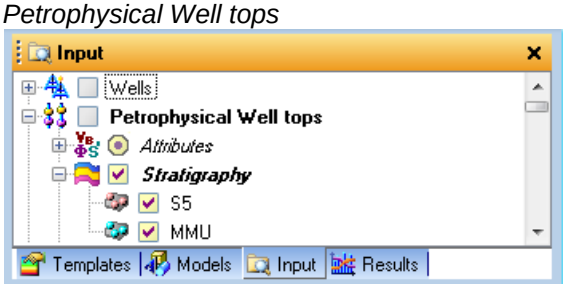

Petrophysical well tops are those well tops that were picked from the well logs. Only MMU and S5 can be picked with reasonable confidence from the GR log. These well tops have been used for the seismic to well tie and presentation of residual maps for the TD conversion applied.

New Age_Biostrat well tops (and surfaces)

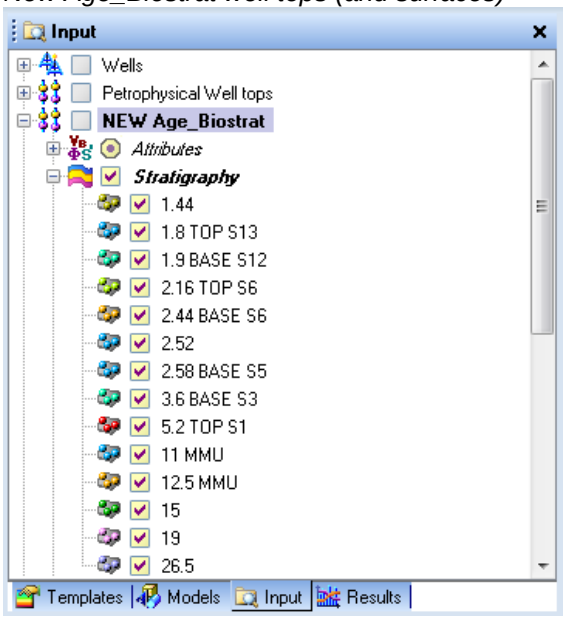

These well tops are based on the biostratigraphic analysis and represent the depths at which biostratigraphic marker occur.
Most markers presented are related to the top or base of the identified sequences (S1-S13) within the studied SNS delta interval. Different ages of the MMU are related to the diachronous character of the hiatus (see Chapter 2 for explanation). Biomarkers with ages >12.5 Ma or <1.8 Ma occur below respectively above the studied interval.

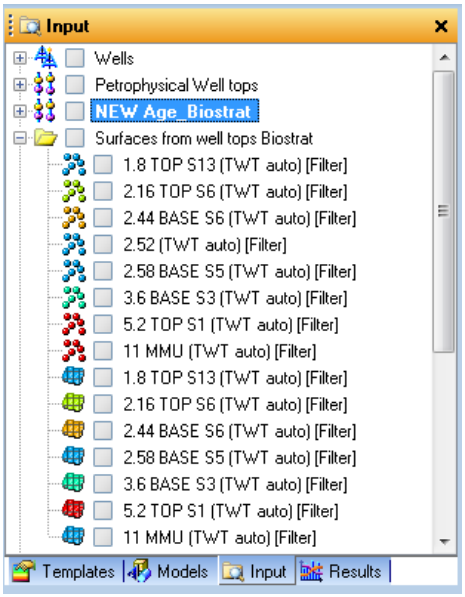

Based on the vertical position of biomarkers at well location alone, surfaces were reconstructed. Although these surfaces do not provide the detail of the seismically interpreted counterparts, it gives a rough indication of regional trends. These have been used in areas were seismic interpretations was problematic.

Cultural Data

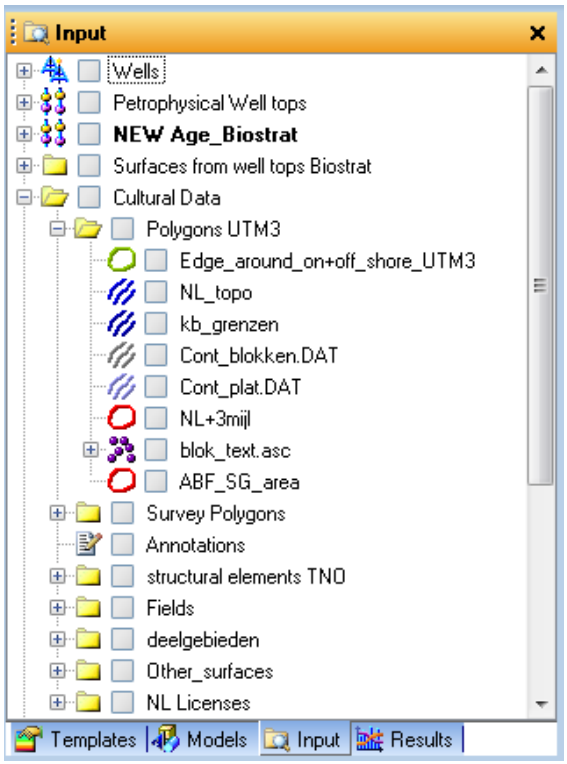

All geographical, O&G field, and license data that can be used in creating map plots.

Faults

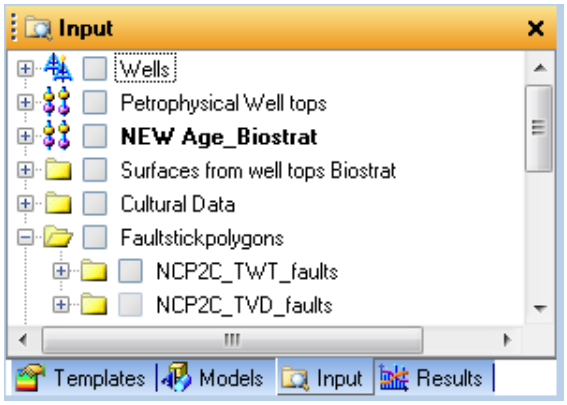

Fault sticks from the NCP2 regional mapping program. Area NCP2 approximately corresponds to the studied area. Faults are available both in TWT and TVD.

Brigth Spots

BS classification EBN

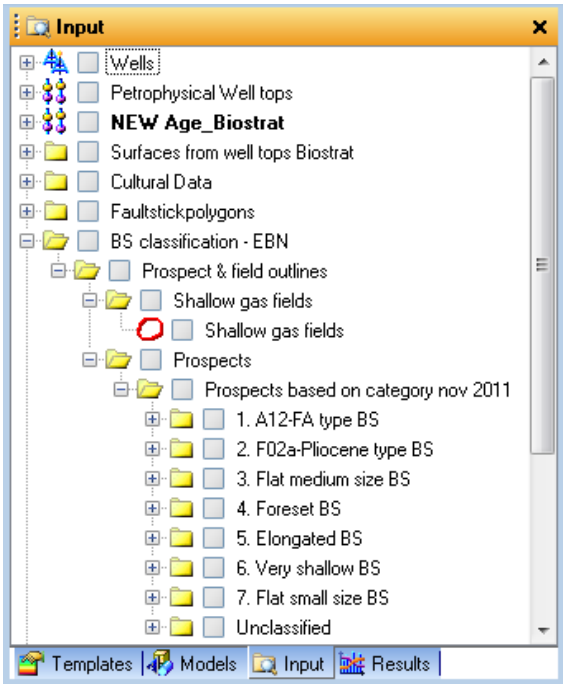

BS classes according EBN (Nov 2011) note that the classes represented here are slightly different. The EBN classes were updated in 2012, results are not included here. The polygon outlines of the identified BS, however, remain unchanged.

BS surfaces/polygons TNO-JIP

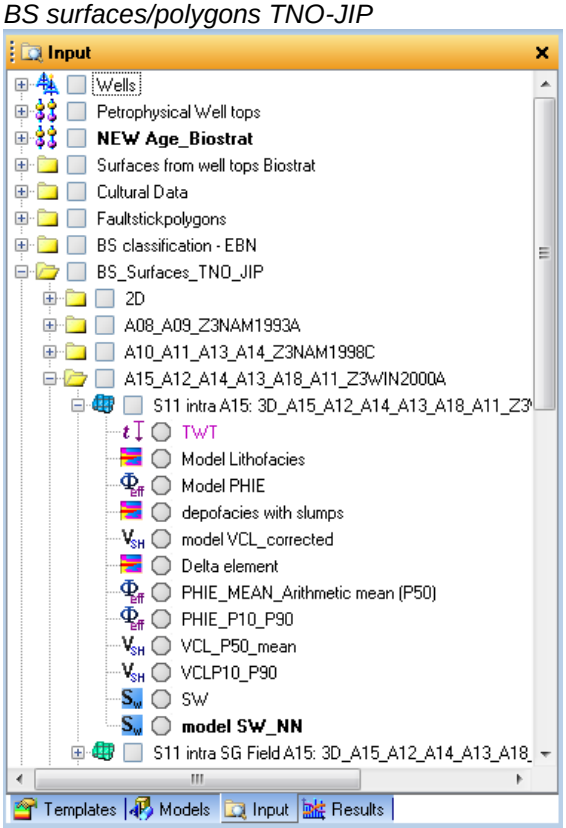

All individual BS were interpreted based on available 2D and 3D seismic data. Only BS in 3D-covered areas could be autotracked (see Chapter 7 for explanation). Surfaces are created from all individual BS, which were named according to the name convention (sequence, internal order, seismic survey used).

Polygon outlines of all BS surfaces are stored in the folder: *BS_polygons_TNO_JIP.* These were exported to ArcGIS to make the BS property maps (see Chapter 8 and Appendix I).

All surfaces have a list of attributes representing property extractions from the property model at the surface (see Chapter 5 for explanation). The average property values at the surface were exported to the BS data base.

Final surfaces ABF model

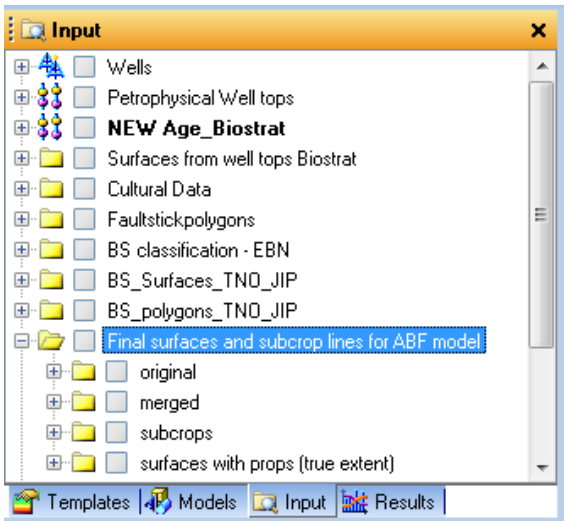

Based on the seismic interpretation surfaces were created. The folder original contains the true extent of the interpretation. These may contain geometrical errors, e.g. downlap or toplap surfaces that do not merge, or surfaces that “bend” below stratigraphically older surfaces. These are all problems related to the surface making process and need to be corrected for.
The folder merged contains these corrected surfaces, which all have a full area extent (where surfaces merge, thickness is zero). These merges surfaces were used to construct the Geo model. The subcrop folder contains the true areal extent of surfaces. The folder surfaces with props, contains all surfaces (true areal extent) with property attributes. These properties represent average values from extracted from the entire zone beneath the (top) surfaces.

Other data

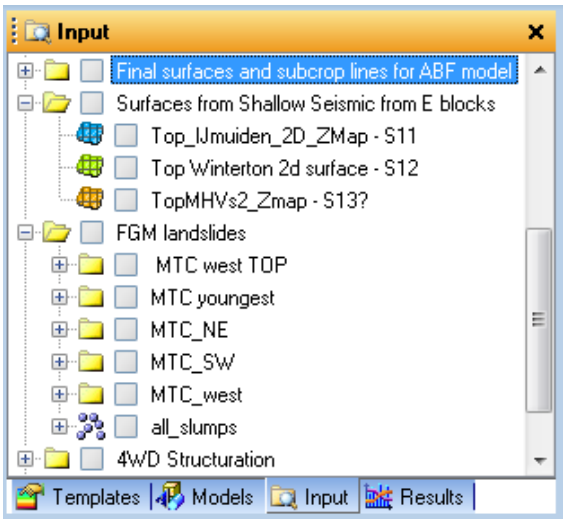

Surfaces based on interpretation from Shallow Seismic data in the E blocks, includes three surfaces that correspond to S11-S13 and which were used to constrain the interpretation and stratigraphic control presented herein.
FGM landsides, include point sets (from surfaces) that represent landslide bodies. The point sets were used to alter the grid cells in “depositional element” property were appropriate (as such adding the 10th facies types “slumps”).
The folder 4WD structuration contains information on elevation increase for all stratigraphic intervals. Based on structural anomaly maps. Outcome was used to make inferences on when 4WD traps were formed.

Property mode of the ABF blocks

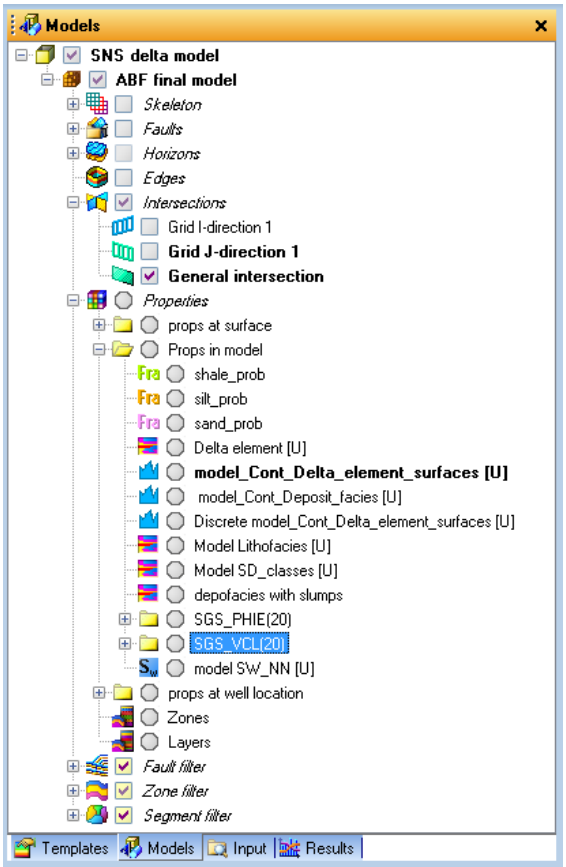

Both petrophysical estimations (Vcl, PHIE, Sw), and Facies (discrete) logs that are upscaled to the model resolution (layer thickness) and reside in the folder "*props at well location".* After populating the entire model the upscaled values can easily be displayed using filter options. To be able to display both upscaled and modelled props ("*props in model*"), the upscaled are kept in a separate folder. "*Props at surface"* contain the delta element information at the surface, which is used as input for the delta element property throughout the model.
The folder *"Horizons"* contains all Merged surfaces described above.
Zones correspond to the sequences and can be filtered with the zone filter
Layers correspond to the layering of the sequences and can be filtered with the Layer filter